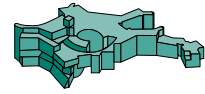




Technische Universität München



Max-Planck-Institut für Astrophysik

Modeling neutrino-driven core-collapse supernova explosions in three dimensions

Tobias Fabian Melson

Vollständiger Abdruck der von der Fakultät für Physik der Technischen Universität München zur Erlangung des akademischen Grades eines

Doktors der Naturwissenschaften (Dr. rer. nat.)

genehmigten Dissertation.

Vorsitzende:

Prof. Dr. Elisa Resconi

Prüfer der Dissertation:

1. Priv.-Doz. Dr. Hans-Thomas Janka

2. Prof. Dr. Alejandro Ibarra

3. Prof. Dr. Friedrich Röpke (schriftliche Beurteilung)

Die Dissertation wurde am 04.07.2016 bei der Technischen Universität München eingereicht und durch die Fakultät für Physik am 19.09.2016 angenommen.

Contents

| | |
|--|-----------|
| 1. Core-collapse supernovae | 5 |
| 1.1. Introduction | 5 |
| 1.2. From core collapse to shock stagnation | 6 |
| 1.3. Shock revival by neutrino heating | 6 |
| 1.4. Breaking of spherical symmetry | 7 |
| 1.5. Simulations | 8 |
| 1.6. Subject of this thesis | 10 |
| 2. Vertex-Prometheus | 11 |
| 2.1. Hydrodynamics | 11 |
| 2.2. Equation of state | 12 |
| 2.3. Neutrino transport | 12 |
| 2.4. Numerical implementation | 15 |
| 2.4.1. Hydrodynamics | 15 |
| 2.4.2. Neutrino transport | 16 |
| 2.5. Neutrino interactions | 17 |
| 3. Computational grids | 19 |
| 3.1. Spherical polar grid | 19 |
| 3.1.1. Overview | 19 |
| 3.1.2. Implementation | 20 |
| 3.2. Yin-Yang grid | 21 |
| 3.2.1. Definition and transformations | 21 |
| 3.2.2. Advantages over the spherical polar grid | 22 |
| 3.2.3. Surface integrals | 23 |
| 3.2.4. Implementation for the hydrodynamics | 23 |
| 3.2.5. Implementation for the neutrino transport | 25 |
| 3.2.6. Implementation for distributed-memory systems | 25 |
| 3.2.7. Conserved quantities | 25 |
| 3.3. Static angular mesh refinement | 26 |
| 3.3.1. Treatment of the hydrodynamics | 27 |
| 3.3.2. Flux correction | 27 |
| 3.3.3. Treatment of the neutrino transport | 28 |
| 3.3.4. Taylor-Sedov test | 28 |
| 3.4. Code scaling | 31 |
| 4. Explosion of a $9.6 M_{\odot}$ star | 33 |
| 4.1. Progenitor | 34 |
| 4.2. Numerical setup | 35 |

| | | |
|------------------------------|---|------------|
| 4.3. | Results | 36 |
| 4.3.1. | Overview | 36 |
| 4.3.2. | Differences between 2D and 3D | 45 |
| 4.3.3. | Lepton-number emission dipole | 55 |
| 4.4. | Summary and discussion | 62 |
| 5. | Explosion of a $20 M_{\odot}$ star | 65 |
| 5.1. | Progenitor | 66 |
| 5.2. | Strangeness correction | 67 |
| 5.3. | Numerical setup | 69 |
| 5.4. | Results | 70 |
| 5.4.1. | Overview | 70 |
| 5.4.2. | Effects of the strangeness correction | 78 |
| 5.4.3. | SASI and convection | 84 |
| 5.5. | Summary and discussion | 89 |
| 6. | High-resolution 3D simulation | 93 |
| 6.1. | Physical and numerical setup | 95 |
| 6.2. | Results | 96 |
| 6.2.1. | Overview | 96 |
| 6.2.2. | Energy and momentum fluxes | 105 |
| 6.2.3. | Kinetic energy spectra | 109 |
| 6.2.4. | Numerical viscosity and effective Reynolds number | 115 |
| 6.3. | Summary and discussion | 122 |
| 7. | Conclusions | 125 |
| Appendix | | 129 |
| A. | Aitoff projection | 129 |
| List of abbreviations | | 131 |
| Bibliography | | 133 |

1. Core-collapse supernovae

1.1. Introduction

Supernovae are tremendous explosions of massive stars at the end of their lives. These violent events expel stellar material into space and thus contribute significantly to the cosmic cycle of matter by enriching the interstellar medium with heavy elements. Already in ancient history, astronomers observed supernovae with the naked eye owing to their extraordinary brightness. They are among the most luminous events in the universe and can outshine their host galaxies for weeks.

There are two fundamentally different physical processes that are termed “supernova”: thermonuclear explosions of white dwarfs and core collapses of massive stars. In this work, we will discuss the latter being referred to as “core-collapse supernovae”. Besides their high luminosities, hundred times more energy is carried away by vast numbers of neutrinos playing a key role in the explosion mechanism (Colgate & White, 1966). Core-collapse supernovae are birthplaces of neutron stars and black holes, which are unique laboratories for studying matter under extreme conditions (Baade & Zwicky, 1934).

Understanding the explosion mechanism of core-collapse supernovae is indispensable for obtaining answers to several key questions. Under which conditions are heavy elements produced during the explosion and what amounts are ejected into space? What are the properties of the compact objects left behind? What is the relation between the properties of the progenitor stars and the supernova remnants?

Although light curves and spectra of the electromagnetic radiation are nowadays routinely measured, the explosion mechanism itself occurring within the first second after core collapse can hardly be studied based on these data. Instead, measuring the temporal evolution of the neutrino emission and the gravitational wave signal will allow for looking deep into the center of the stellar core and deducing details of the explosion mechanism. Unfortunately, only a few core-collapse supernovae per century occur close enough in order to be measurable in this way by detectors on Earth (Reed, 2005). The last neutrino signal was determined in 1987 for a supernova in the Large Magellanic Cloud (SN 1987A) demonstrating that neutrinos indeed play a key role during the explosion (e.g., Panagia, 2013). A gravitational wave signal from a core-collapse supernova has not been detected yet (see Abbott et al., 2016, for a recent attempt).

In order to validate theoretical models of core-collapse supernovae and to study the explosion process systematically in detail, numerical simulations are indispensable. In this work, we will present simulations in three dimensions, i.e. without symmetry constraints, performed with state-of-the-art neutrino treatment. These are the first simulations of their kind yielding successful explosions.

The common paradigm of the explosion mechanism will be described below, compiled from review articles by Bethe (1990), Janka (2012), Janka et al. (2012), Burrows (2013),

Foglizzo et al. (2015), and Janka et al. (2016). We will then motivate and explain the aim of this work.

1.2. From core collapse to shock stagnation

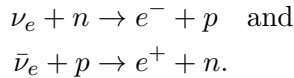
During their evolution, stars synthesize chemical elements in nuclear fusion reactions. The raw material for each burning stage is provided by the “ashes” of the previous fusion process. An onion-shell structure is thus established in the stellar interior with subsequently heavier nuclei towards the center. Massive stars heavier than about nine times the mass of the sun form an iron core surrounded by shells consisting of silicon, oxygen, neon, carbon, helium, and hydrogen. Nuclear fusion of iron-group elements does not release further energy, because these nuclei are most tightly bound. Silicon shell burning gradually increases the iron core mass, whose inwards gravitational pull is stabilized by the degeneracy pressure of the electrons. At this stage, the iron core resembles a white dwarf, which becomes gravitationally unstable beyond its Chandrasekhar mass limit. Two processes trigger and accelerate the collapse of the iron core by reducing the effective adiabatic index below $4/3$. On the one hand, rising temperatures enhance photo-dissociation of iron-group nuclei into alpha particles and free nucleons, which consumes thermal energy. On the other hand, electron captures on heavy nuclei become more frequent as the density increases, so that energy and lepton number are carried away by escaping neutrinos. During core collapse, neutrinos become trapped above a density of $10^{12} \text{ g cm}^{-3}$, because their diffusion timescale starts exceeding the free-fall timescale. The inner core continues collapsing adiabatically and homologously, while the outer core proceeds its supersonic infall.

Repulsive nuclear forces lead to an abrupt stiffening of the equation of state at a density of $\sim 2.7 \times 10^{14} \text{ g cm}^{-3}$. The collapse comes to a stop, however, the inner core overshoots the new equilibrium due to its high inertia and it rebounds. Sound waves are unleashed, which steepen into a shock when they reach the supersonically infalling outer core. As the shock propagates outwards, it loses energy, because heavy nuclei falling through the shock are dissociated into free nucleons. This consumes about 8.8 MeV per nucleon or $1.7 \times 10^{52} \text{ erg } M_{\odot}^{-1}$. When the shock passes a density of $10^{11} \text{ g cm}^{-3}$, neutrinos previously trapped behind the shock can suddenly escape and carry away energy in the neutrino burst. After a few milliseconds, the shock stalls due to these energy losses at a radius between 100 and 200 km and becomes an accretion shock with post-shock velocities pointing inwards. Material accreted through the shock slowly settles onto the hot “proto-neutron star” (PNS) born in the center. The layer between the shock and the PNS surface is in quasi-hydrostatic equilibrium (Janka, 2001). As the PNS cools by neutrino losses on timescales of seconds, it slowly contracts and the shock gradually retreats inwards.

1.3. Shock revival by neutrino heating

In order to successfully disrupt the star, a mechanism is required that deposits enough energy behind the stalled shock to revive it. Several processes were proposed, but many of them can be invalidated (see compilation in Janka, 2012). The most promising candidate is the “delayed neutrino-driven explosion mechanism” introduced by Bethe & Wilson (1985) based on the idea of Colgate & White (1966). In these pioneering works,

it was noticed that the gravitational binding energy released when the core collapses from a few thousand kilometers to several tens of kilometers is converted into internal energy providing a large reservoir for powering the explosion. Neutrinos being created in the PNS slowly diffuse through its interior to the neutrinosphere from where they can stream out nearly freely. They carry away energy and lepton number and deposit a small fraction of their energy between the neutrinosphere and the shock surface mainly by the charged-current reactions



The specific value of the heating due to neutrino absorption declines as r^{-2} , while cooling by neutrino emission due to the inverse reactions falls off steeply with r^{-6} (Janka, 2001). Consequently, neutrino heating balances neutrino cooling at a certain radius. Below this so-called “gain radius”, a layer of net neutrino cooling exists (“cooling layer”) with the inner boundary approximately being located at the neutrinosphere. The region of net neutrino heating between the gain radius and the shock is called “gain layer” (see Fig. 1.1). Successful revival of the stalled shock can only be achieved if the energy deposition in the gain layer is sufficiently large to overcome the ram pressure maintained by the infalling stellar shells.

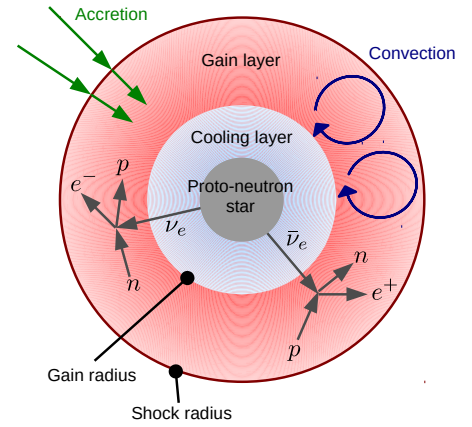


Fig. 1.1.: Sketch of the stalled-shock phase

1.4. Breaking of spherical symmetry

The simple spherically symmetric picture described above does not hold in reality. Several hydrodynamic instabilities exist that can lead to strong deformations and violent non-radial fluid motions.

There is overwhelming evidence from observations that core-collapse supernovae explode asymmetrically (Wang & Wheeler, 2008). During the explosion of SN 1987A, material was distributed highly aspherically and metal-rich clumps were mixed into the hydrogen envelope of the star (Hillebrandt & Höflich, 1989; Arnett et al., 1989; Maeda et al., 2008). It was shown in numerical models that this was caused by large-scale anisotropies at the onset of explosion (Kifonidis et al., 2003; Kifonidis et al., 2006; Hammer et al., 2010; Wongwathanarat et al., 2013; Utrobin et al., 2015). Also observations of the supernova remnant “Cassiopeia A” proved the asphericity shortly after core bounce. From measurements of the ^{44}Ti distribution, it could be inferred that low-mode convective motions occurred during shock revival (Grefenstette et al., 2014).

Neutron stars were observed travelling with several hundred kilometers per second through space (Hobbs et al., 2005). These high “kick” velocities can be explained by large-scale deformations in the early phase of the supernova explosion (Scheck et al., 2006; Wongwathanarat et al., 2010b, 2013).

Non-radial fluid motions behind the stalled shock are not only byproducts of the explosion but important ingredients for successful shock revival. Especially the gain layer

is not a calm region but convectively unstable. Neutrino heating is strongest slightly above the gain radius and weaker further out, which creates a negative entropy gradient (Bethe, 1990). Buoyant Rayleigh-Taylor mushrooms emerge and rise towards the shock. Convective overturn transports low-entropy material down to the gain radius and prevents freshly heated gas from being advected into the cooling layer. The dwell time of fluid elements in the gain layer is thus considerably longer than in spherical symmetry. Additionally, the shock is pushed outwards by high-entropy bubbles, which prolongs the time accreted matter is exposed to neutrino heating. The favorable effects of this neutrino-driven post-shock convection for shock revival were discussed in numerous studies (Herant et al., 1994; Burrows et al., 1995; Janka & Müller, 1996; Fryer & Warren, 2002, 2004; Foglizzo et al., 2006; Marek & Janka, 2009; Müller et al., 2012a; Murphy et al., 2013).

Another process that triggers large-scale asymmetries is the “standing accretion-shock instability” (SASI; Blondin et al., 2003). It manifests itself as a low-mode oscillation of the shock surface and is understood as an advective-acoustic cycle (Foglizzo, 2002; Guilet & Foglizzo, 2012). Entropy and vorticity perturbations are accreted from the shock towards the PNS. In the deceleration region above the PNS surface, pressure waves are created, which propagate outwards and perturb the surface of the accretion shock, thus establishing a feedback cycle. The SASI enhances the energy deposition in the gain layer, because the shock is regularly pushed to larger radii and secondary convection is triggered by violent shear flows (Scheck et al., 2008; Marek & Janka, 2009; Müller et al., 2012b,a; Hanke et al., 2013). Besides a “sloshing” mode where the shock oscillates from one side to the other, also a spiral mode can develop, which additionally stores kinetic energy in its rotational motion (Blondin & Mezzacappa, 2007; Yamasaki & Foglizzo, 2008; Iwakami et al., 2008, 2009; Fernández, 2010, 2015; Kazeroni et al., 2016).

1.5. Simulations

With the help of core-collapse supernova simulations, the explosion mechanism can be studied in detail, despite lacking measurements of neutrino signals or gravitational waves from a galactic event. Numerical models have to include an accurate description of the hydrodynamics, an energy-dependent multi-flavor neutrino transport scheme (see Mezzacappa et al., 2004, for an overview), and state-of-the-art neutrino-matter interactions (e.g., Buras et al., 2006b). Due to the complexity of the involved physical processes, these simulations were restricted to spherical symmetry (one dimension, 1D) and axial symmetry (two dimensions, 2D) in the past. Only in recent years, growing computational power allows for modeling supernovae in three dimensions (3D) without symmetry constraints.

Core-collapse supernovae do not explode in spherical symmetry, because crucial hydrodynamic instabilities are neglected by this symmetry assumption. This was ascertained in state-of-the-art 1D simulations, which did not yield explosions for stars heavier than about ten solar masses (Burrows et al., 1995; Rampp, 2000; Mezzacappa et al., 2001; Liebendörfer et al., 2001; Sumiyoshi et al., 2005). The neutrino energy deposition in the gain layer turned out to be too low to overcome the ram pressure of the accreted material. Only very light progenitors can explode in spherically symmetric models, because their outer shells are dilute and the ram pressure onto the shock is

therefore particularly low (Kitaura et al., 2006).

Simulations in axial symmetry with sophisticated neutrino transport can nowadays be performed routinely. Meanwhile, a large set of successfully exploding 2D simulations exists (Buras et al., 2006a,b; Bruenn et al., 2009; Marek & Janka, 2009; Suwa et al., 2010; Müller et al., 2012a,b; Bruenn et al., 2013; O'Connor & Couch, 2015; Nakamura et al., 2015; Suwa et al., 2016; Bruenn et al., 2016; Summa et al., 2016). These models differ in their physical and numerical input, but they have an important conclusion in common. Non-radial flows in the gain layer strongly support the neutrino heating process to finally revive the shock, which confirms the concept of the neutrino-driven mechanism. Nevertheless, the artificial symmetry constraint in 2D implies several drawbacks. All fluid structures are elongated into toroidal shapes, which suppresses some hydrodynamic instabilities like the SASI spiral mode. Furthermore, explosions in 2D occur predominantly along the polar directions (e.g., O'Connor & Couch, 2015; Bruenn et al., 2016; Summa et al., 2016), because the fluid cannot cross the axis for numerical reasons and is therefore channeled into radial motions. Another serious problem of 2D modeling is the unphysical behavior of turbulent processes. The fluid in the gain layer has very high Reynolds numbers and is therefore clearly turbulent (Abdikamalov et al., 2015). Following the theory of Kolmogorov (1941), this implies that kinetic energy is usually transported from the largest scales progressively to smaller scales, until it is dissipated into internal energy. However, this “forward cascade” does not hold in 2D, where kinetic energy is artificially accumulated at large scales (Kraichnan, 1967; Frisch & Sulem, 1984; Boffetta & Musacchio, 2010).

Hence, 3D simulations without symmetry restrictions are needed to explore details of the explosion mechanism. Studies in 2D should be regarded as an intermediate step, before large sets of 3D simulations with state-of-the-art neutrino treatment can be computationally afforded. Hereby, it is important to remain at the same level of sophistication as in latest 2D studies. Since the first 3D core-collapse supernova simulations of Fryer & Warren (2002, 2004), 3D modeling was always at the limits of what is feasible on supercomputers. The numerical setups of these early works were simplified accordingly, with a plain neutrino transport neglecting any energy dependence. More recently, explosions in 3D simulations were obtained by groups using parametrized neutrino heating (Couch, 2013; Couch & O'Connor, 2014; Abdikamalov et al., 2015) and neutrino transport schemes that employ simplifying assumptions for the neutrino flux density and the neutrino pressure (Takiwaki et al., 2012, 2014; Lentz et al., 2015; Müller, 2015). The Garching group applied a more sophisticated transport solver, which evolves the neutrino flux density and consistently computes higher-order terms – such as the neutrino pressure – using the solution of the underlying Boltzmann equation. They did not obtain explosions in 3D for progenitors of 11.2 , 20 , and $27 M_{\odot}$, while the corresponding 2D models exploded successfully (Hanke et al., 2013; Tamborra et al., 2013; Hanke, 2014; Tamborra et al., 2014a,b).

Simulations of core-collapse supernovae that are dedicated to studying the explosion mechanism in 3D should include the most precise neutrino transport treatment, the most accurate neutrino interaction rates, and the highest grid resolution feasible using currently available computational resources. In this context, supernova modelers concern themselves with several key questions. **(A)** Is it possible to obtain energetic explosions in 3D, even though shock revival seems to be delayed in 3D and explosion energies of many 2D models are low compared to observations? **(B)** Are the marginal

failures of 3D simulations in comparison to their successful 2D counterparts a hint towards missing physics in the current models? **(C)** How does the lack in numerical resolution of current 3D simulations influence the effects of non-radial fluid flows and turbulence in the gain layer?

1.6. Subject of this thesis

In this thesis, we will address these three questions by performing core-collapse supernova simulations in 3D with our elaborate neutrino-hydrodynamics code VERTEX-PROMETHEUS (see description in Chapt. 2). The explosions presented in this work are the first successfully exploding 3D models obtained with our simulation tool and therefore important achievements taken by themselves.

(A) As long as large sets of state-of-the-art 3D simulations are computationally not feasible, 2D simulations are still indispensable to systematically investigate the explosion mechanism of core-collapse supernovae. It is therefore particularly important to understand how findings gained in 2D are related to 3D. It was discovered in numerous studies that the different directions of the turbulent energy cascade seem to artificially favor explosions in 2D and delay shock revival in 3D (Hanke et al., 2013; Couch, 2013; Couch & O'Connor, 2014; Takiwaki et al., 2012, 2014; Lentz et al., 2015). However, the differences between 2D and 3D *after* the onset of explosion were not investigated before. It is not at all certain that 3D explosions must be weaker than their corresponding 2D counterparts. In Chapt. 4, we will indeed demonstrate that the explosion of a $9.6 M_{\odot}$ star is more powerful in 3D due to turbulent effects in the gain layer, which affect the efficiency of neutrino cooling. We will argue that involving the third dimension is not generally disadvantageous for developing energetic explosions.

(B) Sophisticated 3D simulations do not explode robustly yet, which suggests that certain physical ingredients are potentially missing in current supernova models. In Chapt. 5, we will show that a previously failed 3D simulation of a $20 M_{\odot}$ star computed with VERTEX-PROMETHEUS can be turned into a successfully exploding model by modifying the neutrino opacities in the range of current uncertainties. Experimentally and theoretically motivated strange-quark contributions to the nucleon spin change the opacities for neutrino-nucleon scattering at a level of 10%. It will be shown that neutrino heating is enhanced if this strangeness correction is applied. We will conclude that this opacity modification can be considered as a template for other neutrino interaction uncertainties and that the previously failed 3D models of the Garching group were fairly close to the explosion threshold.

(C) Core-collapse supernova simulations in 3D exhaust the resources available on current supercomputers. Hence, the accuracy of their numerical discretization is rather limited if the level of sophistication in the neutrino treatment is high. Especially the behavior of turbulent processes depends on the spatial resolution of the computational grid. In order to use a higher grid resolution compared to previous VERTEX-PROMETHEUS models, we will feature a new mesh refinement technique in Chapt. 3, whose low numerical overhead in combination with the axis-free Yin-Yang grid allows for efficiently modeling core-collapse supernovae. We will present a high-resolution 3D simulation computed with this refined grid in Chapt. 6 and compare it to a less resolved 3D case. A novel approach for measuring the numerical viscosity from the turbulent energy spectrum will be introduced and applied to both 3D models.

2. Vertex-Prometheus

The core-collapse supernova simulations presented in this thesis were performed with the VERTEX-PROMETHEUS code that combines stellar matter hydrodynamics and neutrino radiation transport. In this chapter, we will present the fundamental equations for both parts of the code and explain how these are numerically implemented.

VERTEX-PROMETHEUS has been developed by Rampp & Janka (2002) for spherically symmetric (one-dimensional, 1D) problems and extended to axisymmetric (two-dimensional, 2D) models by Buras et al. (2006b). Recently, Hanke (2014) has upgraded the code to fully three-dimensional (3D) setups. Further details about the underlying equations and the numerical treatment can be found in Rampp (2000). The equations and methods described in this chapter are taken from the aforementioned works if not otherwise referenced.

2.1. Hydrodynamics

Matter in the interior of a massive star can be described by the compressible Euler equations for an ideal, inviscid fluid because viscosity and heat conduction by physical effects are negligible (Müller, 1998). The set of equations for mass, momentum, and energy conservation reads

$$\frac{\partial \rho}{\partial t} + \nabla \cdot (\rho \vec{v}) = 0, \quad (2.1a)$$

$$\frac{\partial \rho \vec{v}}{\partial t} + \nabla \cdot (\rho \vec{v} \otimes \vec{v}) + \nabla P = -\rho \nabla \Phi + \vec{Q}_M, \quad (2.1b)$$

$$\frac{\partial \rho \epsilon}{\partial t} + \nabla \cdot ((\rho \epsilon + P) \vec{v}) = -\rho \vec{v} \cdot \nabla \Phi + Q_E + \vec{v} \cdot \vec{Q}_M, \quad (2.1c)$$

where the primitive variables ρ , \vec{v} , and ϵ are the baryon density, the velocity, and the total specific energy, respectively. ϵ is the sum of the specific internal energy e and the specific kinetic energy, i.e. $\epsilon = e + \frac{1}{2} |\vec{v}|^2$. \vec{Q}_M and Q_E denote source terms for momentum and energy exchange, respectively, due to neutrino interactions. The calculation of the gravitational potential Φ is explained in Sect. 2.4.1. The pressure P is given by the equation of state (see Sect. 2.2).

Stellar matter has a certain chemical composition. It consists of nucleons and various nuclei, whose mass fractions X_i are defined as

$$X_i = A_i \frac{n_i}{n_B}, \quad (2.2)$$

where A_i is the atomic number and n_i the number density of the nuclear species i . n_B denotes the baryon number density. In order to follow the advection of the different nuclear species, additional conservation equations are solved,

$$\frac{\partial \rho X_i}{\partial t} + \nabla \cdot (\rho X_i \vec{v}) = Q_{N_i}. \quad (2.3)$$

The source terms Q_{N_i} account for changes due to nuclear reactions. If nuclear statistical equilibrium (NSE) holds, the composition can be determined from the current thermodynamic state (see Sect. 2.2 for details).

Another conservation equation has to be solved for the electron fraction Y_e being defined as

$$Y_e = \frac{n_{e^-} - n_{e^+}}{n_B}. \quad (2.4)$$

This advection equation reads

$$\frac{\partial \rho Y_e}{\partial t} + \nabla \cdot (\rho Y_e \vec{v}) = Q_N. \quad (2.5)$$

Changes in the net electron number density are given by the source term Q_N , which is a result of the neutrino transport calculation.

2.2. Equation of state

The pressure in Eqs. (2.1) is a function of the current thermodynamic state, i.e. $P = P(\rho, e, Y_e, X_i)$. This functional dependence – the equation of state (EOS) – has to be computed in the whole range of conditions relevant for a core-collapse supernova, i.e. $10^5 \text{ g cm}^{-3} \lesssim \rho \lesssim 3.4 \times 10^{14} \text{ g cm}^{-3}$. Therefore, the EOS is divided into a low-density and a high-density regime. These are separated by a threshold density ρ_{EOS} .

Below ρ_{EOS} , a low-density EOS is applied, which describes nucleons and nuclei as classical Boltzmann gases, electrons and positrons as (non-)degenerate Fermi gases, and also includes photons (Janka, 1999).

Nuclear statistical equilibrium (NSE) is assumed above a certain threshold temperature T_{NSE} . Below that limit, nuclear burning, dissociation, and recombination are modeled in an approximate fashion (see Rampf & Janka, 2002, Appendix B.2), where the essential reactions happen instantaneously and determine the source terms Q_{N_i} in Eq. (2.3). Above T_{NSE} , NSE can be assumed and the chemical composition becomes a function of the thermodynamic variables, i.e. $X_i = X_i(\rho, e, Y_e)$.

The equation of state for dense matter is poorly known. Fortunately, ever tighter constraints from measurements of neutron star properties reduce the number of suitable EOS models (see, e.g., Fischer et al., 2014; Lattimer & Prakash, 2016). In this work, we use the high-density EOS of Lattimer & Swesty (1991) with a nuclear incompressibility parameter of 220 MeV (referred to as LS220) above ρ_{EOS} . It is based on the compressible liquid drop model taking nucleons, α particles, and one representative heavy nucleus into account. NSE is assumed above a temperature of 0.5 MeV. This EOS is compatible with astronomical measurements and has been heavily applied in previous core-collapse supernova simulations (e.g., Hanke et al., 2013; Tamborra et al., 2014a; Lentz et al., 2015; Abdikamalov et al., 2015; Müller, 2015; Roberts et al., 2016; Summa et al., 2016).

2.3. Neutrino transport

Neutrinos cannot be regarded as another fluid component of the stellar matter because their mean free path is large compared to the typical dimensions of the system in the region where they interact with the stellar matter. Consequently, they are treated as radiation and assumed to be massless particles. This is justified because the neutrino

rest masses are very small compared to their energies in the core-collapse supernova context (cf. Olive & Particle Data Group, 2014).

A statistical ensemble of particles is represented by the particle distribution function $f(\vec{r}, \vec{p}, t)$, which essentially gives the number of particles in the phase-space volume $d^3\vec{r}d^3\vec{p}$ at the position \vec{r} with momentum \vec{p} at the time t . Commonly, the specific intensity \mathcal{I} is considered instead, such that

$$\mathcal{I}(\vec{r}, \hat{n}, \varepsilon, t) \hat{n} \cdot \hat{r} d\varepsilon dA d\Omega dt \quad (2.6)$$

is the amount of energy in the energy interval $[\varepsilon, \varepsilon + d\varepsilon]$ transported through the surface element dA with its normal $\hat{r} = \vec{r}/|\vec{r}|$ in the direction \hat{n} into the solid angle $d\Omega$ during the time dt . There is a simple relation between \mathcal{I} and f ,

$$\mathcal{I} = \frac{\varepsilon^3}{h^3 c^2} f, \quad (2.7)$$

where c is the speed of light and h is Planck's constant.

The evolution of the specific intensity is described by the Boltzmann equation,

$$\frac{1}{c} \frac{\partial \mathcal{I}}{\partial t} + \hat{n} \cdot \nabla \mathcal{I} = C[\mathcal{I}]. \quad (2.8)$$

The source term appearing on the right-hand side of Eq. (2.8) is the so-called collision integral, which describes emission, scattering, and absorption of neutrinos. Due to its dependency on integrals of the specific intensity, Eq. (2.8) becomes an integro-partial differential equation. Solving such an equation is very difficult from a numerical point of view. Especially the direct solution can only be gained with great computational effort. Therefore, a different solution strategy has to be considered, namely the expansion of Eq. (2.8) into angular moments, $(4\pi)^{-1} \int d\Omega$, $(4\pi)^{-1} \int d\Omega \hat{n}$, etc. At this stage, the obtained infinite set of moment equations is equivalent to the original Boltzmann equation. However, because every moment depends on ever higher moments, the system has to be truncated and closed at a certain level. In the VERTEX-PROMETHEUS code, a two-moment closure is applied, which is gained by the so-called variable Eddington factor technique (see explanation below).

The complexity of the transport problem is further reduced by assuming that the specific intensity is axisymmetric around the radial direction and the flux is thus purely radial, i.e. $\mathcal{I} = \mathcal{I}(\vec{r}, \mu, \varepsilon, t)$, where $\mu := \hat{r} \cdot \hat{n}$. With this assumption, the angular moments simplify according to $\int d\Omega = 2\pi \int_{-1}^1 d\mu$, and the first moments of the specific intensity

can be defined as

$$J(\vec{r}, \varepsilon, t) := \frac{1}{2} \int_{-1}^1 d\mu \mathcal{I}(\vec{r}, \mu, \varepsilon, t), \quad (2.9a)$$

$$H(\vec{r}, \varepsilon, t) := \frac{1}{2} \int_{-1}^1 d\mu \mu \mathcal{I}(\vec{r}, \mu, \varepsilon, t), \quad (2.9b)$$

$$K(\vec{r}, \varepsilon, t) := \frac{1}{2} \int_{-1}^1 d\mu \mu^2 \mathcal{I}(\vec{r}, \mu, \varepsilon, t), \quad (2.9c)$$

$$L(\vec{r}, \varepsilon, t) := \frac{1}{2} \int_{-1}^1 d\mu \mu^3 \mathcal{I}(\vec{r}, \mu, \varepsilon, t). \quad (2.9d)$$

⋮

Besides the reduction of the computational effort, the expansion into angular moments has also a physical motivation. The directional dependence of the specific intensity is not relevant. Only integrals over the angles are important for the interaction of the radiation field with the fluid. The first two moments, J and H , can directly be interpreted as neutrino energy density and neutrino energy flux, respectively.

As already mentioned, the moment equations are closed with a variable Eddington factor method. The Eddington factors $f_K = K/J$ and $f_L = L/J$ are determined from the solution of a simplified Boltzmann equation in an iterative procedure. Estimates for J and H are used to compute the right-hand side of the simplified equation, which can then be solved. With the new Eddington factors, updated estimates for the moments can be calculated from the moment equations. This procedure is repeated until f_K and f_L are converged.

Finally, the source terms for the hydrodynamic equations can be determined. Although the neutrino flux is assumed to have only a radial component, non-radial advection of neutrinos and non-radial neutrino pressure gradients have to be considered in the optically thick region (Buras et al., 2006b; Hanke, 2014). Therefore, the angular components of the momentum source term \vec{Q}_M do not vanish. The source terms for Eqs. (2.1) and Eq. (2.5) are given by

$$Q_E = - \int_0^\infty d\varepsilon \int d\Omega C[\mathcal{I}], \quad (2.10a)$$

$$\vec{Q}_M = - \frac{1}{c} \int_0^\infty d\varepsilon \int d\Omega \hat{n} C[\mathcal{I}], \quad (2.10b)$$

$$Q_N = -m_B \int_0^\infty d\varepsilon \varepsilon^{-1} \int d\Omega C[\mathcal{I}], \quad (2.10c)$$

where m_B is the baryon mass.

Two important diagnostic quantities are often used to characterize the neutrino radiation field, the mean energy $\langle \varepsilon \rangle$ and the luminosity L (not to be confused with the third angular moment, Eq. (2.9d)). These two quantities are defined as

$$\langle \varepsilon \rangle(r, t) = \frac{\int d\Omega \int_0^\infty d\varepsilon J(\vec{r}, \varepsilon, t)}{\int d\Omega \int_0^\infty d\varepsilon \varepsilon^{-1} J(\vec{r}, \varepsilon, t)} \quad (2.11)$$

and

$$L(r, t) = r^2 \int d\Omega \int_0^\infty d\varepsilon H(\vec{r}, \varepsilon, t) \quad (2.12)$$

at a certain radial distance r and time t .

2.4. Numerical implementation

The equations of radiation hydrodynamics are solved in an operator-split procedure in VERTEX-PROMETHEUS. For instance, a conservation equation of the form

$$\frac{\partial \rho \mathcal{X}}{\partial t} + \nabla \cdot (\rho \mathcal{X} \vec{v}) = Q_{\mathcal{X}} \quad (2.13)$$

is split into two equations,

$$\frac{\partial \rho \mathcal{X}}{\partial t} + \nabla \cdot (\rho \mathcal{X} \vec{v}) = 0 \quad (2.14)$$

and

$$\rho \mathcal{X} \Delta t = Q_{\mathcal{X}}, \quad (2.15)$$

where \mathcal{X} is a placeholder for a primitive variable and Δt denotes the length of the timestep. In this example, Eq. (2.14) is solved by the hydrodynamics module. The source term $Q_{\mathcal{X}}$ is computed in the neutrino transport part and finally applied according to Eq. (2.15).

In the following two sections, the numerical implementation of the two VERTEX-PROMETHEUS modules is presented.

2.4.1. Hydrodynamics

The hydrodynamics module of VERTEX-PROMETHEUS is based on the well-known PROMETHEUS code (Fryxell et al., 1989), which is a Newtonian finite-volume solver for the conservation equations (2.1), (2.3), and (2.5). PROMETHEUS solves hydrodynamic problems on orthogonal grids in spherical symmetry (1D), axial symmetry (2D), or full three dimensions (3D) with high numerical accuracy. It uses the piecewise parabolic method (PPM; Colella & Woodward, 1984), which is third-order accurate in space and second-order in time, for reconstruction. An exact Riemann solver calculates one-dimensional Riemann problems (“sweeps”) that are extracted from the multi-dimensional equations by Strang splitting (Strang, 1968). In the vicinity of strong shocks, the HLLE solver (Einfeldt, 1988) is used to avoid odd-even decoupling (Quirk, 1994). Boundary conditions for the Riemann solvers are provided by appropriately filled ghost cells. The consistent multi-fluid advection method (CMA; Plewa & Müller, 1999) is applied to ensure accurate advection of the 25 different nuclear species included in our models.

The hydrodynamics in VERTEX-PROMETHEUS is treated in a purely Newtonian description, however, the gravitational potential includes general-relativistic effects. It is deduced from the Tolman-Oppenheimer-Volkoff (TOV) equation as described by Marek et al. (2006, *Case A*). The gravitational potential is dominated by the density distribution of the proto-neutron star, which hardly deviates from spherical symmetry. All simulations in this work are therefore performed with a spherically symmetric potential based on angle-averaged quantities.

Different computational meshes are available in the 2D and 3D setups of VERTEX-PROMETHEUS. These grids are described in detail in Chapter 3 as being one of the important aspects of this thesis.

The timestep of PROMETHEUS is constrained by the Courant-Friedrichs-Lowy (CFL; Courant et al., 1928) criterion, which is restrictive for small grid cells, high velocities, and high speeds of sound.

The core collapse is always computed in spherical symmetry with a pseudo-Lagrangian radial grid. At core bounce, 400 logarithmically distributed radial zones are set up. The radial grid is fixed but gradually refined during the simulation to ensure sufficiently high resolution of the cooling region and the proto-neutron star surface. For 2D or 3D simulations, breaking of spherical symmetry is achieved by 0.1% density perturbations at 10 ms after core bounce in the whole computational domain.

During collapse, the EOS threshold density ρ_{EOS} (see Sect. 2.2) is set to values between $3 \times 10^7 \text{ g cm}^{-3}$ and $3 \times 10^8 \text{ g cm}^{-3}$. The exact value will be mentioned in the corresponding introductory sections of the following chapters. After core bounce, $\rho_{\text{EOS}} = 10^{11} \text{ g cm}^{-3}$ for all models.

There are two different treatments for the NSE threshold temperature T_{NSE} . It is either set to a constant value of 0.5 MeV, or it is set to 0.5 MeV for infalling matter and to 0.343 MeV for neutrino-heated high-entropy matter. Again, which of these cases is applied for the simulations in this thesis will be mentioned in the following chapters.

2.4.2. Neutrino transport

The neutrino transport solver VERTEX computes spherical radiation transport problems with the variable Eddington factor method (see Sect. 2.3 for details). This is done for each angular bin, i.e. for each radial ray, in an implicit way. In the optically thick regime above a density of $10^{12} \text{ g cm}^{-3}$, non-radial neutrino advection and contributions from non-radial neutrino pressure gradients are taken into account in order to avoid unphysical convection in the proto-neutron star (Buras et al., 2006b). The whole treatment is referred to as “ray-by-ray plus”.

VERTEX computes transport solutions for three neutrino species, ν_e , $\bar{\nu}_e$, and $\nu_x = \{\nu_\mu, \bar{\nu}_\mu, \nu_\tau, \bar{\nu}_\tau\}$. The heavy-lepton neutrinos are combined into a single representative type ν_x because they only participate in neutral-current processes and are treated equally. Consequently, the source terms Q_E and \vec{Q}_M for Eqs. (2.1) must be summed over all neutrino species, $Q_E = \sum_\nu Q_E(\nu)$ and $\vec{Q}_M = \sum_\nu \vec{Q}_M(\nu)$, respectively. The right-hand side of Eq. (2.5) is $Q_N = Q_N(\nu_e) - Q_N(\bar{\nu}_e)$.

The transport part of VERTEX-PROMETHEUS is fully energy dependent and operates on energy bins. In this work, we employ 12 logarithmically spaced bins from 0 to 380 MeV. Energy bin coupling is taken into account.

For numerical stability, the moment equations are transformed into and solved in the fluid’s comoving frame up to $\mathcal{O}(v/c)$. Thus, additional terms appear in Eq. (2.8)

accounting, among others, for redshift and time dilatation effects.

Due to the time-implicit solution strategy of the neutrino transport calculation, its timestep is larger than the hydrodynamic timestep. Several PROMETHEUS substeps are therefore computed during one VERTEX step. This is beneficial since the wall clock time for gaining the transport solution is much longer than for solving the hydrodynamic equations.

2.5. Neutrino interactions

A variety of neutrino-matter and neutrino-neutrino interactions is included in VERTEX-PROMETHEUS. In Tab. 2.1, a compilation of these reactions is given together with corresponding references to the literature. Details about the numerical implementation can be found in Rampp & Janka (2002), Buras et al. (2003), and Buras et al. (2006b, esp. Appendix A).

| Reaction | References |
|--|---|
| $\nu e^\pm \rightleftharpoons \nu e^\pm$ | Mezzacappa & Bruenn (1993a); Cernohorsky (1994) |
| $\nu A \rightleftharpoons \nu A$ | Horowitz (1997); Bruenn & Mezzacappa (1997) |
| $\nu N \rightleftharpoons \nu N$ | Burrows & Sawyer (1998) |
| $\nu_e n \rightleftharpoons e^- p$ | Burrows & Sawyer (1999) |
| $\bar{\nu}_e p \rightleftharpoons e^+ n$ | Burrows & Sawyer (1999) |
| $\nu_e A' \rightleftharpoons e^- A$ | Bruenn (1985); Mezzacappa & Bruenn (1993b) |
| $\nu \bar{\nu} \rightleftharpoons e^- e^+$ | Bruenn (1985); Pons et al. (1998) |
| $\nu \bar{\nu} N N \rightleftharpoons N N$ | Hannestad & Raffelt (1998) |
| $\nu_{\mu,\tau} \bar{\nu}_{\mu,\tau} \rightleftharpoons \nu_e \bar{\nu}_e$ | Buras et al. (2003) |
| $\nu_{\mu,\tau} \nu_e \rightleftharpoons \nu_{\mu,\tau} \nu_e$ | Buras et al. (2003) |
| $\bar{\nu}_{\mu,\tau} \bar{\nu}_e \rightleftharpoons \bar{\nu}_{\mu,\tau} \bar{\nu}_e$ | Buras et al. (2003) |

Tab. 2.1.: Neutrino interactions included in the VERTEX-PROMETHEUS code. ν is a placeholder for any neutrino or antineutrino. A and N denote nuclei and nucleons, respectively.

3. Computational grids

In order to solve equations numerically, the involved quantities must be discretized on a computational grid. It should always be chosen appropriately in order to, for example, conserve symmetries of the investigated physical problem or express equations in a simple way. In this work, we model core-collapse supernovae which are spherical events to first order, although multi-dimensional effects are essential for the explosion mechanism and can lead to strong deformation (see the following chapters for examples). Therefore, it is convenient to use spherical grids that are able to preserve spherical symmetry accurately. Several computational meshes exist fulfilling this requirement (e.g., Ronchi et al., 1996; Kageyama & Sato, 2004; Calhoun et al., 2008; Reisswig et al., 2013). Two different spherical grids are available in the VERTEX-PROMETHEUS code and will be described in detail in this chapter: the common spherical polar grid and the Yin-Yang grid. Moreover, a new mesh refinement technique will be explained in which the angular grid resolution can be varied in different radial intervals.

The PROMETHEUS code (Fryxell et al., 1989) is used with the well-known spherical polar coordinates (r, θ, ϕ) in VERTEX-PROMETHEUS. This tuple is reduced to (r, θ) and (r) for axisymmetric (2D) and spherically symmetric (1D) models, respectively. In this chapter, we are only considering three-dimensional (3D) models covering the full 4π sphere, although many explanations given below are also applicable to 2D models.

3.1. Spherical polar grid

3.1.1. Overview

The spherical mesh configuration with $r \in [0, R_{\max}]$, $\theta \in [0, \pi]$, and $\phi \in [0, 2\pi]$ is referred to as the spherical polar grid in this work. Its radial zones are distributed logarithmically up to a maximum radius R_{\max} of usually 10^9 cm. At the outer edge of the grid an inflow boundary condition is applied with a constant mass inflow rate. The angular zones are spaced equidistantly with reflecting boundaries in θ direction and periodic boundaries in ϕ direction. This computational mesh has been successfully used in numerous 3D core-collapse supernova simulations with VERTEX-PROMETHEUS (Hanke et al., 2012, 2013; Tamborra et al., 2014a; Melson et al., 2015a).

For a given radius, two grid singularities exist at the poles of the spherical polar grid (where $\theta = 0$ and $\theta = \pi$). Meridians (i.e. lines of constant ϕ) converge towards the poles and cause the grid cells lying on a spherical shell to become narrower and eventually wedge-shaped directly at the polar axis. Two drawbacks emerging from this behavior are explained in the following paragraphs.

Timestep constraints. As already described in Sect. 2.4.1, the hydrodynamic timestep is constrained by the Courant-Friedrichs-Lowy (CFL) condition, which scales with the grid cell size. Usually, the narrowest cells determine the timestep, at least if the

velocities are not extraordinarily high elsewhere. In our case, the smallest cells are located at the polar regions for a given constant radius.

Axis artifacts. In 3D core-collapse supernova simulations, it has been observed that shortly after core bounce buoyant Rayleigh-Taylor mushrooms first rise at the poles before they are distributed stochastically across the sphere (e.g., Wongwathanarat et al., 2010a; Müller, 2015). Generally, neutrino-heated high-entropy bubbles only rise if buoyancy overcomes drag forces. The latter contain contributions from the implicit viscosity of the numerical scheme. This “numerical viscosity” (e.g., Müller, 1998) will be further addressed in Chapt. 6. In short, a higher grid resolution, i.e. smaller grid cells, reduce the numerical viscosity and allow buoyant bubbles to rise faster along the axis. Although the described issue becomes subsidiary for the dynamics of the model as soon as convection has fully developed, the polar singularities remain potential sources for numerical artifacts.

To sum up, we observe that the small cells near the axis, on the one hand, strongly constrain the timestep of our hydrodynamic scheme and, on the other hand, lead to a reduced numerical viscosity that possibly causes axis artifacts. Consequently, it would be beneficial to have a spherical grid whose cells are equal in size across the angular domain. In Sect. 3.2, we present such a computational mesh – the Yin-Yang grid – which mitigates the problems of the conventional spherical polar grid and is therefore perfectly suited for replacing the latter.

3.1.2. Implementation

Before explaining the Yin-Yang grid in the next section, we will depict the numerical implementation of the spherical polar grid here.

The implementation of the spherical polar grid in the VERTEX-PROMETHEUS code is based on directional Strang splitting as mentioned in Sect. 2.4.1. Boundary conditions for the extracted one-dimensional Riemann sweeps are supplied by appending ghost cells to their ends. These additional cells are filled with the required primitive variables before the Riemann problems are solved. On shared-memory architectures, this procedure is straightforward. However, difficulties arise on distributed-memory systems, where the data for the ghost cells has to be communicated explicitly. Technically, the domain decomposition is done in the angular domain, such that every compute node consisting typically of 16 compute cores hosts a certain part of the angular grid and full radial sweeps. No communication is therefore necessary in the radial direction, which is beneficial for the non-local ray-by-ray neutrino transport. Communication is only required for θ and ϕ sweeps and for neutrino advection terms and neutrino pressure gradients in the optically thick regime (cf. Sect. 2.4.2). Generally, every neutrino transport ray is assigned to one compute core. This setup ensures VERTEX-PROMETHEUS’s excellent computational efficiency (Marek et al., 2014) and linear scaling behavior (see Fig. 3.5).

For a given radius, the timestep is constrained by the cells at the poles as described above. Furthermore, the grid cell sizes converge towards the origin, which is another grid singularity. Hence, a strategy to allow for longer hydrodynamic timesteps in 3D simulations with the spherical polar grid is to treat the innermost core with a radius of

10 km in spherical symmetry (1D). This is justified because this region is convectively stable and non-radial fluid velocity components are negligible. Riemann problems in the angular directions can be ignored and the timestep is therefore only constrained by the radial extent of the zones. Ghost cells at the outer boundary of this 1D core are provided by angular averages of the innermost zones of the 3D region. At the interface between these two domains, an algorithm ensures that conservation laws are exactly fulfilled. This procedure is described in detail in Sect. 3.3.2.

3.2. Yin-Yang grid

The Yin-Yang grid is a composite of two geometrically identical grid patches (called *Yin* and *Yang*) which together form a spherical grid. Its construction was introduced by Kageyama & Sato (2004) and first applied to geophysical problems. We will briefly summarize the properties of this grid, give the necessary coordinate transformations, and explain the implementation into the VERTEX-PROMETHEUS code.

3.2.1. Definition and transformations

Both grid patches of the Yin-Yang grid are low-latitude subsets of the spherical polar grid and therefore locally described by spherical polar coordinates (r, θ_Y, ϕ_Y) , where the subscript “Y” is a placeholder for “Yin” and “Yang”. The angular coordinates are defined in the intervals

$$\theta_Y \in \left[\frac{\pi}{4}, \frac{3\pi}{4} \right], \quad (3.1a)$$

$$\phi_Y \in \left[-\frac{3\pi}{4}, \frac{3\pi}{4} \right]. \quad (3.1b)$$

Yin and *Yang* have identical local coordinates but are rotated against each other and overlapped such that the whole sphere is covered (see Fig. 3.1 for a three-dimensional visualization). Kageyama & Sato (2004) presented the following transformations based on a global Cartesian coordinate system. For the *Yin* grid part, they defined

$$\begin{pmatrix} x \\ y \\ z \end{pmatrix} = \begin{pmatrix} r \sin \theta_{\text{Yin}} \cos \phi_{\text{Yin}} \\ r \sin \theta_{\text{Yin}} \sin \phi_{\text{Yin}} \\ r \cos \theta_{\text{Yin}} \end{pmatrix}. \quad (3.2)$$

After the rotation matrix

$$\begin{pmatrix} -1 & 0 & 0 \\ 0 & 0 & 1 \\ 0 & 1 & 0 \end{pmatrix} \quad (3.3)$$

is applied, the transformation for the *Yang* part reads

$$\begin{pmatrix} x \\ y \\ z \end{pmatrix} = \begin{pmatrix} -r \sin \theta_{\text{Yang}} \cos \phi_{\text{Yang}} \\ r \cos \theta_{\text{Yang}} \\ r \sin \theta_{\text{Yang}} \sin \phi_{\text{Yang}} \end{pmatrix}. \quad (3.4)$$

Note that the radial axes are equal in both grid parts and therefore not distinguished. The two equations (3.2) and (3.4) can be combined into a single transformation for the

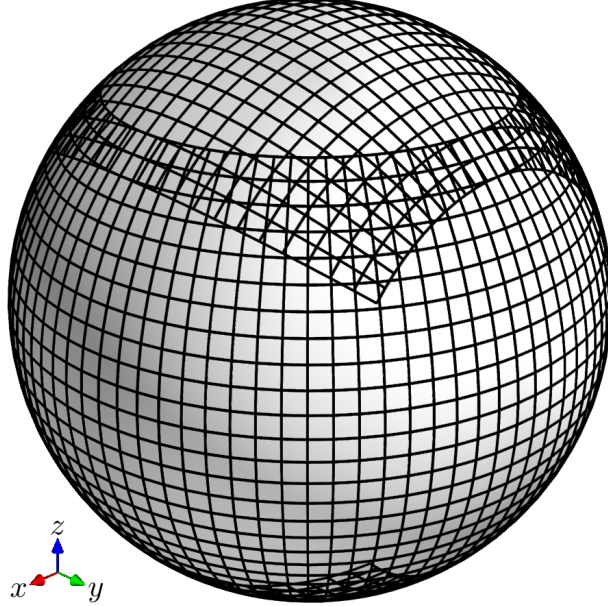


Fig. 3.1.: Visualization of the Yin-Yang grid cell edges for a given constant radius and an angular grid resolution of 4° .

Yin and *Yang* angular coordinates,

$$\theta_{\text{Yang}} = \arccos(\sin \theta_{\text{Yin}} \sin \phi_{\text{Yin}}), \quad (3.5a)$$

$$\phi_{\text{Yang}} = \arctan\left(-\frac{\cos \theta_{\text{Yin}}}{\sin \theta_{\text{Yin}} \cos \phi_{\text{Yin}}}\right), \quad (3.5b)$$

where the appropriate inverse transformation is obtained by interchanging the subscripts “Yin” and “Yang”.

The transformation for vector components is

$$\begin{pmatrix} v_r \\ v_\theta \\ v_\phi \end{pmatrix}_{\text{Yang}} = \begin{pmatrix} 1 & 0 & 0 \\ 0 & -\sin \phi_{\text{Yin}} \sin \phi_{\text{Yang}} & -\cos \phi_{\text{Yin}} (\sin \theta_{\text{Yang}})^{-1} \\ 0 & \cos \phi_{\text{Yin}} (\sin \theta_{\text{Yang}})^{-1} & -\sin \phi_{\text{Yin}} \sin \phi_{\text{Yang}} \end{pmatrix} \begin{pmatrix} v_r \\ v_\theta \\ v_\phi \end{pmatrix}_{\text{Yin}}. \quad (3.6)$$

Here, the inverse transformation can again be gained by interchanging the subscripts.

3.2.2. Advantages over the spherical polar grid

The most prominent advantage of the Yin-Yang grid construction is that the polar regions of the spherical polar grid are excised. Problems in connection with the grid singularities at the axis as described in Sect. 3.1 are circumvented. Additionally, the cell sizes at constant radius are fairly equal throughout the grid patches. To be more specific, the cell area

$$dA = r^2 \sin \theta_Y d\theta_Y d\phi_Y \quad (3.7)$$

only varies marginally in the interval defined in Eq. (3.1a) for a constant radius r . As a consequence, the CFL timestep on the Yin-Yang grid is longer than on the spherical

polar grid for a given radius and a given angular resolution of the coarsest cells. However, instead of taking the advantage of a larger timestep, the radius of the spherically symmetric inner core is reduced from 10 km to about 1.6 km (cf. Sect. 3.1.2) so that the timestep remains similar to the spherical polar grid case. Reducing the size of the core is required for long-term simulations in which the bottom of the convectively unstable layer in the proto-neutron star interior can shrink to a radius of 10 km or less. Since the calculation of a hydrodynamic step is computationally cheap compared to a neutrino transport step, no notable overhead occurs by this practice.

Furthermore, the usage of the Yin-Yang grid in a numerical scheme that has been developed for spherical coordinates is only slightly more difficult. The fact that *Yin* and *Yang* are locally spherical grids allows for applying the same equations as for the conventional spherical polar grid. Only a small computational overhead has to be taken into account, which will be described in the following sections.

3.2.3. Surface integrals

Integrals over the whole computational domain of the Yin-Yang grid (e.g. for determining the spherically symmetric gravitational potential) are not trivial. From the construction of the grid with its overlapping region, it is obvious that a surface integral over the whole sphere is not just the sum of both grid patches because

$$\int_{\frac{\pi}{4}}^{\frac{3\pi}{4}} \sin \theta_Y d\theta_Y \int_{-\frac{3\pi}{4}}^{\frac{3\pi}{4}} d\phi_Y \approx 2.12\pi > 2\pi, \quad (3.8)$$

where the integration boundaries are defined in Eqs. (3.1). Instead, a “surface weight” $w(\theta_Y, \phi_Y)$ has to be defined such that

$$S_Y := \int_{\frac{\pi}{4}}^{\frac{3\pi}{4}} \sin \theta_Y d\theta_Y \int_{-\frac{3\pi}{4}}^{\frac{3\pi}{4}} d\phi_Y w(\theta_Y, \phi_Y), \quad (3.9)$$

where “Y” is again a placeholder for “Yin” and “Yang”, and

$$S_{\text{Yin}} + S_{\text{Yang}} \stackrel{!}{=} 4\pi. \quad (3.10)$$

The algorithm for determining the weight function $w(\theta_Y, \phi_Y)$ was introduced by Peng et al. (2006). For cells located completely inside the Yin-Yang overlap, the weight is set to 0.5, whereas cells entirely outside are weighted with 1. For the remaining cases, the fraction of the cell area lying inside the overlap region is integrated numerically.

3.2.4. Implementation for the hydrodynamics

The Yin-Yang grid implementation into the hydrodynamics module of the VERTEX-PROMETHEUS code was done by Melson (2013) for shared-memory systems. It was guided by the work of Wongwathanarat et al. (2010a), who implemented the grid into a different PROMETHEUS-based supernova code. In this section, we will briefly summarize how the hydrodynamics is treated on the Yin-Yang grid. Our extension of this grid for

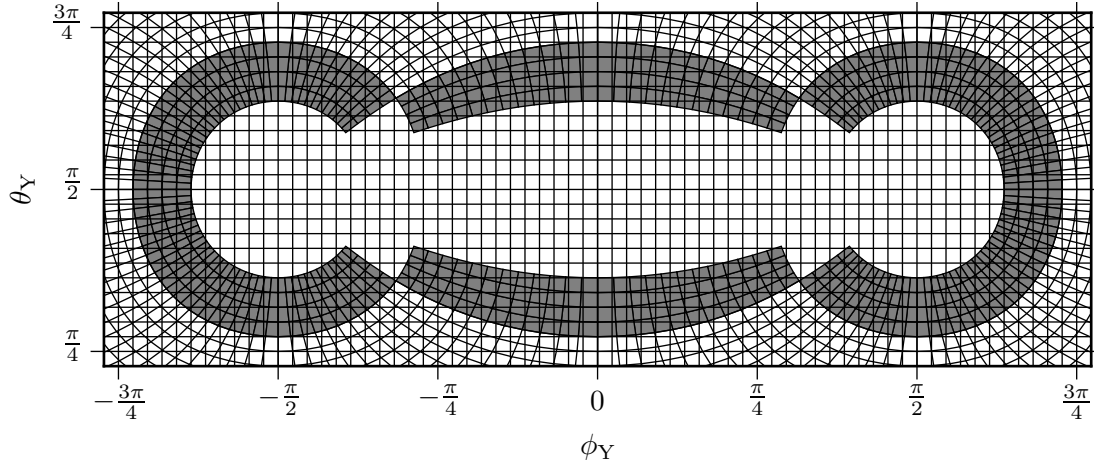


Fig. 3.2.: Angular grid of one Yin-Yang patch with local coordinates θ_Y and ϕ_Y . The overlap with the other grid part (white cells at the edges of the plot) and its ghost cells (gray-shaded cells) can be seen. A seam of four ghost cells is necessary in VERTEX-PROMETHEUS. Note the non-trivial distorted shape of the ghost zones.

the neutrino transport solver and the implementation for distributed-memory systems will be outlined in the following two sections.

As *Yin* and *Yang* are locally described by spherical coordinates, the solution procedure of the hydrodynamic equations is identical to the case of the spherical polar grid. It is especially noteworthy that both grid patches can be treated equally and the directional Strang splitting is done independently of each other. Because *Yin* and *Yang* share the same radial axis, no special procedure is required for the radial sweep.

Usually, a seam of “buffer cells” is added to the four edges of the *Yin* and *Yang* angular domains (visible in Fig. 3.1). These additional cells ensure that the sphere is covered completely despite possible numerical inaccuracies of the grid cell positions.

The only link between *Yin* and *Yang* in the hydrodynamics part of the VERTEX-PROMETHEUS code is realized by exchanging data for the ghost cells of the θ_Y and ϕ_Y sweeps. These cells are visualized in Fig. 3.2 as gray-shaded areas. At the beginning of a hydrodynamic timestep, the ghost cell centers are expressed in coordinates of the corresponding other grid patch using Eqs. (3.5). The grid cells hosting the required data are determined and interpolation weights are computed. All required conserved quantities are then interpolated bilinearly onto the centers of the ghost cells. After that, the momentum components are transformed applying the vector transformation as in Eq. (3.6).

Unlike Wongwathanarat et al. (2010a), who filled the ghost zones for every sweep separately, we update the ghost cell values only at the beginning of a hydrodynamic step. The ghost zones are part of the computational domain in our implementation and their quantities are consistently evolved in the three directional sweeps. It turned out that this procedure enhances numerical stability, which is plausible, because a consistent hydrodynamic state is reached only after all sweeps have been solved.

3.2.5. Implementation for the neutrino transport

The ray-by-ray plus strategy of the VERTEX-PROMETHEUS code only requires additional Yin-Yang overhead for the non-radial neutrino advection terms and the non-radial neutrino pressure gradients. Similarly to the ghost cells above, the required quantities for the angular neutrino transport terms for one Yin-Yang grid part are interpolated from the other patch. The neutrino transport solution itself is computed on radial rays and therefore no additional special treatment is needed.

3.2.6. Implementation for distributed-memory systems

Exchanging ghost cell values for the Yin-Yang grid is especially complicated on distributed-memory architectures. As already mentioned in Sect. 3.1.2, the domain decomposition is done in the angular directions, which is the best strategy for the ray-by-ray neutrino transport. Besides the usual next-neighbor communication for nodes storing angular domain subsets from the interior of the *Yin* and *Yang* grids, additional data exchange is necessary for nodes at the edges of both grid parts. Obviously, filling the ghost cells requires a point-to-point communication procedure because of the non-trivial arrangement of these cells (cf. Fig. 3.2). For every ghost zone, it has to be determined which node hosts the data needed for the interpolation and to which node the interpolated quantities have to be sent.

Despite this communication overhead of the Yin-Yang grid, its scaling behavior in our implementation is excellent as illustrated in Fig. 3.5. This is related to the fact that – given a certain problem size – the number of point-to-point communication operations for an individual node decreases with increasing number of compute cores, i.e. smaller individual angular domain chunks.

3.2.7. Conserved quantities

Although the Yin-Yang grid has several advantages over the spherical polar grid, there exists a drawback that is caused by its composite character. Because the values for the ghost cells are interpolated from the respective other grid patch, physically conserved quantities, like the total mass or the total energy, are not automatically numerically conserved. PROMETHEUS is in principle able to exactly conserve these quantities, but only for coherent grid configurations, i.e. for the spherical polar grid or the Yin-Yang grid parts individually. Numerical inaccuracies, however, occur at the edges of *Yin* and *Yang* due to the ghost cell interpolation procedure.

Increasing the grid resolution helps enhancing the accuracy, but comes with the price of a higher computational cost. Using a higher-order interpolation for the ghost cells shows only a minor improvement and potentially introduces further errors. Both ideas can therefore not easily be realized. Alternatively, Peng et al. (2006) described an algorithm that is theoretically able to exactly conserve all quantities. It compares the Riemann fluxes across the grid edges in θ_Y and ϕ_Y directions with fluxes deduced from the underlying grid part at the same spatial position. Both fluxes should be equal and hence differences result in updates of conserved variables in the cells at the grid edge. Unfortunately, this algorithm turns out to be numerically unstable and can therefore not be applied.

But even without further modifications, the conservation laws in our simulations are

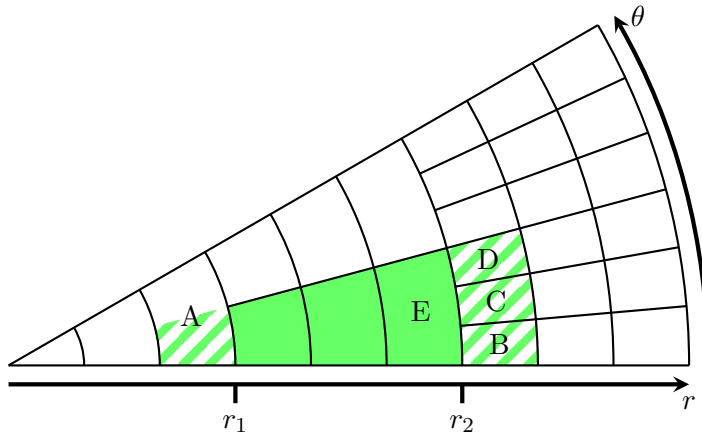


Fig. 3.3.: Example of a setup with the static mesh refinement (SMR) in two dimensions. The angular resolution increases to a factor of 6 from the center to the outer edge of the grid. The ghost cells for the green-shaded radial sweep between r_1 and r_2 are illustrated as green hatched areas.

violated only by about 10^{-3} over several hundred milliseconds. In the case of typical rotating models, which have large continuous fluxes across the Yin-Yang boundaries, an accuracy of at worst several 10^{-3} is maintained (Summa, 2016). Nevertheless, we will describe a procedure in the remaining sections of this chapter that allows for increasing the angular resolution and therefore also the accuracy to which conservation laws are fulfilled.

3.3. Static angular mesh refinement

Both the spherical polar grid and the Yin-Yang grid have a common disadvantage. The surface element $dA = r^2 \sin \theta_Y d\theta d\phi$ is proportional to the radius squared. For a given constant angular resolution, the effective size of the grid cells grows with increasing radius. Here, we present a new static mesh refinement (SMR) technique, which compensates for the diverging structure of these spherical grids. The physical motivation for increasing the effective resolution will be addressed in Chapt. 6, where we will apply the new grid to a three-dimensional core-collapse supernova simulation including neutrino transport.

The SMR setup allows us to define certain radial intervals with different angular resolution. An example for such a setup is given in Fig. 3.3 in two dimensions for coordinates (r, θ) . Although this was chosen for the sake of simplicity here, the discussion is completely analogue for the 3D case. Let us define the angular resolution for $r < r_1$ as ψ . Then, the resolution between r_1 and r_2 is 2ψ , and further refined to 6ψ for $r > r_2$.

Generally, arbitrary integer refinement steps and an arbitrary number of concentric layers can be chosen in our implementation. Note that the inner spherically symmetric volume, which is used to allow for larger hydrodynamic timesteps (cf. Sect. 3.1.2), can be understood as a special case with the lowest possible angular resolution corresponding to the whole sphere.

3.3.1. Treatment of the hydrodynamics

Generally, the SMR procedure only affects the radial direction. The computations of θ and ϕ sweeps remain unchanged. Besides the spherical polar grid, using the Yin-Yang grid is thus also possible and only requires a slight modification. As the angular resolution changes in the computational domain, the Yin-Yang ghost cell positions are different for each refinement layer, which has to be considered when data is exchanged between both grid patches.

Radial sweeps are computed separately for every layer. For an example, consider the green filled grid cells in Fig. 3.3, for which the radial sweep should be calculated. Let us assume that one ghost cell is needed below and one above this sweep, depicted as green hatched areas. For the lower end, the ghost cell data can directly be taken from cell A. This is because finite-volume methods generally assume that values in a cell always represent averages. For the upper end of the sweep, we need to average over cells B, C, and D to get the required data. Generally, averaging is required for the ghost cells located at the finer neighboring layer. This is the reason why only integer refinement steps are allowed in the SMR construction. Otherwise, computing the averages would be difficult and introduce additional interpolation errors.

3.3.2. Flux correction

If we naively used the averaged ghost cell data from the finer layer at the outer end of a radial sweep, numerical inaccuracies would occur resulting in the violation of conservation laws. In order to ensure exact conservation of the conserved quantities from Eqs. (2.1), (2.3), and (2.5), a “flux correction” algorithm is applied acting on the outermost cell of each refinement region. We will explain this procedure with the aid of Fig. 3.3. Note that the flux correction is also done for the spherically symmetric innermost volume, which has been introduced to mitigate the timestep constraints at the grid origin.

In our example illustrated in Fig. 3.3, the flux correction considers the interface between the cell E and the cells B, C, and D at r_2 . After all radial sweeps are calculated, the quantity \mathcal{X} – a placeholder for a conserved quantities in our hydrodynamic scheme – should be exactly conserved. The considered interface at r_2 is part of four different radial sweeps: the sweep between r_1 and r_2 containing the cell E, and the three sweeps beyond r_2 containing the cells B, C, and D. In the following, we discuss the different Riemann fluxes of \mathcal{X} at the interfaces between these four cells and their corresponding ghost zones. Let \mathcal{F}_E be the flux density of \mathcal{X} at the *upper* edge of the cell E. Likewise, \mathcal{F}_B , \mathcal{F}_C , and \mathcal{F}_D , denote the flux densities at the *lower* boundaries of the cells B, C, and D, respectively. All these fluxes are evaluated at the interface r_2 with positive values corresponding to the radially outflowing direction. The areas of the cell interfaces are labeled A_E , A_B , A_C , and A_D . Theoretically, it should hold

$$\mathcal{F}_E A_E \stackrel{!}{=} \mathcal{F}_B A_B + \mathcal{F}_C A_C + \mathcal{F}_D A_D. \quad (3.11)$$

This is, however, not guaranteed numerically. In order to cure this problem, the value of \mathcal{X} in the cell E is updated to

$$\mathcal{X}_{\text{new}} = \mathcal{X} + \Delta t \frac{\mathcal{F}_E A_E - \mathcal{F}_B A_B - \mathcal{F}_C A_C - \mathcal{F}_D A_D}{V_E}, \quad (3.12)$$

where Δt is the timestep length and V_E the volume of the cell E. In this way, differences of Riemann fluxes are converted into updates of conserved quantities. This is done for all variables at all interfaces between layers of different angular resolution to ensure that conservation laws are fulfilled numerically.

3.3.3. Treatment of the neutrino transport

The implementation of the neutrino transport requires some modifications if the SMR procedure is used. Generally, the computational grids, on which the hydrodynamics and the radiation transport are computed, have to be identical in the regime where neutrinos are tightly coupled to the stellar matter. Otherwise, the source terms given by the transport solution are not well-balanced with the internal energy density of the fluid, such that deviations from thermodynamic equilibrium would arise (Rampp & Janka, 2002). These, in turn, would cause numerical oscillations harming the simulation.

In the context of the SMR grid, the coarsest angular grid of the innermost multidimensional refinement layer must coincide with the transport angular grid. For example, the complete wedge shown in Fig. 3.3 would be one transport ray with the first refinement step at r_1 being in a region where the neutrino opacity is already sufficiently low and neutrinos are not expected to reach equilibrium with the fluid. For $r > r_1$, the input for the neutrino transport solver is obtained by angular averages of the hydrodynamic quantities, similar to the filling procedure of the ghost cells of different angular resolution patches. The computed source terms for the hydrodynamic equations are finally applied to all cells in the particular transport ray.

3.3.4. Taylor-Sedov test

In order to demonstrate the capabilities of the SMR grid construction, we present simulations of a three-dimensional hydrodynamic test problem, a so-called Taylor-Sedov blast wave. A spherical shock wave is unleashed by a certain amount of energy in a small volume. It propagates into a low-pressure environment and expands in a self-similar manner. The analytical solution of the problem can be calculated for any point in time (Sedov, 1959; Landau & Lifshitz, 1987).

We conducted two simulations on the Yin-Yang grid with and without the SMR modification. Both setups have an equidistant radial grid of 500 zones with an outer grid boundary R_{\max} of 5×10^7 cm. The angular grid configurations are listed in Tab. 3.1.

| Setup | Angular resolution | | |
|-------------------|--------------------|-----|---------------------------------------|
| Yin-Yang | 1.8° | for | $0 \leq r \leq R_{\max}$ |
| Yin-Yang with SMR | 1.8° | for | $0 \leq r < 5 \times 10^6$ cm |
| | 0.9° | for | 5×10^6 cm $\leq r < 10^7$ cm |
| | 0.45° | for | 10^7 cm $\leq r \leq R_{\max}$ |

Tab. 3.1.: Setups for the Taylor-Sedov blast wave test. The outer radius of the grid is $R_{\max} = 5 \times 10^7$ cm.

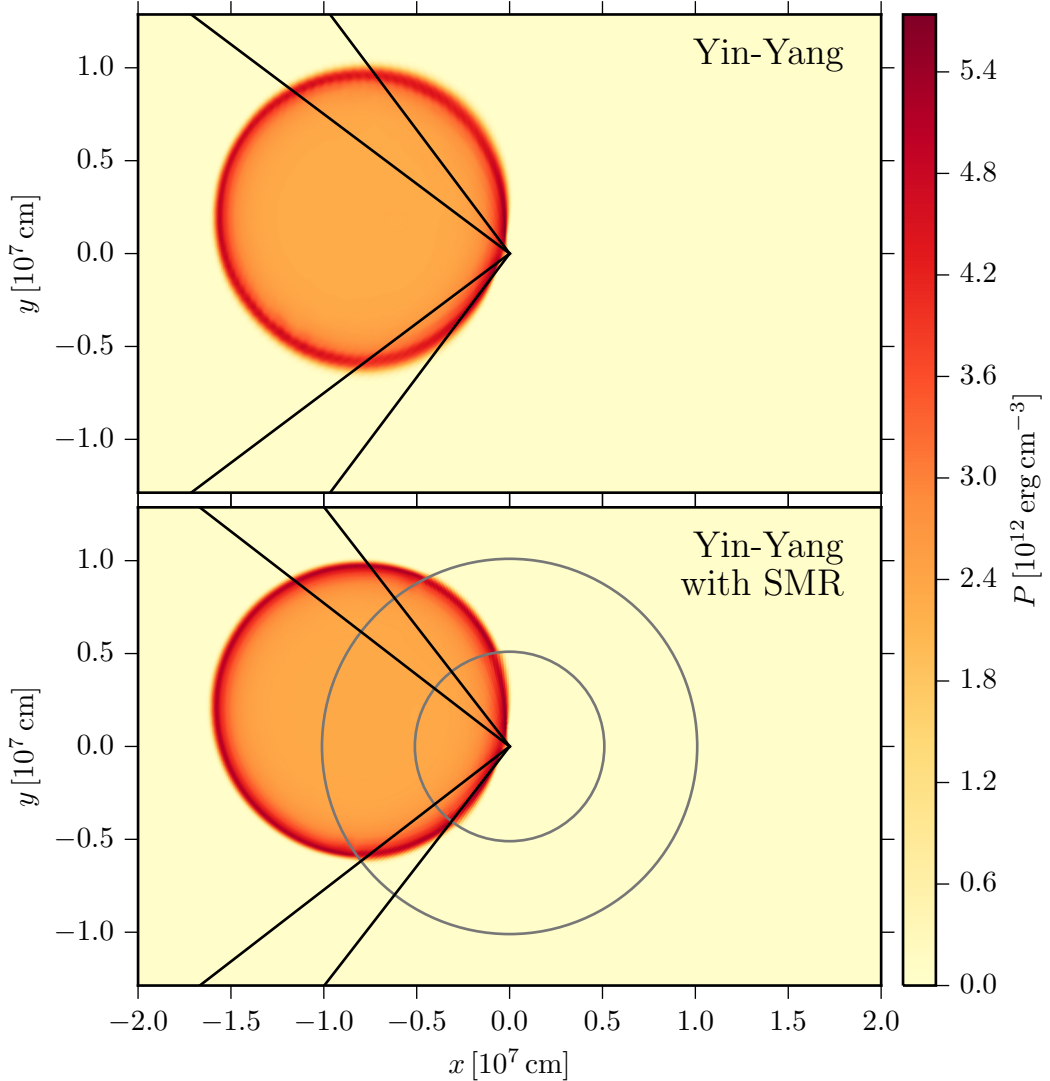


Fig. 3.4.: Taylor-Sedov test on the Yin-Yang grid, with and without the SMR, at $t = 3.5$ s. The pressure distribution in the plane $z = 0$ is color-coded. Black lines indicate the grid edges of *Yin* and *Yang*, so that the Yin-Yang overlap region is enclosed by them. Gray circles mark the boundary between different refinement layers of the SMR setup (cf. Tab. 3.1).

We initialize an off-center Taylor-Sedov explosion around the point

$$\begin{pmatrix} x_0 \\ y_0 \\ z_0 \end{pmatrix} = \begin{pmatrix} -8 \times 10^6 \text{ cm} \\ 2 \times 10^6 \text{ cm} \\ 0 \end{pmatrix}. \quad (3.13)$$

The analytical solution of the blast wave with an initial energy input of 2×10^{34} erg is interpolated onto the grid at $t = 0.2$ s after ignition. At this time, the radius of the spherical shock is about 2.5×10^6 cm. It propagates into surrounding matter that has a density of 10 g cm^{-3} and a pressure of 10^7 erg cm^{-3} . An analytical ideal gas equation of state is used with an adiabatic index of 1.4. Gravity is switched off in the test runs.

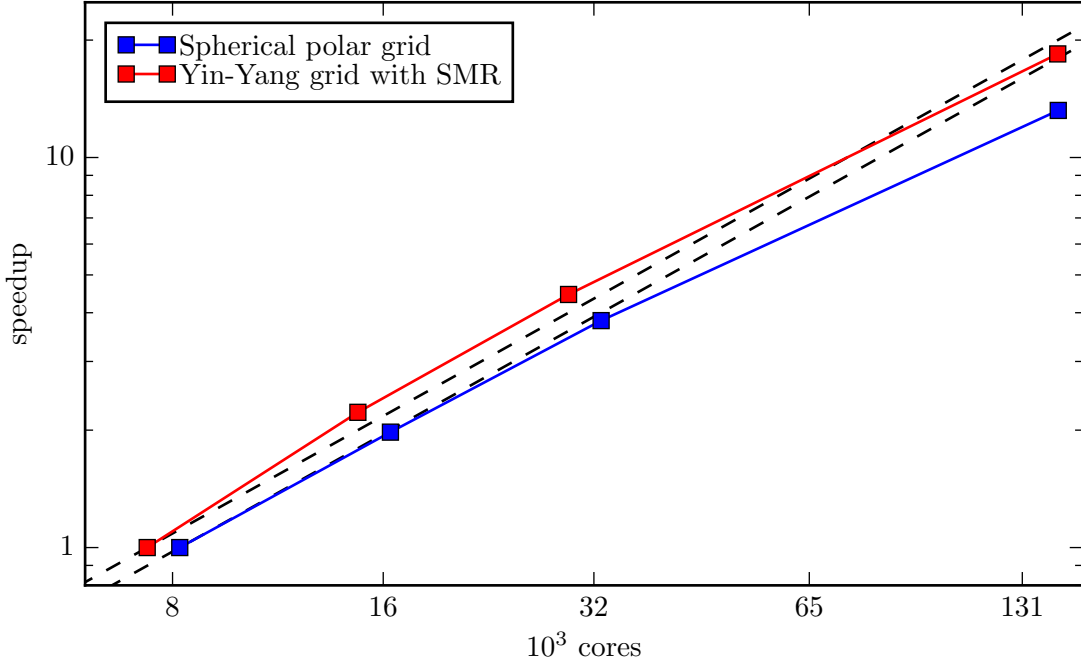


Fig. 3.5.: Strong scaling of the VERTEX-PROMETHEUS code on the SuperMUC system (LRZ, Garching). The speedup, i.e. the wall-clock time per step normalized to a reference value, is shown as a function of the number of compute cores. Note that the problem size is kept constant and the size of the angular domain subsets on one node therefore decrease with increasing number of cores. Blue and red lines show the behavior of the code with the spherical polar grid and the Yin-Yang grid with enabled static mesh refinement (SMR), respectively. Black dashed lines depict a theoretically ideal scaling. The data was obtained during SuperMUC’s Extreme Scaling Workshop 2016 and resulted in awarding us the Extreme Scaling Award 2016.

In Fig. 3.4, the pressure distribution in the plane $z = 0$ is shown for both test models at 3.5 s after ignition. First, it can be seen that the shocks remain spherical when they pass the Yin-Yang grid edges indicated by black lines. Numerical artifacts due to the interpolation procedure for the ghost cells are not visible. The same is true for the SMR case, where the shock wave has to pass Yin-Yang boundaries and interfaces between different resolution layers. Especially the passage from a region of higher angular grid resolution into a layer of lower resolution does not trigger numerical problems. Slight deformations of the shock waves appear near the grid origin, which is related to the reflecting boundary condition there and the distorted shape of the cells in its vicinity.

Second and most importantly, the higher angular resolution of the SMR scheme maintains a sharper discontinuity of the shock as expected. Especially comparing the layers of 2° and 0.5° resolution reveals the enhanced sharpness of the blast wave.

In this simple 3D test, we have shown that the SMR implementation does not trigger numerical artifacts at the propagating shock. Note that if this example included neutrino transport, the number of transport rays would be the same in both test simulations. Since the wall-clock time is dominated by the neutrino transport, the computa-

tional cost of both simulations would be fairly equal. This was exactly the motivation for implementing the static angular mesh refinement.

3.4. Code scaling

An important aspect of VERTEX-PROMETHEUS’s code performance is its excellent strong scaling. For a given problem size, the number of compute cores is varied and the time needed for a single timestep is measured. Ideally, the number of cores should be inversely proportional to the wall-clock time per step.

In Fig. 3.5, we show the strong scaling of our latest code version with physical and numerical settings that would be similarly used in production for both the standard spherical polar grid and the Yin-Yang grid. In the latter case, we have also enabled the static mesh refinement procedure with an angular resolution of 0.3° at the finest level. VERTEX-PROMETHEUS scales almost linearly up to 147,456 cores on the SuperMUC system (LRZ, Garching) without indications for an upper limit, where the scaling breaks down. This remarkable result demonstrates that we will be able to use future high-performance computers efficiently on hundreds of thousands of cores.

4. Explosion of a $9.6 M_{\odot}$ star

Modeling core-collapse supernovae with sophisticated neutrino transport has reached the third spatial dimension only in recent years thanks to growing computational power. First insights into the explosion mechanism could be obtained in self-consistent three-dimensional (3D) simulations and it turned out that there are fundamental differences to previous axisymmetric (2D) models being related to the imposed symmetry constraint of the latter. Besides numerical deficiencies at the axis, fluid structures are artificially elongated into toroidal shapes in axisymmetry. Hence, hydrodynamic instabilities being important for shock revival behave differently in 2D and 3D. Studies in 2D have become routine these days, but the lessons learned from these investigations cannot be easily extrapolated to 3D. By comparing 2D with 3D, two important questions arise concerning the onset of explosion:

1. Do 3D models explode more readily and earlier than their 2D counterparts?
2. Do 2D and 3D simulations behave differently *after* the onset of explosion?

The first question has been discussed in the literature in great detail. Results from parametric simulations by Nordhaus et al. (2010) claimed that the critical luminosity – i.e. the neutrino luminosity required to revive the shock assuming steady-state conditions (Burrows & Goshy, 1993) – is lower in 2D compared to spherically symmetric (1D) models and even further reduced in 3D. Similarly, Burrows et al. (2012) and Dolence et al. (2013) found earlier explosions in 3D despite less power in large-scale fluid motions. Other works, however, contradicted these findings. Hanke et al. (2012) observed that 2D and 3D models require similar neutrino luminosities and that 3D results approach the 1D case for sufficiently high angular resolution. These authors also noticed that large-scale motions of the flow drive shock expansion. Couch (2013) found later explosions in 3D and emphasized that the largest buoyant plumes with a large volume-to-surface ratio push the shock outwards. All these works were performed with a simple neutrino light bulb scheme. Nevertheless, the findings of the latter studies already emphasize the role of large-scale fluid structures for the explosion mechanism.

An important difference between 2D and 3D models is turbulent energy transport. Usually, kinetic energy is injected at some large scale and transported down the inertial range to the dissipation range, where it is dissipated into internal energy (Landau & Lifshitz, 1987). This forward energy cascade holds in 3D, whereas the artificially imposed symmetry in 2D leads to an inverse energy transport accumulating power at large scales (Kraichnan, 1967; Frisch & Sulem, 1984; Boffetta & Musacchio, 2010). The importance of the different behavior of the turbulent energy cascade in 2D and 3D was discussed by various parametric studies (e.g., Hanke et al., 2012; Couch, 2013). With their neutrino leakage scheme, Couch & O’Connor (2014) stressed that explosions are artificially favored in 2D, since kinetic energy is stored at large scales. Takiwaki et al. (2012, 2014) also obtained later explosions in 3D with the isotropic diffusion source approximation, a purely Newtonian treatment of the hydrodynamics, and a somewhat

outdated equation of state. Likewise, Lentz et al. (2015) obtained later explosions in 3D with a flux-limited diffusion scheme and noticed that many small buoyant plumes develop in 3D compared to a few large ones in 2D. From a more general point of view, Couch & Ott (2015) argued that overestimated turbulence in 2D brings a model closer to the explosion threshold compared to 3D.

Nearly all of the latest works agree that the different directions of the turbulent energy cascade seem to artificially enhance explosions in 2D and delay shock revival in 3D. However, the second question – how 2D and 3D models behave *after* the onset of explosion – was not addressed so far. It is not at all clear that 3D simulations should develop weaker explosions compared to 2D if shock revival is initiated simultaneously in both cases. In this chapter, we will investigate this issue and present the very first successfully exploding 3D core-collapse supernova simulation performed with the VERTEX-PROMETHEUS code. Together with a corresponding 2D model exploding at the same time, we will have the unique possibility to directly compare the fluid dynamics during the explosion. It will be shown that the influence of the turbulent cascade boosts the 3D model to a 10% higher explosion energy. The results of this chapter were partially published in Melson et al. (2015b).

First, we will describe the progenitor star and the numerical setup. Then, the characteristics and dynamics of the explosion will be explained in detail, especially why the explosion is more energetic in 3D. Finally, additional interesting observations concerning the lepton-number emission will be discussed.

4.1. Progenitor

The initial model used for this study is a zero-metallicity iron-core star with a zero-age main sequence (ZAMS) mass of $9.6 M_{\odot}$. It is referred to as “z9.6” in the literature and was provided by Heger (2012). Details about the stellar evolution calculation for this stellar model can be found in Heger & Woosley (2010). Woosley & Heger (2015) presented an extensive discussion about stars in the appropriate mass range, although not explicitly for metal-free stars.

A 2D core-collapse supernova simulation with this progenitor was performed by Müller et al. (2013), who determined the gravitational wave signal during the explosion. Sukhbold et al. (2016) argued that the z9.6 star behaves similarly to their lightest solar-metallicity star of $9.0 M_{\odot}$ and can therefore be discussed in the context of a Crab supernova progenitor.

In Fig. 4.1, several profiles of the $9.6 M_{\odot}$ model are shown as functions of radius and enclosed mass. The most abundant species of different shells are marked with blue labels. The iron core with a mass of $1.30 M_{\odot}$ is surrounded by a thin shell consisting mainly of silicon and oxygen. A steep density gradient outside of this layer separates it from the dilute outer stellar shells. To be more precise, the compactness parameter $\xi_{2.5}$ (O’Connor & Ott, 2011) of the progenitor is 7.65×10^{-5} and thus orders of magnitude lower than typical values for heavier stars (cf. Ertl et al., 2016). Due to this density configuration, the mass-accretion rate on the stalled supernova shock and hence the ram pressure caused by infalling material are expected to drop quickly to a very low value, which is a common phenomenon of low-mass progenitors. Explosions can therefore be achieved quite easily even in spherically symmetric core-collapse supernova simulations.

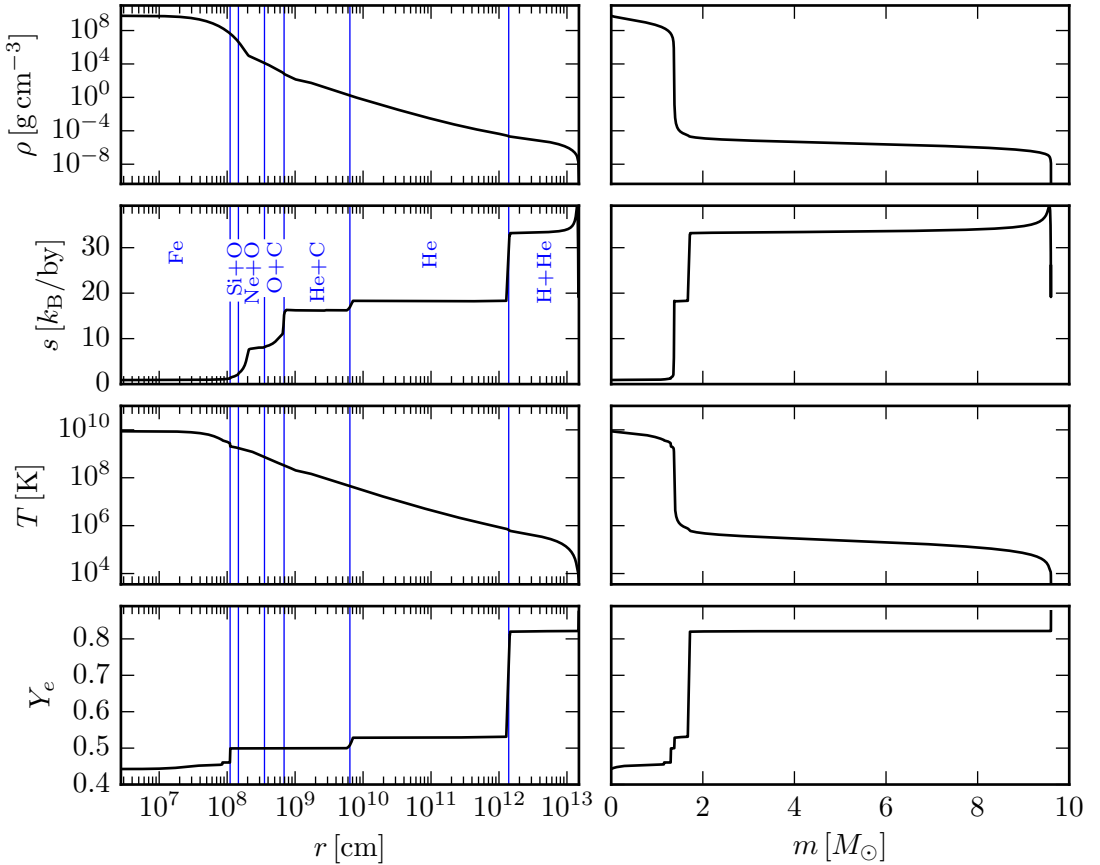


Fig. 4.1.: Profiles of the density ρ , the entropy per baryon s , the temperature T , and the electron fraction Y_e of the $9.6 M_\odot$ progenitor as functions of radius r (left panels) and enclosed mass m (right panels). Blue vertical lines indicate shell interfaces and blue labels show the most abundant species in these shells.

4.2. Numerical setup

We have simulated the $9.6 M_\odot$ progenitor in spherical symmetry (one dimension, 1D), axial symmetry (two dimensions, 2D), and full three dimensions (3D). All details about the general numerical setup can be found in Sect. 2.4. Particularly, the 3D simulation was performed on the axis-free Yin-Yang grid. The angular resolution of the 2D and 3D models was set to 2° , with the innermost 1.6 km treated in spherical symmetry.

Except for dimensionality, all models discussed in this chapter were run with identical physical and numerical settings.

We used the LS220 high-density equation of state (cf. Sect. 2.2). The threshold density ρ_{EOS} between the high-density and low-density EOS was set to $6 \times 10^7 \text{ g cm}^{-3}$ during collapse and to $10^{11} \text{ g cm}^{-3}$ afterwards. NSE was considered above a temperature of 0.5 MeV.

The radial grid was gradually refined during the simulations in order to sufficiently resolve the cooling region and the proto-neutron star surface. Note that this was done similarly in 1D, 2D, and 3D, so that the radial axes are identical in all models for a given point in time ensuring comparability of the results.

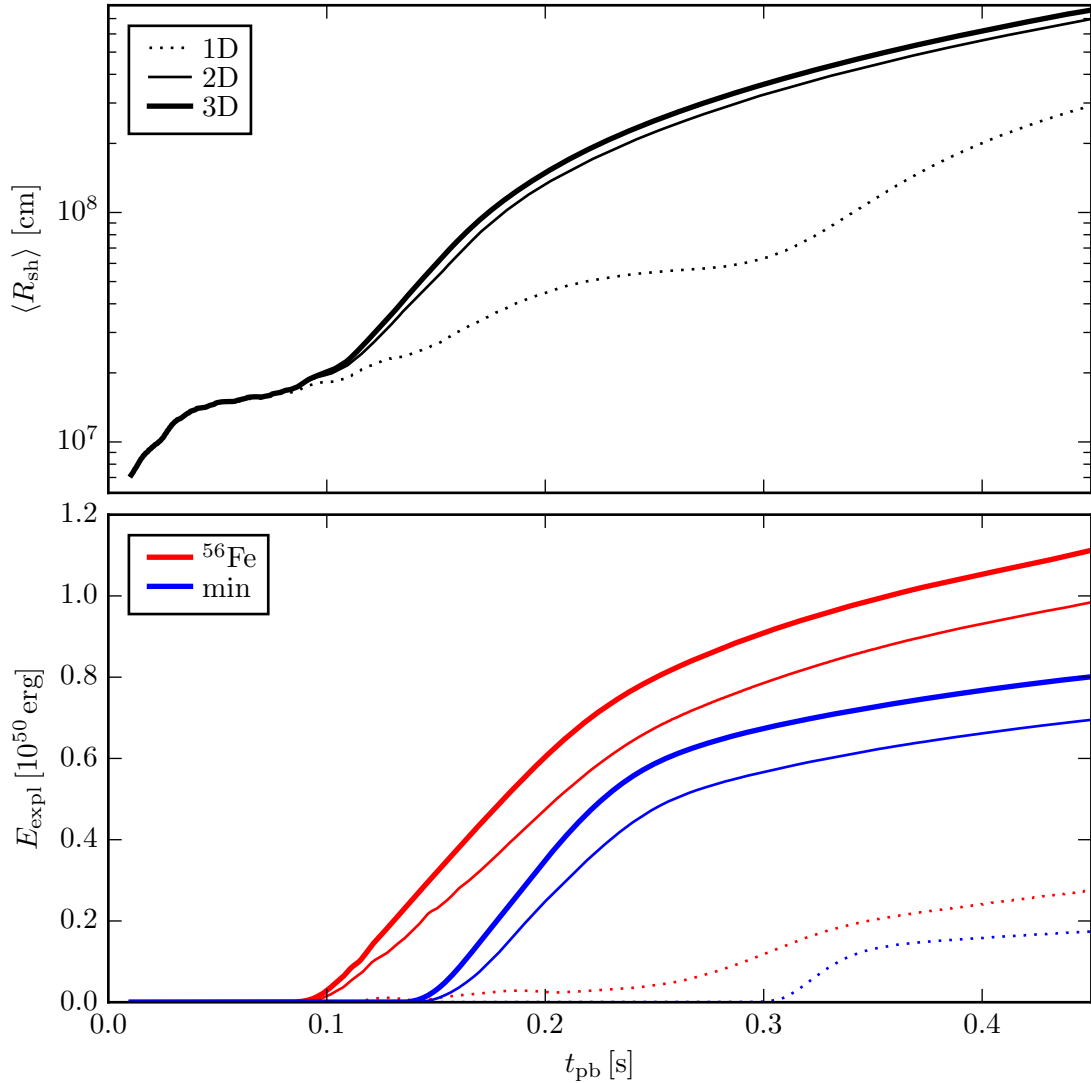


Fig. 4.2.: Angle-averaged shock radii $\langle R_{\text{sh}} \rangle$ and diagnostic explosion energies E_{expl} as functions of post-bounce time t_{pb} . Dashed, thin solid, and thick solid lines correspond to the 1D, 2D, and 3D model, respectively. Blue and red lines depict the lower and upper limits of the explosion energy (see text and Eq. (4.3)).

4.3. Results

4.3.1. Overview

As already mentioned above, the structure of the progenitor facilitates an explosion in all cases, i.e. in 1D, 2D, and 3D¹. The angle-averaged shock radii $\langle R_{\text{sh}} \rangle$ in Fig. 4.2 clearly demonstrate the success of all models. Generally, angle-averaged quantities in

¹Movies of the 3D model can be found at <http://www.mpa-garching.mpg.de/ccsnarchive/movies/>.

this work are defined as

$$\langle \mathcal{X} \rangle := \frac{\int d\Omega \mathcal{X}}{\int d\Omega}, \quad (4.1)$$

where the integrals in the 3D Yin-Yang case have to be computed applying the procedure mentioned in Sect. 3.2.3. As usual, all time axes are normalized to the bounce time, which is given by the time when the entropy per baryon exceeds a value of $3.2 \text{ k}_B/\text{by}$ at the newly-formed shock wave.

Usually, the supernova shock stagnates at a radius between 100 and 200 km, typically followed by a phase of shock retreat, before it is possibly revived by neutrino heating. In the models discussed here, however, the stagnation phase is only very short due to the low ram pressure of the infalling material. Neutrino heating is strong enough to continuously drive the shock outwards. In this context, both multi-dimensional models explode directly and nearly at the same time, whereas the 1D explosion is weaker and more delayed. If we define the explosion time as the time when the average shock radius reaches 400 km, the 2D and 3D models explode at 138 and 134 ms, respectively. This gives us the unique opportunity to directly compare the explosion dynamics of both multi-dimensional models and deduce differences caused by the dimensionality. Interestingly, for example, the shock expansion in 3D is faster than in 2D. At 400 ms after core bounce, the shock expansion rate is $\sim 2.8 \times 10^9 \text{ cm s}^{-1}$ in 3D and $\sim 2.5 \times 10^9 \text{ cm s}^{-1}$ in 2D. At the end of the 3D simulation, i.e. at 450 ms, the shock has reached an averaged radius of about 7600 km. The minimum and maximum shock radii at this time are 7200 and 8200 km, respectively, representing only a slight deformation from a spherical shape.

The intermediate shock delay and following re-acceleration in 1D at 250 ms coincides with a rapid drop of the mass-accretion rate. This demonstrates that the 1D model is only marginally above the explosion threshold and that both multi-dimensional models explode more robustly. Although even the 1D model explodes, hydrodynamic instabilities play an important role during the explosions of the 2D and 3D models. Their different behavior is the essential point in our discussion here.

Our obtained value for the explosion times in 2D and 3D are compatible with other simulations of the same progenitor reported in the literature. Müller et al. (2013) found an explosion at 125 ms after bounce in a general-relativistic 2D simulation. The parametric 1D model with simpler neutrino transport by Sukhbold et al. (2016) explodes at ~ 125 ms measured when the shock reaches 500 km. This agreement is not surprising, because the onset of explosion mostly depends on the progenitor structure in case of this specific star.

An important quantity for characterizing a core-collapse supernova is its explosion energy. From our first-principle simulations, it is not possible to deduce its final value, because we cannot follow the evolution long enough due to constrained computational resources. A common quantity considered instead is the so-called diagnostic energy E_{expl} , which is defined as the total energy of all unbound material in the post-shock layer,

$$E_{\text{expl}} = \int_{r < R_{\text{sh}}} dV \Theta(\epsilon) \rho \epsilon. \quad (4.2)$$

Here, ϵ denotes the total specific energy. $\Theta(\epsilon)$ is the Heaviside step function only selecting fluid elements with positive total energy. The integral is computed in the layer behind the angle-dependent shock radius.

We investigate two different cases for ϵ ,

$$\epsilon = e + \frac{1}{2} |\vec{v}|^2 + \Phi + \begin{cases} 0 & \text{Case min,} \\ (e_{\text{bind}}^{\text{Fe}} - e_{\text{bind}}^{\text{curr}}) & \text{Case } {}^{56}\text{Fe,} \end{cases} \quad (4.3)$$

where $e_{\text{bind}}^{\text{curr}}$ represents the specific binding energy given the current chemical composition and $e_{\text{bind}}^{\text{Fe}}$ the specific binding energy assuming a complete recombination into ${}^{56}\text{Fe}$. Φ denotes the Newtonian gravitational potential. As explained by Scheck et al. (2006, Appendix C), two major sources contribute to the explosion energy: recombination of matter into iron-group nuclei and the neutrino-driven wind. Neutrino heating provides only enough energy to marginally unbind the material. The temperature in unbound fluid elements decreases as they propagate outwards and nucleons can recombine into heavier nuclei. Therefore, the additional term of the second case in Eq. (4.3) accounts for the binding energy that is released if all nucleons recombine into iron. Because iron-group nuclei are the most tightly bound nuclei, our two cases give a lower and upper limit of the diagnostic explosion energy for a given point in time.

In Fig. 4.2, the two cases of the diagnostic explosion energy are shown. It can be clearly seen that the energy is higher and grows faster in 3D compared to 2D. The growth rate at 130 ms is about $5 \times 10^{50} \text{ erg s}^{-1}$ in 2D versus more than $6 \times 10^{50} \text{ erg s}^{-1}$ in 3D. The difference of the explosion energies between 2D and 3D saturates already at 200 ms. After that, the neutrino-driven wind leads to a continuous increase of the energy impeding an estimate of the saturated value. However, it is obvious that the value of the explosion energy at 450 ms is larger in 3D with $(0.80 \dots 1.11) \times 10^{50} \text{ erg}$ compared to $(0.69 \dots 0.98) \times 10^{50} \text{ erg}$ in 2D. The material ahead of the shock is only loosely bound with a binding energy of about $-8.8 \times 10^{47} \text{ erg}$ and will therefore not considerably influence the energy budget. The 2D-3D difference of the explosion energies is in the range $(1.0 \dots 1.3) \times 10^{49} \text{ erg}$ for the two cases defined in Eq. (4.3). Correspondingly, the diagnostic explosion energy in 3D is about 10% higher than in 2D. This can only be justified by the different dimensionality, because the explosions set in at the same time in 2D and 3D and the physical setups of both models are identical. We will explain the reason for the more energetic explosion in 3D later in this chapter.

The lower limit of E_{expl} in 1D becomes positive only after 300 ms. Its value at 450 ms is $(0.17 \dots 0.28) \times 10^{50} \text{ erg}$, which demonstrates again that the explosion of the spherically symmetric model is very weak.

The global fluid structures of the 2D and 3D models can be seen in Fig. 4.3. At $\sim 70 \text{ ms}$ after core bounce, convection in the gain layer develops due to a negative entropy gradient created by neutrino heating. Large Rayleigh-Taylor mushrooms rise towards the shock leading to a slight shock surface deformation. The layer directly behind the shock remains laminar and is pushed ahead of the buoyant bubbles by PdV work. Convective activity is also visible in the top row of Fig. 4.4, where high-entropy bubbles are visualized by iso-entropy surfaces. In the early phase, the size of the mushrooms is similar in 2D and 3D. However, the 2D flow pattern starts to differ from the 3D case shortly after 100 ms, because the 3D flow cascades to smaller scales due to turbulent activity. This can be seen in Fig. 4.3 at 200 ms, where larger-scale fluid structures survive in 2D, whereas fragmentation of high-entropy bubbles commences in 3D. Turbulent cascading is also apparent in the middle and bottom rows of Fig. 4.4, where the mushrooms are fragmented into finer patterns already at 200 ms. After the onset of explosion, convection freezes out and the ejecta expand in a self-similar way.

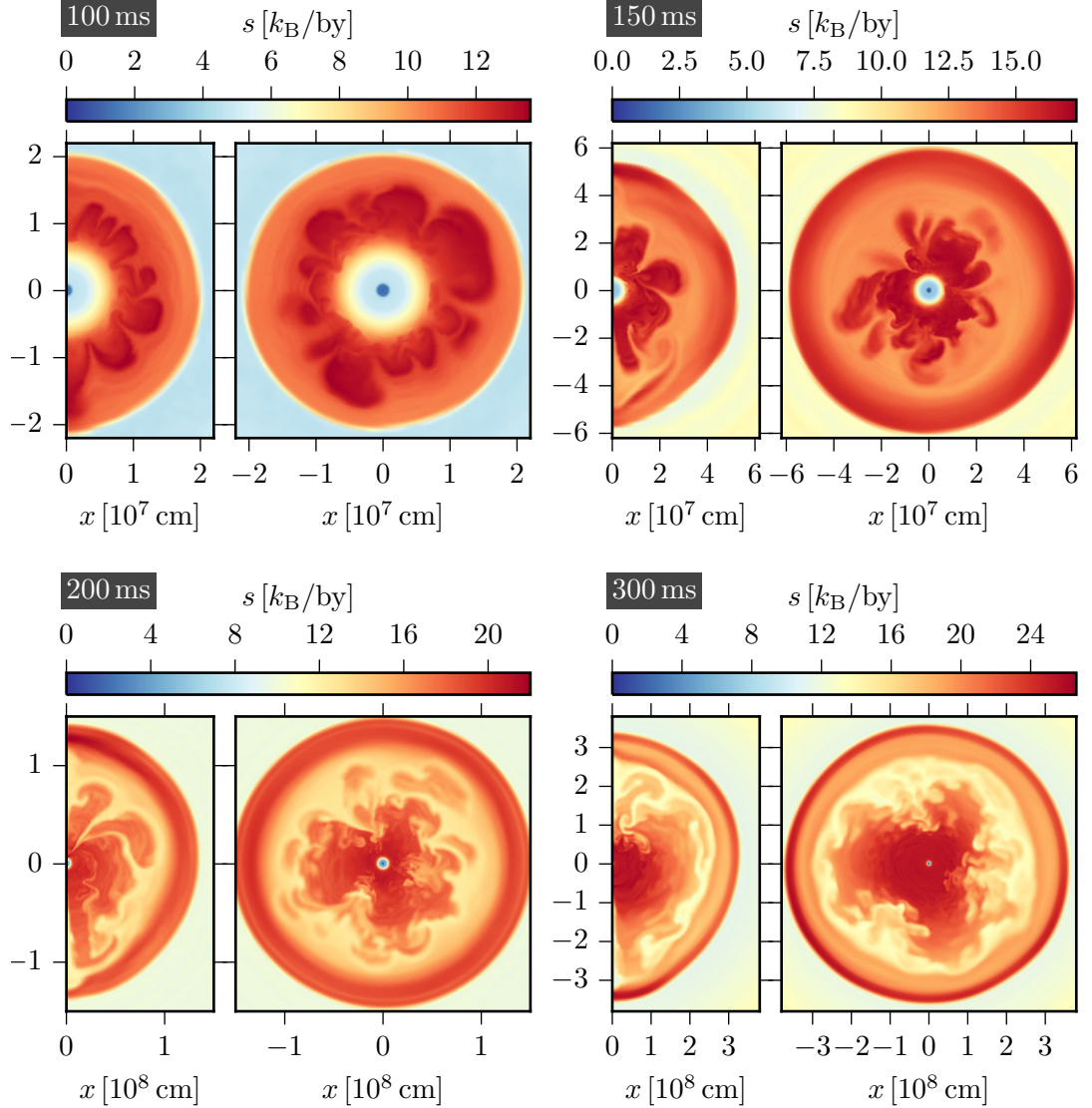


Fig. 4.3.: Color-coded entropy per baryon s in the plane $y = 0$ at 100, 150, 200, and 300 ms after bounce. For each given point in time, the 2D and 3D models are shown in the left and right sub-panels, respectively. Note the different color and length scales.

We will extend the discussion on turbulent effects in a more quantitative manner later in this chapter.

The shock remains nearly spherical in 2D and 3D without indications for the standing accretion-shock instability (SASI; Blondin et al., 2003). Its growth rate depends on the time needed for accreting matter from the shock to the coupling region of the advective-acoustic cycle in the vicinity of the neutron star surface. For long advection times, the SASI growth rate is low (Scheck et al., 2008). In our 3D model, it takes about 100 ms to transport material entering the gain layer at 50 ms post bounce from the shock to the proto-neutron star surface. Due to this long time, the SASI growth is suppressed and it cannot develop.

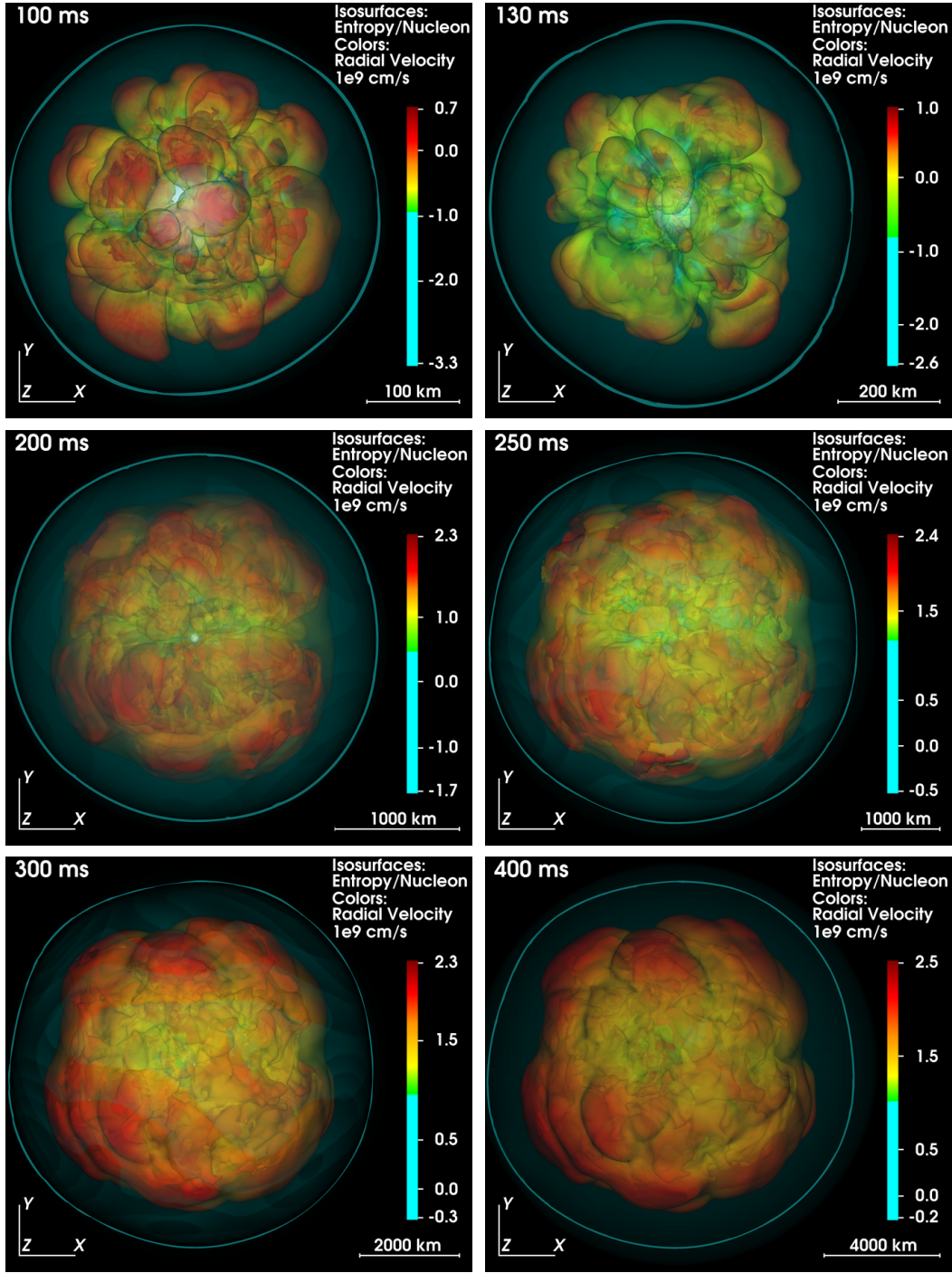


Fig. 4.4.: Volume-rendering of the 3D model at six different times. Surfaces of constant entropy per baryon are shown together with the color-coded radial velocity in units of 10^9 cm s^{-1} . The neutron star surface at a density of $10^{11} \text{ g cm}^{-3}$ is visible as a light blue sphere in the center. Greenish circular lines indicate the shock positions. Yardsticks demonstrate the dimensions of the exploding model. (Visualization: E. Erastova & M. Rampp)

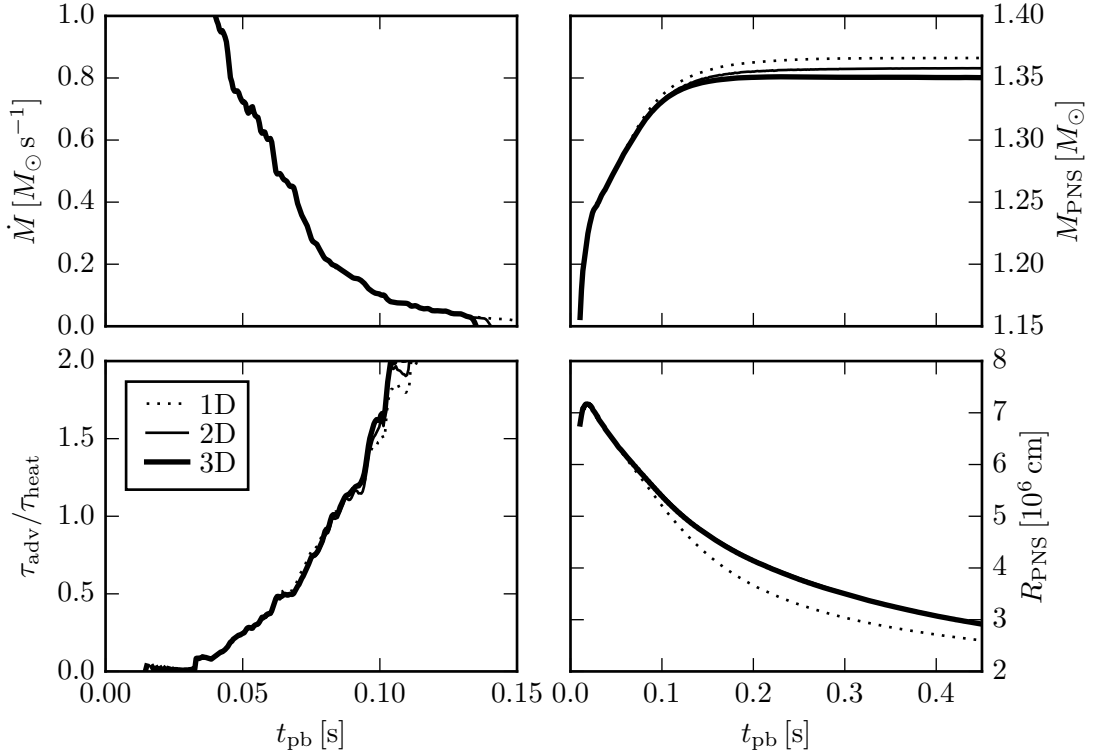


Fig. 4.5.: Mass-accretion rates \dot{M} measured at a radius of 400 km, timescale ratios $\tau_{\text{adv}} / \tau_{\text{heat}}$ of advection and heating timescales, baryonic masses M_{PNS} of the proto-neutron star, and its radii R_{PNS} as functions of post-bounce time t_{pb} . Note the different time axes in the left and right columns.

As already mentioned above, the mass-accretion rate drops quickly as a function of time for the $9.6 M_{\odot}$ progenitor. It is defined as

$$\dot{M} = -r^2 \int d\Omega \rho v_r \quad (4.4)$$

and measured at a radius of 400 km. Since $v_r < 0$ for infalling matter, $\dot{M} > 0$. In Fig. 4.5, we show the mass-accretion rates for the 1D, 2D, and 3D models. As expected, \dot{M} is equal in all cases, because it is determined by the density profile of the progenitor. The sign of \dot{M} changes when the shock reaches a radius of 400 km, due to the fact that it is measured at this distance.

There is a lot of effort in the core-collapse supernova community to find a criterion with which the success of an explosion can be predicted (O'Connor & Ott, 2011; Pejcha & Thompson, 2012; Murphy & Dolence, 2015; Müller & Janka, 2015; Ertl et al., 2016). The idea is that the explosion characteristics can be estimated either at core bounce or directly from the progenitor structure. Instead, we consider a much simpler relation, which sufficiently well determines how close a model is to explosion for our purposes: the well-known ratio of advection and heating timescales (see, e.g., Janka, 2012). We define the advection timescale similar to Murphy & Burrows (2008) as

$$\tau_{\text{adv}} = \frac{M_{\text{gain}}}{\dot{M}}, \quad (4.5)$$

where M_{gain} denotes the gain layer mass,

$$M_{\text{gain}} = \int_{R_{\text{gain}} < r < R_{\text{sh}}} dV \rho. \quad (4.6)$$

It gives an estimate of the time matter spends in the gain layer and is exposed to neutrino heating (Buras et al., 2006a). The heating timescale is given by

$$\tau_{\text{heat}} = -\frac{E_{\text{gain}}}{\dot{Q}_{\text{gain}}}, \quad (4.7)$$

with the total energy of the gain layer

$$E_{\text{gain}} = \int_{R_{\text{gain}} < r < R_{\text{sh}}} dV \rho \epsilon \quad (4.8)$$

and the heating rate

$$\dot{Q}_{\text{gain}} = \int_{R_{\text{gain}} < r < R_{\text{sh}}} dV \rho \dot{q}. \quad (4.9)$$

Here, ϵ is the total specific energy as defined in Eq. (4.3, *Case min*). \dot{q} is the specific net heating rate. τ_{heat} measures the time needed to deposit enough energy to unbind the gain layer. If the timescale ratio $\tau_{\text{adv}}/\tau_{\text{heat}}$ exceeds unity, a model is expected to be close to a successful explosion. This threshold should not be considered exact, but it roughly estimates whether neutrino heating can overcome the ram pressure of the infalling material. For the 3D model, the ratio reaches unity at 82 ms, which is about 50 ms before the explosion sets in. Together with its fast growth, the timescale ratio can be used as an indicator for the success of our models prior to explosion.

In the right column of Fig. 4.5, we present properties of the proto-neutron star (PNS). Its final baryonic mass is determined by the amount of accreted stellar material and depends on the dimensionality of the model. For example, at 450 ms post bounce, $M_{\text{PNS}} \approx 1.350 M_{\odot}$ in 3D, whereas $M_{\text{PNS}} \approx 1.358 M_{\odot}$ in 2D. The accretion of mass ceases earlier in the 3D case compared to the 2D model. This is nicely visible in Fig. 4.6, where the mass-infall rate of downflows being defined as

$$\dot{M}_{v_r < 0} = r^2 \int d\Omega \Theta(-v_r) \rho v_r \quad (4.10)$$

is plotted as a function of radius for different times. Already at 150 ms, a gap opens in the mass-infall rate both in 2D and 3D, which means that there is no accretion in a certain radial interval. According to Marek & Janka (2009), mass accretion stops when the angle-averaged radial velocity behind the shock exceeds the local escape velocity,

$$v_{\text{esc}} = \sqrt{\frac{2G \langle M_{\text{sh}} \rangle}{\langle R_{\text{sh}} \rangle}}, \quad (4.11)$$

where G is the gravitational constant and $\langle M_{\text{sh}} \rangle$ the mass enclosed by the shock (computed from angle-averaged profiles). At ~ 200 ms, the post-shock velocity becomes greater than v_{esc} in our 3D model. For later times, the gap in $\dot{M}_{v_r < 0}$ widens with the

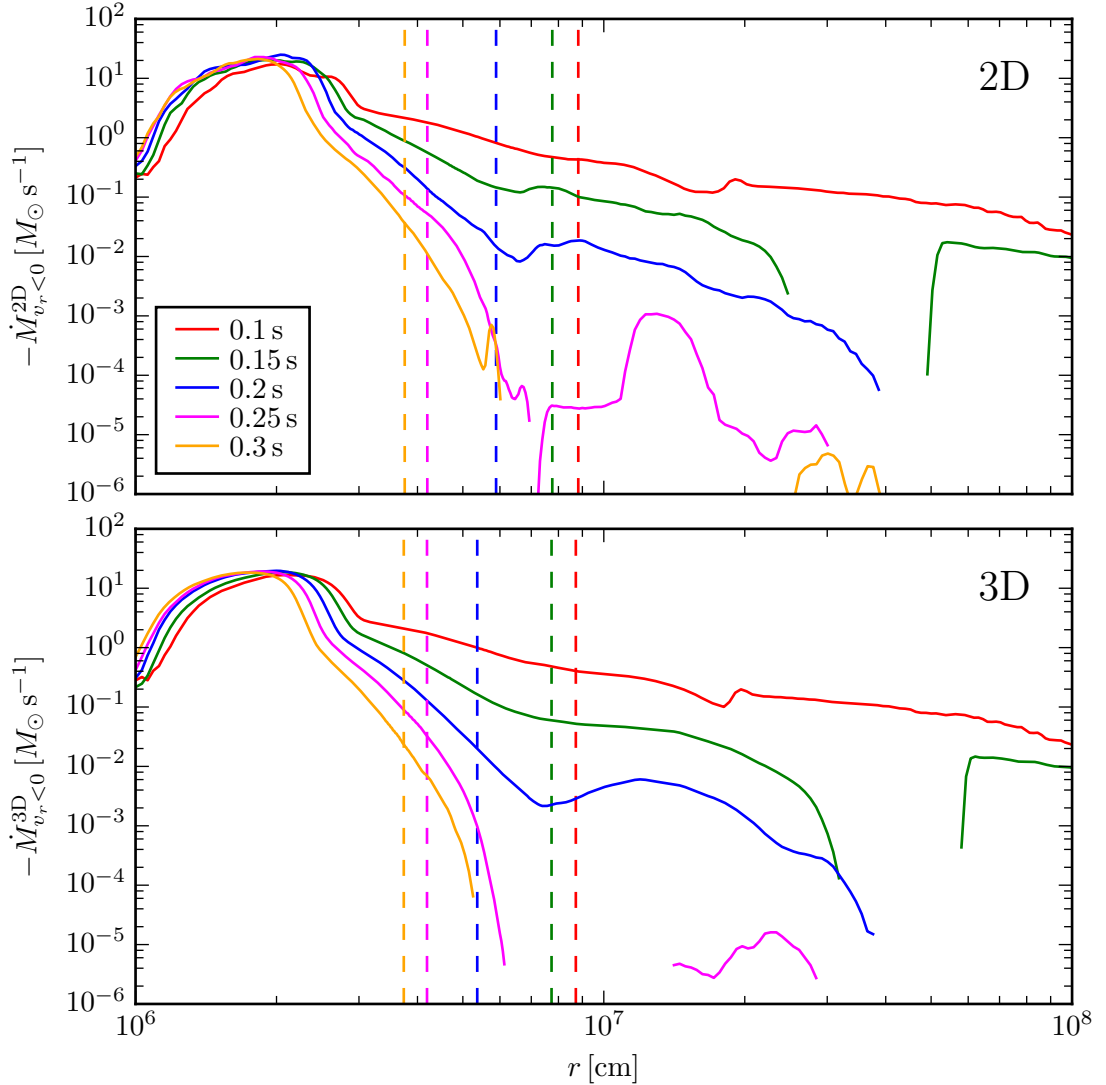


Fig. 4.6.: Mass-infall rates of downflows in 2D (*upper panel*) and 3D (*lower panel*) for different times (see Eq. (4.10) for the definition). The angle-averaged gain radii $\langle R_{\text{gain}} \rangle$ for these times are marked by vertical dashed lines.

absolute value in 3D being below the 2D case. Hence, the higher mass-infall rate in 2D causes the proto-neutron star to become heavier. In order to compare the obtained proto-neutron star mass with astronomical measurements, we have to convert the baryonic mass into the gravitational mass. Lattimer & Prakash (2001) give a formula which allows us to estimate the final gravitational mass of the neutron star M_{PNS}^g . It reads

$$\frac{M_{\text{PNS}} - M_{\text{PNS}}^g}{M_{\text{PNS}}^g} = \frac{0.6\beta}{1 - 0.5\beta}, \quad (4.12)$$

where

$$\beta = \frac{GM_{\text{PNS}}^g}{R_{\text{cold}}c^2}, \quad (4.13)$$

with the gravitational constant G and the speed of light c . Inserting a baryonic mass

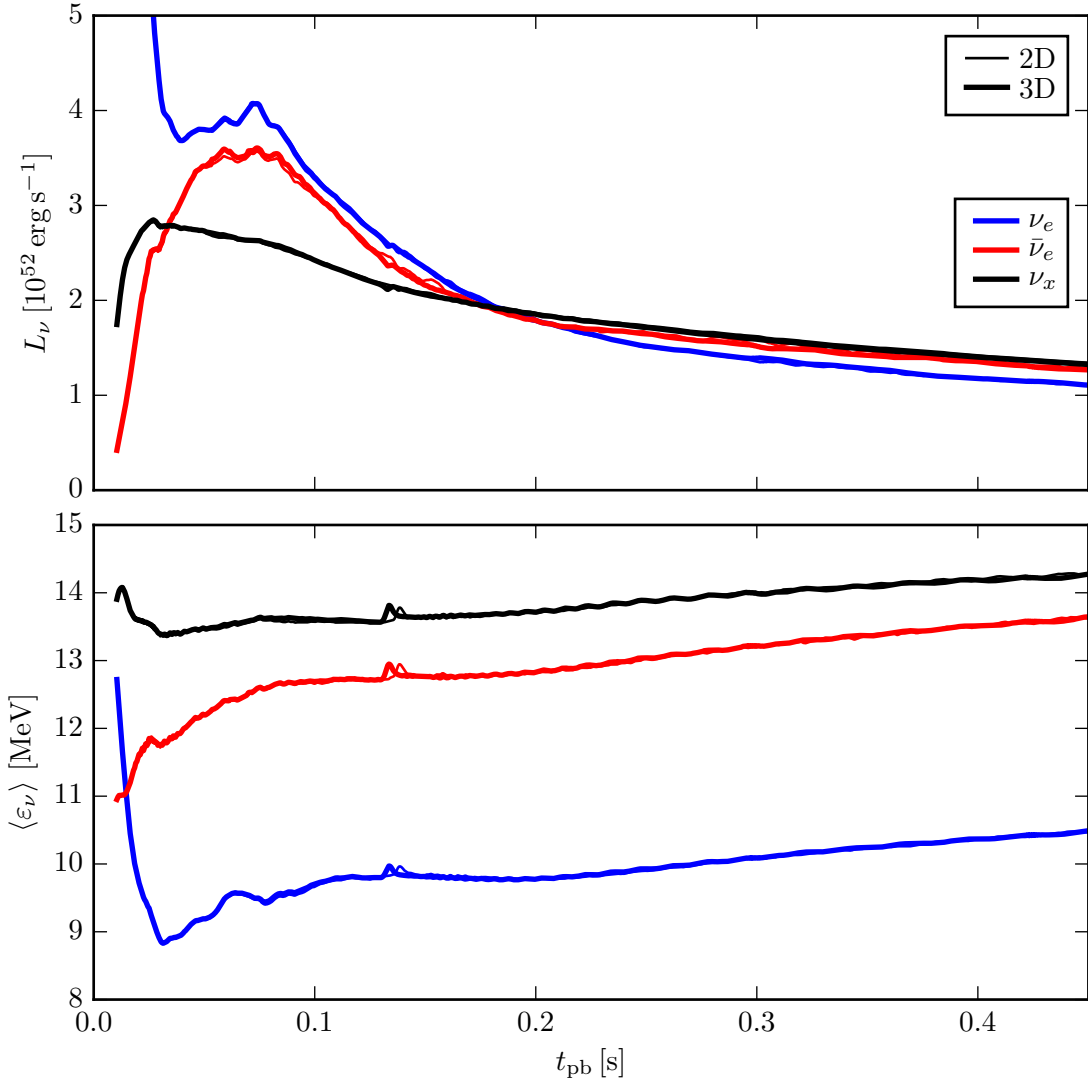


Fig. 4.7.: Luminosities L_{ν} and mean energies $\langle \varepsilon_{\nu} \rangle$ for the involved neutrino species (ν_e , $\bar{\nu}_e$, and ν_x) as functions of time. See Eqs. (2.12) and (2.11), respectively, for their definition. These quantities are measured at a distance of 400 km from the center. The small bumps in the mean energies are triggered when the shock reaches this distance. Note that the lines lie nearly on top of each other.

of $1.35 M_{\odot}$ and estimating a radius of 12 km for the cold neutron star R_{cold} , we get a final gravitational mass of $1.23 M_{\odot}$ for the 3D model. Kiziltan et al. (2013) presented a compilation of neutron star mass measurements and an estimate of the mass distribution. Our value is very close to the peak value of their mass distribution for double neutron star systems, which is at $1.33 M_{\odot}$. It is also well compatible with individual mass determinations mentioned in their work.

The radii of the proto-neutron stars are equal in 2D and 3D with 29 km at 450 ms. In 1D, however, it is smaller – 26 km – because PNS convection cannot be modeled self-consistently in spherical symmetry. Convection in the PNS enhances energy transport

and thus gives additional pressure support. The PNS radii are therefore larger in multi-dimensional simulations.

We show the neutrino luminosities and mean energies in Fig. 4.7. Both quantities are essentially equal in 2D and 3D for all neutrino species. A typical drop in the luminosities is usually observed when the mass-accretion rate decreases at composition interfaces. However, the accretion luminosity is generally very low in these models due to the low density of infalling shells. Therefore, the total luminosities do not show strong variations but evolve smoothly. The difference in the explosion energies between 2D and 3D cannot be attributed to a different neutrino energy deposition in the gain layer, since the luminosities and the mean energies are equal in both cases.

4.3.2. Differences between 2D and 3D

In this section, we will describe in detail why the explosion is more energetic in 3D compared to the 2D model. The fact that both simulations show successful explosions at the same time allows us to directly compare the fluid structures and properties.

As already mentioned in the introduction of this chapter, the turbulent energy cascade works differently in 2D and 3D. Large structures fragment to smaller scales in 3D, whereas the opposite is true in 2D. This effect is reflected in Fig. 4.8, where we show the angle-averaged non-radial velocity of the two models. Beginning at ~ 100 ms, red areas behind the shock indicate large non-radial velocities. However, it is obvious that the patterns are different in the two simulations. While the distribution is much smoother in the 3D case, the 2D model exhibits patches with high extrema. The statistical variance is lower in 3D and the angle-averaged distribution is smoothed out, because the turbulent structures are smaller. In contrast to this, the fluctuations of the angle-averaged non-radial velocities are more violent in 2D, due to the fact that the fluid structures are larger.

There are mass shells that settle down onto the proto-neutron star surface and are expelled a few 100 ms later. This is evidence for the neutrino-driven wind in which neutrinos deposit enough energy to unbind material long after the onset of explosion. The diagnostic explosion energy meanwhile grows continuously (cf. Fig. 4.2).

The 3D mass shells show a peculiar behavior after 300 ms post bounce. Because the spacing between the outermost mass coordinates is only $10^{-3} M_\odot$, even small variations of the density structure are noticeable in Fig. 4.8 as spikes in the solid black lines. Due to the violation of conservation laws on the order of 10^{-3} on the Yin-Yang grid (cf. Sect. 3.2.7), the mass coordinates are not as smooth as in the 2D simulation. These small variations, however, do not influence the explosion dynamics of the 3D model.

To discuss the influence of turbulent effects more quantitatively, we integrate the non-radial kinetic energy over the gain layer and hereby define the turbulent kinetic energy as

$$E_{\text{kin},\theta,\phi}^{\text{gain}} = \int_{R_{\text{gain}} < r < R_{\text{sh}}} dV \frac{1}{2} \rho (v_\theta^2 + v_\phi^2). \quad (4.14)$$

Accordingly, the same quantity can be calculated in the cooling layer,

$$E_{\text{kin},\theta,\phi}^{\text{cool}} = \int_{R_{\tau=3} < r < R_{\text{gain}}} dV \frac{1}{2} \rho (v_\theta^2 + v_\phi^2). \quad (4.15)$$

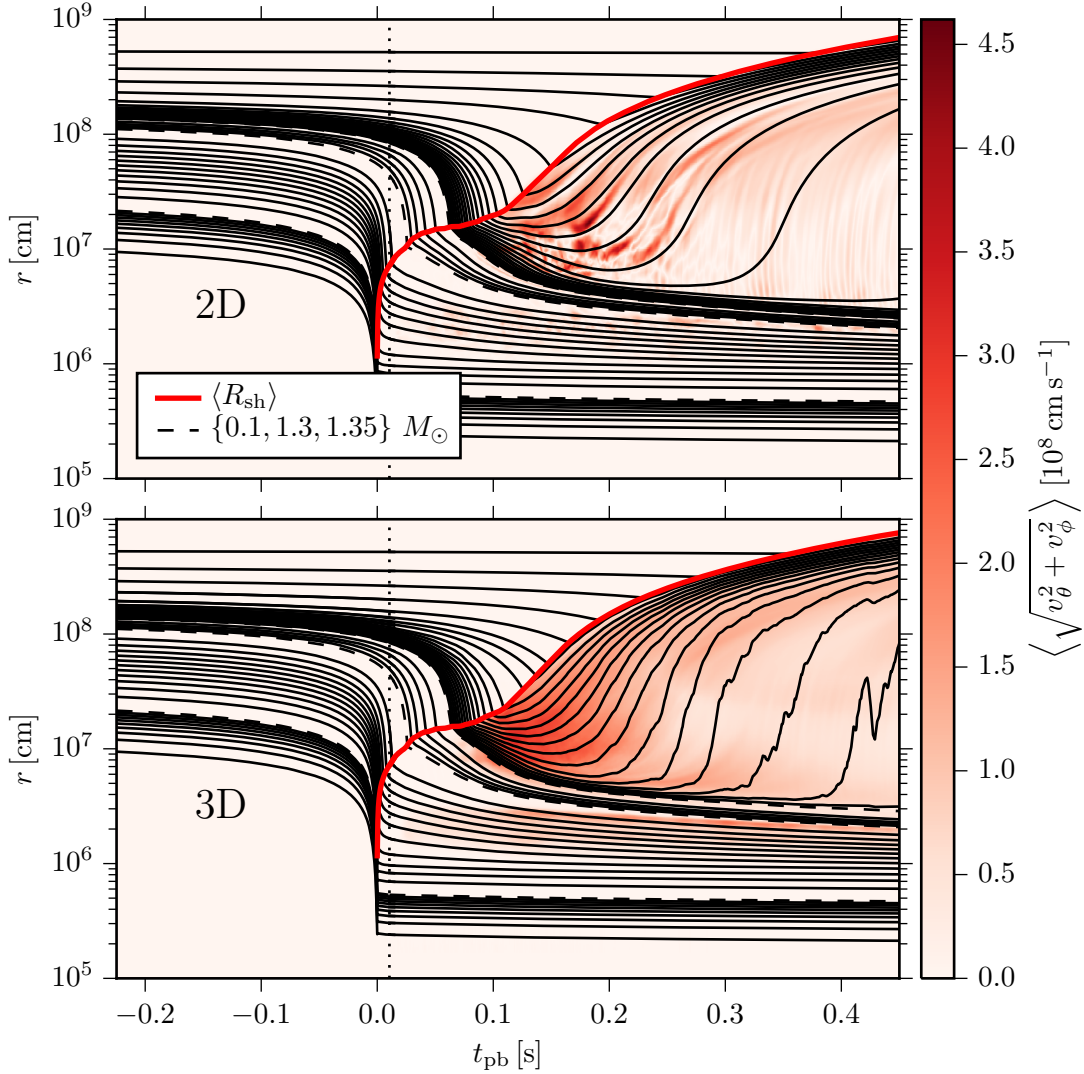


Fig. 4.8.: Mass shells of the 2D and 3D models, i.e. radii vs. time for given enclosed masses, with angle-averaged non-radial velocities as color coding. Black lines follow certain mass coordinates. The enclosed masses for the dashed black lines are labeled in the legend of the plot. The spacing of the solid black lines are different in certain intervals – 0.01, 0.1, 0.01, and 0.001 M_{\odot} from inside outwards – separated by the three dashed lines. Solid red lines show the angle-averaged shock radii. The multi-dimensional simulations were mapped from a 1D model at 10 ms after bounce marked by vertical dotted lines. In the 2D case, $v_{\phi} \equiv 0$.

Although the cooling layer is bounded by the gain radius at the outer end, its inner boundary is somewhat arbitrary. In this chapter, we set the inner radius to $R_{\tau=3}$ being the point where the angle-averaged optical depth of electron neutrinos is equal to 3.

It can be clearly seen in Fig. 4.9 that there is a pronounced difference between the gain and the cooling layers with respect to the turbulent kinetic energies. The time dependence in 3D is smoother because of the smaller turbulent structures that reduce

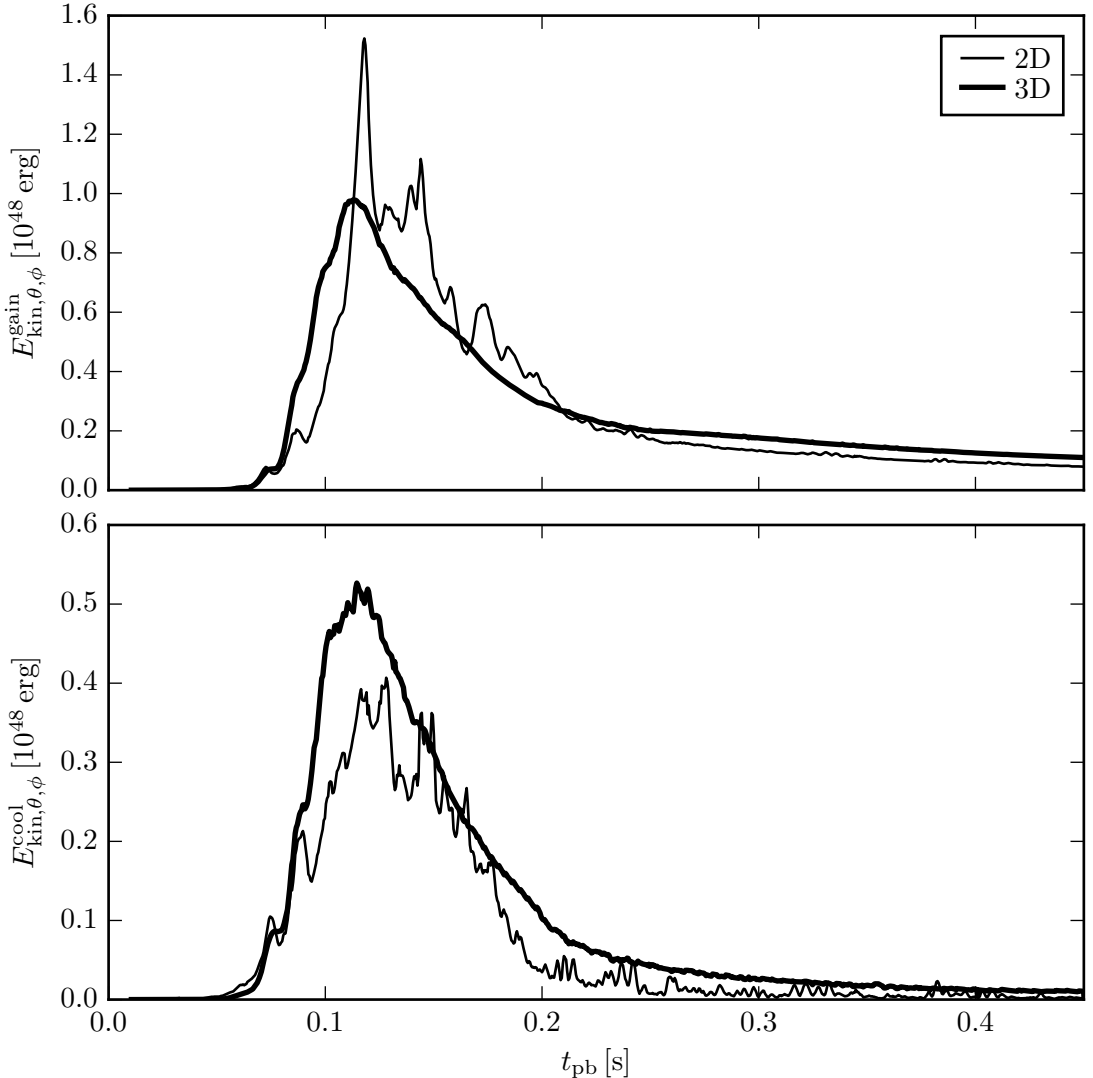


Fig. 4.9.: Turbulent kinetic energies in the gain and the cooling layer, respectively, as defined in Eqs. (4.14) and (4.15).

the statistical variance. Contrarily, the 2D value shows a noisier behavior with strong peaks. In the time interval between 100 and 200 ms, in which the difference in the explosion energy between 2D and 3D builds up, the turbulent kinetic energy in the gain layer is lower in 3D, in contrast to the cooling layer where it is higher. The turbulent pressure, which is computed from the Reynolds stress tensor and suggested to contribute to the pressure balance at the shock (Murphy et al., 2013; Couch & Ott, 2015), is therefore lower in 3D and cannot be used to explain the faster shock expansion and the more energetic explosion.

Generally, stellar matter is advected through the gain layer into the cooling layer. Since $E_{\text{kin},\theta,\phi}^{\text{gain}}$ of the 2D model is greater than in the 3D case and vice versa for $E_{\text{kin},\theta,\phi}^{\text{cool}}$ in the time interval between 100 and 200 ms, there must be some mechanism that dissipates kinetic energy in 2D more efficiently than in 3D. The described discrepancy can otherwise not arise. We will show and explain below that dissipation of downdrafts

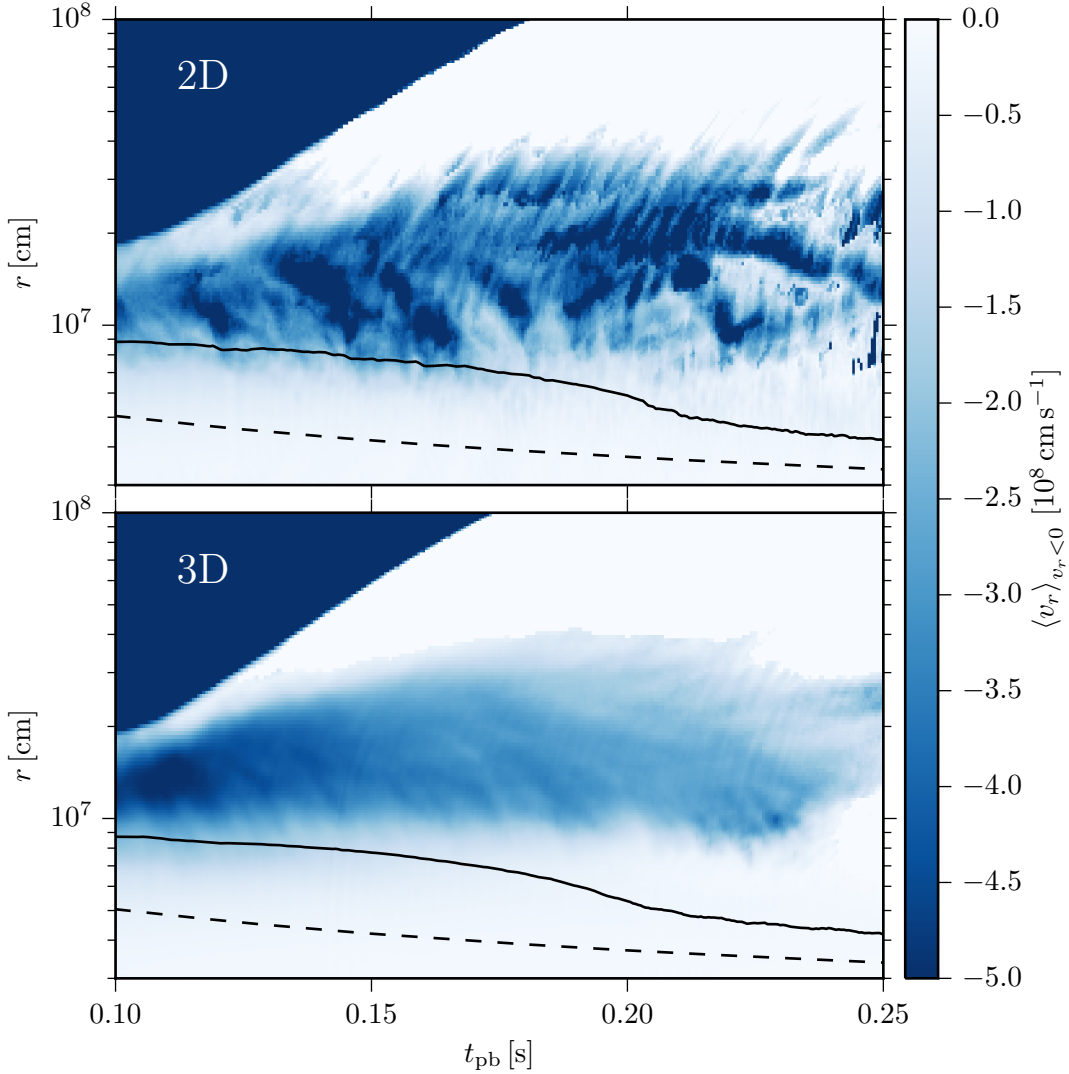


Fig. 4.10.: Angle-averaged radial velocities of downflows in 2D and 3D (see Eq. (4.16) for the definition of the averaging procedure). Solid black lines indicate the angle-averaged gain radii, whereas dashed lines show the positions of $R_{\tau=3}$ being defined as the radius where the angle-averaged optical depth of electron neutrinos is equal to 3. The cooling layers are situated between these lines.

penetrating into the cooling layer is indeed more efficient in 2D.

To investigate the damping of the turbulent kinetic energy further, we introduce a new averaging procedure,

$$\langle \mathcal{X} \rangle_{v_r < 0} := \frac{\int d\Omega \Theta(-v_r) \mathcal{X}}{\int d\Omega \Theta(-v_r)}, \quad (4.16)$$

being the angle average over downflows. Only grid cells with velocities pointing inwards are considered for the average.

In Fig. 4.10, we show the quantity $\langle v_r \rangle_{v_r < 0}$, which is the angle-averaged radial velocity

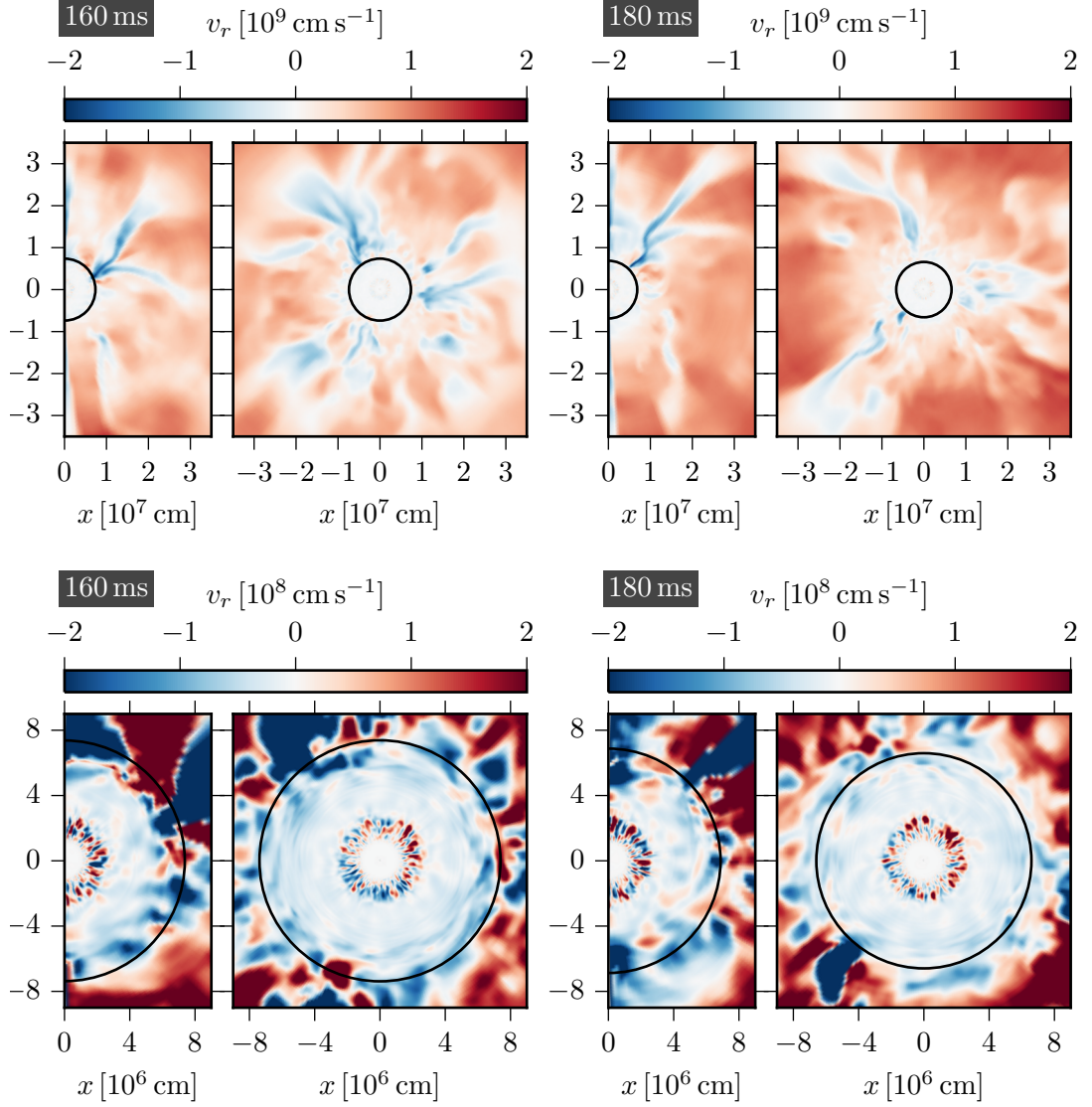


Fig. 4.11.: Color-coded radial velocities in the plane $y = 0$ in 2D and 3D at 160 ms (*left column*) and 180 ms (*right column*). The gain radii are indicated by black circles. The bottom row is a close-up of the top row with a different color scale.

of downflows. Dark blue regions in the upper left corners of both panels indicate the pre-shock region. White areas depict domains without downdrafts. The flow pattern in the gain layer looks differently in 2D and 3D. As already demonstrated in Fig. 4.8, we observe again that the angle-averaged distribution is smoother and more coherent in 3D due to the presence of smaller-scale turbulent structures. In 2D, the extrema of $\langle v_r \rangle_{v_r < 0}$ are higher and the patterns change rapidly. Particularly, the inner boundaries of the downflows show a distinct behavior. In 2D, the flow penetrates deeper into the cooling layer, which is enclosed by solid and dashed lines. When mass accretion has ceased after 200 ms post bounce (cf. Fig. 4.6), the downflows do not reach the cooling layer anymore.

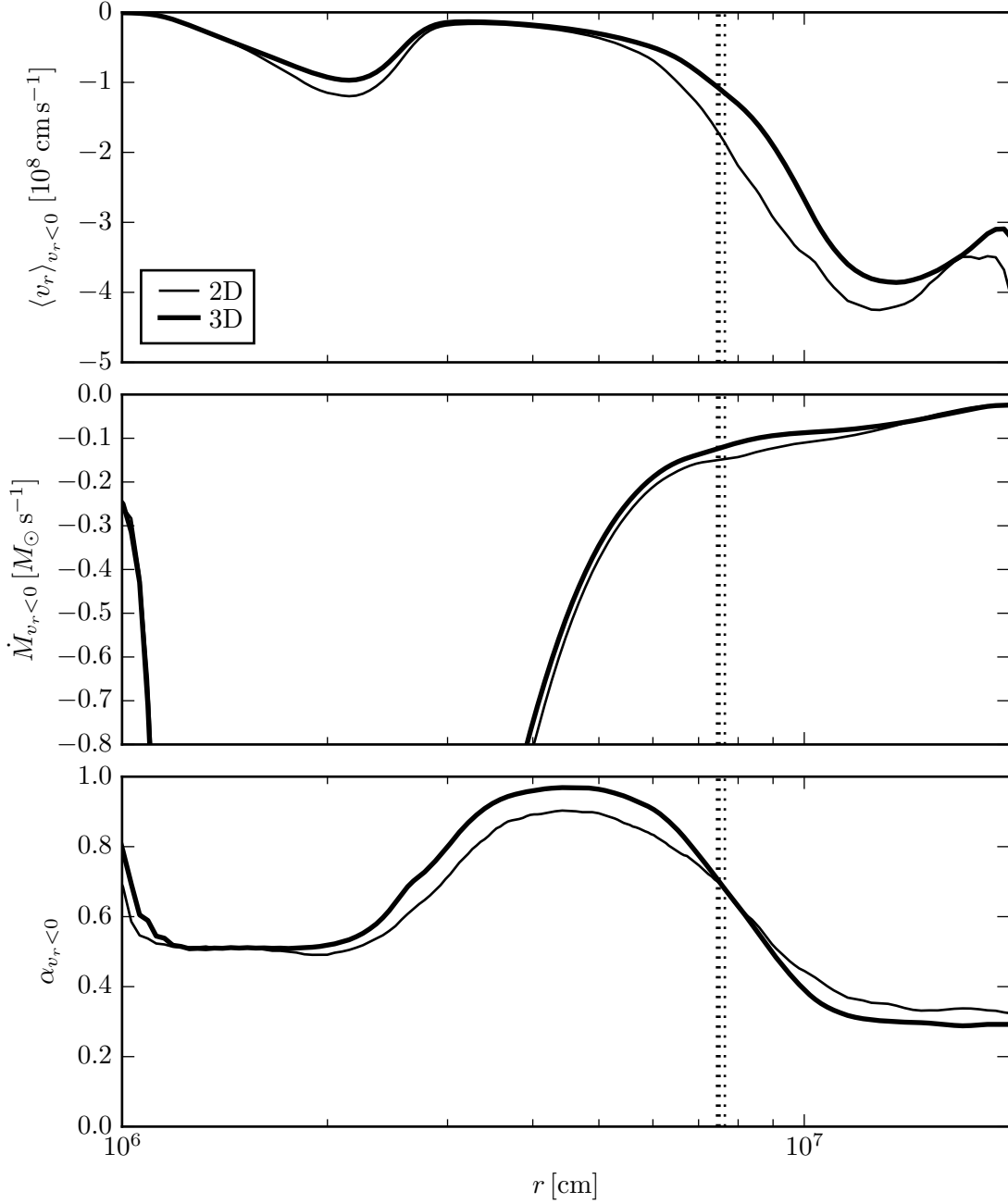


Fig. 4.12.: Angle-averaged radial velocities of downflows $\langle v_r \rangle_{v_r < 0}$, mass-infall rates of downflows $\dot{M}_{v_r < 0}$, and downflow filling factors $\alpha_{v_r < 0}$ in 2D and 3D. See Eqs. (4.16), (4.10), and (4.17), respectively, for their definitions. The quantities are averaged over the time interval $100 \text{ ms} \leq t_{\text{pb}} \leq 200 \text{ ms}$. Vertical dotted lines depict the angle-averaged gain radii in 2D (thin dotted line) and 3D (thick dotted line), averaged over the same time interval.

These findings can be affirmed by examining the structures of the downflows in Fig. 4.11. Blue funnels represent fluid motions with negative radial velocities. At a first glance, the number of downflows in 3D is larger than in 2D, where in the latter case

one prominent funnel exists near the equator. This is in accordance with the discussion above regarding the fragmentation of fluid structures to smaller scales in 3D. In the bottom row of Fig. 4.11, we show the detailed fluid motion at the gain radius with the same color coding but different color scale. It can be clearly seen that the downflows advance deeper into the cooling layer in 2D and that the stellar matter remains more calmly at the gain radius in 3D. Downflows in 2D reach not only deeper layers but also higher absolute radial velocities before entering the cooling layer, illustrated by darker blue colors. Note that the region at a radius of ~ 20 km with strong activity depicts convection inside the proto-neutron star.

As usually observed in 2D simulations and also in Fig. 4.11, downdrafts exist at the symmetry axis, which is a consequence of the reflecting boundaries in θ direction. The fluid cannot cross the axis and is thus channeled into radial motions there.

Our observations concerning the structures of the downdrafts can be consolidated even further. In Fig. 4.12, we show various quantities being averaged over the crucial time interval between 100 and 200 ms, in which the 2D-3D difference in the explosion energies builds up. Note that we do not introduce a special notation for the time averages for the sake of simplicity.

The angle-averaged velocity of downflows $\langle v_r \rangle_{v_r < 0}$ has already been shown time-dependently in Fig. 4.10. After averaging over time, it can be seen that its absolute value is larger in 2D in the gain layer and especially at the gain radius, marked by vertical dotted lines. Interestingly, the gradient of $\langle v_r \rangle_{v_r < 0}$ in the vicinity of the gain radius is much steeper in the 2D case. Hence, the downflows seem to be decelerated more abruptly and kinetic energy is dissipated more violently in 2D.

Besides the higher absolute radial velocity, the 2D downflows also carry more mass, which is visible by a lower (negative) mass-infall rate. The fact that more mass is transported into the cooling layer in 2D has already been shown in Fig. 4.6 and is in line with our observation of a heavier proto-neutron star in this case.

For studying the angular size of the downflows, we introduce the “downflow filling factor”

$$\alpha_{v_r < 0} := \frac{\int d\Omega \Theta(-v_r)}{\int d\Omega}, \quad (4.17)$$

which is shown in the bottom row of Fig. 4.12. In the gain layer, the time average of $\alpha_{v_r < 0}$ is larger in 2D compared to 3D, which means than the downflows occupy more space. This seems to contradict what we have observed in Fig. 4.11. Although the number of downflows is lower in 2D, their integrated angular size is larger, because they have the shape of toroidal sheets in axial symmetry instead of funnels in a full 3D model. In the cooling layer, the relation of the downflow filling factors in 2D and 3D inverses. Stronger deceleration in 2D obviously reduces the space filled by downdrafts more quickly.

More mass is transported into the cooling layer in 2D with higher velocities, but then decelerated more rapidly below the gain radius. The dissipation of kinetic energy is thus more violent in 2D. Sound waves steepen into shocks as downflows penetrate into the cooling region. We show these deceleration shocks in Fig. 4.13, where the relative density variation is color-coded. The density contrast in the 2D simulation is much more pronounced at the upper edge of the cooling layer. Strong shocks are visible in 2D, whereas the 3D model remains more calm. We have therefore identified the mechanism with which kinetic energy is dissipated more efficiently in 2D compared to

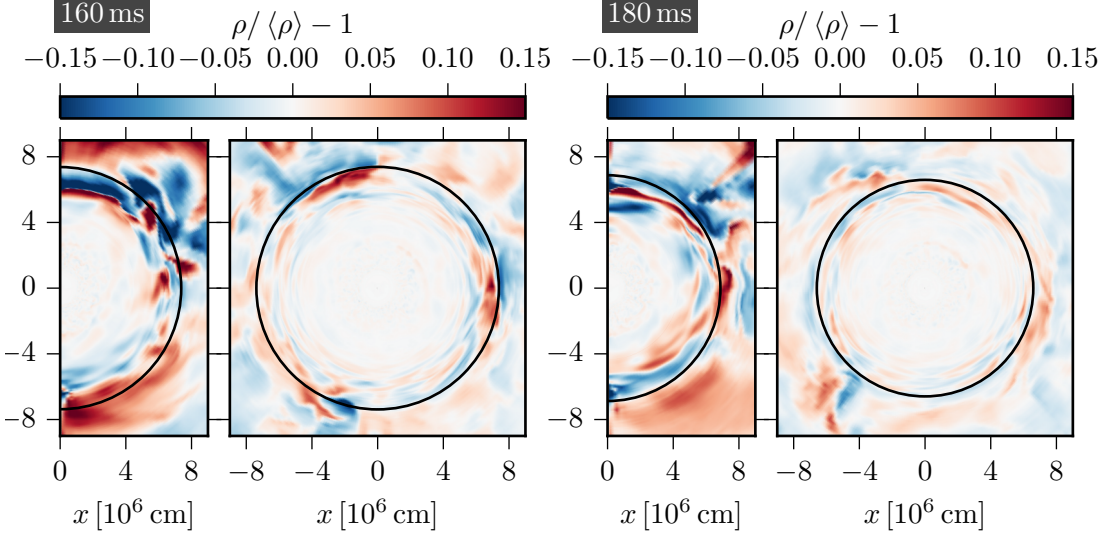


Fig. 4.13.: Density contrast in 2D and 3D at the same times and in the same orientation as Fig. 4.11. Again, the gain radii are marked by black circles.

the 3D case.

The enhanced dissipation of kinetic energy into internal energy in 2D must result in a higher temperature in the cooling layer compared to 3D. In Fig. 4.14, we demonstrate that this is indeed the case. The difference of the angle-averaged temperatures $\langle T_{3D} \rangle - \langle T_{2D} \rangle$ in the cooling layers is negative and the material is obviously hotter in the 2D case there. Although the temperature difference of $\sim 5 \times 10^8$ K is small compared to the absolute value of several 10^{10} K, the effect on the neutrino emission rates is distinct. They depend strongly on the temperature, i.e. e^{\pm} captures and e^+e^- pair annihilation scale with T^6 and T^9 , respectively (e.g., Bethe & Wilson, 1985). Consequently, the angle-averaged net heating rate $\langle \dot{q} \rangle$ shown in Fig. 4.14 is more negative in the cooling layer in 2D corresponding to a 30% higher specific cooling rate compared to 3D. On the contrary, the heating rates are fairly equal in both models, because the temperature is only marginally higher in the gain layer in 3D.

The effect of enhanced neutrino cooling in 2D can also be seen in Fig. 4.15, where we show the total heating and cooling rates as functions of time. The latter is given by

$$\dot{Q}_{\text{cool}} = \int_{R_{\tau=3} < r < R_{\text{gain}}} dV \rho \dot{q}. \quad (4.18)$$

In the crucial time interval between 100 and 200 ms, the absolute value of the cooling rate is higher in 2D, whereas no difference between 2D and 3D is present for the heating rates. This is in line with our analysis of the specific net heating rate \dot{q} above. Even though this finding is only slightly visible in the instantaneous values, the time-integrated heating and cooling rates in Fig. 4.15 doubtlessly demonstrate that the 2D model cools more efficiently than its 3D counterpart during the considered time interval, while the heating is effectively equal. To be more specific, the absolute value of the time-integrated cooling rate is about 2% lower in 3D at 450 ms, which corresponds to a difference of about 4×10^{49} erg. At the same time, the deposited energy by neutrino heating in the gain layer is only 0.4% or $\sim 2 \times 10^{48}$ erg higher in 3D.

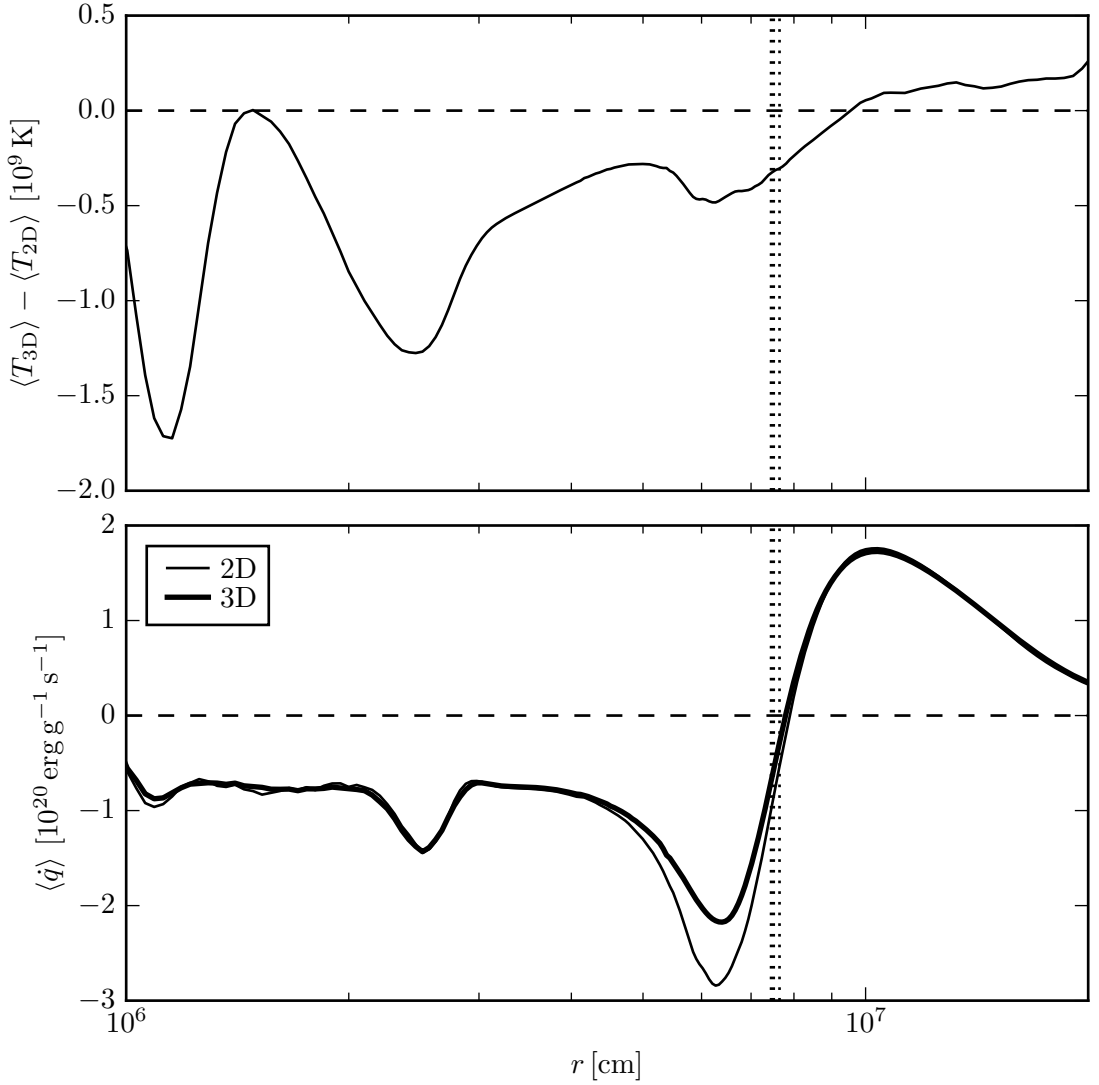


Fig. 4.14.: Difference of 3D and 2D values of the angle-averaged temperature $\langle T \rangle$ (*upper panel*) and angle-averaged net specific heating rates $\langle \dot{q} \rangle$ (*lower panel*) as functions of radius. The quantities are averaged over the time interval $100\text{ ms} \leq t_{\text{pb}} \leq 200\text{ ms}$. Vertical dotted lines depict the angle-averaged gain radii in 2D (*thin dotted line*) and 3D (*thick dotted line*), time-averaged over the same interval.

The gain radius R_{gain} marks the point where the net heating rate is zero, i.e. where neutrino heating balances neutrino cooling. We have explained above that the absolute value of the cooling rate in 2D is higher than in 3D and that the heating rates are essentially equal in both cases. It directly follows that the angle-averaged gain radius is larger in 2D, which can be seen in Fig. 4.16. At 200 ms after bounce, for example, $\langle R_{\text{gain}} \rangle$ is at 58.9 km in 2D and 53.7 km in 3D.

Also in Fig. 4.16, the 2D and 3D values of the lower bounds of the cooling layers, $R_{\tau=3}$, are presented. These are equal in both simulations, which implies a higher mass

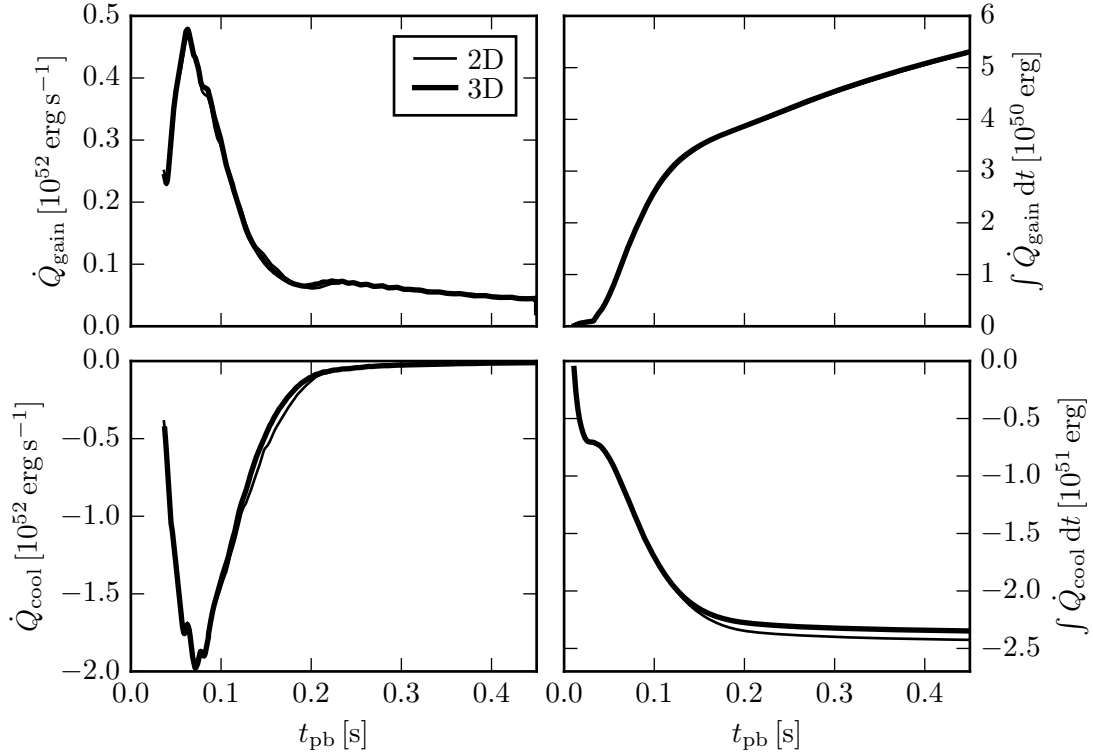


Fig. 4.15.: Total heating and cooling rates, \dot{Q}_{gain} and \dot{Q}_{cool} (see Eqs. (4.9) and (4.18)) in 2D and 3D. The instantaneous and time-integrated values are shown in the left and right panels, respectively.

in the cooling layer,

$$M_{\text{cool}} = \int_{R_{\tau=3} < r < R_{\text{gain}}} dV \rho, \quad (4.19)$$

in 2D. Most important, however, is the gain layer mass, which is significantly larger in 3D. It can be seen in Fig. 4.16 that the difference in M_{gain} of $1.2 \times 10^{-3} M_{\odot}$ builds up between 100 and 200 ms and remains nearly constant afterwards. This difference in the gain layer mass is exactly the reason for the higher explosion energy in 3D, because the energy being released when free nucleons recombine into alpha particles and further into heavy nuclei can easily account for the explosion energy difference. Assuming a binding energy of 7 MeV/nucleon for alpha particles and 8.8 MeV/nucleon for iron-group nuclei, the recombination of $1.2 \times 10^{-3} M_{\odot}$ of free nucleons yields between 1.6×10^{49} erg and 2.0×10^{49} erg. From Fig. 4.2, we have concluded that the diagnostic explosion energy (assuming a recombination into ^{56}Fe) is about 1.3×10^{49} erg higher in the 3D case. From this it follows that we can explain the higher explosion energy in 3D by a higher recombination energy of the more massive gain layer compared to 2D.

In this section, we have discussed differences between 2D and 3D that appear subtle but are relevant to understand the behavior of the diagnostic quantities in both cases. We have compiled a complex causal chain that culminates in a higher explosion energy in 3D. The underlying process is the fundamentally distinct behavior of the turbulent energy cascade in 2D compared to the more realistic 3D case. We will summarize our

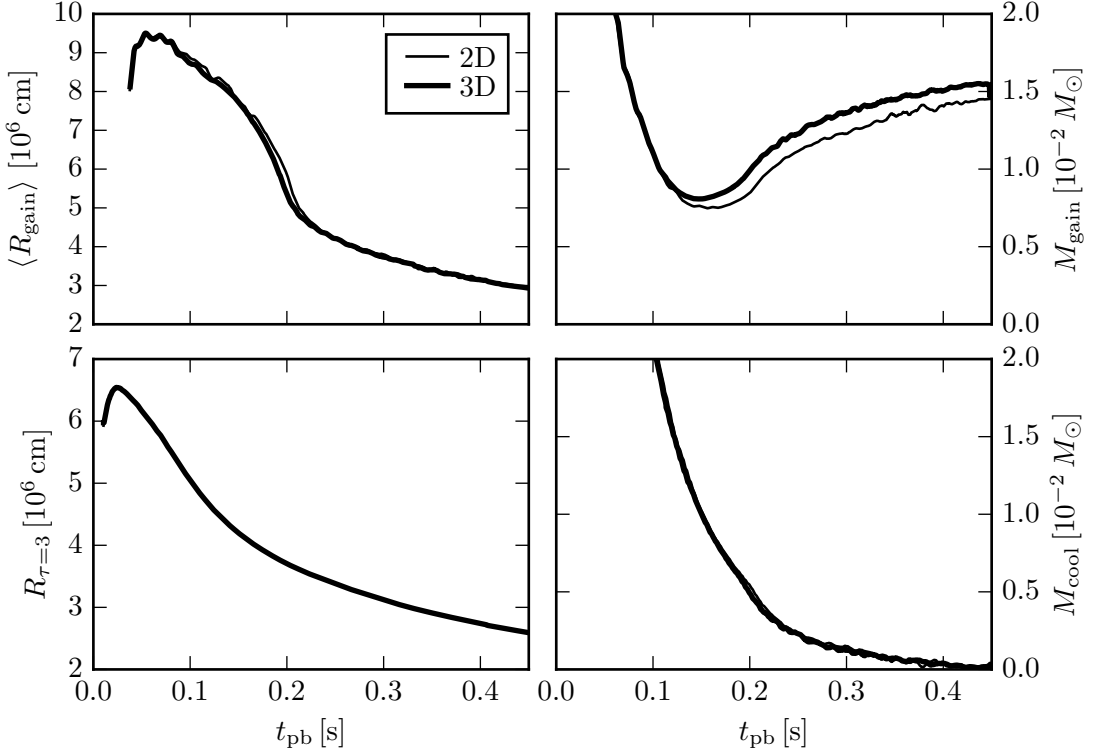


Fig. 4.16.: Angle-averaged gain radii $\langle R_{\text{gain}} \rangle$, lower bounds of the cooling layers $R_{\tau=3}$, gain layer masses M_{gain} , and cooling layer masses M_{cool} as functions of time in 2D and 3D.

findings later and also compare them to other results reported in the literature.

Seen individually, neither the properties nor the outflow dynamics of the 3D explosion itself are particularly spectacular. The shock remains relatively spherical due to the absence of a stagnation phase and SASI sloshing or spiral modes. Nevertheless, an interesting result can be derived in terms of another instability that yields a dipolar emission of the lepton-number flux and was previously found in other non-exploding 3D models. We will show and discuss the occurrence of this phenomenon in our 3D simulation in the next section.

4.3.3. Lepton-number emission dipole

Recently, Tamborra et al. (2014a) have reported on a new phenomenon, which was found in all three-dimensional simulations performed with the VERTEX-PROMETHEUS code. Between 100 and 200 ms after bounce, a strong dipole of the lepton-number flux density emerges, i.e. the number flux density of ν_e is maximal in a certain direction, while the maximum of the $\bar{\nu}_e$ number flux density is at the opposite side. Remarkably, the dipole remains quite stable for hundreds of milliseconds both in amplitude and direction. It drifts only slowly compared to typical timescales of convection or the SASI. Tamborra et al. (2014a) therefore termed it “Lepton-number emission self-sustained asymmetry” or “LESA” in short.

Although a thorough mathematical analysis or isolated toy model simulation of this

instability is not yet available, Tamborra et al. (2014a) with additions of Janka et al. (2016) presented a possible explanation for the feedback cycle. Convection in the proto-neutron star is enhanced in one hemisphere possibly due to the interplay of stabilizing and destabilizing terms in the Ledoux criterion. Material with high electron fraction from the proto-neutron star interior is thus accumulated on one side below the neutrinosphere. The number flux density of electron neutrinos is therefore higher in this direction. Because electron antineutrinos have a greater mean energy than electron neutrinos, neutrino heating is stronger in the hemisphere of higher $\bar{\nu}_e$ flux. This pushes the shock to larger radii leading to a deflection of the accretion flow to the hemisphere of higher Y_e , where fresh material is deposited. In this way, a feedback cycle is established that can persist for hundreds of milliseconds.

There is an ongoing debate whether the LESA phenomenon is a numerical artifact of current 3D simulations. It has been observed by groups working with other simulation codes (see discussion in Janka et al., 2016), so that it is certainly not related to the VERTEX-PROMETHEUS code itself. However, all these codes use the ray-by-ray approximation for neutrino transport and – although being unlikely – it can therefore currently not be excluded that LESA is an artifact of this scheme.

If the LESA asymmetry existed in nature, it would have important implications (see Janka et al., 2016). First, observations of the supernova neutrino signal would depend on the viewing angle (Tamborra et al., 2014b). Second, the conditions for nucleosynthesis would depend on the direction, because the LESA dipole would leave its imprint on the Y_e distribution of the ejecta. Third, the asymmetric neutrino emission would cause a proto-neutron star kick of considerable value (Geßner, 2014).

In this section, we show the LESA in our three-dimensional simulation of the $9.6 M_{\odot}$ progenitor. With this model, we can provide two important observations that support the current explanation of the phenomenon. One the one hand, we see a strong LESA dipole in our axis-free Yin-Yang setup, which underlines that the asymmetry is not related to the numerical grid and especially not to the axis of the spherical polar grid previously used by Tamborra et al. (2014a). On the other hand, we observe that the dipole decays into a quadrupole at about 370 ms most likely due to the cessation of matter accretion onto the proto-neutron star.

For our discussion, we decompose the lepton-number flux density $F_{\nu_e} - F_{\bar{\nu}_e}$ into spherical harmonics. F_{ν_e} and $F_{\bar{\nu}_e}$ denote the individual radial number flux densities of ν_e and $\bar{\nu}_e$, respectively. The real spherical harmonics are defined as

$$Y_{\ell}^m(\theta, \phi) = \begin{cases} \sqrt{2}N_{\ell}^m P_{\ell}^m(\cos \theta) \cos(m\phi) & m > 0 \\ N_{\ell}^0 P_{\ell}^0(\cos \theta) & m = 0 \\ \sqrt{2}N_{\ell}^{|m|} P_{\ell}^{|m|}(\cos \theta) \sin(|m|\phi) & m < 0 \end{cases} \quad (4.20)$$

with normalization factors

$$N_{\ell}^m = \sqrt{\frac{2\ell+1}{4\pi} \frac{(\ell-m)!}{(\ell+m)!}} \quad (4.21)$$

and associated Legendre polynomials $P_{\ell}^m(\cos \theta)$. The coefficients for the multipole analysis are

$$c_{\ell}^m = \sqrt{\frac{4\pi}{2\ell+1}} \int d\Omega r^2 [F_{\nu_e}(\theta, \phi) - F_{\bar{\nu}_e}(\theta, \phi)] Y_{\ell}^m(\theta, \phi). \quad (4.22)$$

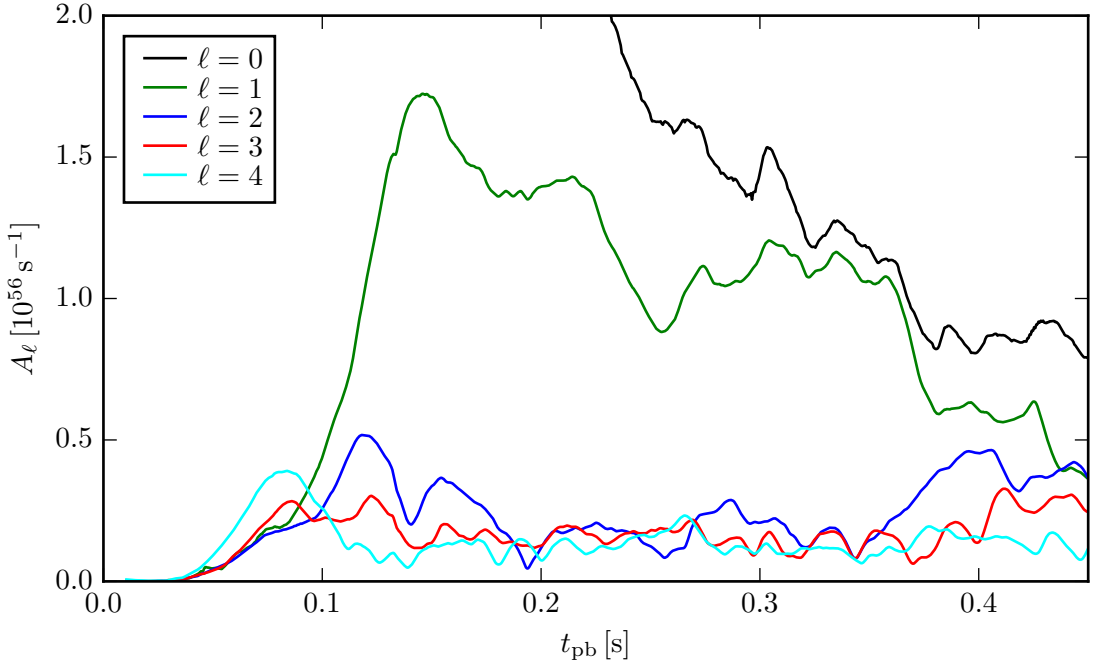


Fig. 4.17.: Multipole moments of the lepton-number flux density of the 3D model as defined in Eq. (4.24).

In our chosen normalization, the reconstruction reads

$$F_{\nu_e}(\theta, \phi) - F_{\bar{\nu}_e}(\theta, \phi) = \frac{1}{r^2} \sum_{\ell=0}^{\infty} \sqrt{\frac{2\ell+1}{4\pi}} \sum_{m=-\ell}^{\ell} c_{\ell}^m Y_{\ell}^m(\theta, \phi). \quad (4.23)$$

From the coefficients c_{ℓ}^m , the multipole moments can be calculated according to

$$A_{\ell} = \sqrt{\sum_{m=-\ell}^{\ell} (c_{\ell}^m)^2}. \quad (4.24)$$

In Fig. 4.17, we present the first five multipole moments A_{ℓ} of the lepton-number flux density. It can be clearly seen that a strong dipole component grows exponentially until 130 ms, decreases gradually after the maximum is reached at 146 ms, until it finally decays at 370 ms. At this time, the quadrupole moment increases significantly and the octupole moment follows this trend. The decay of the LESA dipole correlates with the time when accretion flows do not reach the proto-neutron star anymore (cf. Fig. 4.6). This indicates that accretion of matter plays an important role in the feedback cycle stabilizing the dipolar asymmetry.

In order to compare with the results of Tamborra et al. (2014a) also quantitatively, we show the monopole and the dipole in the upper row of Fig. 4.18 in the same way as their Fig. 3. Tamborra et al. (2014a) have chosen a different normalization of the dipole component so that their notation translates as $A_{\text{Monopole}} = A_0$ and $A_{\text{Dipole}} = 3A_1$. When the monopole and dipole terms become equal in their definition, the flux maximum in dipole direction reaches twice the angular average and vanishes in the

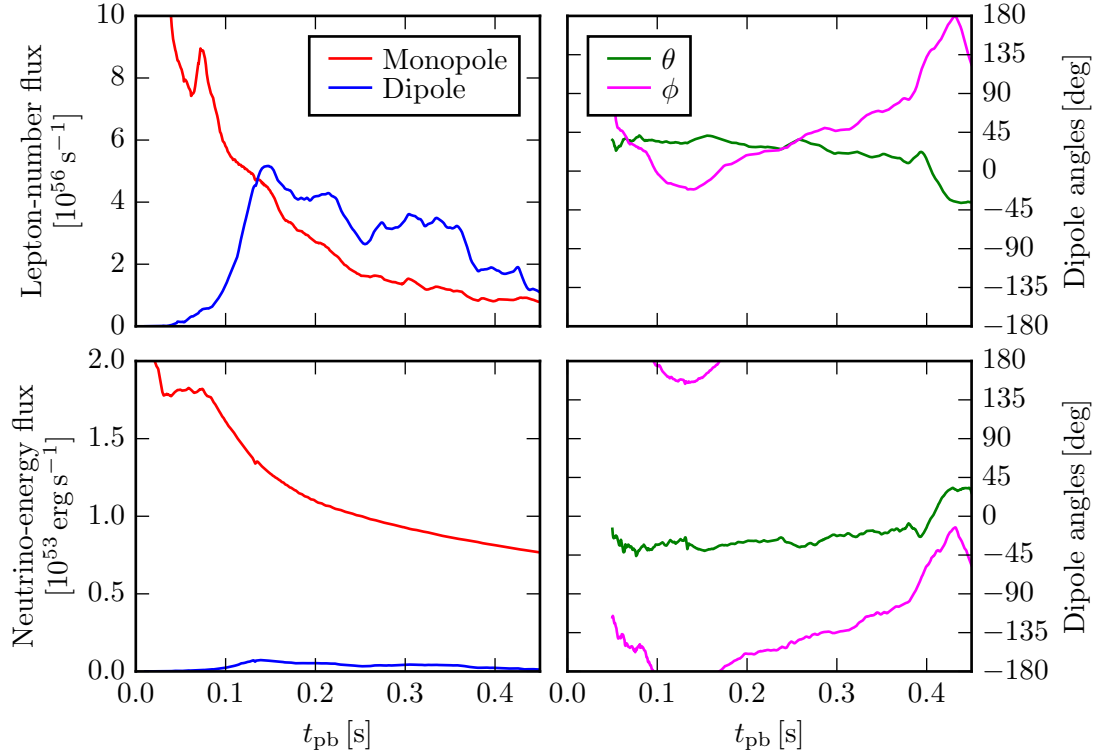


Fig. 4.18.: Monopole and dipole amplitudes of the lepton-number flux density $F_{\nu_e} - F_{\bar{\nu}_e}$ (*upper left panel*) and the neutrino-energy flux density F_e (*lower left panel*) together with the angles of their dipole directions (*right panels*). The normalization of the multipoles and their illustration is similar to Tamborra et al. (2014a, Fig. 3). Note that the amplitudes shown here are related to the values in Fig. 4.17 as $A_{\text{Monopole}} = A_0$ and $A_{\text{Dipole}} = 3A_1$.

opposite direction. In our model, the lepton-number dipole exceeds the monopole from the time of dipole maximum to the end of the simulation. Its direction remains relatively stable beginning at 150 ms until the dipole decays.

In Fig. 4.18, the monopole and dipole of the neutrino-energy flux density being defined as

$$F_e = F_e(\nu_e) + F_e(\bar{\nu}_e) + 4F_e(\nu_x). \quad (4.25)$$

are also shown. The individual terms denote the energy flux densities of the three neutrino species ν_e , $\bar{\nu}_e$, and $\nu_x = \{\nu_\mu, \bar{\nu}_\mu, \nu_\tau, \bar{\nu}_\tau\}$. These can be calculated similarly to Eq. (2.12) but without the angle integral as

$$F_e(\nu) \equiv F_e(\vec{r}, \nu, t) = \int_0^\infty d\varepsilon H(\vec{r}, \varepsilon, \nu, t). \quad (4.26)$$

Obviously, the amplitude of the neutrino-energy dipole is much smaller than the lepton-number dipole. This is in line with observations of Tamborra et al. (2014a), who saw that the directional variations of the neutrino-energy flux density are at a level of a few percent.

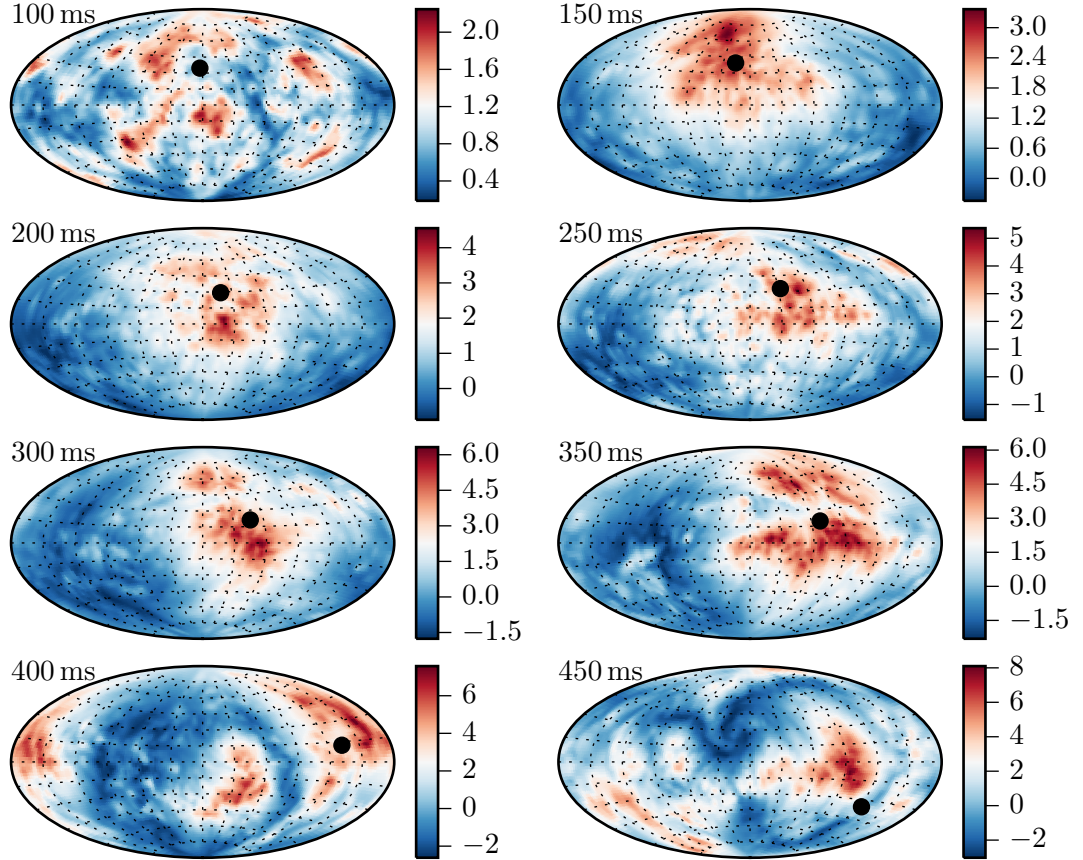


Fig. 4.19.: Aitoff projection of the lepton-number flux density at a fixed radius of 400 km for different times. In each map, the quantity is divided by its angular average, i.e. $(F_{\nu_e} - F_{\bar{\nu}_e}) / \langle F_{\nu_e} - F_{\bar{\nu}_e} \rangle$, and displayed in all directions (4π). Black dots mark the angular positions of the dipoles. The orientation of the coordinate axes in this specific visualization is presented in Appendix A.

The lepton-number and neutrino-energy dipole vectors are parallel but have a different orientation. Deep in the gravitational potential well, the density and pressure distributions of the proto-neutron star are spherical. This can only be achieved if the asymmetry of the electron fraction Y_e is compensated by an appropriate temperature distribution (Janka et al., 2016). In the direction of higher $\bar{\nu}_e$ number flux density, i.e. where Y_e is lower, the temperature must be higher so that the neutrino-energy flux density is larger in this hemisphere. Consequently, the lepton-number dipole is opposite to the neutrino-energy dipole.

The directional distribution of the lepton-number and neutrino-energy flux densities can be seen in Figs. 4.19 and 4.20, respectively. Starting from many small patterns at 100 ms, a distinct lepton-number dipole emerges already at 150 ms. Its direction drifts only slowly for about 200 ms and its shape remains stable (cf. Fig. 4.18). At 400 ms after bounce, the dipole is no longer evident and a quadrupolar distribution is visible. Comparing these observations with the neutrino-energy flux density clearly shows that both quantities behave inversely. Maxima of the lepton-number flux density match

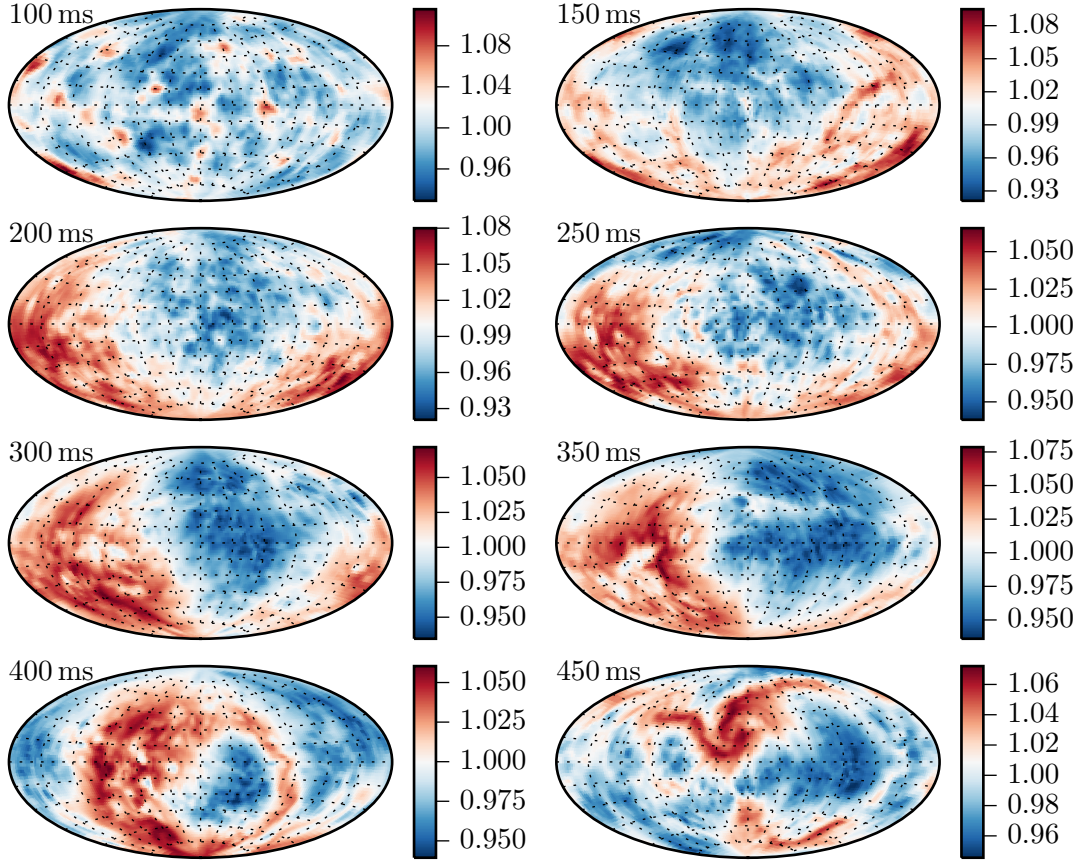


Fig. 4.20.: Same as Fig. 4.19, but for the normalized neutrino-energy flux density $F_e / \langle F_e \rangle$.

minima of the neutrino-energy flux density and vice versa.

Not only the distribution of the discussed quantities can be deduced from Figs. 4.19 and 4.20, but also their value ranges. While the neutrino-energy flux density varies at a level of a few percent, the maxima of the lepton-number flux density can be more than a factor of six larger than the angular averages during the dipole phase.

The temporal evolution of radial profiles of the lepton-number flux is shown in Fig. 4.21. For each point in time, the dipole direction is determined and a local spherical coordinate system is set up with the dipole vector pointing towards the “north pole”. We can then integrate the lepton-number flux density in the “northern” hemisphere, i.e. in the hemisphere of higher ν_e flux, and in the “southern” hemisphere, where the $\bar{\nu}_e$ flux is larger. Fig. 4.21 is therefore similar to Fig. 9 of Tamborra et al. (2014a). Both the formation of the dipole from 50 ms to 100 ms and the successive decay after 350 ms are clearly visible. At 150 ms, i.e. around dipole maximum, the hemispheric lepton-number flux of enhanced ν_e emission is a factor of 3.9 higher than in the opposite hemisphere.

As already mentioned by Tamborra et al. (2014a), the hemispheric difference builds up mainly in the mantle of the proto-neutron star, i.e. below the proto-neutron star surface, which we have illustrated with vertical dotted lines. In our model, the hemispheric fluxes start to deviate from each other at a radius of about 10 km and change sign again slightly below 20 km. This indicates that a complicated mechanism deep in

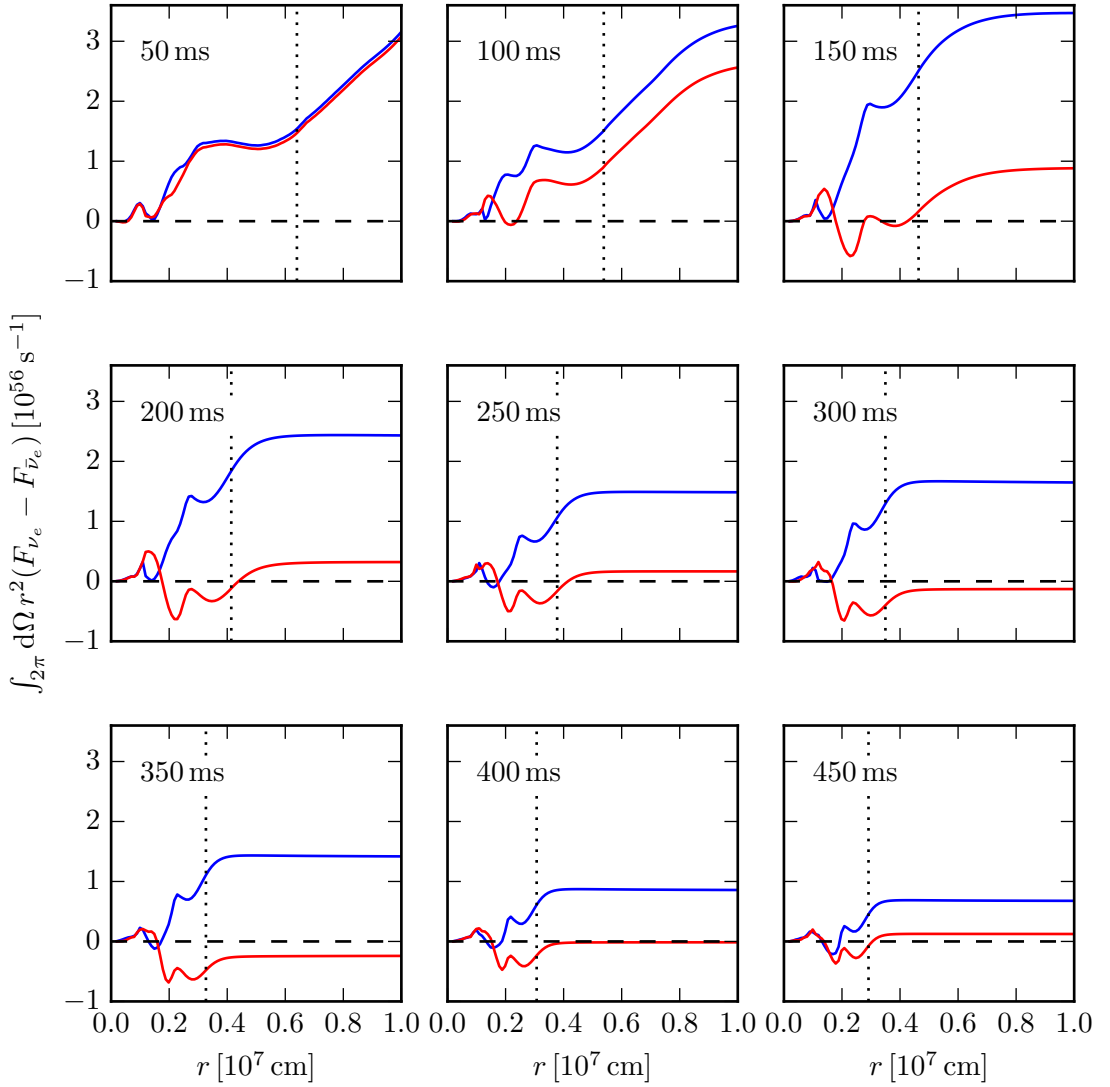


Fig. 4.21.: Radial profiles of the hemispheric lepton-number fluxes in the direction of higher ν_e flux (blue lines) and higher $\bar{\nu}_e$ flux (red lines). Vertical dotted lines indicate the proto-neutron star radii defined by a density of $10^{11} \text{ g cm}^{-3}$. This figure is similar to Tamborra et al. (2014a, Fig. 9).

the proto-neutron star interior is responsible for the growth and stability of the LESA dipole.

Although the phenomenon is not yet completely understood, progress is being made towards a thorough understanding of the LESA (Stockinger, 2015). However, further studies are required that focus on the analytical foundations of the instability or on the question whether the LESA occurs in simulations that do not rely on the ray-by-ray approximation of neutrino transport.

4.4. Summary and discussion

We performed spherically symmetric (1D), axisymmetric (2D), and full 3D core-collapse supernova simulations of a zero-metallicity $9.6 M_{\odot}$ iron-core progenitor with our elaborate neutrino-hydrodynamics code VERTEX-PROMETHEUS. Successful explosions were obtained in all three cases due to the density structure of this specific stellar model. Shock runaway occurred at the same time in 2D and 3D, which offered the unique opportunity to directly compare the fluid dynamics after the onset of explosion.

The diagnostic explosion energy rises to an about 10% higher value in 3D compared to the 2D model in the time interval between 100 and 200 ms after core bounce. This is because turbulent kinetic energy cascades in different directions in 2D and 3D. The fluid fragments to smaller scales and becomes more coherent in 3D, whereas larger structures survive in 2D. More material being accreted from the shock to the proto-neutron star is therefore kept in the gain layer in 3D and the mass-infall rate at the gain radius is lower. Downflows penetrate not as deep into the cooling layer as in 2D and exhibit lower velocities. The dissipation of their kinetic energy in deceleration shocks is thus weaker in 3D resulting in a lower temperature in the cooling layer compared to 2D. Neutrino cooling strongly depends on the temperature and is therefore less efficient in 3D, while the neutrino energy deposition in the gain layer is equal in 2D and 3D. Since the gain radius marks the position where heating balances cooling, it is shifted inwards in 3D and the mass in the gain layer is larger. Recombination of free nucleons of this mass difference into alpha particles and heavy nuclei releases enough energy to account for the higher explosion energy in 3D.

The recently discovered lepton-number emission self-sustained asymmetry (LESA; Tamborra et al., 2014a) was also found in our 3D simulation on the Yin-Yang grid, which demonstrates that the instability is certainly not related to the preferred direction of the spherical polar grid axis. Furthermore, we observed the decay of the LESA dipole and rise of higher-order modes, because the feedback cycle breaks due to ceased matter accretion.

For the first time, we have investigated the different behavior of 2D and 3D models after the onset of explosion in first-principle simulations with sophisticated neutrino transport. Turbulent cascading to smaller scales in 3D leads to a more energetic explosion. Since both models explode easily and basically at the same time, we cannot contribute to the question why 3D models usually tend to explode later and less readily, which is likewise attributed to the different behavior of turbulence between 2D and 3D in the literature (e.g., Hanke et al., 2012; Couch, 2013; Couch & O'Connor, 2014; Couch & Ott, 2015; Lentz et al., 2015).

Similarly, a higher explosion energy in 3D was also reported by Müller (2015) for a heavier $11.2 M_{\odot}$ progenitor. His 3D explosion is more energetic than its 2D counterpart in general-relativistic simulations with a simplified neutrino transport treatment. The reason for this difference is somewhat in line with our findings. The interfaces between downflows and outflows become turbulent in 3D due to the Kelvin-Helmholtz instability, whereas they remain laminar in 2D. Hence, energy is exchanged more efficiently between accretion funnels and neutrino-heated material. Downflows penetrating into the cooling layer therefore have lower velocities in 3D. Their kinetic energy is dissipated by excitation of g-modes that remove energy from the vicinity of the gain radius. This process is more efficient in 2D, so that matter is bound more tightly at the gain radius

compared to the 3D case. The consequent higher mass outflow rate in 3D leads to a more robust increase of the diagnostic explosion energy and a slower growth of the proto-neutron star mass.

The results presented in this chapter therefore seem to hold for other progenitors than our chosen $9.6 M_{\odot}$ model and are possibly a generic feature of three-dimensional turbulence. Core-collapse supernova explosions in 3D might be delayed compared to 2D, but do not necessarily exhibit lower explosion energies. This is particularly important, because the explosion energy observed in 2D simulations is often considerably lower than the canonical value of 10^{51} erg (Marek & Janka, 2009; Suwa et al., 2010; Müller et al., 2012a,b; Bruenn et al., 2013; Nakamura et al., 2015; Suwa et al., 2016). The common argumentation that the forward turbulent cascade to smaller scales in 3D is disadvantageous for the explosion is not a universally valid statement.

It should be noted that our grid resolution is not sufficient to resolve the turbulent energy cascade completely (see Chapt. 6). Nevertheless, increasing the resolution might even amplify the 2D-3D difference. Since kinetic energy is accumulated at large scales in 2D, it is probably not affected much when the resolution is increased, in contrast to the 3D case where the fluid will most likely fragment to smaller scales. Future studies with higher grid resolution are necessary to judge whether our findings remain valid.

5. Explosion of a $20 M_{\odot}$ star

Core-collapse supernova simulations in three dimensions (3D) do not explode robustly yet with state-of-the-art neutrino transport. Explosions are obtained later and less readily compared to their axisymmetric (2D) counterparts for progenitor stars of more than about $10 M_{\odot}$. This was reported for both parametric studies (Hanke et al., 2012; Couch, 2013; Couch & O’Connor, 2014; Couch & Ott, 2015) and for models with neutrino transport based on various levels of sophistication (Takiwaki et al., 2012, 2014; Lentz et al., 2015). As already discussed in the previous chapter, there is consensus in the community that due to the different behavior of the turbulent energy cascade in 2D and 3D, the fluid fragments to small scales in 3D, whereas larger structures remain in 2D. This effect artificially facilitates explosions in 2D and hinders shock revival in 3D. In simulations of the Garching group incorporating sophisticated neutrino transport, 3D models even failed completely, while 2D models exploded successfully for progenitors of 11.2 , 20 , and $27 M_{\odot}$ (Hanke et al., 2013; Tamborra et al., 2013; Hanke, 2014; Tamborra et al., 2014a,b). Only for a low-mass progenitor of $9.6 M_{\odot}$, a successful 3D explosion was obtained (see Chapt. 4).

We have already argued that 2D models behave artificially in several aspects. On the one hand, turbulence does not fragment the fluid to smaller scales, but accumulates power at large scales. On the other hand, the symmetry constraint does not reflect the shape of the fluid structures correctly and suppresses some hydrodynamic instabilities completely such as the spiral SASI mode. Lastly, numerical artifacts occur at the axis causing explosions to occur predominantly along the polar directions. It can therefore not be assumed that 2D simulations cover all processes in a core-collapse supernova correctly. A comparison between 2D and 3D is not able to give the answer why state-of-the-art 3D models of more than $10 M_{\odot}$ fail to explode. Instead, it is important to study what ingredients are potentially missing for obtaining robust explosions in 3D.

Some aspects are not considered in current 3D simulations but are suggested to be important for the explosion mechanism. For example, convective perturbations in the progenitor star – especially of the Si and Si+O layers – prior to core collapse could trigger hydrodynamic instabilities in the gain layer early after bounce and therefore enhance neutrino heating conditions (Arnett & Meakin, 2011; Couch & Ott, 2013; Müller & Janka, 2015; Couch et al., 2015; Müller et al., 2016). Due to computational constraints of stellar evolution, progenitor models are currently provided to us in spherical symmetry, so that multi-dimensional processes are included only in a parametrized way in these setups. Symmetry breaking is achieved by perturbing the fluid after core bounce with relatively low amplitudes. Convection in the gain layer thus requires more time to develop than if perturbations were advected with the infalling stellar shells.

However, in this chapter, we will focus on another deficiency of 3D modeling. There are uncertainties in the neutrino opacities having an impact on neutrino heating and cooling conditions. Modifying them could influence the dynamics in core-collapse supernova simulations and affect their readiness for explosion. Here, we will consider experimentally and theoretically motivated strange-quark contributions to the nucleon

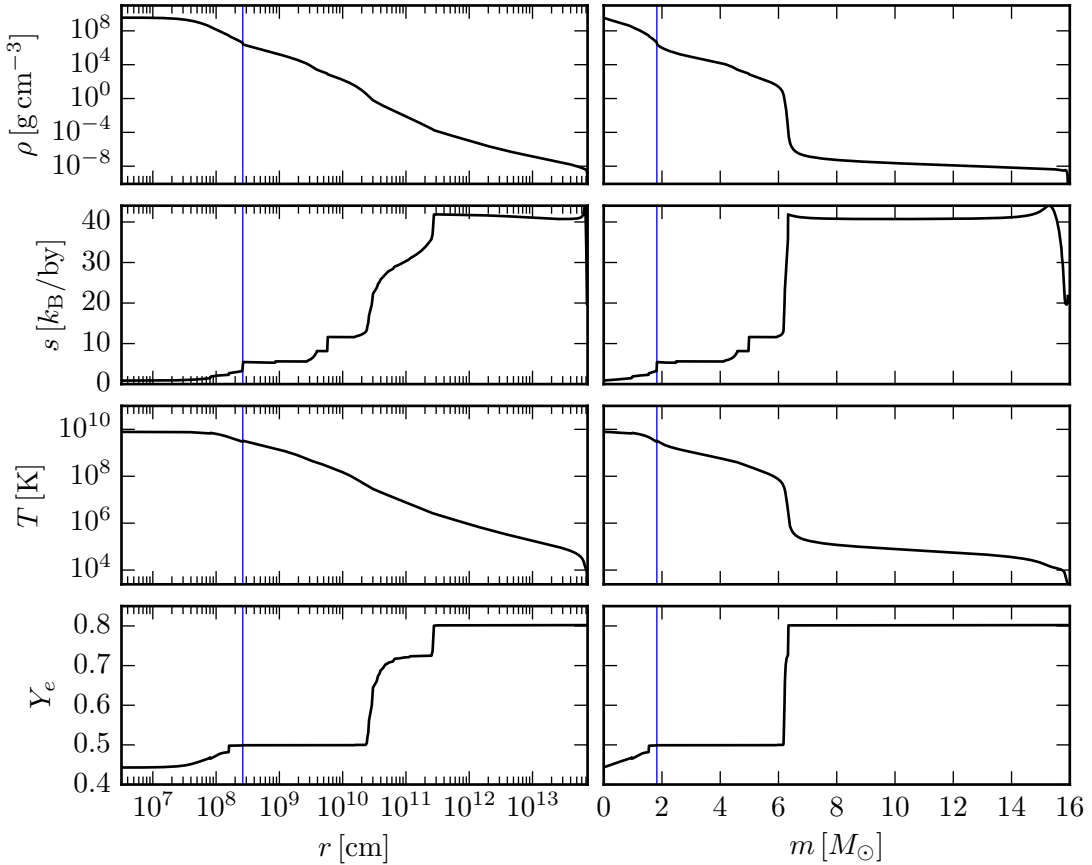


Fig. 5.1.: Profiles of the density ρ , the entropy per baryon s , the temperature T , and the electron fraction Y_e of the $20 M_{\odot}$ progenitor as functions of radius r (*left panels*) and enclosed mass m (*right panels*). Blue vertical lines indicate the Si/Si+O shell interface.

spin, which influence the opacities for neutrino-nucleon scattering. We will demonstrate that a previously failed 3D explosion of a $20 M_{\odot}$ star can be turned into a successful one by modifying the neutrino opacities for neutral-current scattering at a level of 10%. The results discussed in this chapter were partially published in Melson et al. (2015a).

First, we will present the progenitor model used for our study. Then, we will explain the strange-quark correction and describe the numerical setup of our simulations. Finally, the results will be discussed in detail. Note that the definitions of most of the quantities mentioned in this discussion can be found in the previous chapter.

5.1. Progenitor

The initial model for the simulations presented in this chapter is the $20 M_{\odot}$ star of Woosley & Heger (2007). It is a non-rotating progenitor of solar metallicity with a pre-collapse compactness parameter $\xi_{2.5}$ (O'Connor & Ott, 2011) of 0.29.

In Fig. 5.1, we show various progenitor profiles as functions of radius and enclosed mass. A crucial point in the profiles is the Si/Si+O shell interface marked by vertical blue lines. It is characterized by a sharp density decline from 4.5×10^6 to $2.6 \times 10^6 \text{ g cm}^{-3}$

and is located where the entropy exceeds $4 k_B$ per baryon. When it falls through the shock, the mass-accretion rate drops and the ram pressure of the infalling shells is reduced quickly. Shock runaway is commonly initiated only after that time in core-collapse supernova simulations. We will see that also in the models presented here, explosions set in only after the Si/Si+O interface has fallen through the shock.

5.2. Strangeness correction

Strange quarks are expected to be present in the quark sea of the nucleon, thus contributing to the nucleon spin. They influence elastic neutrino-nucleon scattering processes without affecting charged-current reactions. In this section, we will estimate the influence on the neutrino opacities for the three neutrino species ν_e , $\bar{\nu}_e$, and ν_x included in VERTEX-PROMETHEUS.

For iso-energetic neutrino-nucleon scattering, the lowest order transport cross section reads (Horowitz, 2002)

$$\sigma_0^t = \frac{2G_F^2\epsilon^2}{3\pi} (c_v^2 + 5c_a^2), \quad (5.1)$$

where G_F is Fermi's constant and ϵ is the neutrino energy. c_v and c_a are the vector and the axial-vector coupling constant, respectively. The latter are given by

$$c_v = \begin{cases} \frac{1}{2} - 2\sin^2\theta_W & \nu p \rightarrow \nu p \\ -\frac{1}{2} & \nu n \rightarrow \nu n, \end{cases} \quad (5.2a)$$

$$c_a = \begin{cases} \frac{1}{2}g_a & \nu p \rightarrow \nu p \\ -\frac{1}{2}g_a & \nu n \rightarrow \nu n, \end{cases} \quad (5.2b)$$

for neutrino-proton scattering ($\nu p \rightarrow \nu p$) and neutrino-neutron scattering ($\nu n \rightarrow \nu n$), with $\sin^2\theta_W \approx 0.2325$ and $g_a \approx 1.26$ (Olive & Particle Data Group, 2014).

Only the axial-vector component is modified by strange-quark contributions according to

$$c_a = \begin{cases} \frac{1}{2}(g_a - g_a^s) & \nu p \rightarrow \nu p \\ \frac{1}{2}(-g_a - g_a^s) & \nu n \rightarrow \nu n \end{cases} \quad (5.3)$$

(Horowitz, 2002; Hobbs et al., 2016). We can thus write Eq. (5.1) as

$$\sigma_0^t = \frac{G_F^2\epsilon^2}{6\pi} \begin{cases} 5(g_a - g_a^s)^2 & \nu p \rightarrow \nu p \\ 1 + 5(-g_a - g_a^s)^2 & \nu n \rightarrow \nu n, \end{cases} \quad (5.4)$$

where we have assumed $\sin^2\theta_W = 0.25$ for simplicity. Since the strangeness correction g_a^s is negative, the cross section increases for neutrino-proton scattering, while it decreases for neutrino-neutron scattering.

The opacity for neutrino-nucleon scattering can be written as

$$\kappa_{sc} = m_B^{-1} (Y_p \sigma_0^t(\nu p \rightarrow \nu p) + Y_n \sigma_0^t(\nu n \rightarrow \nu n)) \quad (5.5a)$$

$$= \frac{G_F^2\epsilon^2}{6\pi m_B} (5(g_a^2 + (g_a^s)^2) + 10g_a g_a^s(1 - 2Y_e) + 1 - Y_e), \quad (5.5b)$$

where m_B denotes the baryon mass. The proton and neutron fractions are approximated by $Y_p = Y_e$ and $Y_n = 1 - Y_e$, respectively, since post-shock material consists

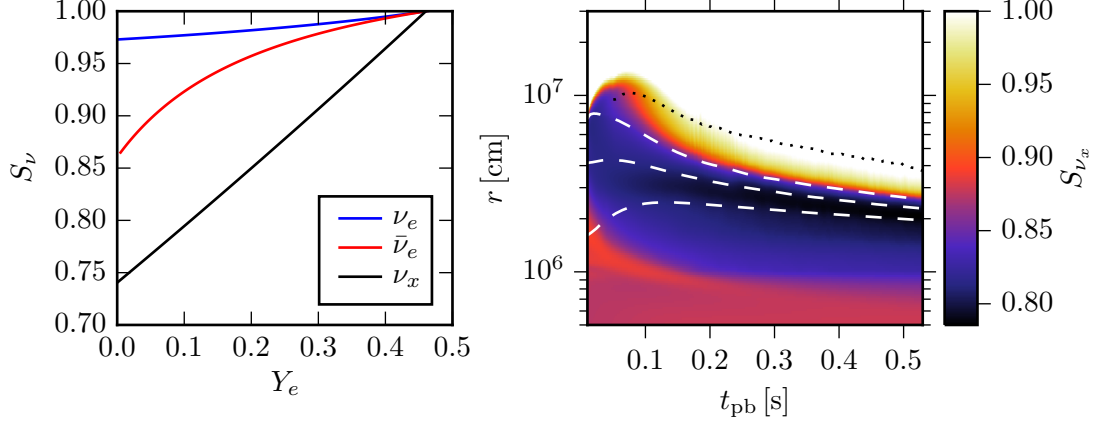


Fig. 5.2.: Neutrino opacity ratios S_{ν} as defined in Eqs. (5.8). The opacities for $g_a^s = -0.2$ are divided by the unchanged values ($g_a^s = 0$). *Left panel:* Ratios S_{ν_e} , $S_{\bar{\nu}_e}$, and S_{ν_x} as functions of Y_e . *Right panel:* Color-coded quantity S_{ν_x} calculated for the angle-averaged Y_e distribution of the model 3Ds (cf. Sect. 5.3). Dashed lines mark radii of constant density with values of $10^{13} \text{ g cm}^{-3}$, $10^{12} \text{ g cm}^{-3}$, and $10^{11} \text{ g cm}^{-3}$ from inside outwards. The angle-averaged gain radius is indicated by a dotted line. t_{pb} denotes the time after core bounce.

almost entirely of free nucleons. For heavy-lepton neutrinos $\nu_x = \{\nu_{\mu}, \bar{\nu}_{\mu}, \nu_{\tau}, \bar{\nu}_{\tau}\}$, the opacity is dominated by κ_{sc} . Other scattering reactions can be neglected, because their cross sections are much smaller (Janka, 2001). For electron neutrinos and electron antineutrinos, however, we need to take charged-current reactions into account. The most important process in this case is absorption on free nucleons, whose zeroth-order cross section is given by

$$\sigma_0 = \frac{G_F^2 \epsilon^2}{\pi} (1 + 3g_a^2) \quad (5.6)$$

(Horowitz, 2002). This yields the opacity

$$\kappa_{\text{abs}} = \frac{G_F^2 \epsilon^2}{\pi m_B} (1 + 3g_a^2) \begin{cases} (1 - Y_e) & \nu_e n \rightarrow e^- p \\ Y_e & \bar{\nu}_e p \rightarrow e^+ n \end{cases} \quad (5.7)$$

for absorption on neutrons and protons, respectively. The corresponding effective opacities for electron (anti)neutrinos can be calculated by combining charged-current absorption and neutral-current scattering opacities according to $\kappa_{\text{eff}} = \sqrt{\kappa_{\text{abs}}(\kappa_{\text{abs}} + \kappa_{\text{sc}})}$ (Rybicki & Lightman, 2004).

In order to quantitatively estimate how the strange-quark correction affects the neutrino opacities, we compute the ratios

$$S_{\nu_e} := \frac{\kappa_{\text{eff}}(g_a^s \neq 0)}{\kappa_{\text{eff}}(g_a^s = 0)} \quad \text{for } \nu_e, \quad S_{\bar{\nu}_e} := \frac{\kappa_{\text{eff}}(g_a^s \neq 0)}{\kappa_{\text{eff}}(g_a^s = 0)} \quad \text{for } \bar{\nu}_e, \quad S_{\nu_x} := \frac{\kappa_{\text{sc}}(g_a^s \neq 0)}{\kappa_{\text{sc}}(g_a^s = 0)} \quad \text{for } \nu_x, \quad (5.8)$$

following the idea of Horowitz (2002). Obviously, the opacity modifications enabled by the strangeness correction depend on Y_e . In Fig. 5.2, we show this dependence of the quantities S_{ν} – the ratios of the modified opacities to the original ones – for the three neutrino species. In all three cases, the numerator is calculated for $g_a^s = -0.2$,

which is the value applied in this work (see discussion below). It can be seen that the opacities are reduced for neutron-rich matter, because the neutrino-nucleon cross section decreases in this regime. In the case of heavy-lepton neutrinos, a reduction of more than 20% is possible for very low Y_e . Since charged-current reactions are not influenced by the strangeness correction, the effective opacities of electron neutrinos and electron antineutrinos are only moderately changed. A reduction of $\sim 3\%$ and $\sim 10\%$ is possible for ν_e and $\bar{\nu}_e$, respectively.

In the right panel of the same Fig. 5.2, the reduction of the neutral-current opacity κ_{sc} is shown color-coded in a radius-time diagram. The ratio S_{ν_x} from Eqs. (5.8) was evaluated for the angle-averaged Y_e distribution of our 3D model with $g_a^s = -0.2$ (model 3Ds, see Sect. 5.3). Lines of constant density are also depicted in Fig. 5.2 in order to estimate the location of the neutrinosphere of ν_x , which is approximately situated where $\rho = (1\dots 4) \times 10^{11} \text{ g cm}^{-3}$. The neutral-current opacity is reduced by $\gtrsim 20\%$ below the proto-neutron star radius being located at $\rho = 10^{11} \text{ g cm}^{-3}$, while S_{ν_x} increases steeply further out. This clearly demonstrates that the strange-quark correction affects the neutrino opacities of all species almost exclusively below the proto-neutron star surface. After about 200 ms post bounce, there is especially no change at the gain radius, which was incorrectly claimed by Hobbs et al. (2016).

The calculations of the opacity reductions are based on zeroth-order cross sections and only the dominant neutrino reactions. Hence, the numbers given above should not be considered exact, however, they provide good estimates for the effect of the strange-quark correction.

We will demonstrate later in this chapter that the neutrino luminosities and the mean energies of all species are considerably enhanced due to the reduction of the neutrino-nucleon scattering opacity. Although the largest opacity modification is seen for heavy-lepton neutrinos, electron (anti)neutrinos are also affected significantly, because the proto-neutron star loses energy on a shorter timescale and therefore contracts faster. This shifts the neutrinospheres of all species to smaller radii and thus to higher temperatures.

For the models discussed in this work, we assume a strangeness correction of $g_a^s = -0.2$. However, latest measurements of the strange-quark contribution by spin-polarized deep inelastic scattering reactions of electrons off nucleons revealed a value of $g_a^s = -0.084 \pm 0.042$ (Hobbs et al., 2016, and references therein). Our choice seems to be somewhat extreme, but the aim of this study is to likewise cover other uncertainties in the neutrino opacities. For example, correlations in low-density nucleon matter reduce the cross sections both for neutrino-proton and neutrino-neutron scattering, which has similar consequences for the opacities as the strange-quark correction (Horowitz, 2016). With our value of $g_a^s = -0.2$, we therefore probe whether currently unconsidered modifications of the neutrino opacities may provide the missing ingredient for a successful explosion in 3D.

5.3. Numerical setup

We performed simulations in axial symmetry (2D) and full three dimensions (3D) of a $20 M_\odot$ progenitor with and without the strange-quark correction. All details about the general numerical setup can be found in Sect. 2.4. The 3D simulations in this chapter were run with the standard spherical polar grid and an innermost spherically symmetric

volume of 10 km. The angular resolution of the 2D and 3D models was set to 2° . As in all VERTEX-PROMETHEUS simulations, the radial grid was gradually refined to ensure a sufficiently high resolution of the cooling region and the proto-neutron star surface.

The 2D and 3D models with enabled strangeness correction of $g_a^s = -0.2$ are labeled as 2Ds and 3Ds, respectively. The simulations with the standard neutrino opacities are referred to as 2Dn and 3Dn. The model 3Dn was already partially discussed in Tamborra et al. (2013), Hanke (2014), and Tamborra et al. (2014a,b), but not in comparison with the exploding model 3Ds.

The threshold density ρ_{EOS} between the LS220 high-density equation of state and the low-density regime during core collapse was erroneously set to $3 \times 10^8 \text{ g cm}^{-3}$ in the simulation 3Dn, while a lower but comparable value was chosen for the three remaining models. We will argue later in this chapter that this modification does not compromise the comparison between the models 3Dn and 3Ds. After core bounce, ρ_{EOS} was set to $10^{11} \text{ g cm}^{-3}$ in all cases. NSE was assumed above a temperature of 0.5 MeV.

5.4. Results

5.4.1. Overview

We begin this section with an overview of the explosion characteristics and will later discuss how the strangeness correction influences the neutrino properties and provide more favorable heating conditions.

The most important result of our investigation is the successful explosion of the model 3Ds, while its comparison run 3Dn fails². This is directly evident from Fig. 5.3, where the angle-averaged shock radii of the two cases are shown together with the corresponding 2D simulations. Until ~ 150 ms after bounce, the shock radii of all models are nearly equal and show the expected behavior of initial propagation out to about 150 km and following retreat. The 3D models evolve similarly until 300 ms with strong presence of the standing accretion-shock instability (SASI; Blondin et al., 2003) indicated by periodic variations of $\langle R_{\text{sh}} \rangle$. The average shock radius of the model 3Dn declines to 79 km at 425 ms, which doubtlessly indicates a failed explosion in this simulation. On the contrary, the shock of the 3D model including strange-quark contributions (3Ds) is revived and propagates outwards with a velocity of about 7000 km s^{-1} to 970 km until 527 ms after core bounce.

As described above, there is a clear trend for 2D models to explode earlier than their 3D counterparts, because kinetic energy is artificially accumulated at large scales (see introduction of Chapt. 4). An earlier explosion is also observed in 2D for the simulations with enabled strangeness correction. In the model 2Ds, the shock reaches a radius of 400 km about 130 ms earlier than in the corresponding 3D model 3Ds. For the models with the standard neutrino opacity set, no explosion was obtained in the 3D case, while the associated 2D model explodes successfully.

In both 2D simulations, violent SASI sloshing along the symmetry axes push the shock surfaces into elongated, prolate shapes. Shock revival occurs about 30 ms earlier in the model 2Dn compared to 2Ds. The explosions proceed into the polar directions in both cases with strong equatorial downflows.

²Movies of both 3D simulations can be found at <http://www.mpa-garching.mpg.de/ccsnarchive/movies/>.

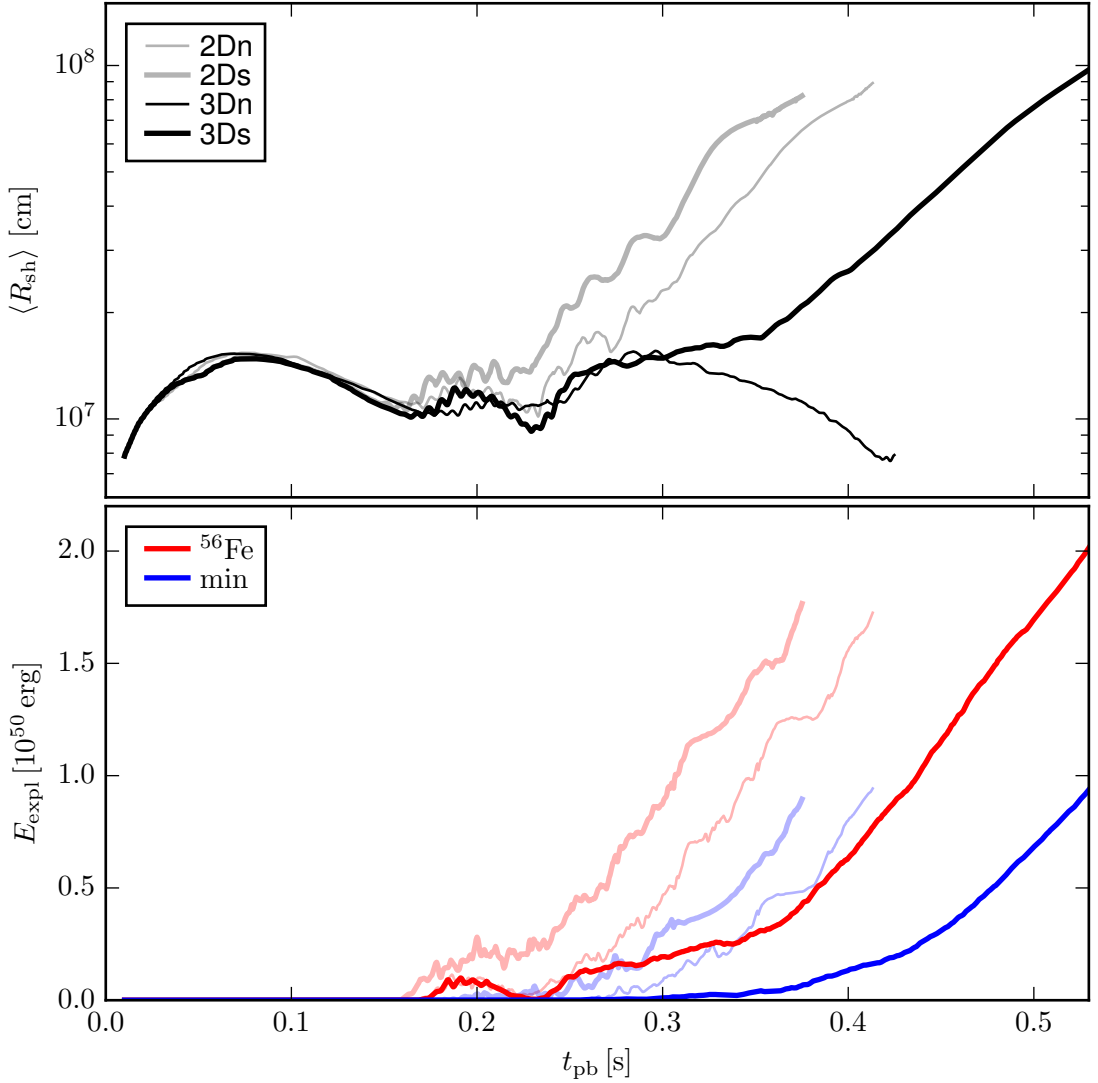


Fig. 5.3.: Angle-averaged shock radii $\langle R_{\text{sh}} \rangle$ and diagnostic explosion energies E_{expl} as functions of post-bounce time t_{pb} . Thin and thick solid lines depict models without and with strange-quark contributions, respectively. Semi-transparent and gray lines represent 2D models. Blue and red lines mark the lower and upper limits, respectively, of the explosion energies (see text).

The diagnostic explosion energy E_{expl} , i.e. the total energy of all unbound post-shock material, is presented in the lower panel of Fig. 5.3. For each model, we show the upper and lower bounds of this quantity assuming the current chemical composition and a complete recombination into ^{56}Fe , respectively (cf. Eq. (4.3) and explanation thereto). For the exploding model 3Ds, the lower and upper bounds of E_{expl} rise to values of $(0.9 \dots 2.0) \times 10^{50}$ erg with growth rates of $(1.0 \dots 1.2) \times 10^{51}$ erg s $^{-1}$. The steep increase of the diagnostic explosion energy is caused by a massive outflow of neutrino-heated matter that is fed by accreted stellar shells. For a quantitative analysis, Fig. 5.4 shows the mass fluxes of infalling and outflowing material measured at the angle-averaged

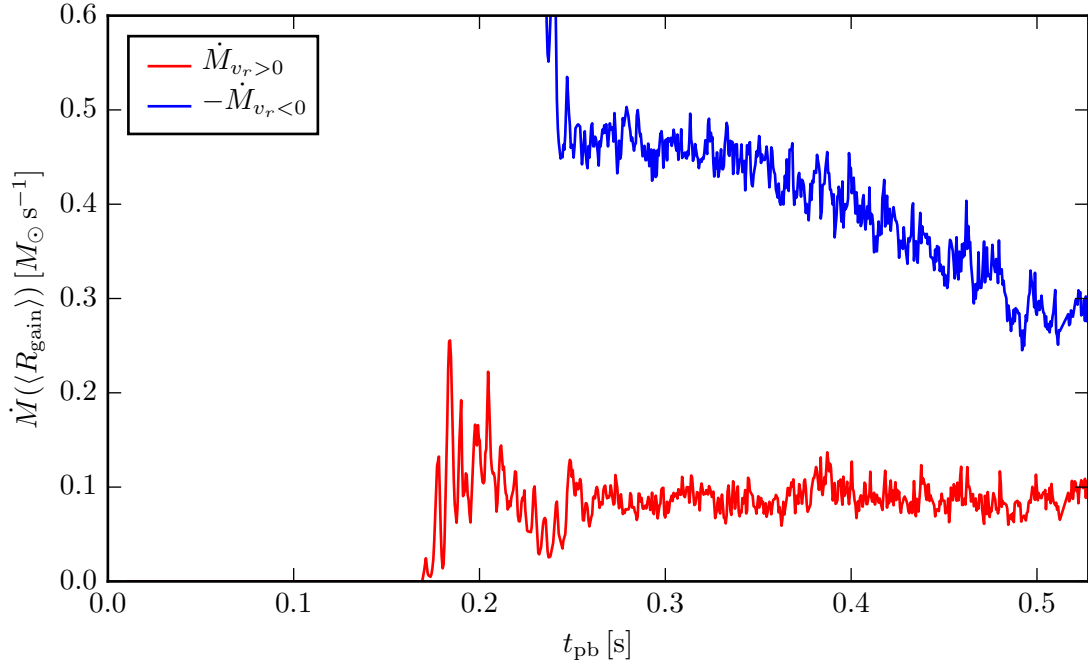


Fig. 5.4.: Mass-outflow rate $\dot{M}_{v_r>0}$ (red) and negative mass-infall rate $-\dot{M}_{v_r<0}$ (blue) of the model 3Ds as functions of time after bounce measured at the angle-averaged gain radius $\langle R_{\text{gain}} \rangle$.

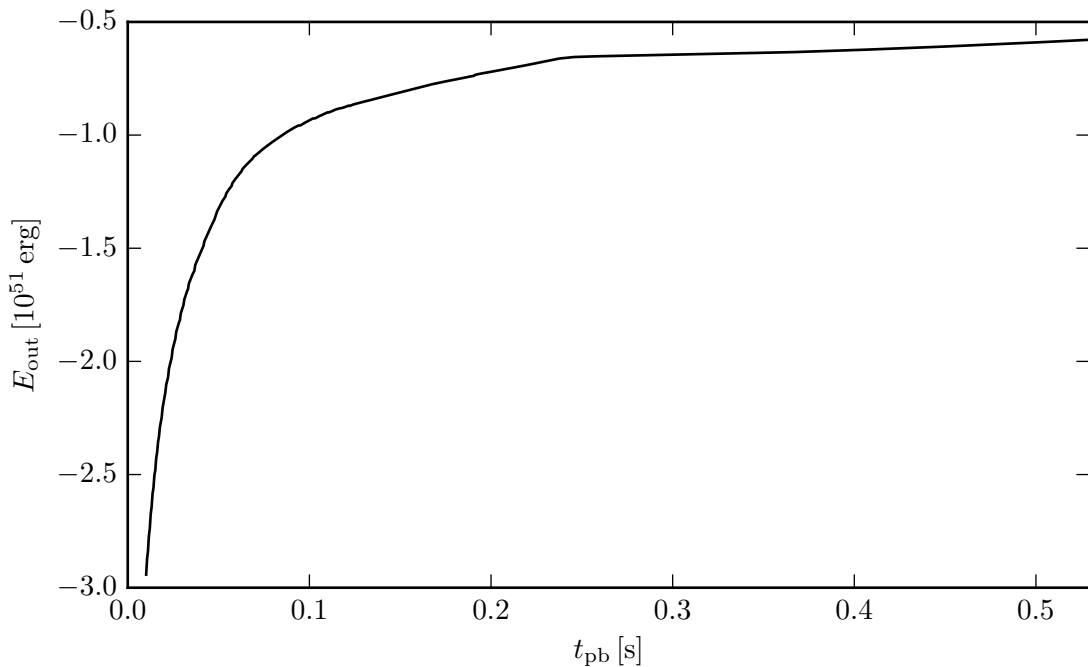


Fig. 5.5.: Binding energy of all material ahead of the shock as a function of post-bounce time for the model 3Ds.

gain radius $\langle R_{\text{gain}} \rangle$ and being defined as

$$\dot{M}_{v_r < 0} = \langle R_{\text{gain}} \rangle^2 \int d\Omega \Theta(-v_r) \rho v_r \quad (5.9a)$$

$$\dot{M}_{v_r > 0} = \langle R_{\text{gain}} \rangle^2 \int d\Omega \Theta(v_r) \rho v_r \quad (5.9b)$$

with the Heaviside step function $\Theta(x)$. The absolute value of the infall rate decreases slowly, while the outflow rate remains relatively constant at a level of $0.1 M_\odot \text{ s}^{-1}$. This outflowing material consists initially of free nucleons but recombines into alpha particles and heavy nuclei as the temperature decreases behind the expanding shock. The released binding energy contributes considerably to the explosion energy E_{expl} (Scheck et al., 2006). According to Müller (2015), about 6 MeV per nucleon can be provided by recombination. The author explained that this value is lower than the typical release of 7 MeV per nucleon for recombination into alpha particles, because energy is lost by turbulent diffusion at the interfaces between outflows and downdrafts. We can thus estimate the growth of E_{expl} for our exploding 3D model as

$$\dot{E}_{\text{expl}} = \frac{6 \text{ MeV}}{m_B} \dot{M}_{v_r > 0} \approx 1.2 \times 10^{51} \left(\frac{\dot{M}_{v_r > 0}}{0.1 M_\odot \text{ s}^{-1}} \right) \text{ erg s}^{-1}. \quad (5.10)$$

This value is equal to the measured growth rate of the model 3Ds.

At the end of the 3Ds simulation, we are not yet able to judge the final saturated explosion energy due to its steep increase. Besides the energy behind the shock, also the binding energy of the overlying stellar shells has to be considered in the total energy budget. In Fig. 5.5, the binding energy of all material ahead of the shock front is depicted for the exploding 3D model. It is calculated up to the outer radius of the progenitor star at $7.4 \times 10^{13} \text{ cm}$ according to

$$E_{\text{out}} = \int_{r > R_{\text{sh}}} dV \rho \epsilon, \quad (5.11)$$

where ϵ is the total specific energy as defined in Eq. (4.3, *Case min*). As the shock propagates outwards and passes the overlying stellar shells, the absolute value of the binding energy E_{out} decreases. At the end of the simulation, the binding energy of the pre-shock layer is about $-5.8 \times 10^{50} \text{ erg}$. Consequently, the total energy budget is still negative, i.e. $E_{\text{expl}} + E_{\text{out}} \approx -3.8 \times 10^{50} \text{ erg}$ (assuming a complete recombination into ^{56}Fe behind the shock). As we have shown above, the continuous mass outflow leads to a steep increase of the explosion energy, so that the energy budget will become positive in a few hundred milliseconds.

An overview of the 3D models can be gained from Fig. 5.6, where the angle-averaged entropy per baryon is shown color-coded in a Kippenhahn diagram. Besides the different shock trajectories, both models differ by their values of the post-shock entropy. Matter behind the shock in the model 3Ds has a higher entropy compared to the model 3Dn. This is evident already before 300 ms after bounce, i.e. before the shock radii of both models start to diverge. Neutrino heating is found to be stronger in the model with enabled strangeness correction, as we will demonstrate below.

An important aspect of shock revival is the Si/Si+O interface that is closely related to a rapid decline of the mass accretion rate (cf. Fig. 5.1). It is visible as a distinct blue

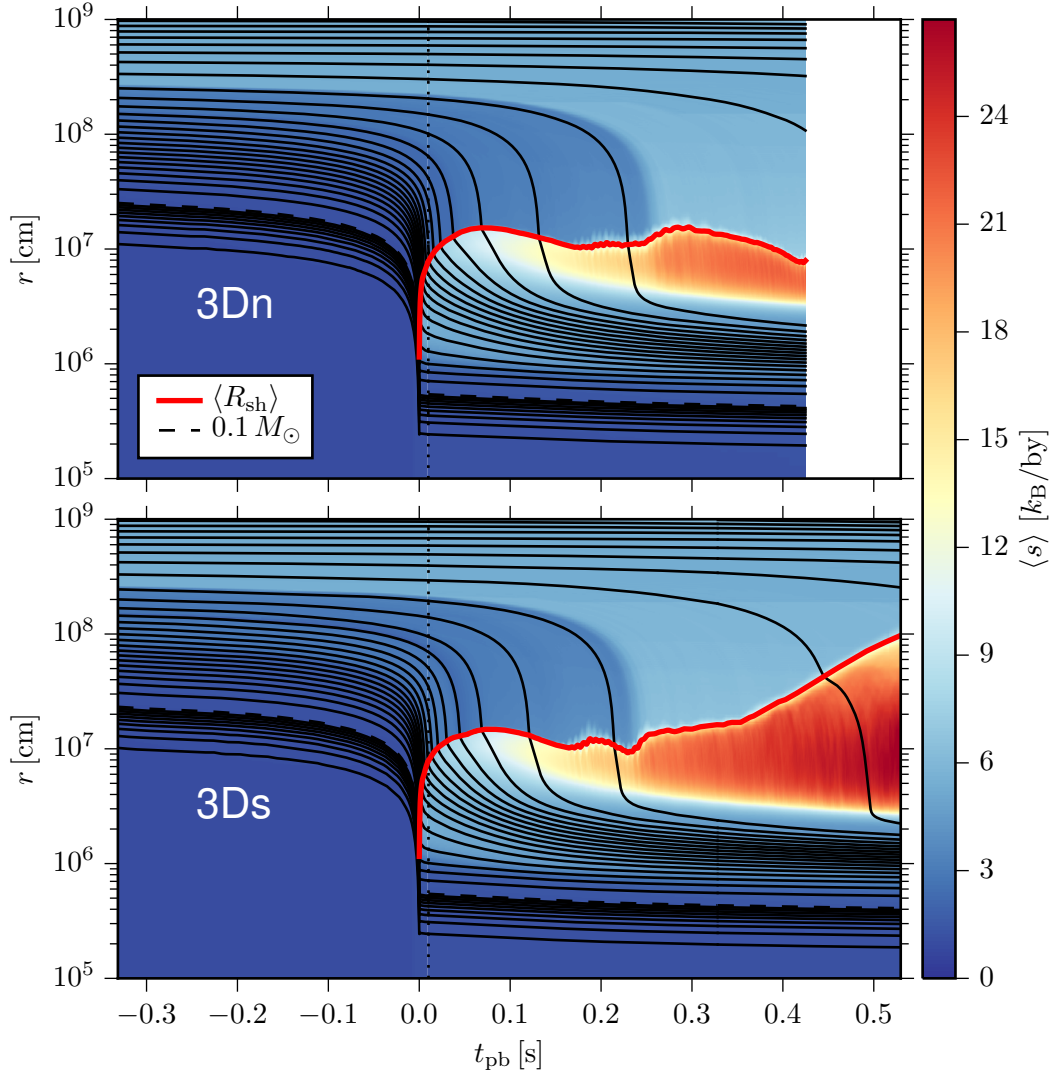


Fig. 5.6.: Mass shells of the models 3Dn and 3Ds, i.e. radii vs. time for given enclosed masses, with angle-averaged entropy as color coding. Black lines follow certain mass coordinates. Dashed black lines mark $0.1 M_{\odot}$ of enclosed mass. The spacing of the innermost 10 solid black lines is $0.01 M_{\odot}$. All remaining lines are spaced by $0.1 M_{\odot}$. Solid red lines show the angle-averaged shock radii. The multi-dimensional simulations were mapped from a 1D model at 10 ms after bounce marked by vertical dotted lines.

color contrast in Fig. 5.6 and arrives at 245 ms and 230 ms in the models 3Dn and 3Ds, respectively. Only in the 3D simulation with strangeness correction, enhanced neutrino heating is strong enough to revive the shock after that time. The other 3D model shows a short period of shock enlargement with following retreat.

The reason for the different arrival times of the Si/Si+O interface in both 3D models is the aforementioned different setting of the threshold density between the high- and low-density equations of state ρ_{EOS} during collapse. The supersonic infall is very sensitive to slight variations of the progenitor profiles that are caused by changes in ρ_{EOS} . Because

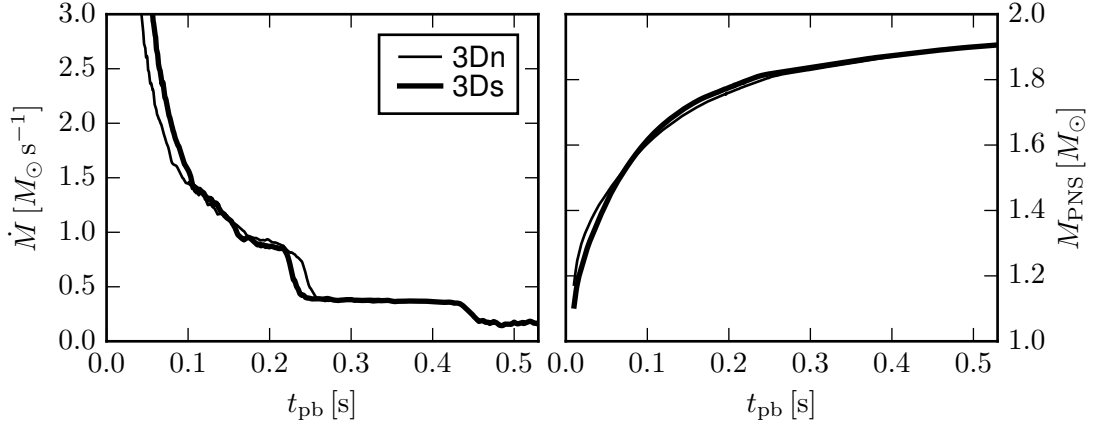


Fig. 5.7.: Mass-accretion rates \dot{M} measured at 400 km and baryonic masses of the proto-neutron stars M_{PNS} as functions of time for the model 3Dn (thin lines) and the model 3Ds (thick lines).

the accretion of the Si/Si+O interface coincides with a rapid decline of the mass-accretion rate \dot{M} , the different arrival times of the interface are also evident in the left panel of Fig. 5.7. Subsequently, after 260 ms post bounce, the mass-accretion rates become equal in the models 3Dn and 3Ds with a value of $\sim 0.37 M_{\odot} \text{s}^{-1}$. Also the baryonic masses of the proto-neutron stars M_{PNS} , which are determined by the amount of accreted matter, are equal in both cases with $1.88 M_{\odot}$ at 425 ms demonstrating that the time shift in \dot{M} does not influence the total amount of accreted material. Since the 3D models diverge in their evolutions only after 300 ms and therefore much later than the arrival times of the Si/Si+O shell interface, a negative influence of the different values for ρ_{EOS} is excluded. A similar observation was made by Summa et al. (2016), who studied different settings for ρ_{EOS} before bounce and did not find a major impact on the post-bounce dynamics.

In Fig. 5.8, we present cross-sectional cuts through both 3D models for different points in time. This visualization with the color-coded entropy per baryon allows for a direct comparison between the models 3Dn and 3Ds, especially before their evolutions diverge. The 3D model without strange-quark contributions develops a SASI sloshing mode at about 170 ms, which shortly afterwards transitions into a spiral mode (Blondin & Mezzacappa, 2007). Its plane is nearly parallel to the plane depicted in Fig. 5.8 and the triple point is therefore nicely visible there. At ~ 300 ms, SASI activity ceases and convection becomes dominant.

The model 3Ds starts developing a SASI sloshing mode earlier at about 150 ms as we will show later in this chapter. It persists for ~ 70 ms and changes into a spiral mode, which however is not as pronounced as in the simulation 3Dn. Until 280 ms post bounce, the SASI weakens and strong convection emerges.

In both simulations, additional mixing occurs in SASI phases due to Rayleigh-Taylor and Kelvin-Helmholtz instabilities (cf. Guilet et al., 2010). Indications for these instabilities are visible at 240 ms in Fig. 5.8 as the shock of the model 3Ds sloshes from one side to the other.

By comparing the fluid patterns of the two 3D simulations at 300 ms, it cannot be judged, which model will explode and which will fail. The only obvious difference is the

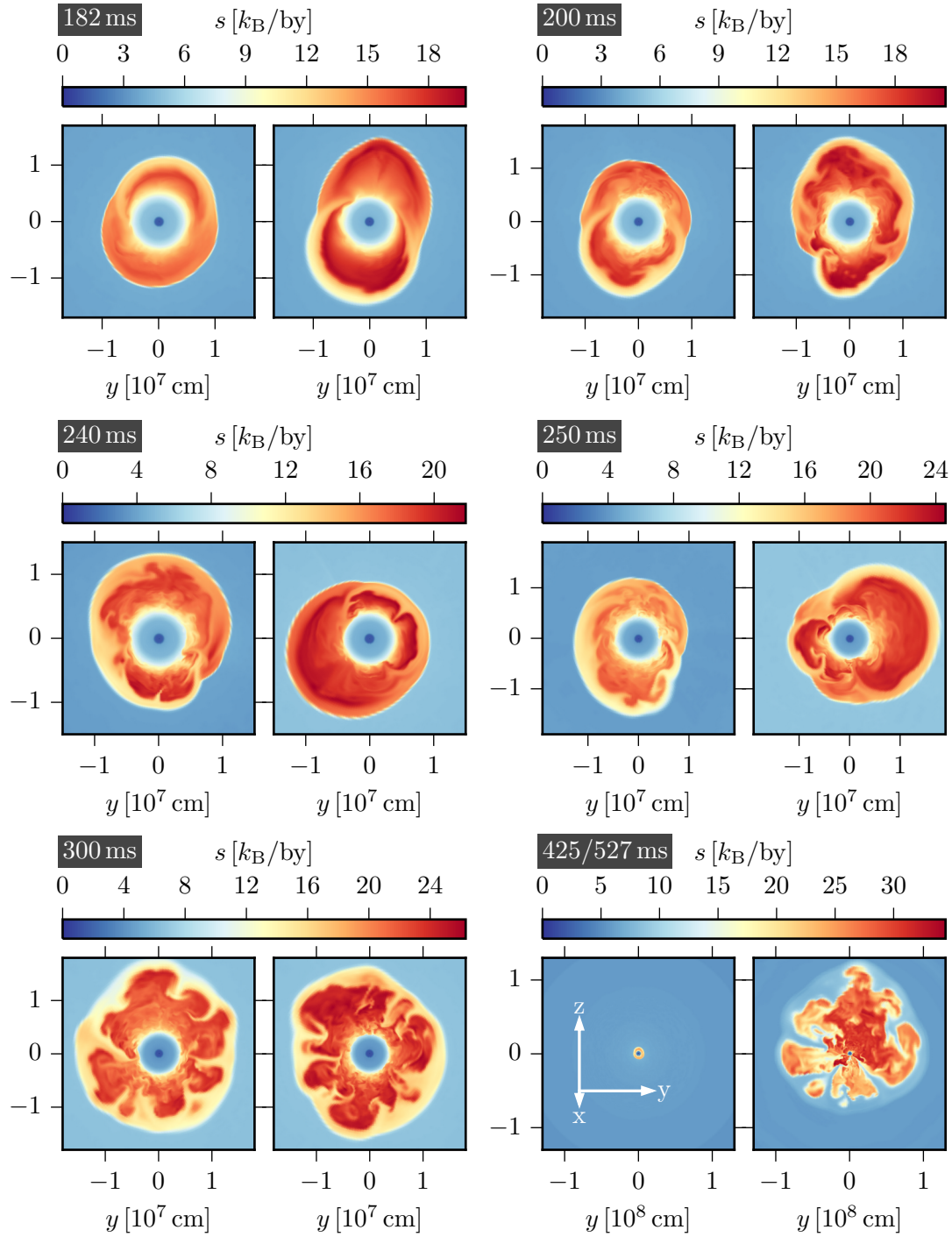


Fig. 5.8.: Color-coded entropy per baryon of the models 3Dn (*left panels*) and 3Ds (*right panels*) for six different times after core bounce. The entropy distribution is depicted in a plane through the origin, whose orientation is indicated by the tripod in the lower right panel. Note that the lower right panel shows two different times corresponding to the end of the two simulations.

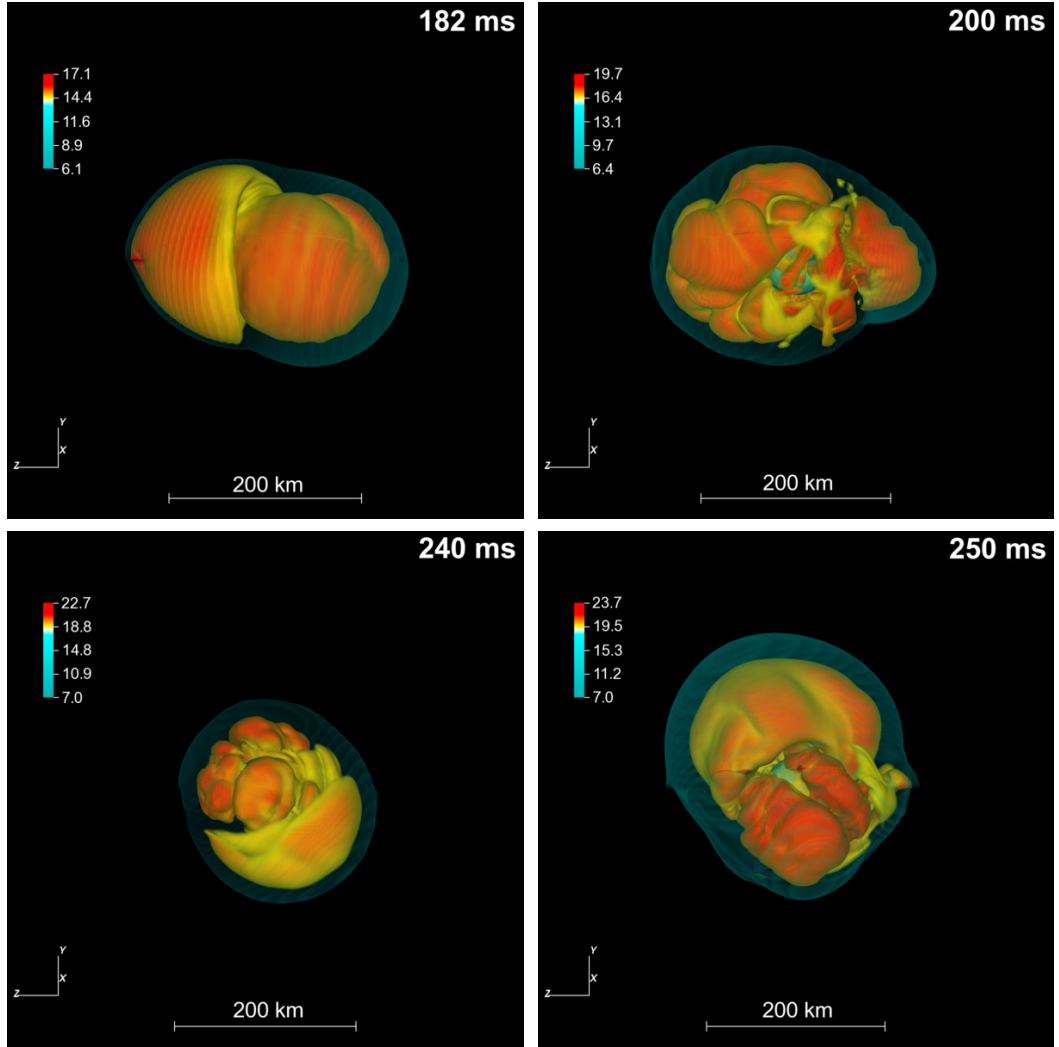


Fig. 5.9.: Volume-rendering of the model 3Ds at four different post-bounce times. Surfaces of high entropy are shown with color coding in units of k_B per baryon. The semi-transparent bluish shock surfaces are clearly visible. The direction of the observer is indicated by tripods and kept constant. Yardsticks demonstrate the dimensions of the exploding model. An interactive 3D rendering is available at <http://iopscience.iop.org/2041-8205/808/2/L42/media>. (*Visualization: A. Döring*)

post-shock entropy being higher in the model involving strangeness. This was already observed in the Kippenhahn diagram Fig. 5.6. It is particularly interesting that the evolution up to 300 ms is very similar in both cases. At the end of the simulation, the exploding model 3Ds becomes highly anisotropic with strong downdrafts and numerous small-scale high-entropy bubbles. This observation is in line with our analysis of mass-infall and mass-outflow rates. As we have shown above, ongoing mass accretion feeds massive outflows that give rise to a steeply increasing diagnostic explosion energy.

The three-dimensional shape of the model 3Ds is illustrated by Figs. 5.9 and 5.10.

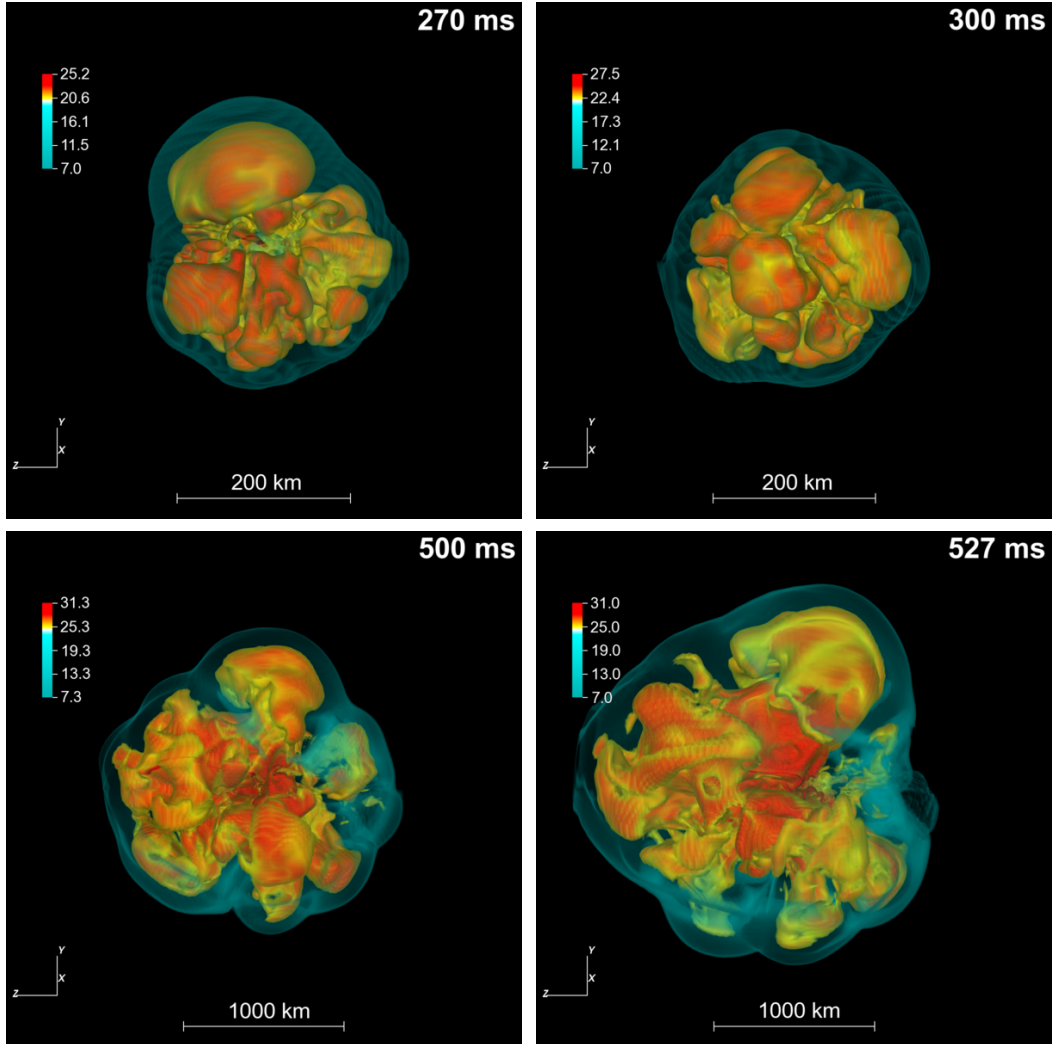


Fig. 5.10.: Same as Fig. 5.9, but at later times.

We have selected the same points in time as in Fig. 5.8 in order to display all phases of the evolution: the SASI sloshing period until ~ 220 ms, the weak SASI spiral mode until 280 ms, and the phase of strong neutrino-induced convection afterwards. Towards the end of the simulation, the expanding high-entropy mushrooms become more ragged. They change their shape dramatically as the massive outflow from inside pushes them outwards. The shock surface propagates out to a distance of ~ 1000 km at the end of the simulation and becomes highly deformed.

5.4.2. Effects of the strangeness correction

In Sect. 5.2, we have explained the influence of the strange-quark contributions on the neutrino opacities for electron neutrinos ν_e , electron antineutrinos $\bar{\nu}_e$, and heavy-lepton neutrinos ν_x . Since the strangeness correction only changes the neutral-current scattering opacities, the largest reduction of the effective opacity was deduced for ν_x . The

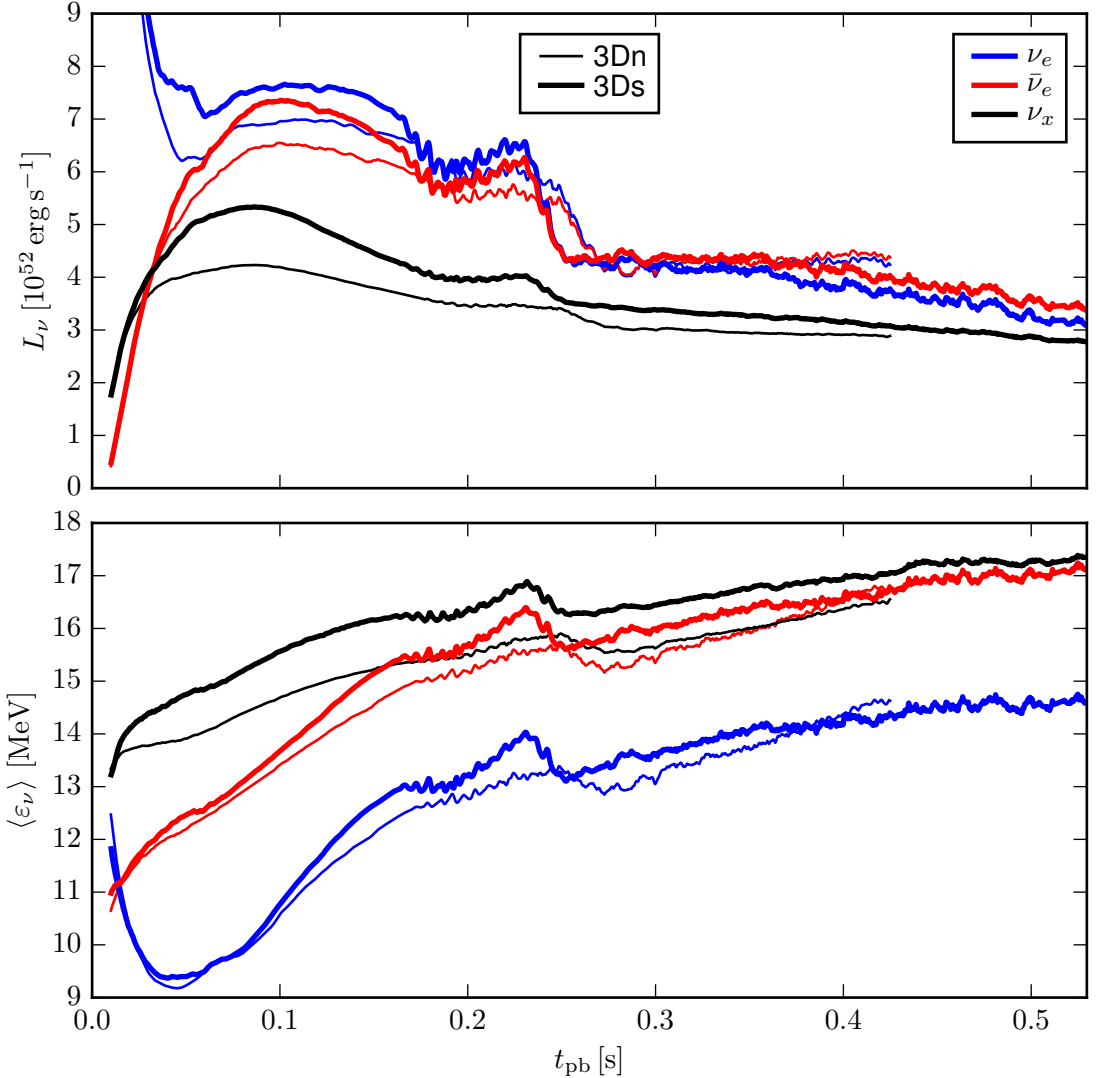


Fig. 5.11.: Neutrino luminosities L_ν and neutrino mean energies $\langle \varepsilon_\nu \rangle$ of the three neutrino species ν_e , $\bar{\nu}_e$, and ν_x for the model 3Dn (*thin lines*) and the model 3Ds (*thick lines*). Both quantities are measured at a distance of 400 km from the center.

other neutrino species also participate in charged-current processes and are therefore less affected. In this section, we will show the consequences of the strange-quark correction on the neutrino luminosities and the mean energies in our 3D models and discuss how neutrino heating is enhanced.

The time dependence of the luminosities and the mean energies is shown in Fig. 5.11 for the two 3D models. The luminosities of all neutrino species are increased in the model 3Ds by 10–13% for ν_e and $\bar{\nu}_e$ and up to 26% for ν_x . Interestingly, these relative differences build up already early and reach their maximum at about 100 ms after bounce. A resulting enhanced neutrino heating is therefore expected to occur also at that time.

After ~ 150 ms post bounce, convection in the post-shock layer and the SASI leave

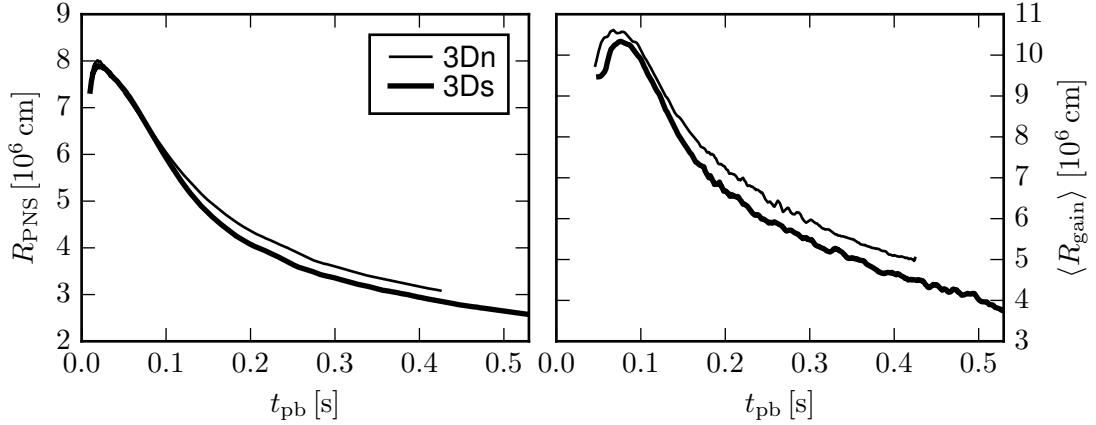


Fig. 5.12.: Proto-neutron star radii R_{PNS} and angle-averaged gain radii $\langle R_{\text{gain}} \rangle$ as functions of time for both 3D models. R_{PNS} is defined where $\rho = 10^{11} \text{ g cm}^{-3}$.

their imprint on the luminosities of electron (anti)neutrinos. Parts of their luminosities are provided by neutrino emission from accreted matter. This accretion luminosity declines, when the Si/Si+O shell interface arrives (see Fig. 5.7). After that, the relative differences between 3Dn and 3Ds decrease and eventually change sign at ~ 300 ms because the non-exploding model 3Dn continues accreting matter at a higher rate compared to the case 3Ds.

Also the mean energies are higher in the model 3Ds compared to 3Dn (see Fig. 5.11). The largest increase occurs for heavy-lepton neutrinos, whose mean energy is persistently 0.8–1 MeV higher in the time interval between 50 ms and 250 ms. The differences in the mean energies of electron (anti)neutrinos grow more slowly between 50 ms and 150 ms to 0.6 MeV. Subsequently, they remain at least 0.3 MeV higher than in the model 3Dn until 350 ms.

Strange-quark contributions enhance the neutrino luminosities and the mean energies of all species considerably, although the effective opacities of electron (anti)neutrinos are only minorly reduced. However, due to the reduction of the neutral-current opacities, more energy is carried away from layers below the proto-neutron star (PNS) surface due to a higher emission of heavy-lepton neutrinos. This leads to an accelerated cooling and thus faster contraction of the PNS, as shown in Fig. 5.12. The neutrinospheres of all species are therefore shifted inwards to higher temperatures, such that the neutrinos leave the PNS with higher mean energies. This effect is visible in the continuous growth of the mean energy differences of electron (anti)neutrinos. Shortly after bounce, these differences between 3Dn and 3Ds are small, because the PNS radii are still equal, but they grow with time as the PNS radii diverge.

The faster contraction of the PNS in the model 3Ds leads to a faster recession of the angle-averaged gain radius as shown in Fig. 5.12. This is because the cooling layer is approximately in hydrostatic equilibrium (Janka, 2001). Additionally, the enhanced neutrino energy input in the gain layer, which we will discuss below, implies an inward shift of the gain radius, since this is the location where neutrino heating balances neutrino cooling.

For the purpose of further estimating where the differences in the neutrino signals

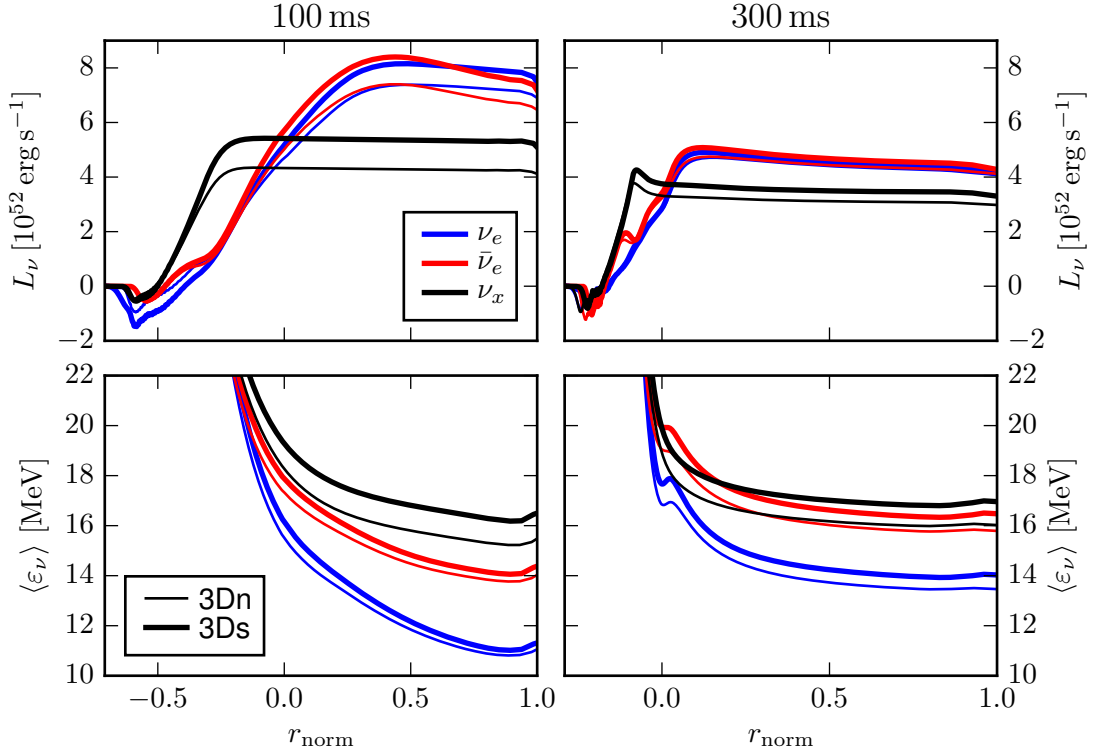


Fig. 5.13.: Radial profiles of the neutrino luminosities L_ν and the neutrino mean energies $\langle \varepsilon_\nu \rangle$ of the two 3D models at 100 ms (*left column*) and 300 ms (*right column*). The radial axes are normalized so that $r_{\text{norm}} = 0$ corresponds to the surface of the proto-neutron star and $r_{\text{norm}} = 1$ marks the angle-averaged shock radius (see Eq. (5.12) for the definition of r_{norm}).

emerge, we show radial profiles of the luminosities and the mean energies in Fig. 5.13. In order to compensate for the different PNS radii in the 3D models, we have normalized the radial axes such that

$$r_{\text{norm}}(r) := \frac{r - R_{\text{PNS}}}{\langle R_{\text{sh}} \rangle - R_{\text{PNS}}} \quad (5.12)$$

with the proto-neutron star radius R_{PNS} being defined where $\rho = 10^{11} \text{ g cm}^{-3}$. The normalized radius r_{norm} varies from 0 at the PNS surface to 1 at the angle-averaged shock radius.

The difference of the luminosities of heavy-lepton neutrinos builds up below the PNS radius, i.e. where $r_{\text{norm}} < 0$. Further out, they have a constant offset, which is in line with our finding that the opacity of ν_x is basically not reduced by strange-quark contributions outside of the PNS (cf. Fig. 5.2, *right panel*). For electron neutrinos and electron antineutrinos, the differences of the luminosities do not grow as steeply as for heavy-lepton neutrinos, because the opacity reductions for ν_e and $\bar{\nu}_e$ as functions of Y_e are shallower than for ν_x (see Fig. 5.2, *left panel*).

The radial profiles of the mean energies of all neutrino species reveal that the differences between the two 3D models occur below the PNS surface and remain constant outside. The enhancement of the mean energies is caused by higher temperatures at $r_{\text{norm}} \leq 0$ due to the faster contraction of the PNS in the case 3Ds.

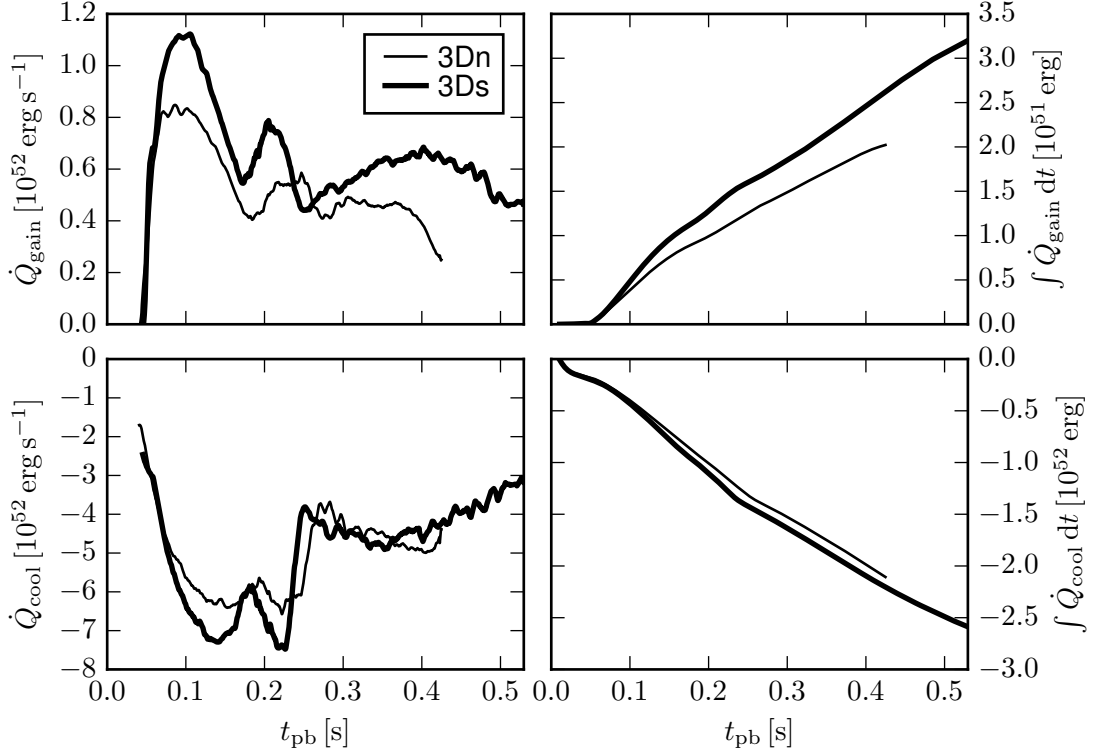


Fig. 5.14.: Total heating and cooling rates, \dot{Q}_{gain} and \dot{Q}_{cool} , of the 3D models. The instantaneous and time-integrated values are shown in the left and right panels, respectively.

As the luminosities and the mean energies of electron (anti)neutrinos are enhanced, the neutrino energy deposition in the gain layer is increased. This can be seen in the upper row of Fig. 5.14, where the instantaneous and time-integrated values of the heating rates \dot{Q}_{gain} are shown. It is obvious that the heating rate is considerably higher in the model 3Ds compared to the case 3Dn. At 90 ms post bounce, the difference reaches its maximum of about $3 \times 10^{51} \text{ erg s}^{-1}$, which coincides with the maximum luminosity differences in Fig. 5.11. The time-integrated value of \dot{Q}_{gain} , i.e. the total energy deposited in the gain layer, is about 25–30% higher in the simulation including strange quarks.

Also the amount of neutrino cooling is increased in the model 3Ds, however, only by a few percent in the time-integrated value. Unlike in the previous chapter, we define the bottom of the cooling layer to be the proto-neutron star surface, so that

$$\dot{Q}_{\text{cool}} = \int_{R_{\text{PNS}} < r < R_{\text{gain}}} dV \rho \dot{q}, \quad (5.13)$$

where \dot{q} is the specific net heating rate. Because the luminosities of electron neutrinos and electron antineutrinos have steeper gradients in 3Ds compared to 3Dn at the bottom of the cooling layer (see Fig. 5.13), more energy is carried away from this region. After the arrival of the Si/Si+O interface, the cooling rates become similar in both 3D models.

As we have shown above, the luminosity differences between 3Ds and 3Dn are maximal at about 90 ms. The total luminosity $L_{\nu_e} + L_{\bar{\nu}_e} + 4L_{\nu_x}$ is about $6 \times 10^{52} \text{ erg s}^{-1}$ higher

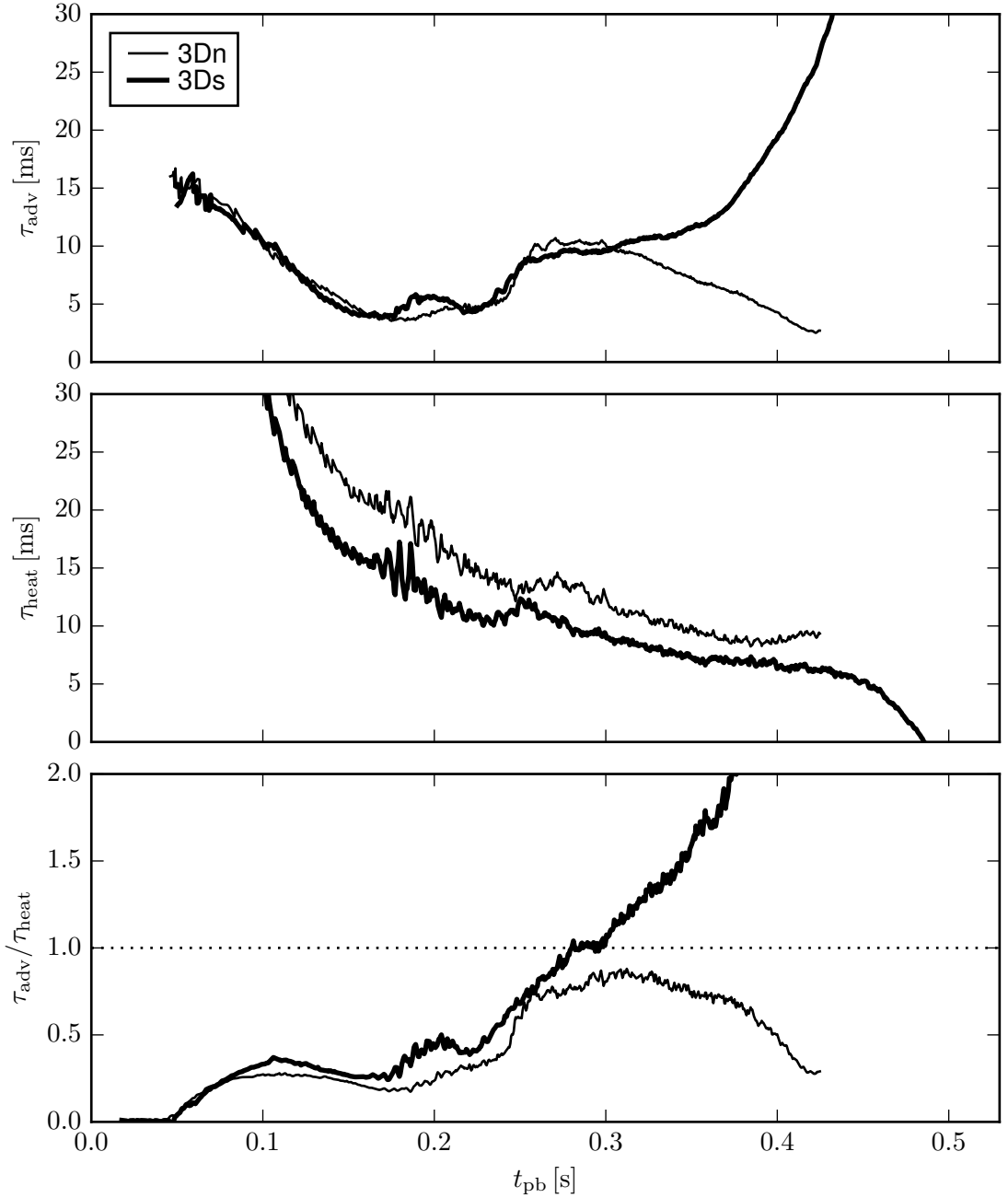


Fig. 5.15.: Advection timescales τ_{adv} , heating timescales τ_{heat} , and their ratios as functions of time for both 3D models.

at that time in the model with strange-quark contributions. However, the absolute value of the cooling rate \dot{Q}_{cool} is only $\sim 7 \times 10^{51} \text{ erg s}^{-1}$ larger. Obviously, the increased neutrino energy loss comes almost completely from below the PNS surface and only a small fraction is added in the cooling layer.

It is noteworthy that the temporal evolutions of the shock radii of both 3D models is very similar until 300 ms, while the neutrino energy deposition is higher already much earlier. As we have shown in Fig. 5.6, the post-shock entropy is larger in the simulation

3Ds due to enhanced neutrino heating. However, the shock is pushed out only after the ram pressure of the infalling shells drop due to the declining mass-accretion rate at the Si/Si+O interface.

The information on the neutrino energy deposition can be summarized in Fig. 5.15, where we show the advection and heating timescales. In the model 3Ds, the heating timescale τ_{heat} – the time needed to deposit enough energy for unbinding the gain layer – is continuously shorter, because the heating rate is higher. The advection timescales τ_{adv} are very similar in both 3D models until 300 ms, because the mass accretion rates are equal and fluid elements need the same time to cross the gain layers. Consequently, the timescale ratio $\tau_{\text{adv}}/\tau_{\text{heat}}$ is higher in the 3Ds model. It reaches unity at 280 ms, while the model 3Dn only rises to a value of 0.88 at 310 ms and declines afterwards. Hence, the threshold value of unity is a good indicator for obtaining a successful explosion in the 3D simulations discussed here.

To sum up, strange-quark contributions decrease the opacities for neutral-current neutrino-nucleon scattering in the region below the proto-neutron star surface. Since electron neutrinos and electron antineutrinos also participate in charged-current reactions, their effective opacities are less influenced. However, the consequent higher energy loss by the emission of heavy-lepton neutrinos leads to a faster contraction of the proto-neutron star. Hence, the neutrinospheres of all species are shifted inwards to higher temperatures, so that their luminosities and mean energies are increased considerably. More energy is therefore deposited in the gain layer amplifying buoyancy and convection and thus providing more favorable heating conditions for a successful explosion in the case 3Ds.

In our discussion, we have not mentioned the corresponding 2D models. However, since the increase of the neutrino luminosities and the mean energies due to strange-quark contributions is established below the proto-neutron star surface, effects of the different dimensionality are subdominant. The discussion presented above is therefore effectively analogous for the 2D simulations.

5.4.3. SASI and convection

In Sect. 5.4.1, we have already mentioned the occurrence of the SASI in our models. However, in this section, we will analyze the strengths and directions of the shock oscillations more quantitatively by decomposing the shock surface into spherical harmonics. Let the real spherical harmonics be defined as

$$Y_{\ell}^m(\theta, \phi) = \begin{cases} \sqrt{2}N_{\ell}^m P_{\ell}^m(\cos \theta) \cos(m\phi) & m > 0 \\ N_{\ell}^0 P_{\ell}^0(\cos \theta) & m = 0 \\ \sqrt{2}N_{\ell}^{|m|} P_{\ell}^{|m|}(\cos \theta) \sin(|m|\phi) & m < 0 \end{cases} \quad (5.14)$$

with normalization factors

$$N_{\ell}^m = \sqrt{\frac{2\ell+1}{4\pi} \frac{(\ell-m)!}{(\ell+m)!}} \quad (5.15)$$

and associated Legendre polynomials $P_{\ell}^m(\cos \theta)$. The coefficients for the decomposition are then given by

$$a_{\ell}^m = \frac{(-1)^m}{\sqrt{4\pi(2\ell+1)}} \int d\Omega R_{\text{sh}}(\theta, \phi) Y_{\ell}^m(\theta, \phi). \quad (5.16)$$

This normalization is chosen such that

$$a_1^{-1} = \langle y_{\text{sh}} \rangle, \quad a_1^0 = \langle z_{\text{sh}} \rangle, \quad a_1^1 = \langle x_{\text{sh}} \rangle, \quad (5.17)$$

where e.g. $\langle x_{\text{sh}} \rangle$ is the angle-averaged x -coordinate of the shock surface. The angle-averaged shock radius can simply be reconstructed by

$$a_0^0 = \langle R_{\text{sh}} \rangle. \quad (5.18)$$

In the two upper panels of Fig. 5.16, we present the coefficients a_1^m normalized to the angle-averaged shock radii a_0^0 for all three Cartesian directions. Gray-shaded areas in the background show the SASI dipole amplitude

$$A_1 = \frac{1}{a_0^0} \sqrt{\sum_{m=-1}^1 (a_1^m)^2}. \quad (5.19)$$

Both 3D simulations are SASI-dominated until ~ 300 ms post bounce. Whether a sloshing or a spiral mode is present can be deduced from the shape of the SASI amplitude A_1 . In a sloshing mode, the shock surface periodically transitions into a more spherical shape, before the next SASI cycle starts. The dipole component is reduced strongly in this phase, which is represented by a deep minimum in A_1 . A spiral mode keeps the strength of the dipole rather constant, so that A_1 does not show deep minima in this case.

From these considerations and with the aid of 3D movies³, we observe a strong spiral mode in the model 3Dn from about 190 ms to 300 ms after bounce with a short sloshing phase before. The model 3Ds develops a sloshing mode between 150 ms and 220 ms with a weak spiral after that persisting until ~ 280 ms.

The SASI growth rate depends on the time needed for transporting matter from the shock to the coupling region of the advective-acoustic cycle being located between the proto-neutron star surface and the gain radius (Scheck et al., 2008). This time is not equal to the advection timescale defined in Eq. (4.5) and plotted in Fig. 5.15, because the latter measures the time infalling matter is exposed to neutrino heating in the gain layer. However, both are closely related to each other – short advection timescales imply short SASI cycle durations and thus high growth rates. For example, the advection time from the angle-averaged shock radius to the neutron star radius at 200 ms post bounce is 12 ms in the model 3Ds, while $\tau_{\text{adv}} \approx 6$ ms. Indeed, the strongest SASI growth in both 3D simulations occurs between 150 ms and 200 ms, which coincides with very low values of τ_{adv} (see Fig. 5.15). At around 300 ms, i.e. shortly before the 3Ds model explodes, the SASI activity ceases in both cases as the advection timescales grow.

Hanke et al. (2013) observed that the transition of SASI sloshing modes into spiral modes is favored by small shock radii. We can confirm this impression with our models. The spiral mode in the simulation 3Dn converts from the previous sloshing at about 190 ms, which coincides with a minimum of the shock radius (cf. Fig. 5.3). In the case 3Ds, the transition occurs at 220 ms, which is the time when the angle-averaged shock radius reaches its smallest value.

³Movies of the models 3Dn and 3Ds can be found at <http://www.mpa-garching.mpg.de/ccsnarchive/movies/>.

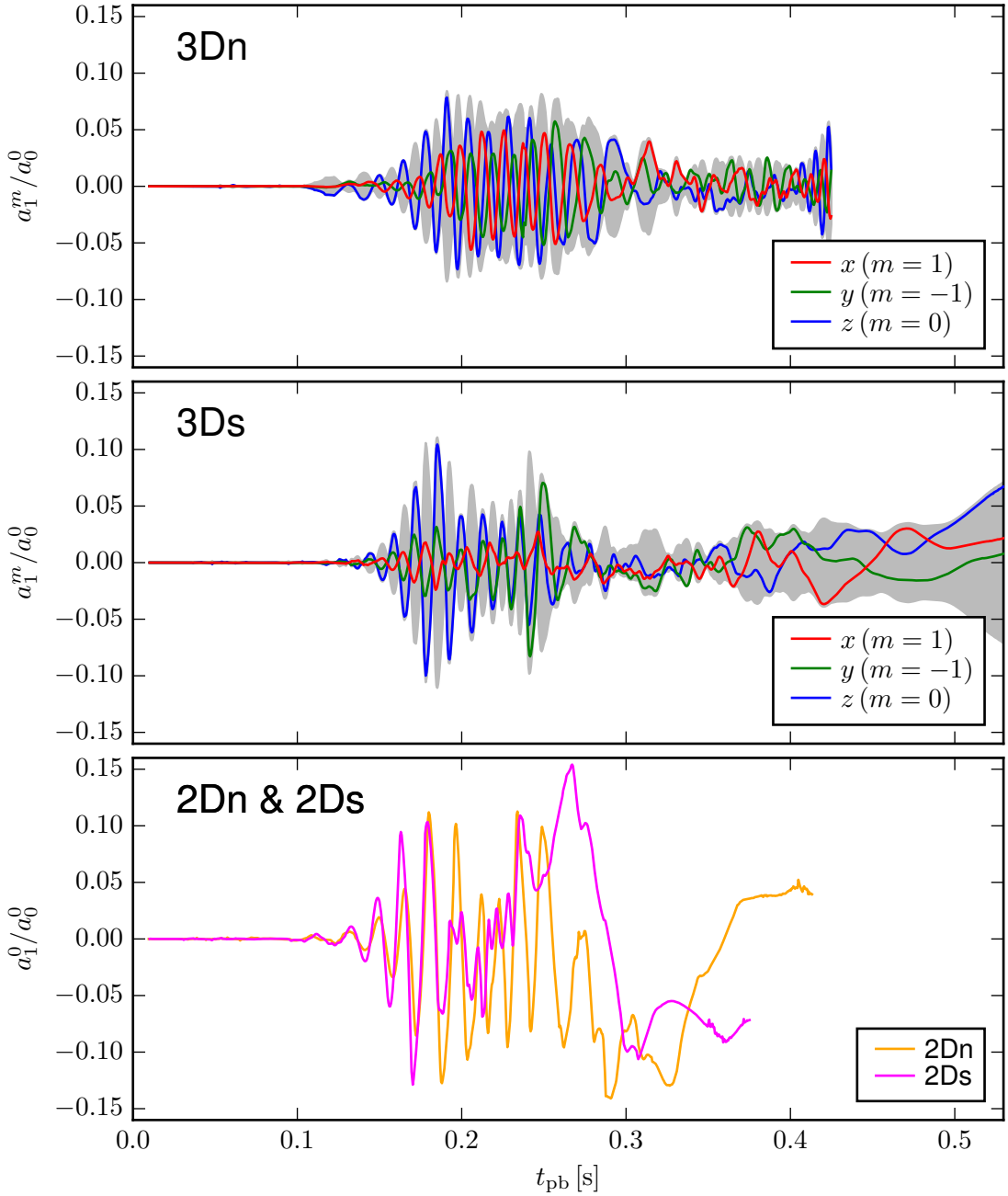


Fig. 5.16.: Coefficients a_{ℓ}^m of the spherical harmonics shock decomposition for $\ell = 1$ normalized to the angle-averaged shock radii. The different components for $m = \{-1, 0, 1\}$ of the two 3D models are given in the upper panels. The values for $m = 0$ of both 2D simulations are displayed in the lower panel. Gray-shaded areas depict the SASI amplitudes and are filled between $-A_1$ and A_1 (cf. Eq. (5.19))

We also present the SASI amplitudes of our 2D models in the lower panel of Fig. 5.16. Due to the axisymmetry in these cases, the dipole is always aligned with the z -axis, i.e. $a_1^{-1} \equiv 0 \equiv a_1^1$. In the 2D model with the standard neutrino opacity set (2Dn), SASI

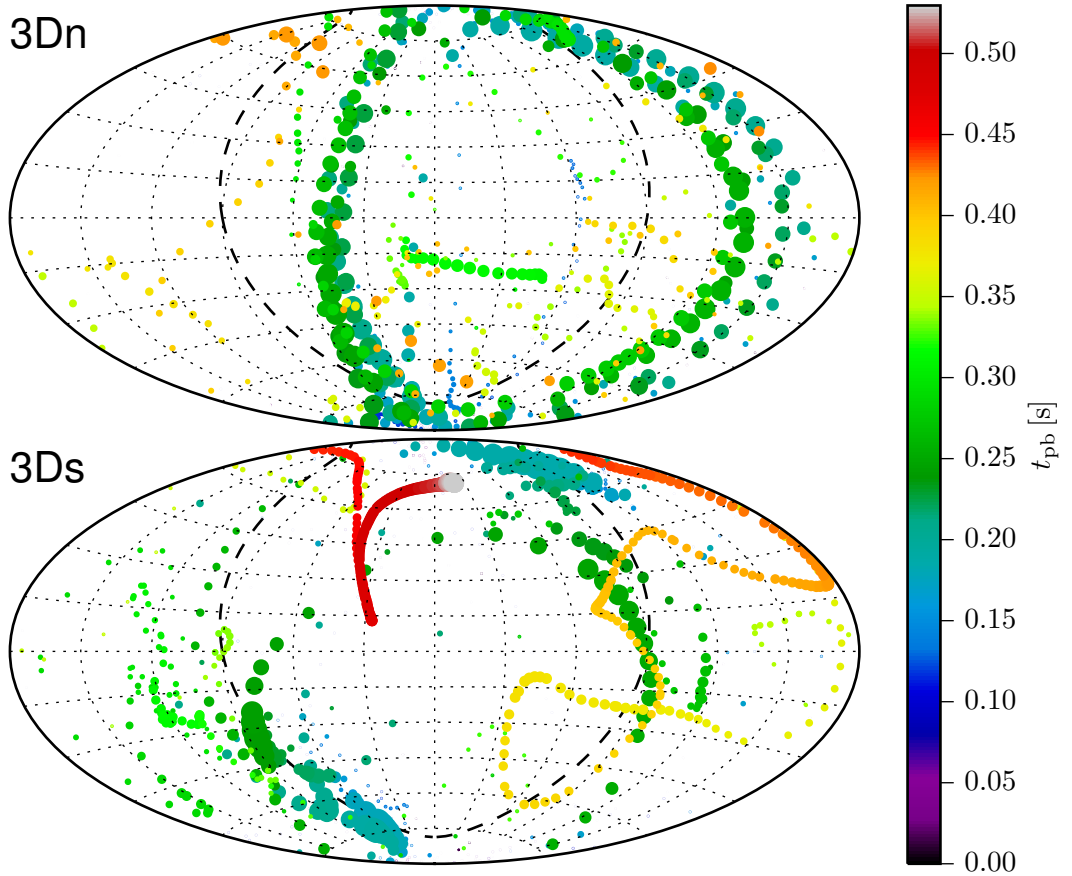


Fig. 5.17.: Aitoff projections of the SASI dipole directions for the two 3D models. Every point marks a certain point in time with colors referring to the post-bounce time t_{pb} . The diameters of the circles correlate with the dipole amplitudes. Dashed black lines show the orientation of the plane used for the visualization in Fig. 5.8.

sloshing starts at around 160 ms and lasts for \sim 100 ms, before shock runaway sets in. The SASI phase in the model 2Ds is shorter and persists from 140 ms to 200 ms post bounce.

Estimating the actual direction of the SASI dipole in 3D from Fig. 5.16 is difficult. We therefore show the dipole directions in Fig. 5.17 in an Aitoff projection for the models 3Dn and 3Ds. The reader is referred to Appendix A for an overview of the positions of the Cartesian axes in these maps. Every point in Fig. 5.17 corresponds to a certain time after bounce and its size scales with the dipole strength. The spiral mode of the model 3Dn is visible as a chain-like distribution of greenish markers in the upper panel. Its spiral motion lies in a plane that is relatively constant with time and close to the plane displayed in Fig. 5.8. The latter is indicated by dashed lines in Fig. 5.17.

The sloshing mode in the simulation 3Ds is visible through blueish markers near the poles. The subsequent spiral phase in this model is represented by greenish dots propagating from the lower left part through the upper region to the right. Towards the end of the simulation after 350 ms, the amplitude of the shock surface dipole is

still noticeable and drifts slowly, which demonstrates that the explosion proceeds very aspherically in this case.

At the end of the SASI episodes, convection in the gain layer becomes the dominant mixing process in our 2D and 3D models. Only in the model 3Dn, buoyancy is evident before the SASI sloshing starts. In order to characterize the linear growth phase of neutrino-driven convection, Foglizzo et al. (2006) introduced the parameter χ , which can be understood as a measure of the time convective perturbations need to grow compared to the time for advecting them out of the gain layer. Large heating rates and long advection timescales favor convective growth and increase χ (Fernández et al., 2014). In our notation, this parameter reads

$$\chi = \frac{\int_{\langle R_{\text{gain}} \rangle}^{\max(R_{\text{sh}})} dr \frac{\text{Im } \omega_{\text{BV}}}{|\langle v_r \rangle|}}{\langle R_{\text{gain}} \rangle}, \quad (5.20)$$

where ω_{BV} is the (complex) Brunt-Väisälä frequency characterizing convective instability. The integral runs from the angle-averaged gain radius to the maximum angle-dependent shock radius. Unlike Müller et al. (2012a) who set the upper bound of the integral to the angle-averaged shock radius, we choose the maximum here in order to cover the gain layer completely.

The Brunt-Väisälä frequency is given by

$$\omega_{\text{BV}}^2 = -\frac{C_{\text{Led}}}{\langle \rho \rangle} \frac{\partial \Phi}{\partial r} \quad (5.21)$$

with the gravitational potential Φ and the Ledoux parameter

$$C_{\text{Led}} = \frac{d\langle \rho \rangle}{dr} - \frac{1}{\langle c_s \rangle^2} \frac{d\langle P \rangle}{dr}. \quad (5.22)$$

The derivation of this formula can be found in Hüdepohl (2014, Appendix B). P denotes the pressure and c_s is the sound speed. Positive values of C_{Led} indicate instability against perturbations. Only fluid elements with local convective instability are taken into account in the calculation of χ . Since this implies $\omega_{\text{BV}}^2 < 0$, the imaginary part of this frequency is considered in Eq. (5.20).

Foglizzo et al. (2006) proposed a threshold value of 3 above which convection grows in the linear regime. In this case, perturbations are not transported out of the gain layer by the accretion flow and their amplitude can rise. However, this value should not be understood as a sharp demarcation of stable and unstable configurations. Especially for large density perturbations, convection can develop in the non-linear regime even if $\chi < 3$ (Foglizzo et al., 2006).

In Fig. 5.18, we present the parameter χ for the simulations discussed in this chapter. The value of 3 is exceeded at about 180–190 ms in the 3D models, while it is reached about 15 ms earlier in the 2D cases. However, except for the model 3Dn, no convective activity is evident before SASI oscillations commence. This underlines that the parameter χ is not applicable during violent SASI phases, because perturbations induced by the SASI are large enough to reach the non-linear regime of convective growth (cf. Summa et al., 2016). Interestingly, convection in the simulation 3Dn emerges shortly after 110 ms post bounce, when the value of χ is less than 2 and therefore well below its threshold. We can thus conclude that the parameter χ cannot be conclusively used to estimate the occurrence of convection in our simulations.

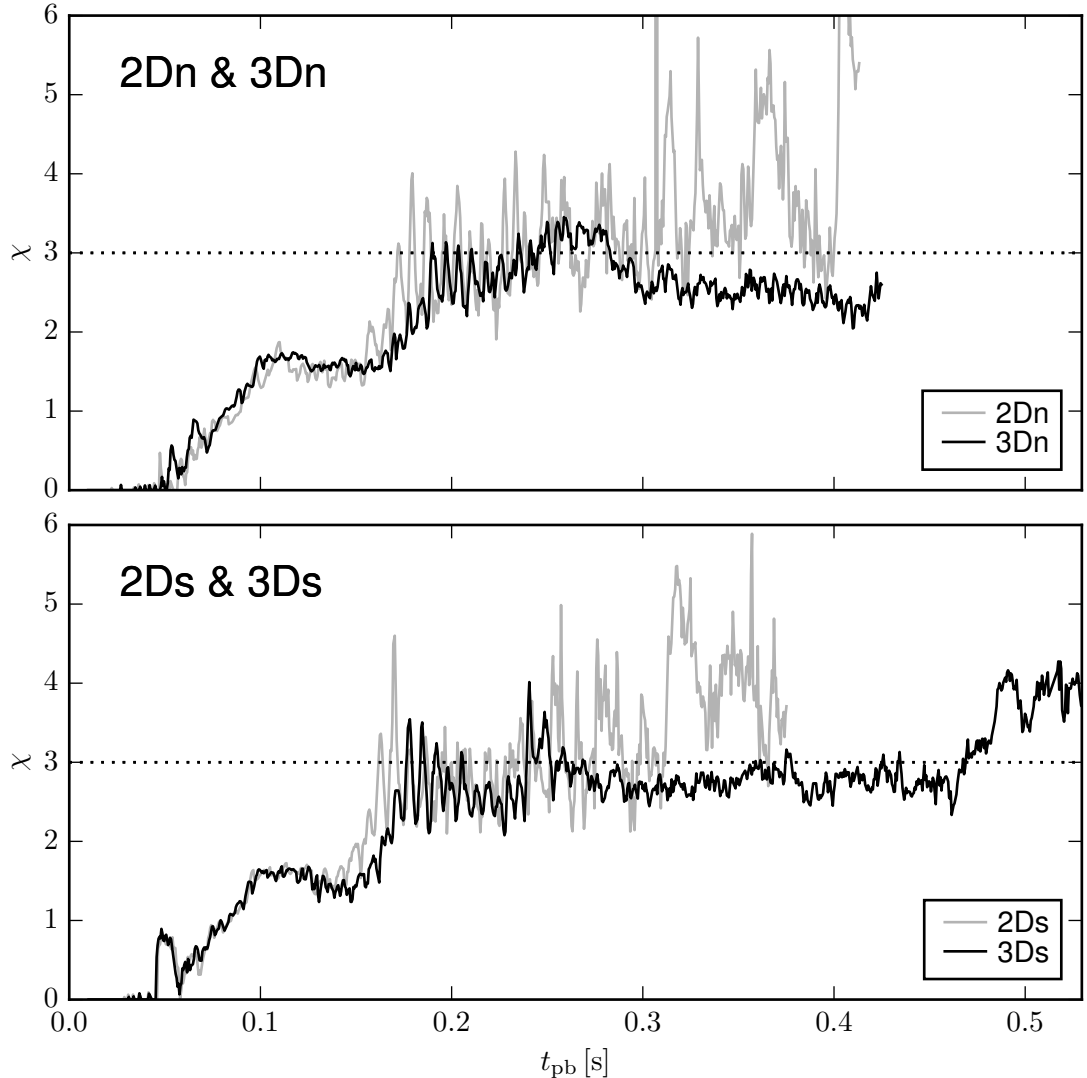


Fig. 5.18.: Parameter χ as defined in Eq. (5.20) for the two 3D models (black lines) and the corresponding 2D models (gray lines) as functions of post-bounce time.

5.5. Summary and discussion

We conducted core-collapse supernova simulations of a $20 M_{\odot}$ star in axisymmetry (2D) and full three dimensions (3D) with our neutrino-hydrodynamics code VERTEX-PROMETHEUS. Since supernova models do not yet explode robustly in 3D, we investigated how uncertainties in the neutrino interaction rates influence the outcome of 3D simulations. VERTEX-PROMETHEUS already includes the most sophisticated set of neutrino interactions applied in core-collapse supernova models, however, strange-quark contributions to the nucleon spin reducing the opacities of neutrino-nucleon scattering were considered here for the first time in multi-dimensional simulations. The 3D model with a strangeness correction of $g_a^s = -0.2$ exploded successfully, while a comparison run with standard neutrino opacities failed. Both 2D models developed explosions, but

strangeness effects favor an earlier shock runaway. In all exploding models, shock revival by neutrino heating occurred after the Si/Si+O shell interface had fallen through the shock due to the rapid decline of the ram pressure maintained by infalling stellar material.

The reduction of the neutral-current opacity due to the strangeness correction can exceed 20% below the proto-neutron star surface, while almost no modification occurs above. Energy is therefore carried away from the proto-neutron star more efficiently, mainly by the enhanced emission of heavy-lepton neutrinos that participate only in neutral-current reactions. The consequent faster contraction of the proto-neutron star shifts the neutrinospheres of all species inwards to higher temperatures. The luminosities and the mean energies of electron neutrinos and electron antineutrinos are thus enhanced considerably, although their effective opacities are only marginally reduced by the strangeness correction. Hence, the neutrino energy deposition in the gain layer is increased providing more favorable conditions for a successful explosion. A similar effect was found for “softer” high-density equations of state that favor a faster contraction of the proto-neutron star and thus also enhance neutrino heating in the gain layer (Marek & Janka, 2009; Suwa et al., 2013).

Strong SASI sloshing and spiral phases characterize the evolutions of both 3D models, until neutrino-driven convection becomes dominant after ~ 300 ms post bounce. Even though the 3D model without strangeness effects develops a violent SASI spiral phase, no explosion is obtained, which is somewhat in conflict with findings of Fernández (2015). This author argued that explosions could be obtained easier if a SASI spiral mode is present, because more kinetic energy is stored in the gain layer due to large non-radial velocities. His analysis is based on parametric models that mimic the shock stagnation phase under the assumptions of a constant mass-accretion rate and a constant proto-neutron star radius. In our non-exploding 3D model, neutrino heating is too weak to overcome the ram pressure of infalling material despite the SASI spiral mode.

Burrows et al. (2012) discussed that an “up-and-down” sloshing motion of the SASI cannot occur in 3D and that spiral modes should always be dominant. We do not agree with these authors. In our analysis, we have shown that the sloshing mode in the 3D model with enabled strangeness correction is strong and its direction remains fairly constant for about 70 ms.

The strangeness correction was already studied in spherically symmetric simulations by Liebendörfer et al. (2002) with a value of $g_a^s = -0.19$ (see also Langanke & Martínez-Pinedo, 2003). These authors also chose a progenitor star of $20 M_{\odot}$, but taken from Nomoto & Hashimoto (1988) and therefore different from ours. They showed that the shock propagates out to a radius of about 180 km with enabled strangeness correction before it retreats again. Although no explosion was found, the shock reaches an about 15 km larger radius compared to the reference model with their standard neutrino opacity set, because more energy is deposited in the gain layer.

Strange-quark contributions to the nucleon spin are motivated from theory and experiments. Recent measurements of deep inelastic scattering reactions of electrons off nucleons yielded a compiled value of $g_a^s = -0.084 \pm 0.042$ (Hobbs et al., 2016, and references therein). In this context, our choice seems to be somewhat extreme, however, other neutrino opacity uncertainties exist that likewise diminish neutral-current opacities and are also covered by our value for g_a^s . For example, correlations in low-density

nucleon matter reduce the cross sections of neutrino-nucleon scattering in a similar way as the strangeness correction (Horowitz, 2016).

We demonstrated that reducing the neutrino-nucleon scattering opacity at a level of 10% can turn a failed 3D simulation into a successfully exploding one. This suggests that previously failed 3D models of the Garching group (see Hanke et al., 2013; Tamborra et al., 2013; Hanke, 2014; Tamborra et al., 2014a,b) were already relatively close to the explosion threshold. In case of the $11.2 M_{\odot}$ model discussed in Hanke (2014), for example, this is especially visible in the temporal evolution of the ratio of advection and heating timescales. The 3D value rises above 1.1 very early and is even greater than in 2D for about 150 ms, but the 3D model eventually fails while the 2D model explodes.

We do not claim that the strangeness correction is the missing ingredient for robustly exploding core-collapse supernova simulations in 3D. Our study rather foregrounds the need for the exact knowledge of all neutrino interaction rates in order to reduce uncertainties in this sector. Of course, this also includes the strange-quark contribution itself, whose theoretically and experimentally determined values show some discrepancy (see Hobbs et al., 2016).

The robustness of our 3D explosion has to be examined in a setup with higher angular grid resolution. More turbulent kinetic energy is then enabled at small scales, which is potentially harmful for shock revival (e.g., Hanke et al., 2012; Couch, 2013; Couch & O'Connor, 2014). We will focus on this issue in the next chapter.

Since previously failed 3D models were possibly close to explosion, other favorable effects could also make the difference between success and failure. For example, convective perturbations in the progenitor star accelerate the growth of hydrodynamic instabilities in the gain layer and could therefore provide more favorable explosion conditions early after bounce (Arnett & Meakin, 2011; Couch & Ott, 2013; Müller & Janka, 2015; Couch et al., 2015). However, self-consistent 3D simulations of supernova progenitors are still in their infancy and applicable initial setups for core-collapse supernova models do not exist yet.

6. High-resolution 3D simulation

For any grid-based numerical simulation of a physical system, the question arises which spatial resolution is needed in order to model all relevant processes sufficiently well. Resolution studies until convergence for core-collapse supernova simulations with sophisticated neutrino transport are desired, but currently not feasible in three dimensions (3D) due to their high computational cost.

The fluid in the core-collapse supernova scenario can be described without explicitly including viscous effects, because the kinematic viscosity is very low and orders of magnitude smaller than the “numerical viscosity” being implicitly inherent to the numerical scheme (e.g., Müller, 1998). For a given hydrodynamical solver, reducing this numerical viscosity can be achieved by increasing the spatial grid resolution. As argued by Couch (2013), true convergence of core-collapse supernova simulations is expected to occur if the effective Reynolds number that depends on the numerical viscosity becomes comparable to the physical Reynolds number. This is far from being achievable in 3D simulations and also not required. Instead, we need to understand, how the models behave on better resolved computational grids and to what extent latest results of 3D studies are reliable.

The physical Reynolds number in the gain layer can reach values as high as 10^{17} (Abdikamalov et al., 2015), which is clearly in the turbulent regime. This has important implications on the distribution of kinetic energy across various scales. In the common picture of turbulence, kinetic energy being injected at some large scale is transported down the inertial range to smaller scales, until it is dissipated into internal energy when viscous effects become relevant (Kolmogorov, 1941; Landau & Lifshitz, 1987). This turbulent transport is caused by parasitic Kelvin-Helmholtz and Rayleigh-Taylor instabilities that extract power from large scales. According to Kolmogorov’s theory for a steady-state and isotropic turbulent flow, the kinetic energy spectrum has a distinct shape in the inertial range. It is still under debate whether this classical turbulence theory is applicable in the supernova context. While Radice et al. (2016) found that the energy cascade is well described by Kolmogorov’s theory, Couch & Ott (2015) argued that turbulence in the gain layer is neither steady-state nor isotropic due to the background accretion flow, strong gradients, and the time-dependence of the accretion rate. The argumentation of Radice et al. (2016) is based on a parametrized simulation with a high angular resolution of 0.09° . This result is, however, not conclusive, because the simulation was mapped from a coarser grid and only evolved for 60 ms.

In the ideal picture, kinetic energy is cascaded down the inertial range without losses and viscosity only affects the dissipation range at the smallest scales (Landau & Lifshitz, 1987). Since an increasing grid resolution reduces the numerical viscosity, details of the turbulent cascade depend on the choice of the computational grid. Abdikamalov et al. (2015) found that the inertial range of the turbulent cascade is dominated by the numerical viscosity and the slope of the spectrum is shallower than the expected ideal scaling. In their 3D adaptive-mesh-refinement simulations, they observed the so-called “bottleneck”, which is understood as an artificial pile-up of kinetic energy

towards small scales being caused by viscous effects. Also Radice et al. (2015, 2016) found a significant influence of the viscosity on the inertial range. Only for a very high grid resolution, a Kolmogorov scaling was recovered in their parametric simulations. Later, Roberts et al. (2016) backpedaled that a low grid resolution does not necessarily imply an accumulation of kinetic energy at large scales. A final conclusion about the dependence of the energy spectrum on the resolution can thus not be drawn from these studies.

The described forward direction of the turbulent energy cascade only holds in three dimensions (3D). In axisymmetric (two-dimensional, 2D) models, however, kinetic energy is artificially accumulated at large scales and only enstrophy – the squared vorticity – is transported to smaller scales leading to a steeper decline of the spectrum (Kraichnan, 1967; Frisch & Sulem, 1984; Boffetta & Musacchio, 2010). This different behavior of the turbulent kinetic energy in 2D and 3D has important consequences on the conditions for shock revival and the dynamics during the explosion (cf. Chapt. 4). Large-scale fluid structures in the gain layer are beneficial for shock revival, because a large volume-to-surface ratio allows buoyancy to overcome drag forces (Hanke et al., 2012; Couch, 2013; Lentz et al., 2015; Roberts et al., 2016). In 3D simulations, explosions usually occur later for higher grid resolutions (Hanke et al., 2012; Couch & O’Connor, 2014; Takiwaki et al., 2014; Abdiakamalov et al., 2015; Roberts et al., 2016). This is often attributed to the amount of kinetic energy at large scales, although a thorough understanding is still lacking. From the 3D simulations of Radice et al. (2016), for example, a clear resolution dependence of the diagnostic quantities – such as the shock radius – cannot be deduced. In 2D, the picture is even more controversial, because some modelers reported earlier explosions in simulations with higher grid resolution (e.g., Hanke et al., 2012; Summa et al., 2016), but others found later explosions (e.g., Couch, 2013).

Besides the kinetic energy cascade, turbulence also provides an effective pressure being a component of the Reynolds stress tensor. This turbulent pressure possibly contributes significantly to the pressure balance at the shock (Couch & Ott, 2015; Abdiakamalov et al., 2015; Radice et al., 2016; Roberts et al., 2016). Some of these authors reported an increasing contribution of the turbulent pressure with enhanced resolution, while others did not find a clear trend.

At this stage, several questions remain open. How does the turbulent energy cascade behaves when the grid resolution is altered? Can we expect the scaling relations from classical turbulence theory to be valid in the core-collapse supernova context? What are the consequences of a high grid resolution for hydrodynamic instabilities in the gain layer and the revival of the stalled shock in 3D? In this chapter, we will try to address these questions by comparing 2D and 3D models with different grid resolutions but equal physical settings. In order to enhance the angular resolution without additional computational cost, we have implemented a static mesh refinement (SMR) technique that allows for choosing different angular grid spacings in certain radial intervals. The angular resolution can subsequently be increased from inside outwards in order to compensate for the diverging structure of the spherical grid. Details about the numerical implementation of the SMR procedure can be found in Sect. 3.3.

We will explain the physical and numerical settings in the next section, followed by a detailed discussion on the differences between the models with varying angular resolution. At the end of the chapter, we will estimate the numerical viscosities and the effective Reynolds numbers of our 3D simulations.

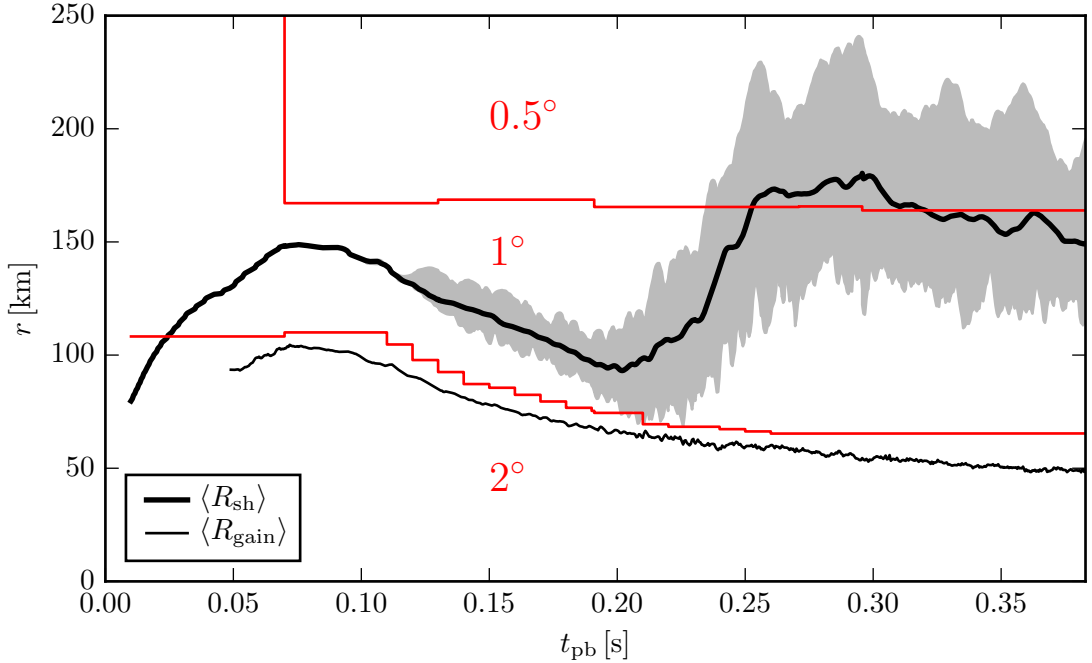


Fig. 6.1.: Angular grid configuration of the model 3Ds.SMR. Thin and thick solid lines depict the angle-averaged gain and shock radius, respectively. Gray-shaded areas indicate the variations of the shock surface with its minimum and maximum extent. Red lines mark the boundaries of the refinement layers. Note that the third layer was added at 70 ms post bounce.

6.1. Physical and numerical setup

We have simulated the post-bounce phase of the $20 M_{\odot}$ star of Woosley & Heger (2007) in axial symmetry (2D) and full three dimensions (3D) with different angular grid spacing, but similar physical settings including the strangeness correction of $g_a^s = -0.2$ (cf. Sect. 5.2). All details about the general numerical setup can be found in Sect. 2.4.

The 3D model with our default grid resolution is referred to as 3Ds and was already discussed in detail in Chapt. 5. It was computed on the standard spherical polar grid with an angular grid spacing of 2° in the entire computational domain, except for the innermost 10 km. This central region was treated in spherical symmetry to avoid severe timestep constraints at the grid origin.

For our high-resolution 3D model 3Ds.SMR, we employed the newly-developed “static mesh refinement” (SMR; see Sect. 3.3) on the Yin-Yang grid with three concentric layers of varying angular resolution (see Fig. 6.1). The innermost spherically symmetric core of 1.6 km radius⁴ is surrounded by a region with a grid spacing of 2° . Slightly above the angle-averaged gain radius, the grid was further refined to 1° . An additional refinement layer of 0.5° was added at 70 ms post bounce outside a radius of 160 km. Extending the region of 1° resolution to a smaller radius and at the same time maintaining the neutrino transport resolution of 2° would be desirable but turns out to be unstable. If the

⁴We have checked that the proto-neutron star is not influenced, when the size of the inner spherically symmetric core is reduced from 10 km to 1.6 km.

computational grid of the transport solver did not coincide with the hydrodynamic mesh in a region of high neutrino optical depth, harmful oscillations around thermodynamic equilibrium would arise (Rampp & Janka, 2002). Numerical inaccuracies would occur when quantities are interpolated from the transport grid to the hydrodynamic grid and vice versa. Consequently, the refinement step from 2° to 1° is located at a radius where the neutrino optical depth is sufficiently low, i.e. around 0.1 to 0.15.

The simulation 3Ds.SMR as well as the 2D runs were performed with a new VERTEX-PROMETHEUS code version⁵. It includes a novel NSE treatment, which assumes NSE above a temperature of 0.5 MeV for infalling matter and above 0.343 MeV for neutrino-heated high-entropy material. Recombination of free nucleons into nuclei is thus treated more accurately compared to the previously applied global threshold of 0.5 MeV. The density ρ_{EOS} between the LS220 high-density equation of state and the low-density regime was set to $3.4 \times 10^7 \text{ g cm}^{-3}$ during core collapse in all models.

Thanks to the SMR technique, the neutrino transport solver operates on the same computational grid with identical angular resolution in both 3D simulations. Only the evolution of the fluid in the model 3Ds.SMR is followed on a finer grid. The computational demands of the 3D models are therefore nearly equal, because solving hydrodynamic problems is computationally cheap and the SMR procedure adds only a small numerical overhead.

In order to allow for detailed comparisons between both 3D runs, the initial density perturbation patterns imposed at 10 ms post bounce were identical.

The physical and numerical settings of the model 3Ds.SMR were similarly used for the 2D models. We performed 2D simulations without the SMR setup on angular grids of 1° and 2° resolution, and simulations with an SMR grid configuration being equal to the corresponding 3D case.

6.2. Results

6.2.1. Overview

As already discussed in detail in the previous chapter, the simulation 3Ds explodes successfully with shock runaway unleashed between 350 and 400 ms. In the model 3Ds.SMR, which has been evolved until 383 ms post bounce, however, the situation is not so clear. At the last data point of the still ongoing simulation, the angle-averaged shock radius $\langle R_{\text{sh}} \rangle$ is 149 km (see Fig. 6.2) with minimum and maximum values of 117 km and 195 km, respectively. We are not yet able to judge whether the model 3Ds.SMR will explode given the temporal evolution of the shock.

Until ~ 130 ms, the shock radii of both 3D models behave similarly with a local maximum at ~ 80 ms post bounce, followed by a gradual retreat. In the model 3Ds.SMR, the angle-averaged shock radius declines to its minimum at 200 ms, before the mass-accretion rate drops as the Si/Si+O shell interface falls through the shock around 230 ms. The consequent rapid shock expansion occurs simultaneously in both 3D models, because the arrival time of the interface is not affected by the different grid reso-

⁵Besides performance improvements and minor changes, the HLLE fluxes of the mass fractions were treated inconsistently in the old code version. Additionally, the charged-current neutrino absorption rates were erroneously averaged over patches of four cells. In the new version, a sign error in the weak magnetism correction leads to slight changes in the neutrino-nucleon scattering opacities for electron neutrinos and electron antineutrinos, which we checked to be insignificant.

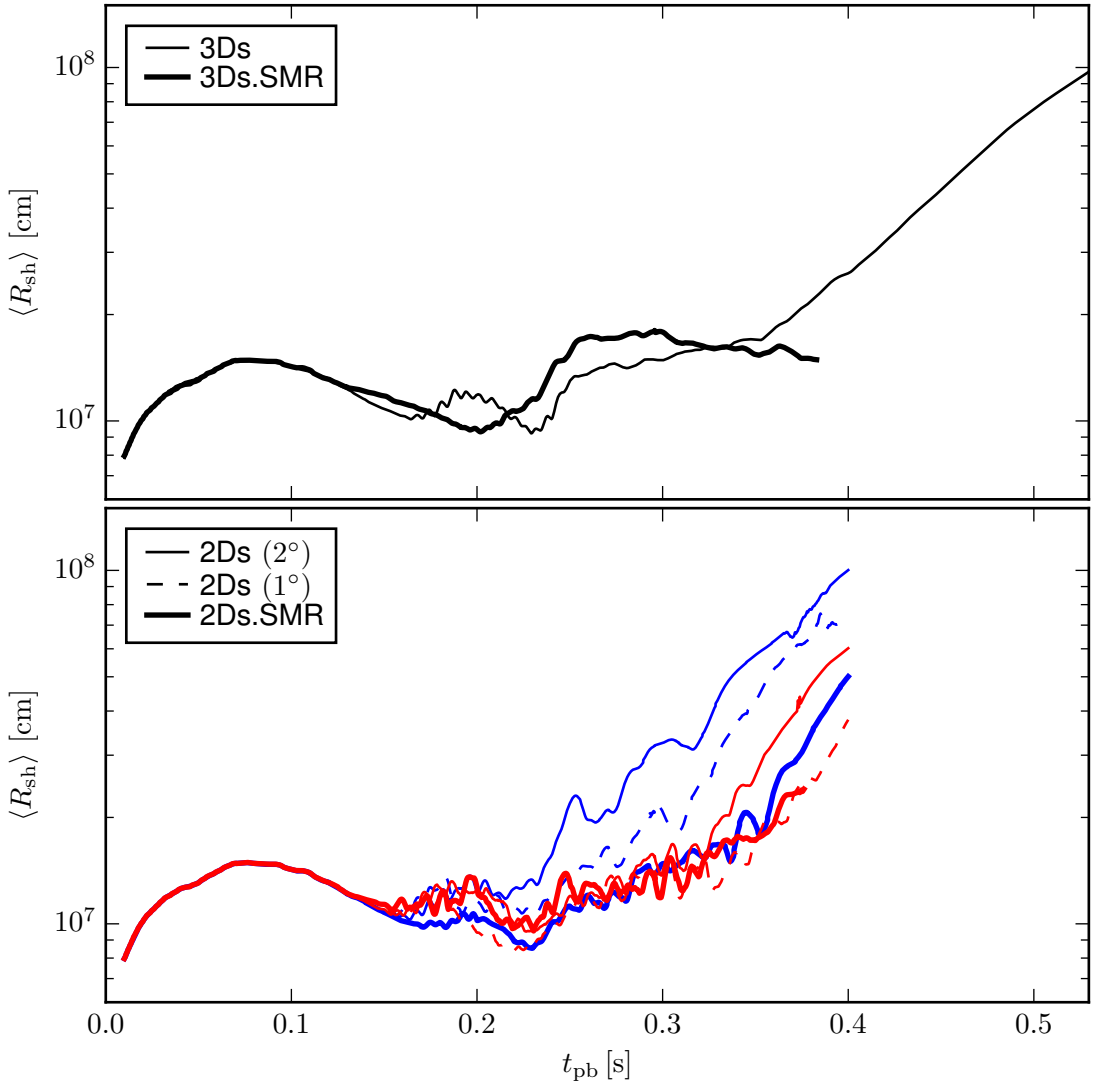


Fig. 6.2.: Angle-averaged shock radii $\langle R_{sh} \rangle$ of the 3D models (*upper panel*) and the 2D models (*lower panel*) as functions of time after bounce t_{pb} . Two sets of 2D simulations were performed with different initial random perturbations (red and blue). Dashed and thin solid lines depict setups with an angular resolution of 1° and 2° , respectively, in the entire computational domain. Thick solid lines correspond to models with the SMR technique.

lution. Until 330 ms post bounce, the shock radius is larger in the high-resolution 3D simulation.

The angle-averaged shock radii of the 2D models displayed in the lower panel of Fig. 6.2 demonstrate the large stochasticity of their temporal evolution. Models plotted with the same line style were computed starting from different initial random perturbations, but otherwise exactly equal configurations. Especially the shock radii of the simulations with 1° angular resolution are several hundred kilometers apart from each other at the same time after core bounce. Summa et al. (2016) similarly observed significant differences caused by variations of the random seed perturbations due to the

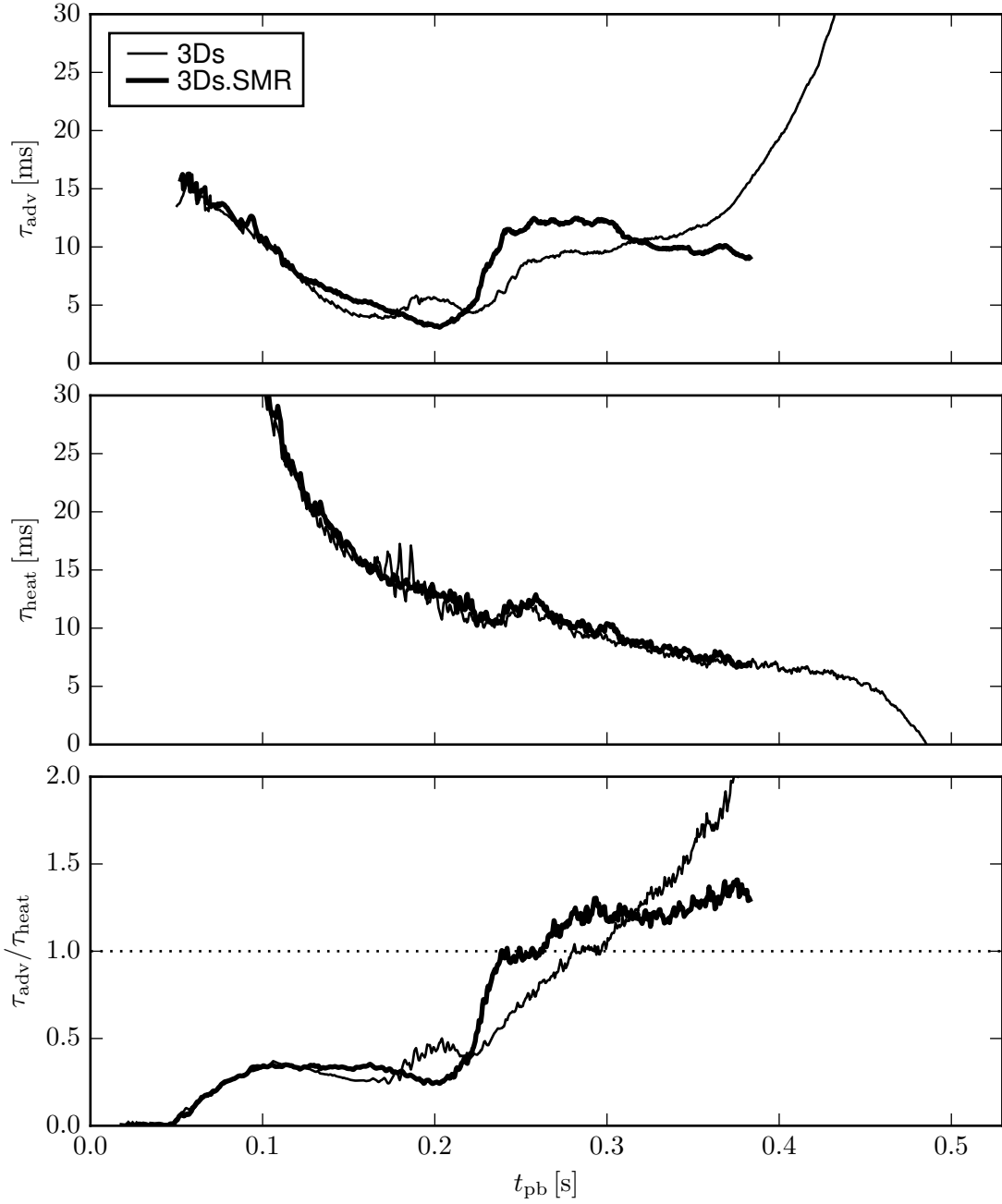


Fig. 6.3.: Advection timescales τ_{adv} , heating timescales τ_{heat} , and their ratios as functions of time for both 3D models.

chaotic behavior of the flow in the post-shock layer. It is clear that from our set of 2D simulations, we are not able to investigate effects caused by differences in the angular grid spacing. A large set of 2D models would be required to estimate the statistical variations, which is, however, beyond the scope of this work. In 3D, we can only compare two single runs due to the high computational cost of these simulations. The 3D models were computed with identical perturbation patterns at 10 ms post bounce and therefore started from the same initial configuration.

In Fig. 6.3, we present the advection and the heating timescales of the 3D models, as well as their ratios (see Eqs. (4.5) and (4.7) for the definitions). The advection timescale $\tau_{\text{adv}} = M_{\text{gain}}/\dot{M}$ is a measure of the time matter is exposed to neutrino heating in the gain layer (Buras et al., 2006a; Murphy & Burrows, 2008). The mass-accretion rates \dot{M} do not differ between both 3D models, because the small perturbations in the supersonically infalling stellar shells cannot grow and the infall profiles therefore do not depend on the grid resolution. Since also the angle-averaged gain radii are equal, the gain layer masses M_{gain} are mainly determined by the shock radii. The advection timescales in Fig. 6.3 thus follow the trends of the angle-averaged shock radii shown in Fig. 6.2. Due to the larger shock radius in the simulation 3Ds.SMR between 220 ms and 330 ms after bounce, the advection timescale is up to 50% longer compared to the case 3Ds.

The heating timescales τ_{heat} of both 3D simulations are equal, i.e. the time needed for unbinding the gain layer by neutrino heating is the same. This is an important observation, because it demonstrates that the neutrino energy deposition in the gain layer is not affected, when the grid resolution is refined by a factor of 2 to 4 there.

Combining both timescales as $\tau_{\text{adv}}/\tau_{\text{heat}}$ is commonly used for determining how close a model is to explosion. A value of unity of this timescale ratio is often considered as a “threshold” for a successful explosion (cf. Sect. 4.3.1), although this number should not be considered exact. In the model 3Ds.SMR, the ratio rises very steeply at ~ 230 ms coinciding with the arrival time of the Si/Si+O interface. $\tau_{\text{adv}}/\tau_{\text{heat}}$ exceeds unity at 240 ms and slowly grows to about 1.3 within the following 140 ms. In the exploding case 3Ds, the timescale ratio exceeds unity much later and grows quickly afterwards. If solely the ratio $\tau_{\text{adv}}/\tau_{\text{heat}}$ was used as an indicator for a successful explosion, shock runaway would be expected at ~ 260 ms in the model 3Ds.SMR. However, despite the large timescale ratio and its very steep increase around 230 ms, the high-resolution 3D simulation does not yet show indications of a successful explosion. Obviously, the diagnostic timescale ratio $\tau_{\text{adv}}/\tau_{\text{heat}}$ fails to predict the success of shock revival in the simulation 3Ds.SMR.

As already indicated by the heating timescales in Fig. 6.3, the energy deposition in the gain layer is nearly equal in both 3D models. Although the total heating rates \dot{Q}_{gain} shown in Fig. 6.4 differ in details, they exhibit the same overall trend. After 250 ms post bounce, the heating rate of the model 3Ds.SMR is slightly larger, but grows similarly compared to the simulation 3Ds. The time-integrated heating rate, i.e. the total deposited energy in the gain layer, is about 2% larger in the high-resolution 3D simulation at 380 ms. In Fig. 6.4, we also show the heating efficiency being defined as

$$\eta_{\text{heat}} = \frac{\dot{Q}_{\text{gain}}}{L_{\nu_e} + L_{\bar{\nu}_e}}, \quad (6.1)$$

where L_{ν_e} and $L_{\bar{\nu}_e}$ are the luminosities of electron neutrinos and electron antineutrinos, respectively. Again, the overall temporal behavior of η_{heat} is equal in both 3D runs. From the heating parameters displayed in Fig. 6.4, we can conclude that the efficiency of neutrino heating does not depend on the chosen grid resolution outside of the gain radius.

In Fig. 6.5, we present cross-sectional cuts through both 3D models displaying the entropy per baryon at different times after core bounce. At a first glance, the high-resolution simulation develops finer structures and more fragmented high-entropy bub-

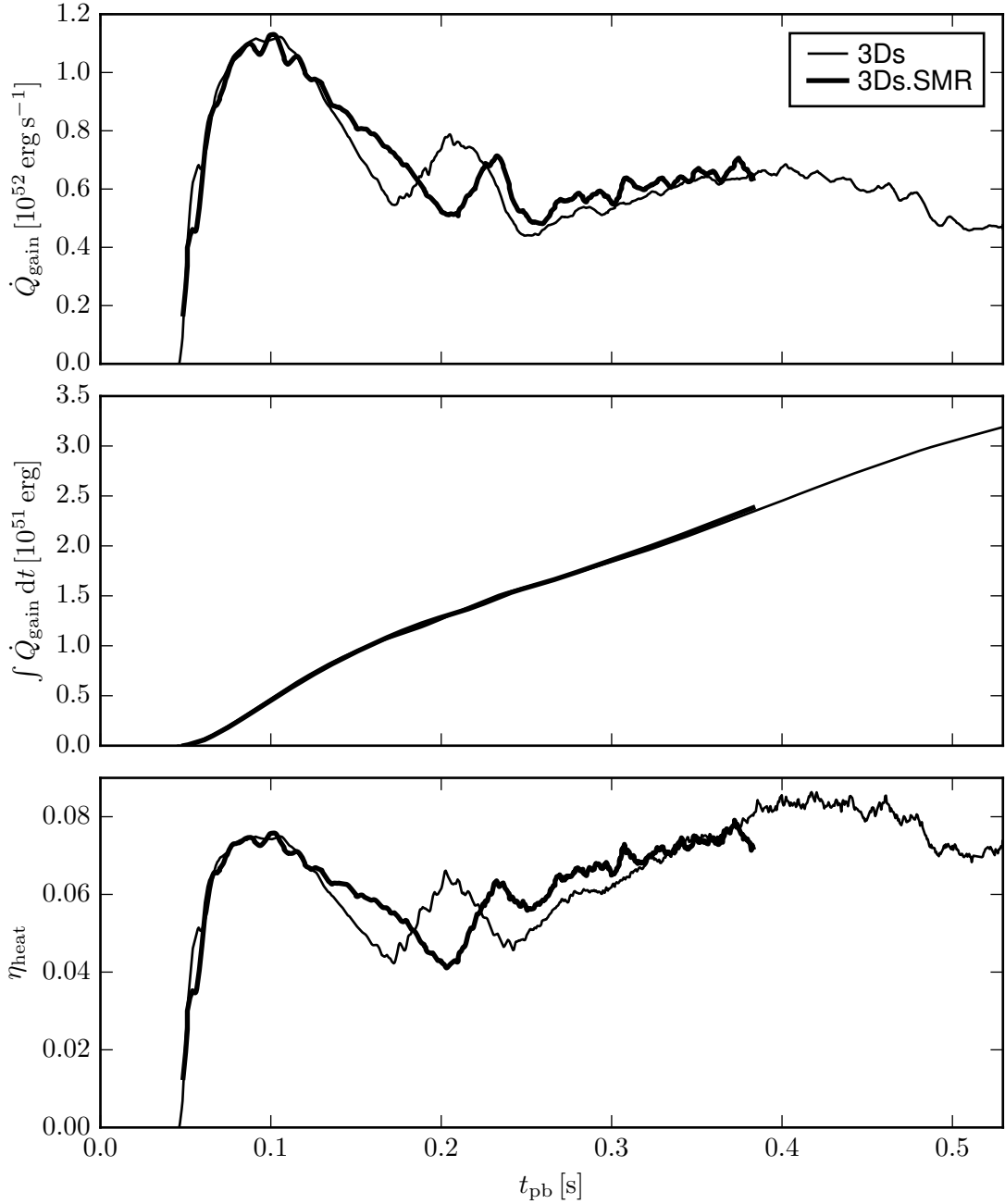


Fig. 6.4.: Total heating rates \dot{Q}_{gain} , total deposited energies in the gain layer $\int \dot{Q}_{\text{gain}} dt$, and heating efficiencies η_{heat} as functions of time.

bles. The heads of the buoyant mushrooms are more ragged in the model 3Ds.SMR and the fluid generally appears more turbulent. Radice et al. (2015) argued that the picture of delimited high-entropy bubbles is an artifact occurring in low-resolution simulations. We cannot confirm this observation with our model 3Ds.SMR, which approximately corresponds to their “4x” case. The neutrino-heated bubbles are still distinct and similar in size compared to the model 3Ds, whose hydrodynamics was evolved on a coarser grid.

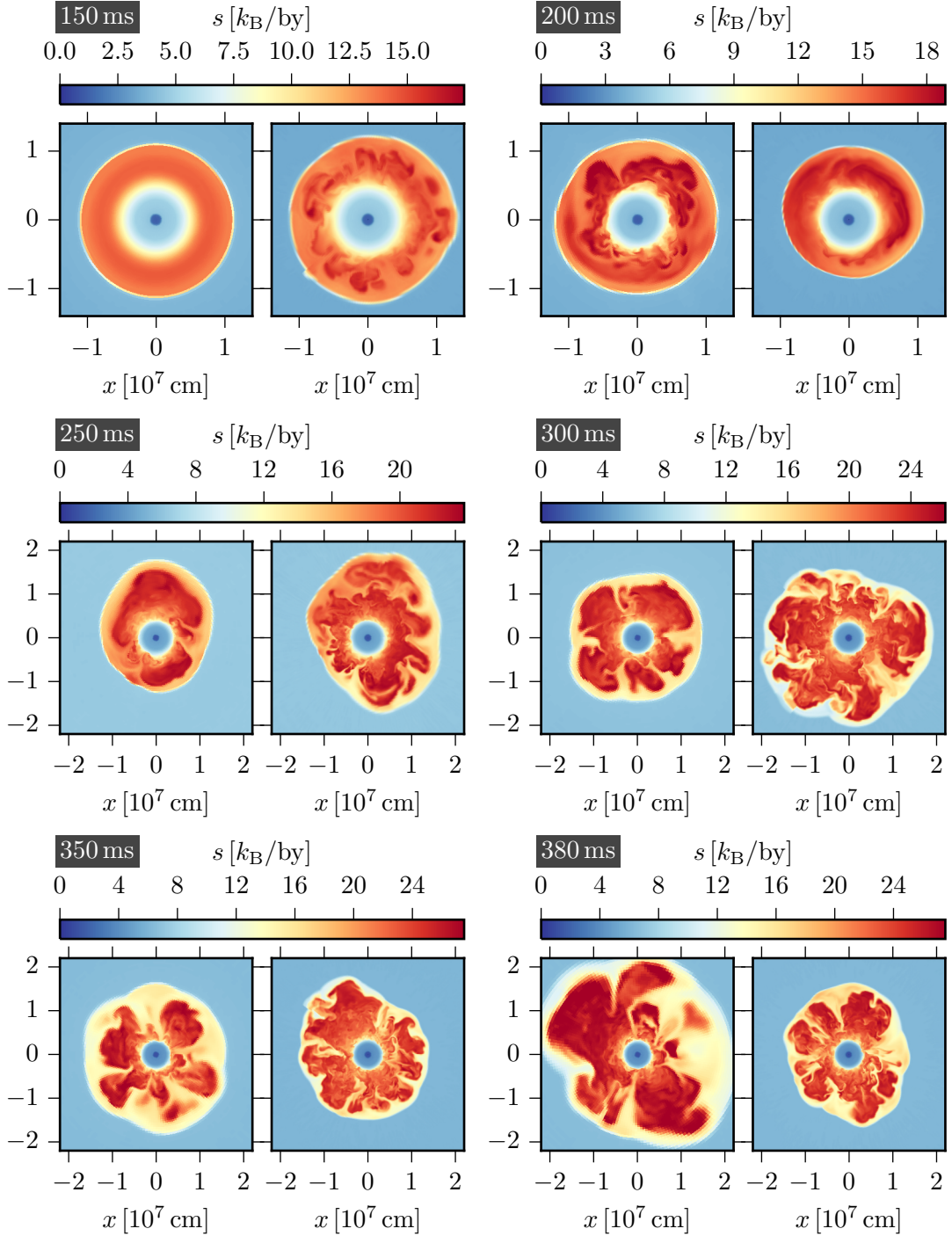


Fig. 6.5.: Color-coded entropy per baryon s of the models 3Ds (*left panels*) and 3Ds.SMR (*right panels*) for six different times after core bounce. The entropy distribution is depicted in the plane $z = 0$.

The occurrence of the SASI can hardly be deduced from Fig. 6.5. We therefore show the coefficients a_1^m of the spherical harmonics decomposition of the shock surface in Fig. 6.6. The reader is referred to Sect. 5.4.3 for the corresponding defining equations.

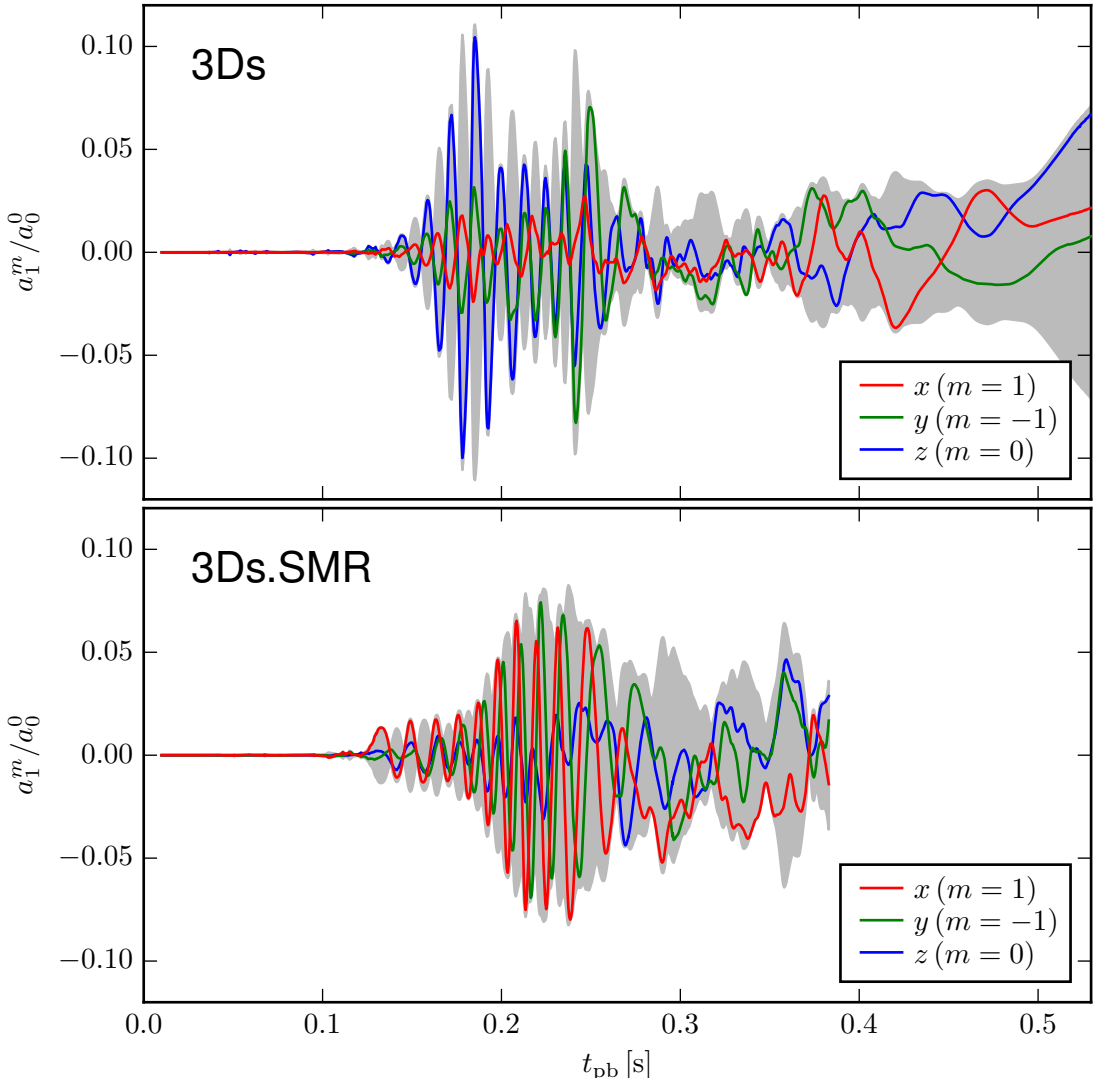


Fig. 6.6.: Coefficients a_ℓ^m of the spherical harmonics shock decomposition for $\ell = 1$ normalized to the angle-averaged shock radii (see Sect. 5.4.3 for the definitions of the coefficients). Gray-shaded areas depict the SASI amplitudes and are filled between $-A_1$ and A_1 (cf. Eq. (5.19)).

In the model 3Ds, SASI sloshing starts at 150 ms and persists for approximately 70 ms. During the phase of strong oscillation, it is aligned with the z -axis, because this is the preferred direction of the spherical polar grid. The sloshing motion turns into a spiral phase continuing until ~ 280 ms after bounce. The occurrence of the SASI is completely different in the simulation 3Ds.SMR. On the Yin-Yang grid without any preferred direction, a spiral mode develops, whose rotational motion lies approximately in the plane $z = 0$. It starts already at 125 ms post bounce and decays at around 270 ms. The maximum amplitude of the spiral mode in the high-resolution simulation 3Ds.SMR is lower than the sloshing amplitude of the model 3Ds.

In Fig. 6.7, we present the turbulent kinetic energy, i.e. the non-radial kinetic energy integrated over the gain layer. In the simulation 3Ds.SMR, it rises already early at

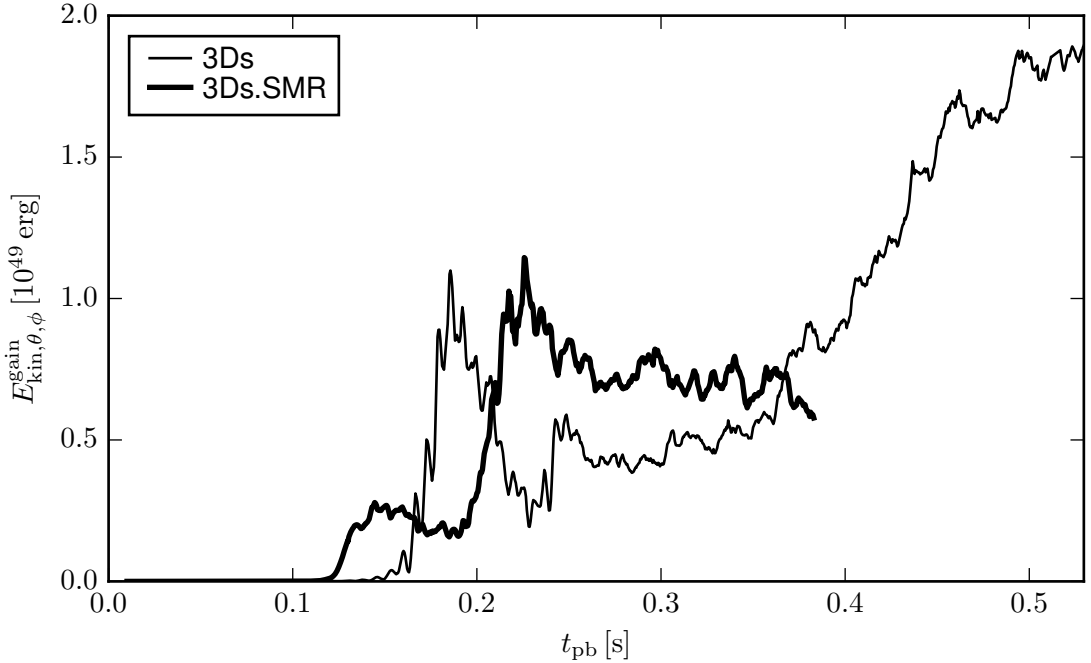


Fig. 6.7.: Turbulent kinetic energies in the gain layer as defined in Eq. (4.14) for the two 3D models.

~ 125 ms due to the growth of the SASI spiral mode that exhibits large non-radial velocities. The turbulent kinetic energy then remains at a low level, but increases quickly 80 ms later and exceeds the value of the model 3Ds. Between 220 and 240 ms after bounce, the non-radial kinetic energy in the gain layer is larger by more than a factor of three in the high-resolution model because of the violent SASI spiral mode, which persists until ~ 280 ms post bounce. After 240 ms post bounce, $E_{\text{kin},\theta,\phi}^{\text{gain}}$ remains approximately twice as large as in the simulation 3Ds for about 60 ms.

Recently, Summa et al. (2016) and Janka et al. (2016) proposed a universal explosion criterion for core-collapse supernovae. They extended the idea of the critical luminosity condition introduced by Burrows & Goshy (1993), which describes the interplay between neutrino heating and mass accretion in spherical symmetry. For a given value of $\dot{M}M_{\text{PNS}}$, i.e. the product of the mass-accretion rate and the proto-neutron star mass, a critical value of $L_\nu \langle \varepsilon_\nu \rangle^2$ exists⁶, which is the product of the neutrino luminosity

$$L_\nu = L_{\nu_e} + L_{\bar{\nu}_e} \quad (6.2)$$

and the luminosity-weighted squared neutrino mean energy

$$\langle \varepsilon_\nu \rangle^2 = \frac{L_{\nu_e} \langle \varepsilon_{\nu_e} \rangle^2 + L_{\bar{\nu}_e} \langle \varepsilon_{\bar{\nu}_e} \rangle^2}{L_\nu}. \quad (6.3)$$

Above this critical threshold, the shock is revived by neutrino heating and can overcome the ram pressure maintained by accreted material. This simple picture, however, does

⁶As done by Janka et al. (2016), we replace the quantity $\langle E_\nu^2 \rangle = \langle \varepsilon_\nu^3 \rangle / \langle \varepsilon_\nu \rangle$ appearing in the derivation of the condition by $\langle \varepsilon_\nu \rangle^2$.

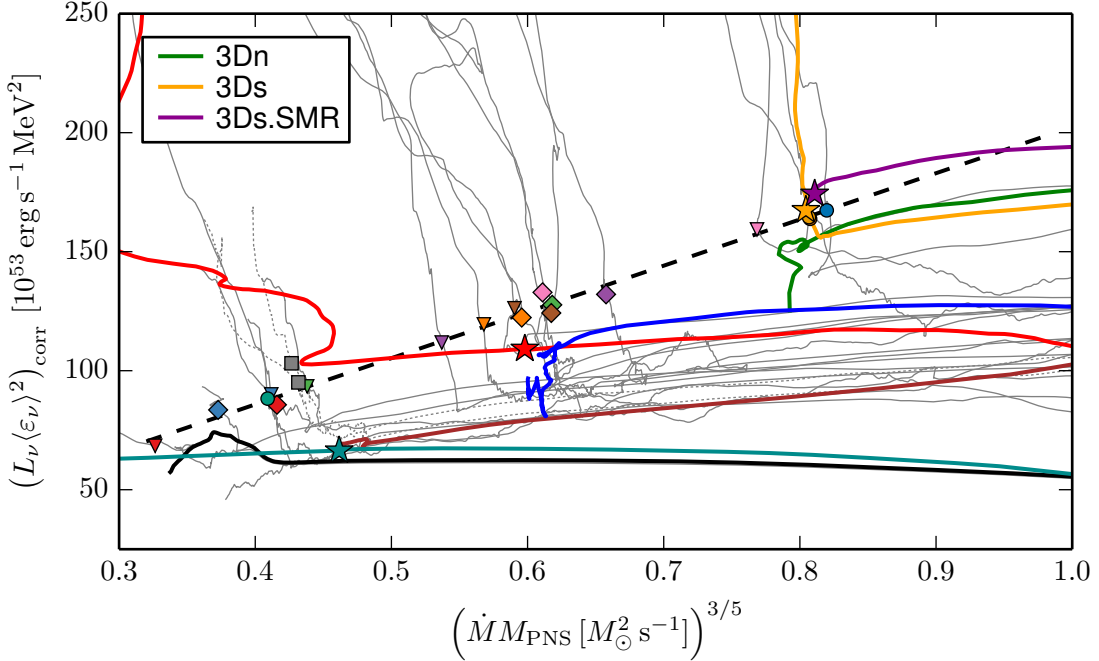


Fig. 6.8.: Critical luminosity condition for various 2D and 3D models. Lines depict the evolution tracks of the 2D models (*gray lines*) and the 3D simulations (*colored lines*). Symbols of different shapes mark the points in time, when the timescale ratios $\tau_{\text{adv}}/\tau_{\text{heat}}$ reach unity. The thick dashed line is a least-squares fit to a 2D subset of these critical points. The 3D models discussed in this work are the simulations 3Dn from Chapt. 5, (green), 3Ds (orange), 3Ds.SMR (purple), and the $9.6 M_\odot$ model from Chapt. 4 (cyan). The remaining colored lines represent other 3D models (see Janka et al., 2016, Fig. 3). Running averages of 25 ms were applied to all values. (*This figure was kindly provided by A. Summa.*)

not include multi-dimensional processes in the gain layer, which are favorable for shock revival in 2D and 3D. Summa et al. (2016) and Janka et al. (2016) therefore took additional terms into account, namely the time dependence of the gain radius, the binding energy of the gain layer, and the turbulent pressure. In the plane spanned by the corrected heating term $(L_\nu \langle \varepsilon_\nu \rangle^2)_{\text{corr}}$ and the accretion term $(\dot{M} M_{\text{PNS}})^{3/5}$, the models propagate on their evolution tracks from right to left (see Fig. 6.8). Remarkably, the points in time, at which the timescale ratios $\tau_{\text{adv}}/\tau_{\text{heat}}$ reach unity, lie on a straight line. This is also true for the exploding model 3Ds. Non-exploding simulations do not reach this line and their trajectories turn downwards. The high-resolution run 3Ds.SMR is an outlier in this respect. Its ratio $\tau_{\text{adv}}/\tau_{\text{heat}}$ exceeds unity at a point being located well above the critical line. The criterion of Summa et al. (2016) and Janka et al. (2016) clearly predicts an explosion in case of our high-resolution 3D model 3Ds.SMR.

Many diagnostic quantities of the high-resolution 3D model appear to be more favorable compared to the model computed on a coarser grid. The angle-averaged shock radius is larger during long phases of the evolution, the time scale ratio exceeds unity earlier and rises permanently, and the non-radial kinetic energy in the gain layer is sig-

nificantly higher. At the same time, slightly more energy is deposited in the gain layer by neutrino heating. Moreover, a strong SASI spiral mode is present that – according to Fernández (2015) – is beneficial for shock revival, because it contains more kinetic energy compared to a sloshing mode that was found in the simulation 3Ds. Also the recently proposed criterion of Summa et al. (2016) and Janka et al. (2016) predicts an explosion. Despite all these findings, the model 3Ds.SMR does not yet show indications for shock revival. In the following section we will try to identify the reason for the unusual behavior of the high-resolution 3D simulation.

6.2.2. Energy and momentum fluxes

In order to assess, why the model 3Ds.SMR has not yet exploded, we analyze the enthalpy, kinetic energy, and momentum flux densities similarly to Meakin & Arnett (2007) and Radice et al. (2016). The considered flux densities are decomposed into a mean and a turbulent component,

$$F_{\mathcal{X}} = \bar{F}_{\mathcal{X}} + F'_{\mathcal{X}}, \quad (6.4)$$

where \mathcal{X} is a placeholder for the different types of fluxes that we will discuss below. The individual terms of the latter equation read

$$F_{\mathcal{X}} = \langle \mathcal{X} v_r \rangle, \quad (6.5a)$$

$$\bar{F}_{\mathcal{X}} = \langle \mathcal{X} \rangle \langle v_r \rangle, \quad (6.5b)$$

$$F'_{\mathcal{X}} = \langle \mathcal{X} (v_r - \langle v_r \rangle) \rangle. \quad (6.5c)$$

In this section, averages are defined as

$$\langle \mathcal{X} \rangle := \frac{\int d\Omega \rho \mathcal{X}}{\int d\Omega \rho}. \quad (6.6)$$

We analyze the flux densities of the enthalpy, the kinetic energy, and the radial momentum, which are given by

$$\mathcal{X} = \begin{cases} \rho e + P & \text{enthalpy "H",} \\ \frac{1}{2} \rho (v_r^2 + v_\theta^2 + v_\phi^2) & \text{kinetic energy "K",} \\ \rho v_r & \text{radial momentum "S".} \end{cases} \quad (6.7)$$

For reference, we note that the component of the Reynolds stress tensor being referred to as “turbulent pressure” in the literature (Couch & Ott, 2015; Abdikamalov et al., 2015; Radice et al., 2016; Roberts et al., 2016) is related to the turbulent momentum flux density according to

$$R_{rr} = r^2 F'_S. \quad (6.8)$$

In Fig. 6.9, we present the quantities defined in the previous equations for the models 3Ds and 3Ds.SMR. They are measured at a constant radius of 100 km in order to avoid including pre-shock material in the analysis and allow for a detailed comparison of both 3D simulations. The time axes in Fig. 6.9 start at 230 ms post bounce corresponding to the arrival time of the Si/Si+O shell interface. This is the interesting phase, during which the revival of the shock in the model 3Ds.SMR would have been expected.

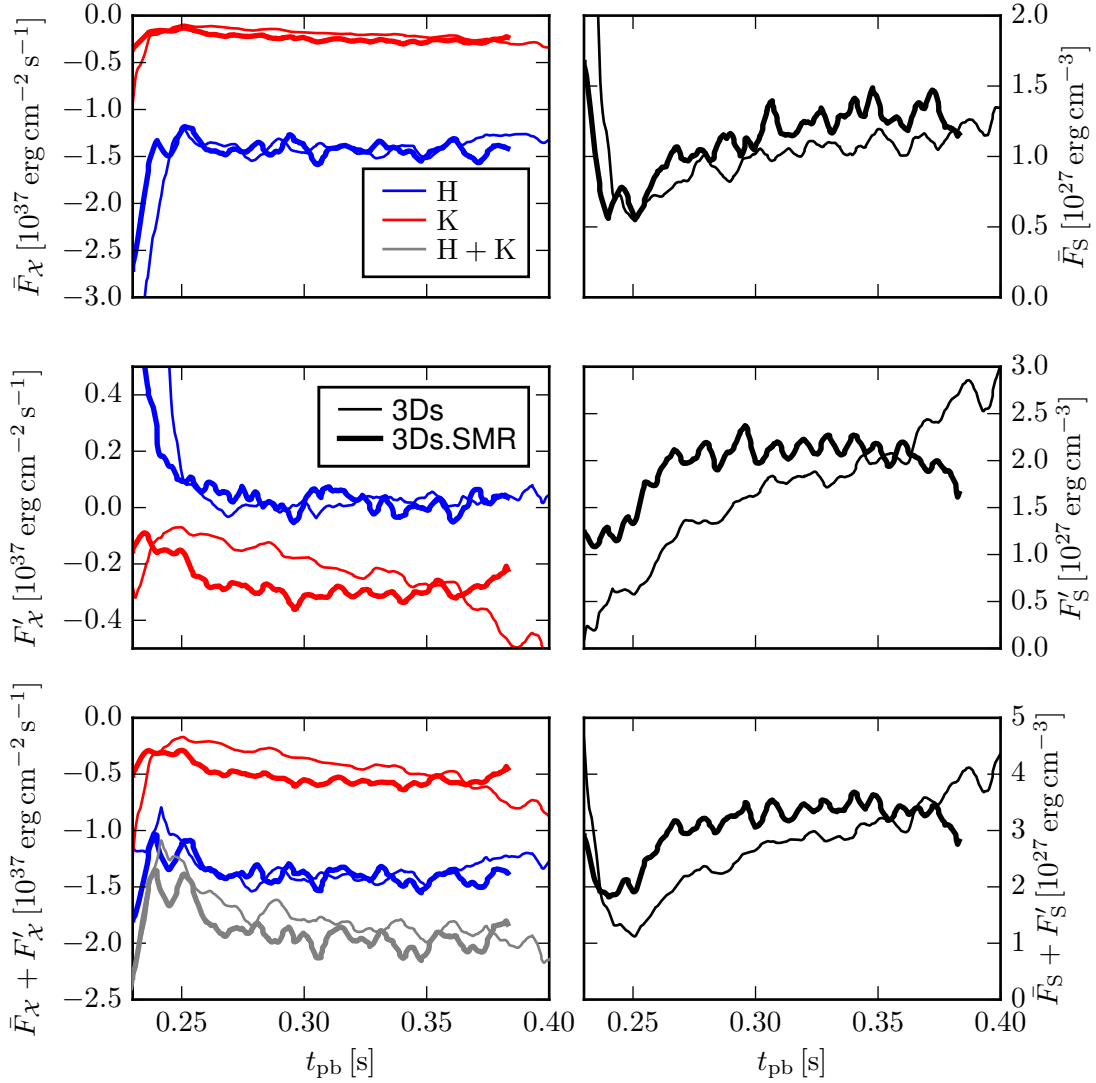


Fig. 6.9.: Enthalpy, kinetic energy (*left column*) and momentum (*right column*) flux densities of the two 3D models measured at a radius of 100 km as functions of post-bounce time. The mean, turbulent, and total flux densities are presented in the upper, middle, and lower panels, respectively. Colors depict different types of fluxes. The corresponding definitions can be found in Eqs. (6.5) in combination with Eq. (6.7).

The mean and turbulent momentum flux densities are larger in the high-resolution 3D simulation during crucial phases of the displayed time interval. By comparing the definition of the mean value \bar{F}_S with Eq. (4.4), it follows that

$$\bar{F}_S \approx -\frac{\dot{M}}{4\pi r^2} \langle v_r \rangle, \quad (6.9)$$

i.e. \bar{F}_S is related to the mass-accretion rate \dot{M} and the angle-averaged radial velocity. Note that this relation is not exact, because we apply a density-weighted averaging procedure in this section and \dot{M} is measured at a radius of 400 km. The steep decline

of \bar{F}_S before 250 ms post bounce can easily be explained by the rapid drop of \dot{M} as the Si/Si+O shell interface is accreted. Subsequently, the mean flux density remains larger in the simulation 3Ds.SMR, because the absolute value of $\langle v_r \rangle$ is higher in this case. Also the turbulent momentum flux density F'_S being proportional to the turbulent pressure R_{rr} is larger in the high-resolution model. As a consequence, the total flux density F_S , which is proportional to the angle-averaged radial kinetic energy, exceeds the 3Ds value considerably until about 350 ms.

The total enthalpy flux densities are negative, because the accretion flow from the shock surface to the gain radius dominates the dynamics. However, their turbulent parts F'_H are greater than zero in both 3D models, i.e. the total downwards enthalpy flux is weakened by turbulent effects. A clear trend between both 3D models does not exist in terms of enthalpy transport.

The kinetic energy flux densities \bar{F}_K and F'_K are also negative due to the global accretion flow. Interestingly, the transport of kinetic energy both in the mean flow and by turbulent processes is enhanced in the model 3Ds.SMR compared to the model 3Ds. For example, the absolute value of the turbulent component $|F'_K|$ is about 80% larger in the high-resolution simulation at 300 ms. At the same time, $|\bar{F}_K|$ is enhanced by $\sim 30\%$.

In order to further investigate, why more kinetic energy is transported downwards in the model 3Ds.SMR, we decompose the flux into an inflow and an outflow component, i.e. we consider fluid elements with $v_r < 0$ and $v_r > 0$, respectively. The two terms are defined as

$$\dot{E}_{v_r>0}^{\text{kin}} := r^2 \int d\Omega \Theta(v_r) \frac{1}{2} \rho (v_r^2 + v_\theta^2 + v_\phi^2) v_r, \quad (6.10a)$$

$$\dot{E}_{v_r<0}^{\text{kin}} := r^2 \int d\Omega \Theta(-v_r) \frac{1}{2} \rho (v_r^2 + v_\theta^2 + v_\phi^2) v_r, \quad (6.10b)$$

where $\Theta(x)$ is the Heaviside step function. The same decomposition is also applied to the mass fluxes according to

$$\dot{M}_{v_r>0} := r^2 \int d\Omega \Theta(v_r) \rho v_r, \quad (6.11a)$$

$$\dot{M}_{v_r<0} := r^2 \int d\Omega \Theta(-v_r) \rho v_r. \quad (6.11b)$$

In Fig. 6.10, we show these components as functions of time at a fixed radius of 100 km. Indeed, the absolute value of the downflow kinetic energy flux $|\dot{E}_{v_r<0}^{\text{kin}}|$ is much larger in the model 3Ds.SMR, whereas the outflow components $\dot{E}_{v_r>0}^{\text{kin}}$ are equal in both 3D simulations. Also the mass flux of downflows $\dot{M}_{v_r<0}$ is enhanced in the high-resolution run. For the mass fluxes of outflows $\dot{M}_{v_r>0}$, a clear trend between the 3D models is not seen.

The angular size of the downflows can be deduced from the “downflow filling factor” being defined as

$$\alpha_{v_r<0} := \frac{\int d\Omega \Theta(-v_r)}{\int d\Omega}. \quad (6.12)$$

It is a measure of the surface fraction occupied by downflows. In both 3D models, $\alpha_{v_r<0}$ is greater than 0.5. Until ~ 300 ms post bounce, the downflows occupy more space in the simulation 3Ds. After that, both models exhibit equal values of $\alpha_{v_r<0}$.

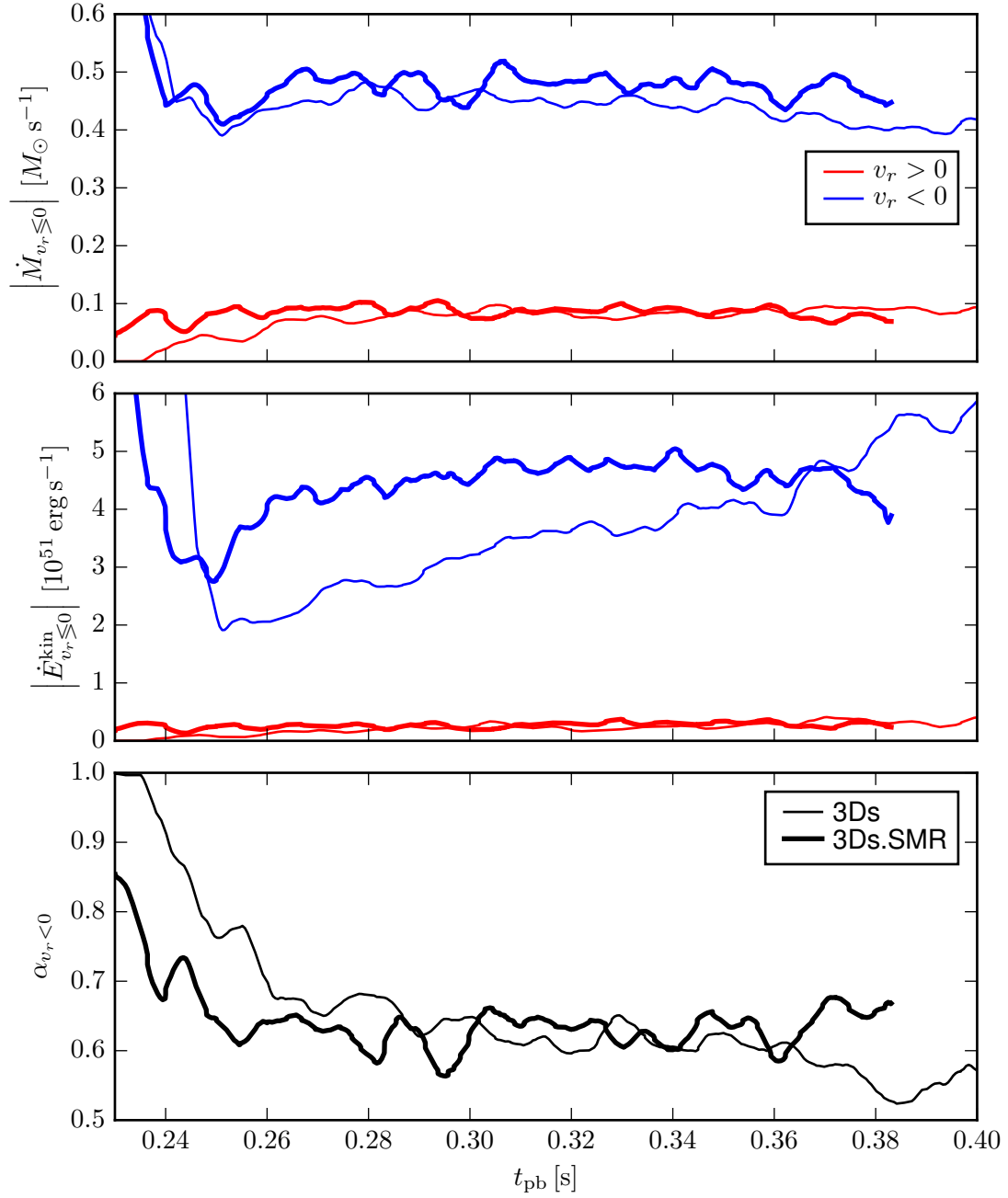


Fig. 6.10.: Mass fluxes of downflows and outflows, $\dot{M}_{v_r < 0}$ and $\dot{M}_{v_r > 0}$ (*upper panel*), kinetic energy fluxes of downflows and outflows, $\dot{E}_{v_r < 0}^{\text{kin}}$ and $\dot{E}_{v_r > 0}^{\text{kin}}$ (*middle panel*), and downflow filling factors $\alpha_{v_r < 0}$ (*lower panel*) for the two 3D models measured as a radius of 100 km. Blue lines depict the absolute values for infalling material, while red lines represent the values for outflowing fluid elements.

At this stage, our hypothesis is that the downflows in the high-resolution simulation transport more mass and significantly more kinetic energy from the shock to the gain radius. Although the turbulent kinetic energy in the gain layer is higher in the model

3Ds.SMR (cf. Fig. 6.7), it is carried away from the shock more efficiently, which is unfavorable for shock revival. The higher turbulent pressure is not able to compensate for this effect. The occupied angular space of the downflows is smaller shortly after the arrival time of the Si/Si+O interface and becomes equal to the case 3Ds afterwards. This implies that the downflows are more compressed in the model 3Ds.SMR compared to the case 3Ds, which is probably caused by a higher non-radial Reynolds stress provided by the turbulent outflows.

Further analysis of this process is postponed to a future publication, once the high-resolution model is sufficiently far evolved in time and a final outcome can be deduced.

6.2.3. Kinetic energy spectra

A fluid transitions from the laminar to the turbulent regime above a certain Reynolds number Re . Turbulence is described phenomenologically and understood as a superposition of eddies of various scales (Landau & Lifshitz, 1987; Pope, 2000). In the common picture sharpened by Kolmogorov (1941), kinetic energy is steadily injected at some large scale L , which is similar to the size of the largest turbulent eddies. These eddies break up into smaller structures and thus transport energy to successively smaller scales. Eventually, below some small scale \mathcal{L} , kinetic energy is dissipated into internal energy by viscous effects.

Kolmogorov (1941) assumed that this turbulent energy cascade only depends on the energy dissipation rate and the viscosity. In the inertial range roughly between L and \mathcal{L} , kinetic energy is carried to smaller scales without losses. From a self-similarity ansatz, it follows that the kinetic energy spectrum $E(k)$ – with k being the wave number – has a universal shape of $E(k) \propto k^{-5/3}$ in the inertial range.⁷ These findings only hold if the fluid structures are locally isotropic, i.e. large-scale anisotropies due to boundary effects can be neglected for sufficiently small scales below L (Pope, 2000). It is not clear, whether this assumption is valid during the shock stagnation phase, because the accretion flow through the gain layer might add a preferred direction not only to the largest turbulent eddies but also to smaller-scale structures (see, e.g., Couch & Ott, 2015).

Here, we assume that Kolmogorov's theory of turbulence is applicable to the core-collapse supernova scenario. In order to quantify the turbulent transport of energy across various scales, the kinetic energy spectrum is calculated for both 3D models at different times after core bounce. Since we are considering stellar cores, which are spherical objects to first order, the kinetic energy is decomposed into spherical harmonics instead of Cartesian wave numbers.

Let the complex spherical harmonics be defined as

$$\tilde{Y}_\ell^m(\theta, \phi) = \begin{cases} N_\ell^m P_\ell^m(\cos \theta) e^{im\phi} & m > 0 \\ N_\ell^0 P_\ell^0(\cos \theta) & m = 0 \\ (-1)^m N_\ell^{|m|} P_\ell^{|m|}(\cos \theta) e^{im\phi} & m < 0 \end{cases} \quad (6.13)$$

with normalization factors

$$N_\ell^m = \sqrt{\frac{2\ell+1}{4\pi} \frac{(\ell-m)!}{(\ell+m)!}} \quad (6.14)$$

⁷To clarify the notation, we write E_k and E_ℓ instead of $E(k)$ and $E(\ell)$ from now on, because the symbol E is also used for the total kinetic energy.

and associated Legendre polynomials $P_\ell^m(\cos\theta)$. The decomposition of the non-radial kinetic energy density at a given radius is then determined by

$$E_\ell = \frac{1}{2} \sum_{m=-\ell}^{\ell} \left| \int d\Omega \sqrt{\rho(v_\theta^2 + v_\phi^2)} \tilde{Y}_\ell^m(\theta, \phi) \right|^2. \quad (6.15)$$

This spectrum is normalized such that the total non-radial kinetic energy density on a spherical shell is the sum over all components of the spectrum,

$$E := \frac{1}{2} \int d\Omega \rho(v_\theta^2 + v_\phi^2) = \sum_{\ell=0}^{\infty} E_\ell. \quad (6.16)$$

The decomposition applied here was similarly used in other works that analyzed the turbulent cascade, for example, Hanke et al. (2012), Couch & O'Connor (2014), Hanke (2014), and Abdikamalov et al. (2015).

For the discussion later in this chapter, we also define the spectrum of the specific kinetic energy as

$$\mathcal{E}_\ell = \frac{1}{2} \sum_{m=-\ell}^{\ell} \left| \int d\Omega \sqrt{v_\theta^2 + v_\phi^2} \tilde{Y}_\ell^m(\theta, \phi) \right|^2. \quad (6.17)$$

Again, the sum over the coefficients gives the total non-radial specific kinetic energy on a spherical shell,

$$\frac{1}{2} \int d\Omega (v_\theta^2 + v_\phi^2) = \sum_{\ell=0}^{\infty} \mathcal{E}_\ell. \quad (6.18)$$

In the following figures, we present energy spectra for the two 3D models 3Ds and 3Ds.SMR at certain times after core bounce. The spectra are measured at a radius R_0 between the angle-averaged gain radius and the minimum shock radius, i.e.,

$$R_0 = \frac{\langle R_{\text{gain}} \rangle + \min(R_{\text{sh}})}{2}. \quad (6.19)$$

This choice assures that we do not include contributions from pre-shock material in our analysis. In order to smooth the data, the energy spectra are averaged over $R_0 \pm 5$ km and $t \pm 2.5$ ms. To guarantee consistency, this averaging is also applied to the total kinetic energy density E .

From the angular grid resolution α of the 3D models, we can calculate the maximum multipole order ℓ_{\max} roughly according to $\ell_{\max} \approx 180^\circ/\alpha$. In the SMR simulation 3Ds.SMR, $\alpha = 1^\circ$ at the location where the spectrum is measured (cf. Fig. 6.1). However, for numerical reasons, we are not able to compute spherical harmonics for $\ell > 150$. Consequently,

$$\ell_{\max} = \begin{cases} 90 & \text{for 3Ds,} \\ 150 & \text{for 3Ds.SMR.} \end{cases} \quad (6.20)$$

In Fig. 6.11 and in the upper panels of Fig. 6.14, we show the turbulent energy spectra as functions of ℓ for five different times after bounce. The largest scales contain most of the total kinetic energy. Their temporal evolution should therefore be in line with the behavior of the non-radial kinetic energy shown in Fig. 6.7. Although it seems that this is not always the case, it should not be forgotten that the monopole term $\ell = 0$,

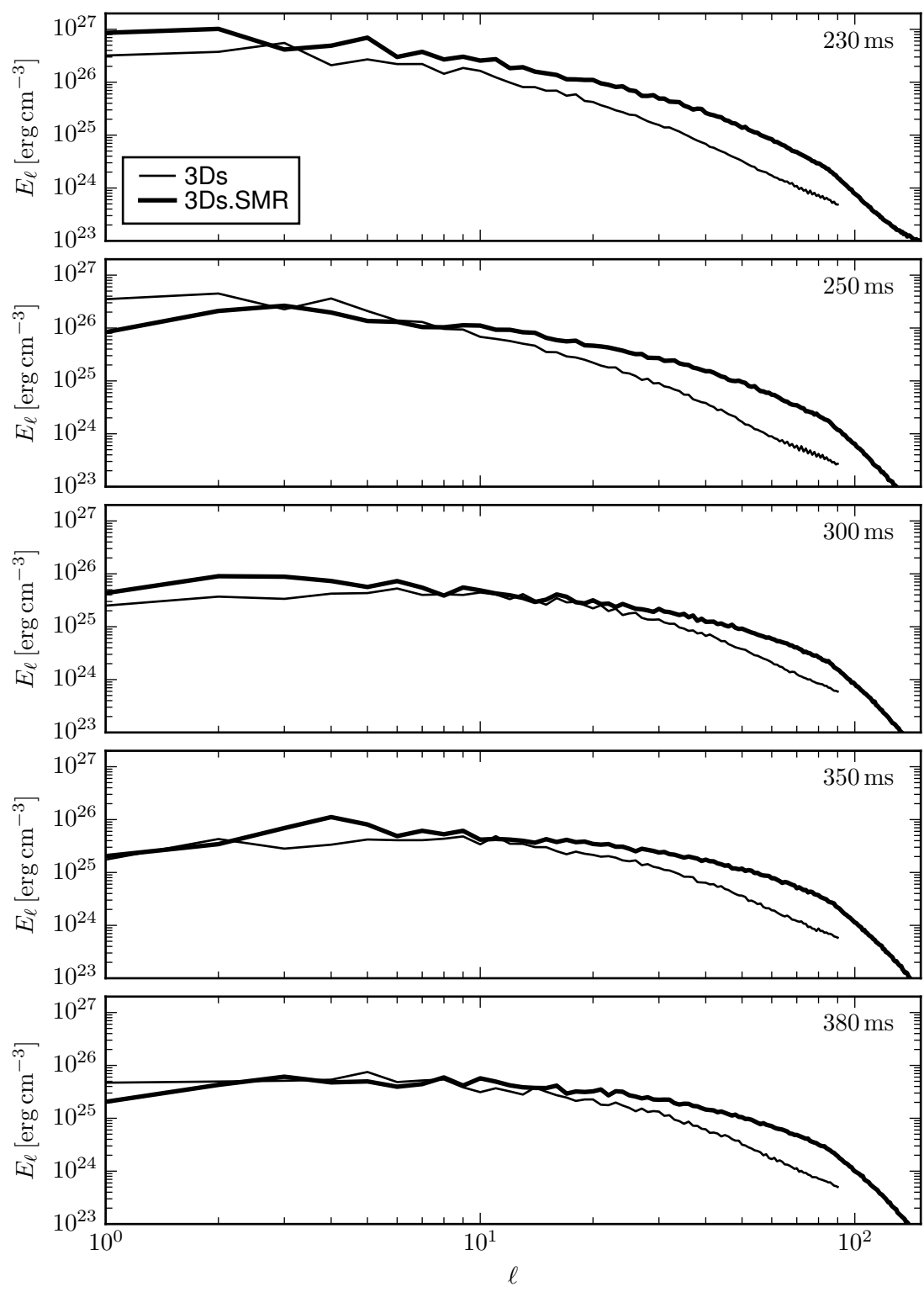


Fig. 6.11.: Kinetic energy spectra E_ℓ for both 3D models at five different times after core bounce (see Eq. (6.15)).

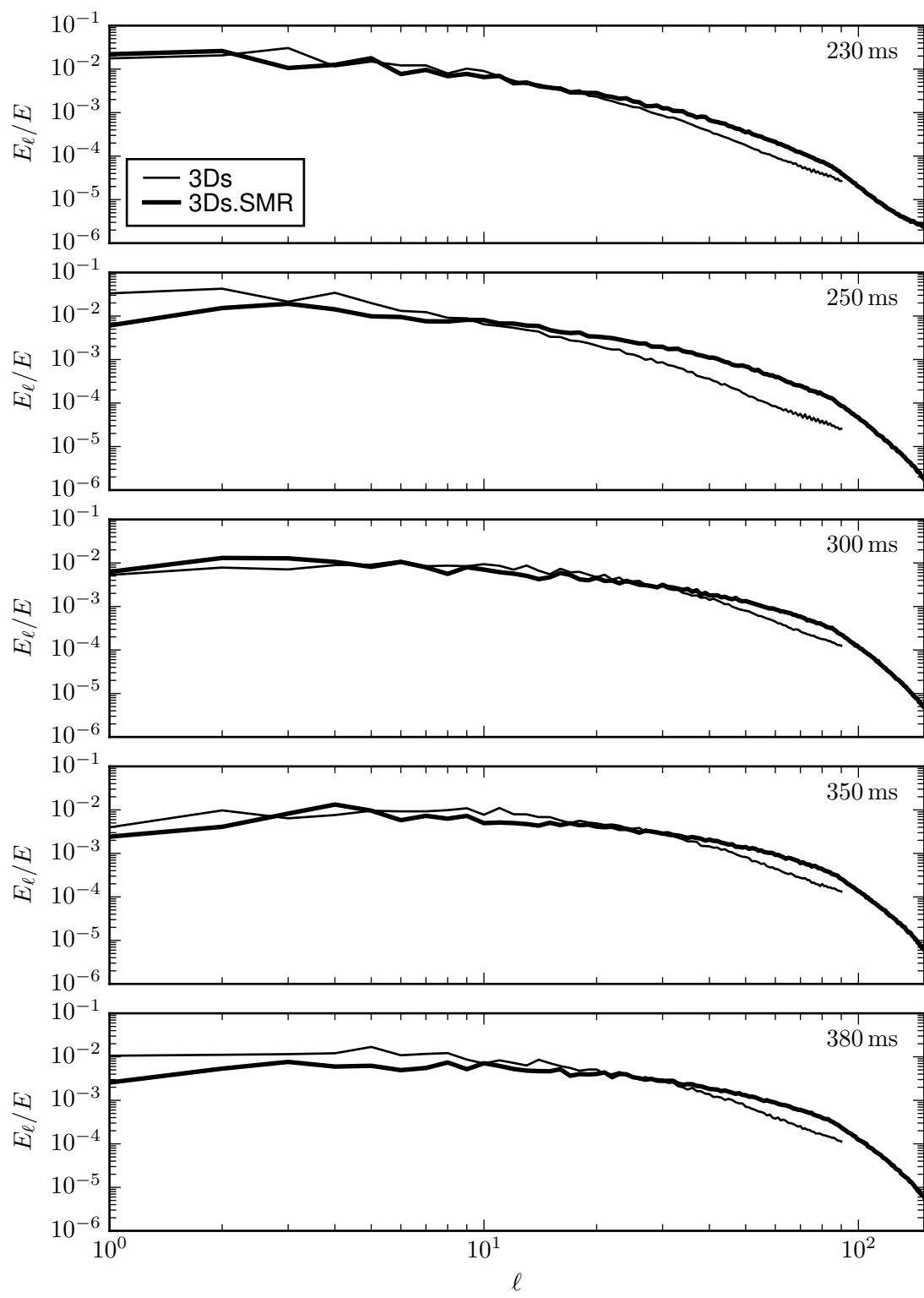


Fig. 6.12.: Same as Fig. 6.11, but normalized to the total kinetic energy density E (see Eq. (6.16)).

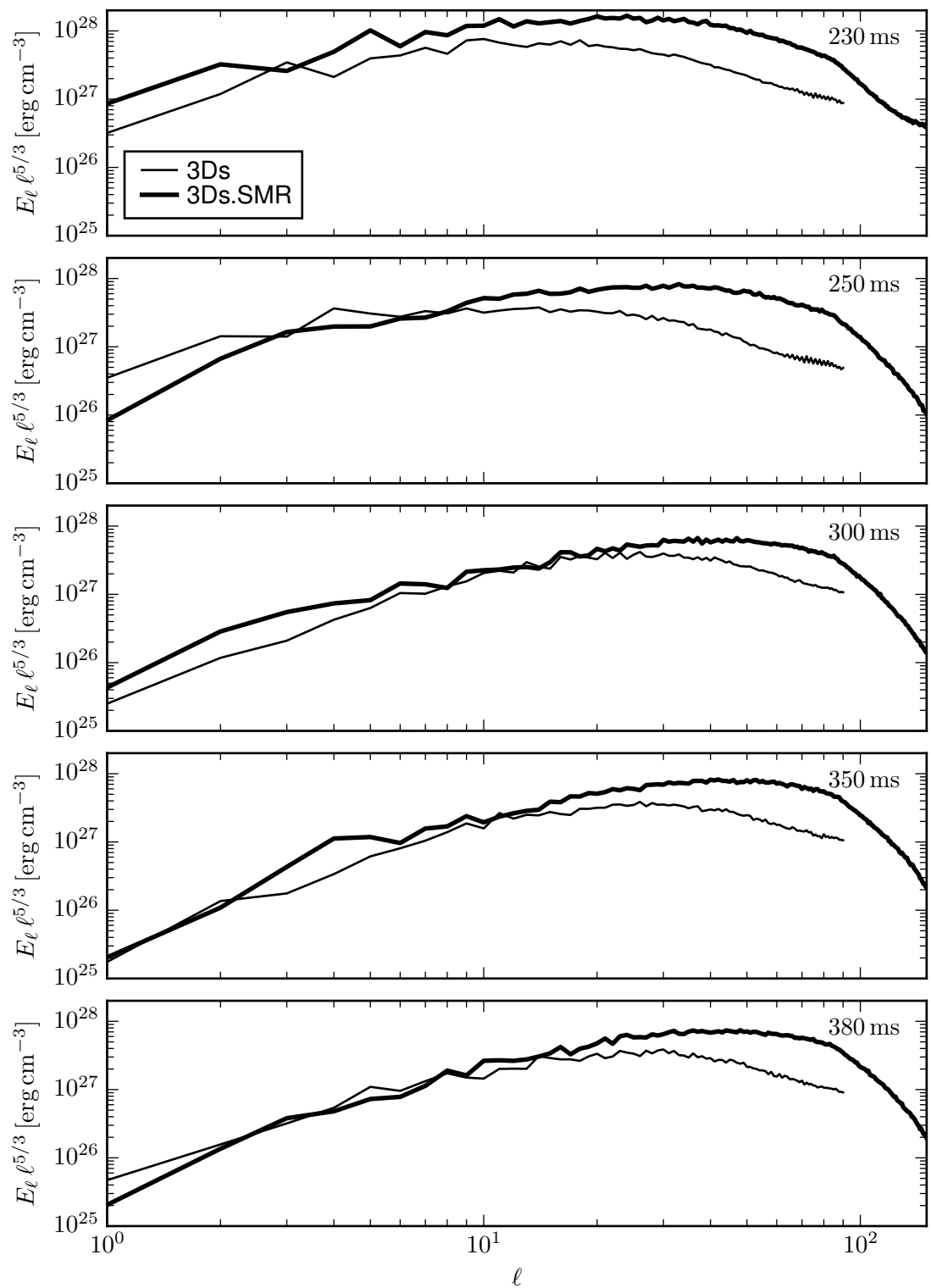


Fig. 6.13.: Same as Fig. 6.11, but multiplied with a factor $\ell^{5/3}$.

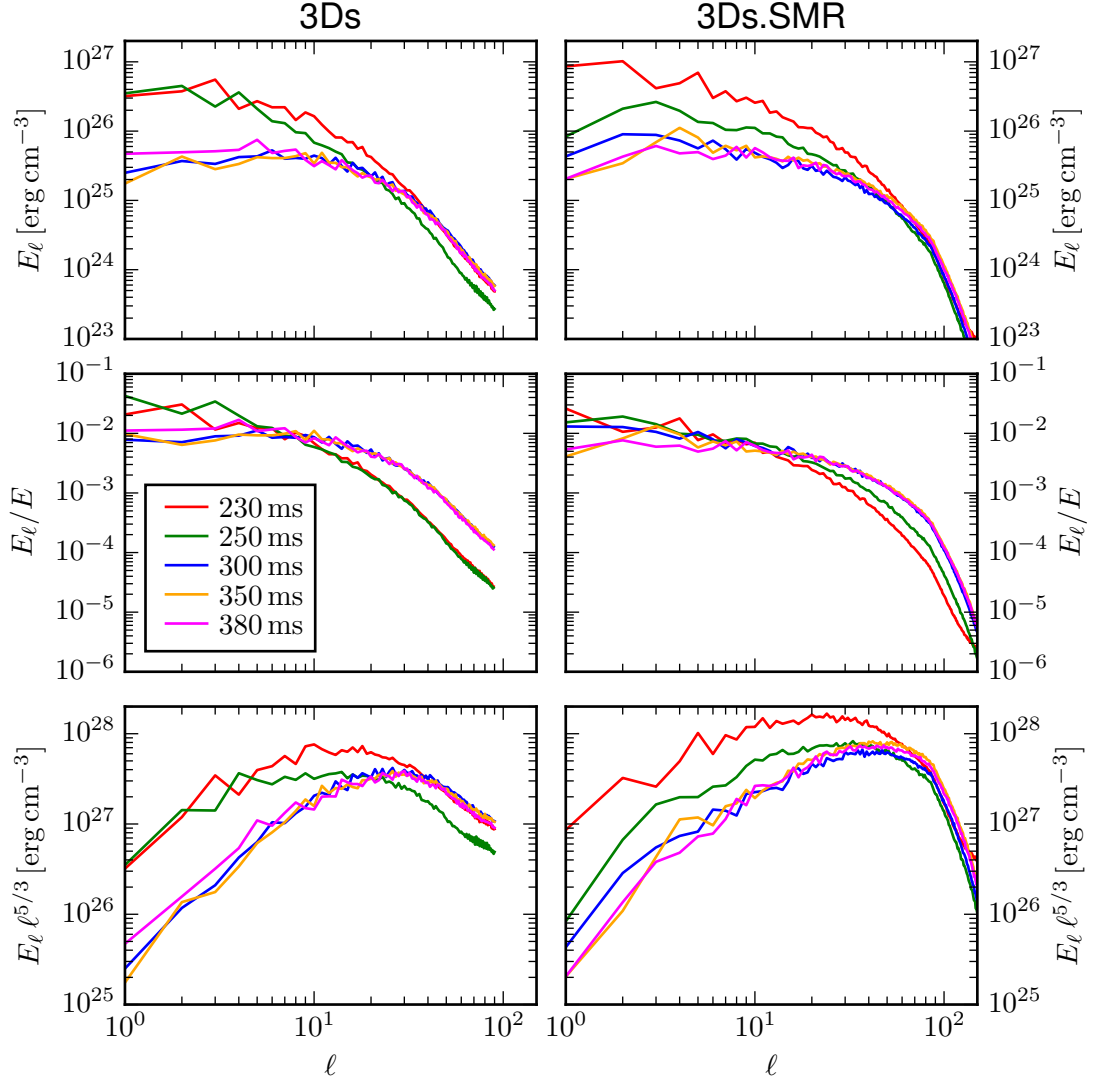


Fig. 6.14.: Kinetic energy spectra E_ℓ (*upper panels*), normalized spectra E_ℓ/E (*middle panels*), and rescaled spectra $E_\ell \ell^{5/3}$ (*lower panels*) for the model 3Ds (*left panels*) and the model 3Ds.SMR (*right panels*) at five different times after bounce.

which is the dominant part, is not shown in Figs. 6.11 and 6.14. Especially the SASI spiral mode in the model 3Ds.SMR has a large monopolar contribution.

We can estimate the multipole order of the largest eddies ℓ_L from simple considerations about their size. The largest possible extent of turbulent structures in the gain layer is

$$L = \langle R_{\text{sh}} \rangle - \langle R_{\text{gain}} \rangle. \quad (6.21)$$

As explained, for example, by Foglizzo et al. (2006), this can be translated into a multipole order according to

$$\ell_L = \frac{\pi R_0}{L}. \quad (6.22)$$

For both 3D models, we find that $\ell_L \approx 3$ between 250 to 380 ms after bounce. Indeed,

the energy spectra peak at $2 \lesssim \ell \lesssim 4$ indicating that kinetic energy is injected in this range.

From 230 to 300 ms post bounce, E_ℓ decreases drastically at large scales, i.e. at low ℓ , and increases at small scales. After 300 ms, the energy spectra remain relatively constant. This behavior can be observed in both 3D models and is related to the temporal evolution of the shock radii. Steady-state turbulence, which is a key assumption of Kolmogorov's theory, seems to be established during phases of shock stagnation without large oscillations caused by the SASI.

In order to further investigate how the spectra evolve with time, we normalize them to the total kinetic energy density on the spherical shell located at the radius R_0 (see Fig. 6.12 and middle panels of Fig. 6.14). As already mentioned before, the amount of kinetic energy at small scales grows in both 3D models until 300 ms after bounce. While in the simulation 3Ds, the increase happens quickly between 250 and 300 ms, kinetic energy is accumulated at small scales more continuously in the case 3Ds.SMR.

An important aspect of Kolmogorov's theory of turbulence is the presence of a $k^{-5/3}$ scaling in the inertial range of the energy spectrum. As we will show below, this translates into an $\ell^{-5/3}$ behavior in our decomposition. Hence, we rescale the spectra as $E_\ell \ell^{5/3}$ in Fig. 6.13 and in the lower panels of Fig. 6.14. The inertial range is then visible as horizontal parts of the rescaled spectra.

Indeed, we can well identify the inertial range of the turbulent energy cascade in our 3D models. At 300 ms, for example, it spans an interval of $15 \lesssim \ell \lesssim 40$ in the model 3Ds and $25 \lesssim \ell \lesssim 70$ in the model 3Ds.SMR. In the high-resolution simulation, the identification of the inertial range is easier, because the dissipation range at smaller scales is nicely visible with its much steeper slope of ℓ^{-7} for $\ell \gtrsim 80$. The dissipation range in the model 3Ds is shallower with an ℓ^{-3} behavior and starts at $\ell \approx 40$.

The value of ℓ , above which kinetic energy is dissipated into internal energy, depends on the grid resolution. In the high-resolution 3D model with a grid spacing of 1° in the gain layer, it is approximately twice as large as in the simulation with an angular resolution of 2° . For both cases, dissipation sets in at a level of a few grid cells. According to Porter et al. (1998) and Sytine et al. (2000), the piecewise parabolic method (PPM; Colella & Woodward, 1984) that is applied in VERTEX-PROMETHEUS dissipates kinetic energy below 2 to 12 grid cells, which is roughly consistent with our estimate.

To sum up, there is evidence that Kolmogorov's theory of steady-state isotropic turbulence can be applied during phases of stock stagnation, in which the SASI does not pump kinetic energy into the lowest modes $\ell \lesssim 2$. In the high-resolution simulation, we see a clear separation between the inertial range with its characteristic slope of $-5/3$ and the dissipation range with a steeper decay.

6.2.4. Numerical viscosity and effective Reynolds number

The kinematic viscosity in the gain layer is of the order of $0.1 \text{ cm}^2 \text{ s}^{-1}$ and thus extremely low (Abdikamalov et al., 2015). We do not include this viscosity explicitly in the equations that are solved for describing the evolution of the fluid (cf. Sect. 2.1). This is because the viscosity implicitly given by the numerical scheme is orders of magnitude larger than the kinematic viscosity (see., e.g., Müller, 1998). Like in all other state-of-the-art core-collapse supernova models, we rely on the implicit large eddy simulation (ILES; Grinstein et al., 2007) paradigm. It assumes that dissipative effects at the

smallest scales are implicitly covered by the numerical viscosity. Instead of solving filtered hydrodynamic equations and creating a sub-grid model for the dissipation of kinetic energy (Boris et al., 1992), the ILES approach assumes that such a sub-grid model is implicitly included at the level of the grid cell size.

Estimating the effective viscosity of a numerical scheme ν_N is difficult. It depends not only on the algorithm itself, but also on its implementation. Even if the numerical viscosity is known for one simulation code, it is not justified to assume an equal viscosity for all codes that make use of the same algorithm for treating the hydrodynamics. Consequently, the numerical viscosity and the effective Reynolds number must be determined for every code separately in order to estimate the influence of dissipative effects. This can only be achieved by measuring characteristic quantities from the output data.

In the following two sections, we will discuss two methods for determining the numerical viscosity and the effective Reynolds number from properties of the kinetic energy spectrum. Both approaches will be applied to our 3D simulations. The first procedure was proposed by Abdikamalov et al. (2015), while the second method has been developed by us and is presented here for the first time. As in the previous section, the energy spectra are averaged over 10 km and 5 ms, and measured at a radius R_0 between the angle-averaged gain radius and the minimum shock radius.

Based on the Taylor microscale

The method of Abdikamalov et al. (2015) is based on determining the so-called Taylor microscale, which is given by (Frisch, 1995; Pope, 2000)

$$\lambda = \sqrt{\frac{5E}{Z}}, \quad (6.23)$$

where E is the total kinetic energy density of non-radial fluid motions,

$$E \approx \sum_{\ell=0}^{\ell_{\max}} E_\ell, \quad (6.24)$$

and Z is the enstrophy, which can be approximated by

$$Z = \frac{1}{R_0^2} \sum_{\ell=0}^{\ell_{\max}} \ell(\ell+1) E_\ell. \quad (6.25)$$

For the upper bound ℓ_{\max} , Abdikamalov et al. (2015) picked a value of 120, while we calculate it from the angular resolution of the model (see Eq. (6.20)).

The Taylor microscale λ has no direct physical interpretation. It is situated somewhere between the characteristic scale of the smallest eddies – the Kolmogorov scale – and the size of the largest structures (Pope, 2000).

Abdikamalov et al. (2015) derived a relation for the effective Reynolds number,

$$\text{Re} = 5 \frac{\tilde{L}^2}{\lambda^2}, \quad (6.26)$$

which is, however, not consistent with the literature. Commonly, a factor of 10 (Pope, 2000; Schmidt, 2014) or even 15 (Tennekes & Lumley, 1972) instead of 5 is applied.

| t_{pb} [ms] | 3Ds | | | 3Ds.SMR | | |
|----------------------|------|---|------------------|---------|---|------------------|
| | Re | ν_N [$10^{13} \text{ cm}^2 \text{ s}^{-1}$] | \tilde{L} [km] | Re | ν_N [$10^{13} \text{ cm}^2 \text{ s}^{-1}$] | \tilde{L} [km] |
| 230 | 49.2 | 50 | 71 | 61.4 | 58 | 63 |
| 250 | 45.6 | 79 | 82 | 60.3 | 50 | 57 |
| 300 | 49.8 | 42 | 54 | 56.4 | 39 | 45 |
| 350 | 49.9 | 47 | 57 | 57.7 | 33 | 39 |
| 380 | 48.7 | 57 | 59 | 59.3 | 35 | 41 |

Tab. 6.1.: Effective Reynolds numbers Re, numerical viscosities ν_N , and energy-containing scales \tilde{L} of the 3D models for different times after core bounce computed using the method of Abdkamalov et al. (2015).

Nevertheless, in order to compare with the results of Abdkamalov et al. (2015), we also use their factor 5 here. At the end of this section, we will further discuss this issue.

The size of the energy-containing eddies \tilde{L} is calculated by Abdkamalov et al. (2015) from the energy spectrum according to

$$\tilde{L} = \pi R_0 \left(1 + \frac{1}{E} \sum_{\ell=0}^{\ell_{\max}} \ell E_\ell \right)^{-1}. \quad (6.27)$$

Finally, the numerical viscosity can be determined from the fundamental relation

$$\nu_N = \frac{v_0 \tilde{L}}{\text{Re}}. \quad (6.28)$$

The characteristic velocity of the largest eddies is deduced from the total kinetic energy density by

$$E = \frac{1}{2} \rho_0 v_0^2. \quad (6.29)$$

Note that also E , ρ_0 , and v_0 are averaged over a radius interval of 10 km and a time range of 5 ms.

In Tab. 6.1, we present the Reynolds numbers and numerical viscosities of both 3D simulations calculated with the method of Abdkamalov et al. (2015). Our Reynolds numbers are compatible with the values of their “ULR” and “LR” cases, which have an angular resolution of 2.16° and 1.08° , respectively. In the model 3Ds.SMR, Re is only 15–30% larger compared to the case 3Ds. This is unexpected, since an increase of the angular resolution by a factor of two should enhance the Reynolds number by a similar factor. Furthermore, also the absolute values of the Reynolds numbers seem to be too low compared to other results discussed in the literature. Keil et al. (1996) estimated a value of $\text{Re} \gtrsim 2000$ for 2D simulations of 1.5° resolution performed with PROMETHEUS based on a systematic study of Porter & Woodward (1994).

The method of Abdkamalov et al. (2015) suffers from the uncertainty of Eq. (6.26). Its application is debatable, because there might be a factor of 2 or even 3 missing. This issue will be discussed later in this section.

For the mentioned reasons, we have developed a different procedure, which yields more realistic values of the numerical viscosity and the effective Reynolds number.

Based on the energy dissipation rate

Our method for measuring the numerical viscosity and the Reynolds number is based on more fundamental properties of the turbulent energy cascade. In the inertial range, the kinetic energy spectrum only depends on the energy dissipation rate ε and is given by (Landau & Lifshitz, 1987; Pope, 2000)

$$\mathcal{E}_k = C \varepsilon^{2/3} k^{-5/3}. \quad (6.30)$$

In order to be consistent with the literature, we employ the spectrum of the specific kinetic energy as defined in Eq. (6.17) rather than of the kinetic energy density. The factor C is a universal constant of $C = 1.62$ and independent of the Reynolds number (Sreenivasan, 1995; Yeung & Zhou, 1997).

Since we decompose the spectrum by use of spherical harmonics, it must be written as a function of the multipole order ℓ instead of the wave number k . This transformation reads

$$k = \frac{\sqrt{\ell(\ell+1)}}{R_0} \approx \frac{\ell}{R_0}, \quad (6.31)$$

where the latter approximation is valid for sufficiently high values of ℓ . The energy spectrum as a function of k ,

$$\mathcal{E}_k dk = C \varepsilon^{2/3} k^{-5/3} dk, \quad (6.32)$$

can then be written as

$$\mathcal{E}_\ell d\ell = C \varepsilon^{2/3} R_0^{5/3} \ell^{-5/3} \frac{d\ell}{R_0}. \quad (6.33)$$

From this relation, we obtain an equation for the energy dissipation rate,

$$\varepsilon(\ell) = \sqrt{\frac{\mathcal{E}_\ell^3 \ell^5}{R_0^2 C^3}}, \quad (6.34)$$

which allows for directly measuring its value from the spectrum. Together with the specific enstrophy \mathcal{Z} calculated according to

$$\mathcal{Z} = \frac{1}{R_0^2} \sum_{\ell=0}^{\ell_{\max}} \ell(\ell+1) \mathcal{E}_\ell, \quad (6.35)$$

we can determine the numerical viscosity from the equation (Tennekes & Lumley, 1972; Pope, 2000)

$$\nu_N = \frac{\varepsilon}{2\mathcal{Z}}. \quad (6.36)$$

Note that the enstrophies defined in Eqs. (6.25) and (6.35) are connected to each other by the relation $Z \approx \rho_0 \mathcal{Z}$, which becomes exact for $\ell_{\max} \rightarrow \infty$.

In Fig. 6.15, we present ε as a function of ℓ for both 3D simulations. The maximum value of the energy dissipation rate is much larger in the model 3Ds.SMR compared to the case 3Ds. It is also shifted to smaller scales in the high-resolution run, because the inertial range is moved to higher ℓ .

The question arises, at which multipole order ℓ the energy dissipation rate should be measured for our purposes. Given Eq. (6.36), the most conservative approach is taking

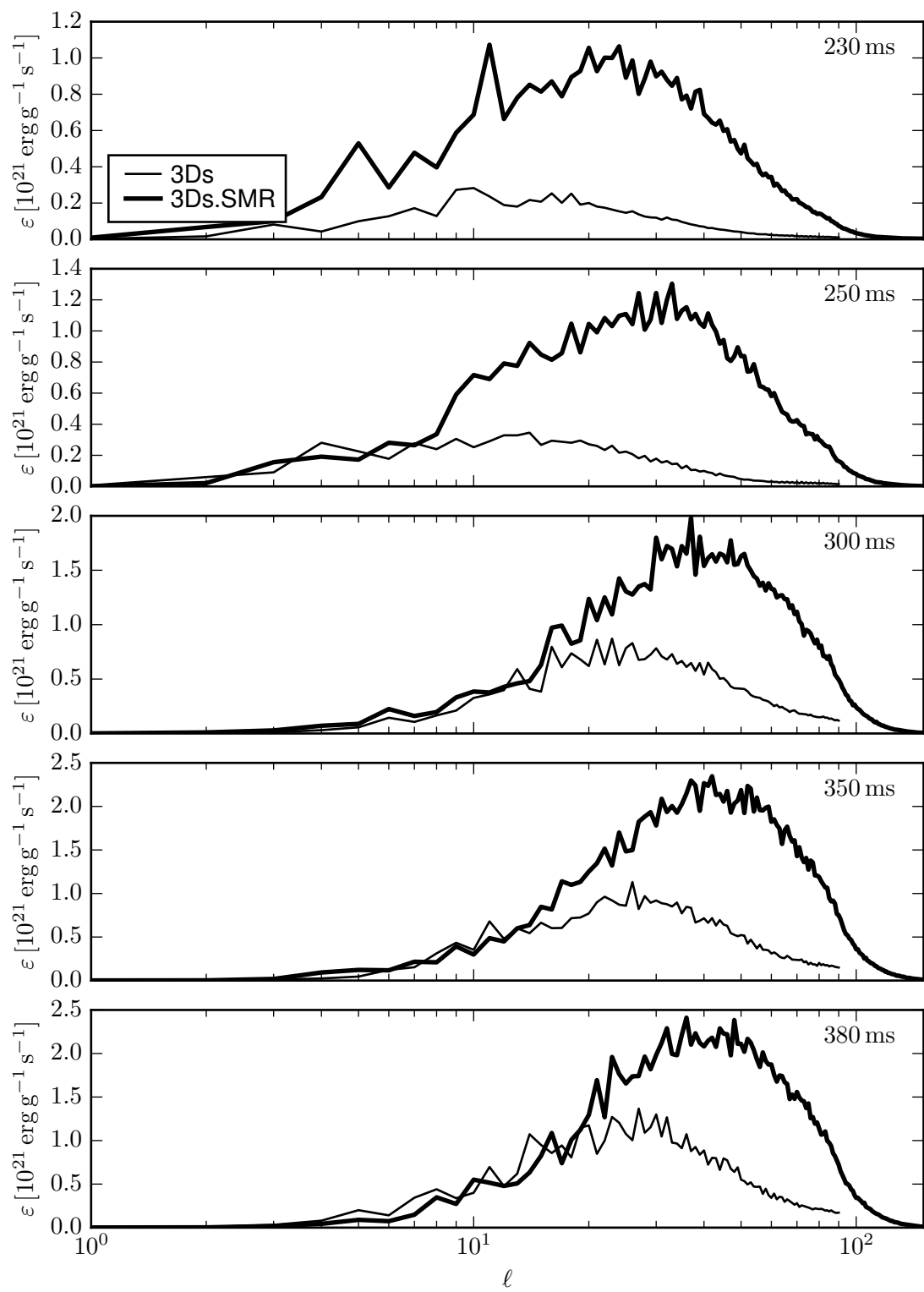


Fig. 6.15.: Energy dissipation rates ε computed according to Eq. (6.34) for both 3D models at different times after core bounce.

| t_{pb} [ms] | 3Ds | | | 3Ds.SMR | | |
|----------------------|--------|---|----------|---------|---|----------|
| | Re | ν_N [$10^{13} \text{ cm}^2 \text{ s}^{-1}$] | L [km] | Re | ν_N [$10^{13} \text{ cm}^2 \text{ s}^{-1}$] | L [km] |
| 230 | 443.5 | 2.5 | 32 | 1309.4 | 2.3 | 54 |
| 250 | 1024.2 | 3.0 | 71 | 1882.7 | 2.7 | 97 |
| 300 | 1084.4 | 3.4 | 94 | 1936.1 | 3.2 | 124 |
| 350 | 1219.7 | 4.2 | 119 | 1977.8 | 2.6 | 104 |
| 380 | 1776.5 | 4.6 | 171 | 1888.7 | 2.8 | 101 |

Tab. 6.2.: Effective Reynolds numbers Re, numerical viscosities ν_N , and energy-containing scales L of the 3D models for different times after core bounce computed with our new approach.

the peak value of ε , because we want to maximize the numerical viscosity, which is known to be large.

Ultimately, we can calculate the effective Reynolds number as

$$\text{Re} = \frac{v_0 L}{\nu_N} \quad (6.37)$$

with v_0 being the characteristic velocity of the largest eddies given by

$$v_0^2 = \int d\Omega (v_\theta^2 + v_\phi^2). \quad (6.38)$$

In contrast to the previous method, L is assumed to be equal to the diameter of the gain layer as already defined in Eq. (6.21).

The Reynolds numbers and numerical viscosities based on the measured energy dissipation rates are shown in Tab. 6.2. With our method, we obtain values for Re that are more consistent with other results for PROMETHEUS documented in the literature (Keil et al., 1996). In the high-resolution simulation, the Reynolds numbers reach values of more than 1900 and are 60–85% larger than in the model with lower angular resolution. Only at 380 ms, Re becomes very high in the exploding simulation 3Ds, because the size of the gain layer grows as the shock propagates outwards and L is therefore boosted to unrealistic values.

During the phase of shock stagnation and ceased SASI activity in the model 3Ds.SMR, i.e. after 250 ms, both the Reynolds numbers and the numerical viscosities remain relatively constant. This indicates that the turbulent cascade is in a steady-state regime during this stage. We do not see evidence that the scaling relations of classical turbulence theory might not be applicable there.

Comparison of the methods

The two approaches described above yield Reynolds numbers and numerical viscosities that differ significantly. In order to analyze, why this is the case, we divide Eqs. (6.26) and (6.28) by Eqs. (6.37) and (6.36), i.e. we divide the values calculated with the method of Abdikamalov et al. (2015) by the values obtained with our procedure. The ratio of the Reynolds numbers reads

$$R_{\text{Re}} := \frac{\text{Re}^{\text{Abdikamalov}}}{\text{Re}^{\text{ours}}} = \frac{\varepsilon \tilde{L}^2}{v_0^3 L} \quad (6.39)$$

and the ratio of the numerical viscosities is given by

$$R_{\nu_N} := \frac{\nu_N^{\text{Abdikamalov}}}{\nu_N^{\text{ours}}} = \frac{v_0^3}{\varepsilon \tilde{L}}. \quad (6.40)$$

Ideally, both quantities – R_{Re} and R_{ν_N} – should be unity. Currently, the ratio R_{Re} is too low, while R_{ν_N} is too large. As a consequence, ε and \tilde{L} are probably underestimated, whereas L and v_0 are presumably overestimated.

The energy dissipation rate ε is directly measured from the energy spectrum according to Eq. (6.34). The only term in Eq. (6.34) being not precisely known is the constant C . However, it was determined to satisfying accuracy and even the largest possible reduction of C within the error bars mentioned by Sreenivasan (1995) would enhance ε by only 18%. For the proposed best value of C , we have measured the peak amplitude of $\varepsilon(\ell)$ to maximize the numerical viscosity. Hence, we conclude that a significant underestimation of the energy dissipation rate is unlikely.

Concerning the length scales of the largest turbulent eddies, it could well be that the value \tilde{L} of Abdikamalov et al. (2015) is too low and our value of L is too large. The calculated values of L are often more than a factor of two greater than \tilde{L} . The true size of the largest eddies is probably between both scales. However, since the ratios R_{Re} and R_{ν_N} depend more strongly on \tilde{L} than on L , an underestimation of \tilde{L} in the approach of Abdikamalov et al. (2015) has a large influence on the results. Unfortunately, the authors did not mention the origin of their Eqs. (29) and (30) for calculating \tilde{L} , which we have cited in Eq. (6.27). Determining the length scale from the spectral shape in this way is unreasonable, because the size of the largest eddies should not depend on the grid resolution. As shown above, the energy injection scale is equal in both 3D simulations providing further evidence that the energy-containing eddies have a universal size independent of the grid spacing. Solely the extent of the gain layer constraints the diameter of the largest turbulent structures, which is exactly the motivation for our choice of L in Eq. (6.21).

Also an overestimation of the characteristic velocity v_0 of the largest eddies could contribute to the discrepancy of the two approaches. In both methods, v_0 is calculated employing Eq. (6.38). Even slightly exaggerated values would boost the ratios R_{Re} and R_{ν_N} significantly. This could happen, for example, if the non-radial velocity components v_θ and v_ϕ did not only describe perturbations around zero, but a global rotational motion existed.

Besides these considerations of over- and underestimated terms, the Reynolds numbers calculated with the approach of Abdikamalov et al. (2015) are generally too low. The factor 5 in Eq. (6.26) is questionable, because it is smaller than what is reported in the literature. Tennekes & Lumley (1972) formulated Eq. (6.26) in a different way,

$$\text{Re} = \frac{15}{A} \frac{\tilde{L}^2}{\lambda^2}, \quad (6.41)$$

where A is an “undetermined constant” of order one. Pope (2000) and Schmidt (2014) used $A = 3/2$, whereas Abdikamalov et al. (2015) and also Couch & Ott (2015) applied $A = 3$. Obviously, there is some ambiguity about the value of this constant. The Reynolds numbers of Abdikamalov et al. (2015) are thus presumably more than a factor of two too small. This highlights an important aspect of turbulence theory. Many equations are obtained from self-similarity considerations and therefore based

only on proportionalities. Scaling factors are then derived from further assumptions or they remain undetermined. Our approach for calculating the numerical viscosity relies on the fundamental relations of Kolmogorov's theory and avoids the usage of other equations. Although our obtained values of the Reynolds numbers might be slightly overestimated due to the dependency on v_0 and L , we are confident that the measured numerical viscosities are reliable.

6.3. Summary and discussion

We performed core-collapse supernova simulations of a $20 M_\odot$ star applying the VERTEX-PROMETHEUS neutrino-hydrodynamics code in full three dimensions (3D) with the aim of investigating effects caused by an increased grid resolution. Axisymmetric models were also considered, but not pursued further because of the large stochastic scatter of their shock radii. Our reference 3D model is the exploding simulation 3Ds discussed in Chapt. 5, which was computed on the standard spherical polar grid with an angular resolution of 2° in the entire computational domain. For the high-resolution 3D model 3Ds.SMR, we applied our newly-developed static mesh refinement technique on the Yin-Yang grid, with an angular resolution of 2° below the gain radius. Slightly above, the grid spacing was set to 1° and further refined to 0.5° outside of 160 km.

After the arrival of the Si/Si+O shell interface, the high-resolution 3D model exhibits a larger angle-averaged shock radius, a higher turbulent kinetic energy in the gain layer, and a larger turbulent pressure compared to the model 3Ds. The ratio of advection and heating timescales exceeds unity earlier and rises continuously to a value of about 1.3. A strong SASI spiral mode is present, which – in contrast to the sloshing mode in the simulation 3Ds – supplies a high non-radial kinetic energy. The energy deposition in the gain layer by neutrino heating is slightly larger in the simulation 3Ds.SMR.

All these diagnostic quantities indicate that the simulation 3Ds.SMR should explode earlier and more robustly than the model 3Ds. This is, however, not the case. Shock revival has not occurred in the high-resolution simulation until 380 ms post bounce, although the explosion of the model 3Ds is already on its way at that time. An enhanced transport of kinetic energy from the shock to the gain radius seems to be the reason for the hindered shock revival in the case 3Ds.SMR, despite a higher turbulent pressure. Couch & Ott (2015) claimed that such an additional pressure contribution is beneficial for shock revival. Even though the shock radius is pushed to larger radii in our high-resolution simulation, the enhanced Reynolds stress is not sufficient to trigger an explosion.

The entropy distribution in the gain layer reveals finer structures in the case 3Ds.SMR, because the kinetic energy cascade is extended to smaller scales. In this model, the inertial range with the classical $-5/3$ scaling is clearly separated from the dissipation range. Energy is injected at a multipole order $\ell \approx 3$ in both 3D models. Their energy spectra remain relatively constant after 300 ms post bounce, which indicates that steady-state turbulence is established in this phase. During periods of shock stagnation without SASI oscillations, the classical turbulence theory based on Kolmogorov's assumptions seems to be applicable in our models. We thus do not agree with Couch & Ott (2015), who argued that Kolmogorov's theory might be generally inappropriate for describing turbulence during the stalled-shock phase because of the directed accretion flow through the gain layer.

For the first time, we measured the numerical viscosities and the effective Reynolds numbers in 3D simulations performed with VERTEX-PROMETHEUS. We applied the procedure of Abdikamalov et al. (2015) based on determining the Taylor microscale. However, this method is questionable, because it yielded implausibly low Reynolds numbers due to inconsistencies and uncertainties in their formulae. Consequently, we developed a new approach based on the fundamental equations of turbulence theory. It relies on measuring the energy dissipation rate from the kinetic energy spectrum and directly relates this to the numerical viscosity. With the new method, we obtained Reynolds numbers of $\gtrsim 1900$ in the model 3Ds.SMR that are consistent with the literature. As expected, the high-resolution run exhibits higher Reynolds numbers and lower numerical viscosities.

Our high-resolution 3D simulation has not exploded until 380 ms post bounce, while the corresponding reference model computed on a coarser grid exploded successfully. Although it might be that the temporal evolution of the simulation 3Ds.SMR is stochastic and an explosion will commence soon, we assume that it will eventually fail. One should, however, be cautious in interpreting this result as a trend that a high grid resolution impedes an explosion. A clear resolution dependence cannot be deduced from two single 3D models, especially because the success of the high-resolution simulation is still uncertain. In any case, further analysis is required in terms of the unfavorable kinetic energy transport in the gain layer that seems to be the reason for the failure of the model 3Ds.SMR.

7. Conclusions

In this work, we presented the first successfully exploding three-dimensional (3D) core-collapse supernova simulations performed with the elaborate neutrino-hydrodynamics code VERTEX-PROMETHEUS. This is an important milestone of supernova modeling, because it demonstrates that neutrino-driven explosions can be obtained in 3D with sophisticated neutrino transport and state-of-the-art neutrino interactions. Successful 3D explosions were obtained before, however, with more simplified neutrino transport schemes compared to ours (Takiwaki et al., 2012, 2014; Lentz et al., 2015; Müller, 2015).

On the basis of a zero-metallicity $9.6 M_{\odot}$ progenitor star, we demonstrated that explosions in 3D can become more energetic than their axisymmetric (2D) counterparts, because the turbulent transport of kinetic energy is fundamentally different in 2D and 3D. Energy cascades to smaller scales in 3D, whereas it is accumulated at large scales in 2D. Turbulent energy transport to small scales in 3D can weaken downflows, which penetrate into the cooling layer with lower velocities. The consequent reduced dissipation of their kinetic energy diminishes the efficiency of neutrino cooling, which boosts the explosion energy to a 10% higher value compared to the 2D case. This is particularly important, because explosion energies obtained in 2D simulations are often at the lower end of the observed value range (Marek & Janka, 2009; Suwa et al., 2010; Müller et al., 2012a,b; Bruenn et al., 2013; Nakamura et al., 2015; Suwa et al., 2016). Nevertheless, it must be noted that the final saturated explosion energies cannot be deduced from self-consistent models at the moment, because it is computationally unaffordable to evolve them for sufficiently long time – especially in 3D.

Preceding works argued that there is a tendency for 3D models to explode less readily than their 2D counterparts, which was likewise attributed to the different characteristics of the turbulent energy cascade in 2D and 3D (e.g., Hanke et al., 2012; Couch & O’Connor, 2014; Takiwaki et al., 2014; Lentz et al., 2015). However, a general disadvantage of the third spatial dimension for energetic core-collapse supernova explosions was disproved with our study. A similar result was presented by Müller (2015), who also found a higher explosion energy in 3D compared to 2D for an $11.2 M_{\odot}$ progenitor. This demonstrates that our 3D model is not an isolated case with respect to its difference to 2D. The question whether heavier progenitor stars could also explode more energetically in 3D can hardly be answered at this stage and requires further investigation.

Previously failed 3D simulations of Hanke et al. (2013), Tamborra et al. (2013), Hanke (2014), and Tamborra et al. (2014a,b) performed with the VERTEX-PROMETHEUS code were already close to the explosion threshold. We demonstrated this by including theoretically and experimentally motivated strange-quark contributions to the nucleon spin (Horowitz, 2002) in a non-exploding 3D model of a $20 M_{\odot}$ star, which then yielded a successful explosion. The strangeness correction of the axial-vector coupling coefficient reduces the neutrino-nucleon scattering opacities at a 10% level mainly below the proto-neutron star surface. Besides the direct enhancement of the luminosities of electron neutrinos and electron antineutrinos, there is a crucial indirect effect. A higher energy loss by the emission of heavy-lepton neutrinos leads to a faster contraction of the proto-

neutron star. The neutrinospheres of all species are therefore shifted inwards to higher temperatures, so that their luminosities and mean energies are increased considerably. This leads to an enhanced energy deposition in the gain layer by neutrino heating and provides more favorable conditions for shock revival.

Hobbs et al. (2016) argued that our chosen value for the strangeness correction was too extreme compared to measurements and theoretical predictions. However, other effects exist that reduce the cross sections of neutrino-nucleon scattering in a similar way as the strangeness correction, for example, correlations in low-density nucleon matter (Horowitz, 2016). We did not claim that the strangeness correction is *the* missing ingredient for robust 3D explosions and that strange-quark contributions have to be included in future simulations. Instead, we emphasized that a profound knowledge of the neutrino opacities is indispensable for accurately simulating neutrino-driven core-collapse supernovae.

We took a first step towards high-resolution 3D simulations with our tool, VERTEX-PROMETHEUS, by implementing a novel refinement procedure for the computational grid. The first application of the new mesh did not give rise to shock revival until the end of the still ongoing simulation, although the model on the coarser grid exploded successfully and the important diagnostic quantities suggested a positive outcome. An enhanced transport of kinetic energy away from the shock seems to be the reason for the potential failure of the high-resolution model, assessed on the basis of the current state of the simulation. We analyzed the turbulent energy spectrum and found indications from which we concluded that Kolmogorov's theory of steady-state and isotropic turbulence is applicable during the stalled-shock phase. Our findings are in contrast to the discussion of Couch & Ott (2015), who speculated that the classical description of turbulence might not be appropriate because of the directed accretion flow through the gain layer and the time-dependence of the accretion rate.

It was found in numerous studies that explosions in 3D are delayed if the resolution of the computational grid is increased (Hanke et al., 2012; Couch & O'Connor, 2014; Takiwaki et al., 2014; Abdikamalov et al., 2015; Roberts et al., 2016). This was originally attributed to a trapping of kinetic energy at large scales occurring in less resolved simulations (Abdikamalov et al., 2015; Radice et al., 2015, 2016). Later, this argument was retracted by Roberts et al. (2016), so that a thorough understanding is still lacking. From the latter works, a clear resolution dependence of the diagnostic quantities, such as the shock radius, cannot be deduced. Neither did we make a statement about how the resolution influences the conditions for shock revival based on our two 3D models, because the statistical significance is too low and the final outcome of our high-resolution 3D simulation is still uncertain. Nevertheless, it is clear that current core-collapse supernova simulations are not converged in the sense that reducing the grid spacing does not alter the results. That is why further resolution studies with sophisticated neutrino transport are required.

In order to quantify the amount of numerical dissipation in VERTEX-PROMETHEUS, we developed a method for determining the numerical viscosity based on measuring the energy dissipation rate from the turbulent spectrum. Our calculated effective Reynolds numbers are compatible with other results reported in the literature, but far from their physical values being expected in the gain layer. This was also observed by Abdikamalov et al. (2015), who used a different method for determining the Reynolds numbers that, however, presumably underestimates their values. It is still under debate what spatial

resolution is required in order to accurately model the core-collapse supernova explosion mechanism and regard simulations as converged.

The ultimate goal of supernova modelers is to achieve robust explosions in 3D simulations with consistent values of all essential observables. With this work, we have shown that explosions can indeed be achieved in 3D with sophisticated neutrino transport and that their explosion energies are not necessarily below the values obtained in 2D simulations. A prerequisite for further progress is, however, that uncertainties in current supernova models are eliminated – such as inaccuracies of neutrino opacities – and that the numerical treatment is verified in resolution studies. Other ingredients for core-collapse supernova simulations were not discussed in this work but also need to be considered, for example, uncertainties in the high-density equation of state (see, e.g., Fischer et al., 2014; Lattimer & Prakash, 2016), effects of rotation (Iwakami et al., 2014; Nakamura et al., 2014), and large-scale perturbations in the progenitor star before collapse (Arnett & Meakin, 2011; Couch & Ott, 2013; Müller & Janka, 2015; Couch et al., 2015). All in all, the first successful 3D explosions awaken the hope that a thorough understanding of the neutrino-driven mechanism comes within reach.

Appendix

A. Aitoff projection

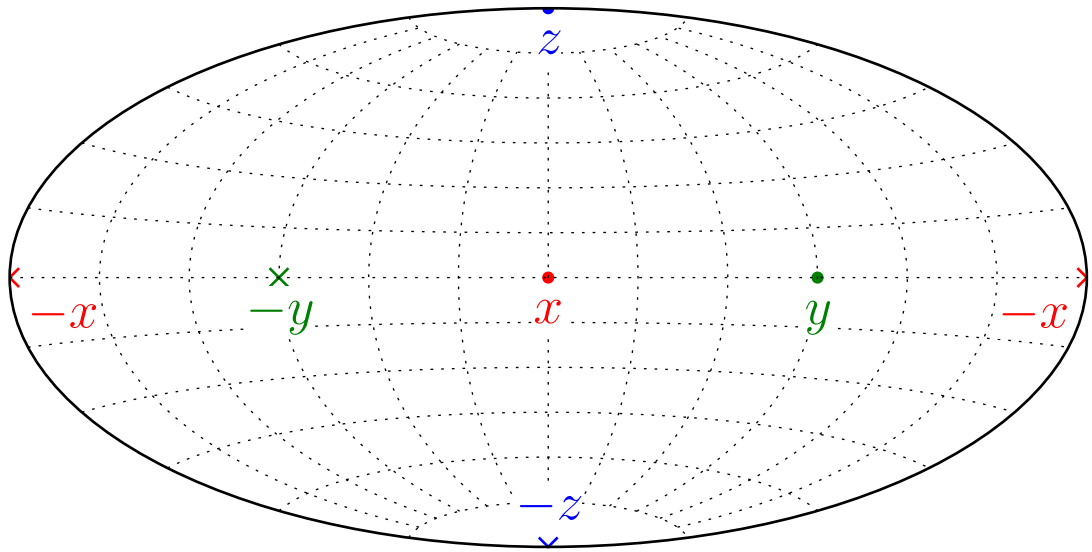


Fig. A.1.: Positions of the coordinate axes x (red), y (green), and z (blue) in the Aitoff projection. Unit vectors pointing towards and away from the reader are marked by dots and crosses, respectively. The dotted mesh shows lines of constant longitude and latitude, respectively.

For displaying all-sky maps in this work, we select the projection introduced by David Aitoff. The orientation of the Cartesian coordinate axes is defined such that the point $(1, 0, 0)$ has the angular coordinates $\theta = \pi/2$ and $\phi = 0$. In Fig. A.1, the orientation of the axes is shown in our chosen definition. The angular positions of the points $(1, 0, 0)$, $(0, 1, 0)$, and $(0, 0, 1)$ are marked by dots, whereas their negative counterparts are depicted with crosses.

List of abbreviations

| | |
|-------|---|
| 1D | One-dimensional, i.e. spherically symmetric |
| 2D | Two-dimensional, i.e. axially symmetric |
| 3D | Three-dimensional |
| CFL | Courant-Friedrichs-Lowy criterion (Courant et al., 1928) |
| EOS | Equation of state |
| LESA | Lepton-number emission self-sustained asymmetry (Tamborra et al., 2014a) |
| LS220 | High-density equation of state by Lattimer & Swesty (1991) with a nuclear incompressibility parameter of 220 MeV |
| NSE | Nuclear statistical equilibrium |
| PNS | Proto-neutron star |
| SASI | Standing accretion-shock instability (Blondin et al., 2003) |
| SMR | Static mesh refinement (see Sect. 3.3) |

Bibliography

- Abbott, B. P., Abbott, R., Abbott, T. D., et al. 2016, e-print, arXiv:1605.01785
- Abdikamalov, E., Ott, C. D., Radice, D., et al. 2015, ApJ, 808, 70
- Arnett, W. D., Bahcall, J. N., Kirshner, R. P., & Woosley, S. E. 1989, ARA&A, 27, 629
- Arnett, W. D., & Meakin, C. 2011, ApJ, 733, 78
- Baade, W., & Zwicky, F. 1934, PNAS, 20, 254
- Bethe, H. A. 1990, RvMP, 62, 801
- Bethe, H. A., & Wilson, J. R. 1985, ApJ, 295, 14
- Blondin, J. M., & Mezzacappa, A. 2007, Nature, 445, 58
- Blondin, J. M., Mezzacappa, A., & DeMarino, C. 2003, ApJ, 584, 971
- Boffetta, G., & Musacchio, S. 2010, PhRvE, 82, 016307
- Boris, J. P., Grinstein, F. F., Oran, E. S., & Kolbe, R. L. 1992, FlDyR, 10, 199
- Bruenn, S. W. 1985, ApJS, 58, 771
- Bruenn, S. W., & Mezzacappa, A. 1997, PhRvD, 56, 7529
- Bruenn, S. W., Mezzacappa, A., Hix, W. R., et al. 2009, in American Institute of Physics Conference Series, Vol. 1111, Proceedings of the International Conference on Probing Stellar Populations Out to the Distant Universe, ed. G. Giobbi, A. Tornambe, G. Raimondo, M. Limongi, L. A. Antonelli, N. Menci, & E. Brocato, 593
- Bruenn, S. W., Mezzacappa, A., Hix, W. R., et al. 2013, ApJL, 767, L6
- Bruenn, S. W., Lentz, E. J., Hix, W. R., et al. 2016, ApJ, 818, 123
- Buras, R., Janka, H.-T., Keil, M. T., Raffelt, G. G., & Rampp, M. 2003, ApJ, 587, 320
- Buras, R., Janka, H.-T., Rampp, M., & Kifonidis, K. 2006a, A&A, 457, 281
- Buras, R., Rampp, M., Janka, H.-T., & Kifonidis, K. 2006b, A&A, 447, 1049
- Burrows, A. 2013, RvMP, 85, 245
- Burrows, A., Dolence, J. C., & Murphy, J. W. 2012, ApJ, 759, 5
- Burrows, A., & Goshy, J. 1993, ApJL, 416, L75

Bibliography

- Burrows, A., Hayes, J., & Fryxell, B. A. 1995, ApJ, 450, 830
- Burrows, A., & Sawyer, R. F. 1998, PhRvC, 58, 554
- . 1999, PhRvC, 59, 510
- Calhoun, D. A., Helzel, C., & Leveque, R. J. 2008, SIAMR, 50, 723
- Cernohorsky, J. 1994, ApJ, 433, 247
- Colella, P., & Woodward, P. R. 1984, JCoPh, 54, 174
- Colgate, S. A., & White, R. H. 1966, ApJ, 143, 626
- Couch, S. M. 2013, ApJ, 775, 35
- Couch, S. M., Chatzopoulos, E., Arnett, W. D., & Timmes, F. X. 2015, ApJL, 808, L21
- Couch, S. M., & O'Connor, E. P. 2014, ApJ, 785, 123
- Couch, S. M., & Ott, C. D. 2013, ApJL, 778, L7
- . 2015, ApJ, 799, 5
- Courant, R., Friedrichs, K., & Lewy, H. 1928, MatAn, 100, 32
- Dolence, J. C., Burrows, A., Murphy, J. W., & Nordhaus, J. 2013, ApJ, 765, 110
- Einfeldt, B. 1988, in Shock Tubes and Waves, ed. H. Groenig, 671
- Ertl, T., Janka, H.-T., Woosley, S. E., Sukhbold, T., & Ugliano, M. 2016, ApJ, 818, 124
- Fernández, R. 2010, ApJ, 725, 1563
- . 2015, MNRAS, 452, 2071
- Fernández, R., Müller, B., Foglizzo, T., & Janka, H.-T. 2014, MNRAS, 440, 2763
- Fischer, T., Hempel, M., Sagert, I., Suwa, Y., & Schaffner-Bielich, J. 2014, EPJA, 50, 46
- Foglizzo, T. 2002, A&A, 392, 353
- Foglizzo, T., Scheck, L., & Janka, H.-T. 2006, ApJ, 652, 1436
- Foglizzo, T., Kazeroni, R., Guilet, J., et al. 2015, PASA, 32, e009
- Frisch, U. 1995, Turbulence (Cambridge University Press)
- Frisch, U., & Sulem, P. L. 1984, PhFl, 27, 1921
- Fryer, C. L., & Warren, M. S. 2002, ApJL, 574, L65
- . 2004, ApJ, 601, 391

- Fryxell, B., Müller, E., & Arnett, D. 1989, in Proceedings of the 5th Workshop on Nuclear Astrophysics, ed. W. Hillebrandt & E. Müller, 100
- Gefßner, A. 2014, Master's thesis, Ludwig-Maximilians-Universität München
- Grefenstette, B. W., Harrison, F. A., Boggs, S. E., et al. 2014, Nature, 506, 339
- Grinstein, F. F., Margolin, L. G., & Rider, W. J. 2007, Implicit Large Eddy Simulation (Cambridge University Press)
- Guilet, J., & Foglizzo, T. 2012, MNRAS, 421, 546
- Guilet, J., Sato, J., & Foglizzo, T. 2010, ApJ, 713, 1350
- Hammer, N. J., Janka, H.-T., & Müller, E. 2010, ApJ, 714, 1371
- Hanke, F. 2014, PhD thesis, Technische Universität München
- Hanke, F., Marek, A., Müller, B., & Janka, H.-T. 2012, ApJ, 755, 138
- Hanke, F., Müller, B., Wongwathanarat, A., Marek, A., & Janka, H.-T. 2013, ApJ, 770, 66
- Hannestad, S., & Raffelt, G. 1998, ApJ, 507, 339
- Heger, A. 2012, private communication
- Heger, A., & Woosley, S. E. 2010, ApJ, 724, 341
- Herant, M., Benz, W., Hix, W. R., Fryer, C. L., & Colgate, S. A. 1994, ApJ, 435, 339
- Hillebrandt, W., & Höflich, P. 1989, RPPh, 52, 1421
- Hobbs, G., Lorimer, D. R., Lyne, A. G., & Kramer, M. 2005, MNRAS, 360, 974
- Hobbs, T. J., Alberg, M., & Miller, G. A. 2016, PhRvC, 93, 052801
- Horowitz, C. J. 1997, PhRvD, 55, 4577
- . 2002, PhRvD, 65, 043001
- . 2016, in preparation
- Hüdepohl, L. 2014, PhD thesis, Technische Universität München
- Iwakami, W., Kotake, K., Ohnishi, N., Yamada, S., & Sawada, K. 2008, ApJ, 678, 1207
- . 2009, ApJ, 700, 232
- Iwakami, W., Nagakura, H., & Yamada, S. 2014, ApJ, 793, 5
- Janka, H.-T. 1999, unpublished
- . 2001, A&A, 368, 527
- . 2012, ARNPS, 62, 407

Bibliography

- Janka, H.-T., Hanke, F., Hüdepohl, L., et al. 2012, PTEP, 2012, 01A309
- Janka, H.-T., Melson, T., & Summa, A. 2016, e-print, arXiv:1602.05576
- Janka, H. T., & Müller, E. 1996, A&A, 306, 167
- Kageyama, A., & Sato, T. 2004, GGG, 5, 9005
- Kazeroni, R., Guilet, J., & Foglizzo, T. 2016, MNRAS, 456, 126
- Keil, W., Janka, H.-T., & Müller, E. 1996, ApJL, 473, L111
- Kifonidis, K., Plewa, T., Janka, H. T., & Müller, E. 2003, A&A, 408, 621
- Kifonidis, K., Plewa, T., Scheck, L., Janka, H.-T., & Müller, E. 2006, A&A, 453, 661
- Kitaura, F. S., Janka, H.-T., & Hillebrandt, W. 2006, A&A, 450, 345
- Kiziltan, B., Kottas, A., De Yoreo, M., & Thorsett, S. E. 2013, ApJ, 778, 66
- Kolmogorov, A. 1941, DoSSR, 30, 301
- Kraichnan, R. H. 1967, PhFl, 10, 1417
- Landau, L. D., & Lifshitz, E. M. 1987, Fluid Mechanics (Elsevier)
- Langanke, K., & Martínez-Pinedo, G. 2003, RvMP, 75, 819
- Lattimer, J. M., & Prakash, M. 2001, ApJ, 550, 426
- . 2016, PhR, 621, 127
- Lattimer, J. M., & Swesty, F. D. 1991, NuPhA, 535, 331
- Lentz, E. J., Bruenn, S. W., Hix, W. R., et al. 2015, ApJL, 807, L31
- Liebendörfer, M., Messer, O. E. B., Mezzacappa, A., & Hix, W. R. 2001, in American Institute of Physics Conference Series, Vol. 586, 20th Texas Symposium on Relativistic Astrophysics, ed. J. C. Wheeler & H. Martel, 472
- Liebendörfer, M., Messer, O. E. B., Mezzacappa, A., et al. 2002, in Proceedings of the 11th Workshop on Nuclear Astrophysics, ed. W. Hillebrandt & E. Müller, 126
- Maeda, K., Kawabata, K., Mazzali, P. A., et al. 2008, Science, 319, 1220
- Marek, A., Dimmelmeier, H., Janka, H.-T., Müller, E., & Buras, R. 2006, A&A, 445, 273
- Marek, A., & Janka, H.-T. 2009, ApJ, 694, 664
- Marek, A., Rampp, M., Hanke, F., & Janka, H.-T. 2014, e-print, arXiv:1404.1719
- Meakin, C. A., & Arnett, D. 2007, ApJ, 667, 448
- Melson, T. 2013, Master's thesis, Ludwig-Maximilians-Universität München
- Melson, T., Janka, H.-T., Bollig, R., et al. 2015a, ApJL, 808, L42

- Melson, T., Janka, H.-T., & Marek, A. 2015b, ApJL, 801, L24
- Mezzacappa, A., & Bruenn, S. W. 1993a, ApJ, 410, 740
- . 1993b, ApJ, 405, 637
- Mezzacappa, A., Liebendörfer, M., Cardall, C. Y., Bronson Messer, O. E., & Bruenn, S. W. 2004, in *Astrophysics and Space Science Library*, Vol. 302, *Astrophysics and Space Science Library*, ed. C. L. Fryer, 99
- Mezzacappa, A., Liebendörfer, M., Messer, O. E., et al. 2001, PhRvL, 86, 1935
- Müller, B. 2015, MNRAS, 453, 287
- Müller, B., & Janka, H.-T. 2015, MNRAS, 448, 2141
- Müller, B., Janka, H.-T., & Heger, A. 2012a, ApJ, 761, 72
- Müller, B., Janka, H.-T., & Marek, A. 2012b, ApJ, 756, 84
- . 2013, ApJ, 766, 43
- Müller, B., Viallet, M., Heger, A., & Janka, H.-T. 2016, e-print, arXiv:1605.01393
- Müller, E. 1998, in *Saas-Fee Advanced Course 27: Computational Methods for Astrophysical Fluid Flow*, ed. O. Steiner & A. Gautschy, 343
- Murphy, J. W., & Burrows, A. 2008, ApJ, 688, 1159
- Murphy, J. W., & Dolence, J. C. 2015, e-print, arXiv:1507.08314
- Murphy, J. W., Dolence, J. C., & Burrows, A. 2013, ApJ, 771, 52
- Nakamura, K., Kuroda, T., Takiwaki, T., & Kotake, K. 2014, ApJ, 793, 45
- Nakamura, K., Takiwaki, T., Kuroda, T., & Kotake, K. 2015, PASJ, 67, 107
- Nomoto, K., & Hashimoto, M. 1988, PhR, 163, 13
- Nordhaus, J., Burrows, A., Almgren, A., & Bell, J. 2010, ApJ, 720, 694
- O'Connor, E., & Couch, S. 2015, e-print, arXiv:1511.07443
- O'Connor, E., & Ott, C. D. 2011, ApJ, 730, 70
- Olive, K. A., & Particle Data Group. 2014, ChPhC, 38, 090001
- Panagia, N. 2013, AcPol, 53, 606
- Pejcha, O., & Thompson, T. A. 2012, ApJ, 746, 106
- Peng, X., Xiao, F., & Takahashi, K. 2006, QJRMS, 132, 979
- Plewa, T., & Müller, E. 1999, A&A, 342, 179
- Pons, J. A., Miralles, J. A., & Ibanez, J. M. A. 1998, A&AS, 129, 343

Bibliography

- Pope, S. B. 2000, Turbulent Flows (Cambridge University Press)
- Porter, D. H., & Woodward, P. R. 1994, ApJS, 93, 309
- Porter, D. H., Woodward, P. R., & Pouquet, A. 1998, PhFl, 10, 237
- Quirk, J. J. 1994, IJNMF, 18, 555
- Radice, D., Couch, S. M., & Ott, C. D. 2015, ComAC, 2, 7
- Radice, D., Ott, C. D., Abdikamalov, E., et al. 2016, ApJ, 820, 76
- Rampp, M. 2000, PhD thesis, Technische Universität München
- Rampp, M., & Janka, H.-T. 2002, A&A, 396, 361
- Reed, B. C. 2005, AJ, 130, 1652
- Reisswig, C., Haas, R., Ott, C. D., et al. 2013, PhRvD, 87, 064023
- Roberts, L. F., Ott, C. D., Haas, R., et al. 2016, e-print, arXiv:1604.07848
- Ronchi, C., Iacono, R., & Paolucci, P. S. 1996, JCoPh, 124, 93
- Rybicki, G. B., & Lightman, A. P. 2004, Radiative processes in astrophysics (Wiley-VCH)
- Scheck, L., Janka, H.-T., Foglizzo, T., & Kifonidis, K. 2008, A&A, 477, 931
- Scheck, L., Kifonidis, K., Janka, H.-T., & Müller, E. 2006, A&A, 457, 963
- Schmidt, W. 2014, Numerical Modelling of Astrophysical Turbulence (Springer)
- Sedov, L. I. 1959, Similarity and Dimensional Methods in Mechanics (Infosearch)
- Sreenivasan, K. R. 1995, PhFl, 7, 2778
- Stockinger, G. 2015, Master's thesis, Technische Universität München
- Strang, G. 1968, SJNA, 5, 506
- Sukhbola, T., Ertl, T., Woosley, S. E., Brown, J. M., & Janka, H.-T. 2016, ApJ, 821, 38
- Sumiyoshi, K., Yamada, S., Suzuki, H., et al. 2005, ApJ, 629, 922
- Summa, A. 2016, private communication
- Summa, A., Hanke, F., Janka, H.-T., et al. 2016, ApJ, 825, 6
- Suwa, Y., Kotake, K., Takiwaki, T., et al. 2010, PASJ, 62, L49
- Suwa, Y., Takiwaki, T., Kotake, K., et al. 2013, ApJ, 764, 99
- Suwa, Y., Yamada, S., Takiwaki, T., & Kotake, K. 2016, ApJ, 816, 43

- Sytine, I. V., Porter, D. H., Woodward, P. R., Hodson, S. W., & Winkler, K.-H. 2000, JCoPh, 158, 225
- Takiwaki, T., Kotake, K., & Suwa, Y. 2012, ApJ, 749, 98
- . 2014, ApJ, 786, 83
- Tamborra, I., Hanke, F., Janka, H.-T., et al. 2014a, ApJ, 792, 96
- Tamborra, I., Hanke, F., Müller, B., Janka, H.-T., & Raffelt, G. 2013, PhRvL, 111, 121104
- Tamborra, I., Raffelt, G., Hanke, F., Janka, H.-T., & Müller, B. 2014b, PhRvD, 90, 045032
- Tennekes, H., & Lumley, J. L. 1972, First Course in Turbulence (MIT Press)
- Utrobin, V. P., Wongwathanarat, A., Janka, H.-T., & Müller, E. 2015, A&A, 581, A40
- Wang, L., & Wheeler, J. C. 2008, ARA&A, 46, 433
- Wongwathanarat, A., Hammer, N. J., & Müller, E. 2010a, A&A, 514, A48
- Wongwathanarat, A., Janka, H.-T., & Müller, E. 2010b, ApJL, 725, L106
- . 2013, A&A, 552, A126
- Woosley, S. E., & Heger, A. 2007, PhR, 442, 269
- . 2015, ApJ, 810, 34
- Yamasaki, T., & Foglizzo, T. 2008, ApJ, 679, 607
- Yeung, P. K., & Zhou, Y. 1997, PhRvE, 56, 1746

Danksagung

Nach drei Jahren und vier Monaten Doktorarbeit und fast neun Jahren am Max-Planck-Institut für Astrophysik ist dies eine gute Gelegenheit, um die Beiträge einiger Menschen zu meiner Arbeit hervorzuheben.

Zuallererst bedanke ich mich herzlich bei *Thomas Janka*, der mir schon unmittelbar nach dem Abitur und dann in weiteren Praktika während meines Studiums die Gelegenheit gab, Einblicke in das faszinierende Forschungsgebiet der Kernkollaps-Supernovae zu erhalten. Seine ausdauernde Unterstützung in den vergangenen Jahren war beispiellos und auch in kritischen Phasen uneingeschränkt. Er hat sich stets Zeit genommen, um über Ergebnisse zu diskutieren und wichtige Denkanstöße für das Voranschreiten meiner Doktorarbeit zu geben. Vielen Dank dafür!

Ich bedanke mich bei den Mitarbeiterinnen und Mitarbeitern des Leibniz-Rechenzentrums (LRZ) und der Max Planck Computing & Data Facility (MPCDF), die bei technischen Problemen immer zügig und kompetent geholfen haben. Insbesondere danke ich *Elena Erastova* und *Markus Rapp* für die dreidimensionale Visualisierung meiner Simulationsdaten in diversen Videos und in Abbildung 4.4.

Andreas Marek danke ich sowohl für seine sehr gute Betreuung während meiner Praktika, als auch für seine andauernde Unterstützung bei der Weiterentwicklung von VERTEX-PROMETHEUS. Seine engagierte Arbeit an unserem Code hat die aufwändigen Simulationen überhaupt erst ermöglicht.

Ich bedanke mich bei *Florian Hanke*, der mir bei den ersten Rechnungen auf den Supercomputern geholfen hat. Bei Problemen mit den Simulationen hatte er stets einen guten Ratschlag für mich parat.

Meinem Bürokollegen *Thomas Ertl* – genannt „kleiner Thomas“ – danke ich für das freundschaftliche Miteinander. Da wir nahezu gleichzeitig angefangen haben, konnten wir uns gegenseitig motivieren und so insbesondere die anstrengenden letzten Phasen der Doktorarbeit meistern.

Alexander Summa möchte ich für die hervorragende Zusammenarbeit im Bereich der dreidimensionalen Simulationen danken. Auch das Ausarbeiten von Rechenzeitanträgen hat stets reibungslos geklappt. Ganz besonders danke ich ihm für seine Geduld beim Korrekturlesen etlicher Abschnitte dieser Arbeit.

Bei *Lorenz Hüdepohl* bedanke ich mich für seine pedantische Art und die vielen hilfreichen Antworten auf technische Fragen rund um unseren Code und die dazugehörige Auswertungssoftware.

Ich bedanke mich auch bei *Robert Bollig*, der durch sein umfassendes Wissen im Bereich des Neutrino-Transports und der Neutrino-Wechselwirkungen ein Ansprechpartner für diesbezügliche Fragen war.

Ewald Müller danke ich für sehr hilfreiche Diskussionen über numerische und hydrodynamische Probleme.

Je voudrais remercier *Maxime Viallet* pour les nombreuses et très utiles discussions sur l'hydrodynamique. Son engagement extraordinaire dans le passage de son projet à moi va certainement me faciliter l'entrée dans mon postdoc.

Merci beaucoup à *Jérôme Guilet* pour les propositions de correction concernant le chapitre 5.

Ich bedanke mich bei *Else Pllumbi* für die Übersetzung der vorangegangenen zwei Paragrafen.

Bei *Oliver Just* bedanke ich mich dafür, dass er sich bei hydrodynamischen Fragen immer Zeit für ausführliche Diskussionen genommen hat. Ebenso danke ich ihm für das Korrekturlesen des Kapitels 3.

Ich bedanke mich bei unserem Praktikanten *Aaron Döring* für die Erstellung der Abbildungen 5.9 und 5.10.

Marius Almanstötter, dessen Bachelorarbeit ich betreut habe, danke ich für sein außerordentliches Engagement und die gute Zusammenarbeit.

Auch allen anderen (ehemaligen) Gruppenmitgliedern, die hier nicht explizit erwähnt wurden, danke ich herzlich für ihre andauernde Hilfsbereitschaft, den freundschaftlichen Umgang und die vielen schönen Stunden auch außerhalb der Arbeit. Durch die tolle Atmosphäre in Thomas' Arbeitsgruppe werde ich die letzten Jahre in bester Erinnerung behalten.

Danke, *Fleur*, für deine Unterstützung, deine Geduld und so vieles mehr...